A HYPERPLASTICITY MODEL FOR CLAY BEHAVIOUR: AN APPLICATION TO BANGKOK CLAY

by

Suched Likitlersuang

Balliol College

Michaelmas Term 2003

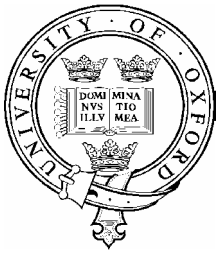

A thesis submitted for the degree of Doctor of Philosophy at the University of Oxford

A HYPERPLASTICITY MODEL FOR CLAY BEHAVIOUR: AN APPLICATION TO BANGKOK CLAY

by

Suched Likitlersuang

Balliol College

Michaelmas Term 2003

A thesis submitted for the degree of Doctor of Philosophy at the University of Oxford

ABSTRACT

The main purpose of this thesis is the development of a new constitutive soil model emphasising the use of thermodynamic principles. This new approach to plasticity modelling, termed 'hyperplasticity', was first developed by Collins and Houlsby (1997) and Houlsby and Puzrin (2000). This idea has been further extended to continuous hyperplasticity in which smooth transitions between elastic and plastic behaviour can be modelled (Puzrin and Houlsby, 2001b). Applying hyperplasticity to this researh, a kinematic hardening model specified by means of two scalar functionals is used to accommodate the effect of stress history on stiffness. A rate-dependent calculation for an approximation of the incremental stress-strain response is introduced. The model developed in the research is named 'kinematic hardening modified Cam-clay (KHMCC) model' and requires eight parameters (plus an extra parameter for rate-dependent analysis). Triaxial test results from the Asian Institute of Technology (AIT) and cyclic undrained triaxial data from Chulalongkorn University are employed to establish the soil parameters for the new model. The model is initially developed in terms of triaxial stress-strain parameters for the purpose of comparison with the experimental data on Bangkok clay. The model is expressed in FORTRAN code for implementation into the OXFEM finite element program. Two examples of real geotechnical projects in Bangkok (a road embankment and tunnelling in soft ground) are analysed under plane strain conditions. Comparisons of the numerical analysis results with field data are made. In addition, factors affecting the results of the analysis such as stress history and K_0, are investigated.

ACKNOWLEDGEMENT

The research would not have been possible without the support of many people whom it is appropriate to acknowledge and thank.

Firstly, I would like to express my profound gratitude and sincere appreciation to Professor Guy T. Houlsby for giving valuable suggestions and guidance throughout my research. I would like to extend my gratitude to Chair Professor A.S. Balasubramaniam for providing triaxial experimental data from AIT. I am also thankful to Assistant Professor Supot Teachavorasinskun for offering a set of cyclic undrained triaxial data from Chulalongkorn University.

Most importantly the support staff and friends in the Civil Engineering research group, I specially thank Dr. Harvey J. Burd for his recommendation on the OXFEM finite element program as well as its numerical implementation. I owe a debt of gratitude to many of my colleagues, in particular to Nguyen Dinh Giang and John Pickhaver and the support staffs, Alison, Karen, Bob as well as the old secretary, Nicola.

I am very grateful to all of my lecturers at Chulalongkorn University for providing general civil engineering background during my study in undergraduate level. The knowledge imparted to me by all the lecturers at AIT during the masters course of my study helped strengthen my knowledge in geotechnical engineering.

I appreciate many helpful discussions with Jarungwit Wongsaroj, who is undergoing a numerical research on tunnelling at Cambridge University. I would also like to thank, Nopphol Witvorapong (B.A., PPE, St. Hugh's college) and Paradorn Rangsimaporn (D.Phil student, Department of Politics and IR, St. Antony's college) for their generous proof and corrections of my thesis draft.

I owe greatest debt of gratitude to my family for their continuous inspiration and moralistic as well as financial support for the first two years of my course. I also acknowledge with gratitude my sponsorship, the Thai Royal Government, for the last year of my course.

Over the course of my doctorate I have many friends throughout the Oxford University in particular in Balliol College, Holywell Manor, 49 Banbury Road and Thai Society. Many thanks are due to all my friends at Oxford University.

TABLE OF CONTENTS

LIST OF SYMBOLS

Symbol	Meaning
a	KHMCC model parameter controlling rate of change of stiffness
a_p	KHMCC model parameter a for p term in triaxial model
a_q	KHMCC model parameter a for q term in triaxial model
b	KHMCC model parameter controlling rate of change of stiffness
b	parameter related to effect of immediate principal stress
b_p	KHMCC model parameter b for p term in triaxial model
b_q	KHMCC model parameter b for q term in triaxial model
c	friction stress in slip component
c_i	friction stress in each slip component of multiple yield surface model
$\hat{c}$	friction function in slip component of infinite yield surface model
c'	cohesion parameter (Mohr-Coulomb failure criteria)
c^*	mathematical constraint
d	dissipation function
$\mathbf{\Delta d_{nG}}^i$	vector of incremental nodal displacements
e	void ratio
e	choice of four energy potentials (u, f, h, g)
f	specific Helmholtz free energy
f'_c	compressive strength of concrete
$\mathbf{\Delta f_G}^i$	vector of incremental nodal forces
g	specific Gibbs free energy
g_x	shear modulus gradient
$\hat{g}$	shear modulus function
h	specific enthalpy
h_c	damping ratio
i	trough width parameter
p	mean effective stress (triaxial stress parameter)
p_0	reference pressure (KHMCC model)
p_a	reference pressure (power function of modulus)
p_c	reference pressure (MCC model)
p_{ini}	initial pressure (after consolidation)
p_m	maximum past pressure
p_x	reference of yield surface
q	deviatoric stress (triaxial stress parameter)
q_u	unconsolidated undrained shear strength
r	KHMCC model parameter controlling plastic stiffness
n	number of yield surface
n	degree of power function
s	specific entropy
s_u	undrained shear strength
t	time
u	specific internal energy
Δu	excess pore pressure
u, v, w	displacement components in Cartesian coordinates
v	specific volume
w	flow potential (rate-independent material)

y	yield function
y_i	each yield function of multiple yield surface model
$\hat{y}$	yield functional of infinite yield surface model
z	force potential (rate-dependent material)
z	depth
AS	axi-symmetry condition
CID	isotropic consolidated drained triaxial compression test
CIU	isotropic consolidated undrained triaxial compression test
CK_0DC	K_0 consolidated drained triaxial compression test
CK_0DE	K_0 consolidated drained triaxial extension test
CK_0UC	K_0 consolidated undrained triaxial compression test
CK_0UE	K_0 consolidated undrained triaxial extension test
CR	compression ratio
CRS	constant rate of strain consolidometer test
CSL	critical state line
CSSM	critical state soil mechanics
E	elastic Young's modulus
E'	drained Young's modulus
E_{50}	secant Young's modulus at 50% of strength
E_p	plastic Young's modulus
E_{sec}	secant Young's modulus at particular stress
E_T	tangential Young's modulus
E_u	undrained Young's modulus
EVM	elastic Von Mises model
FEM	finite element method
G	elastic shear modulus
G_{ini}	initial shear modulus
G_{sec}	secant shear modulus at particular stress
H	hardening parameter
H_p	hardening parameter for p term
H_q	hardening parameter for q term
H_i	each of hardening parameters of multiple yield surface model
H_{pi}	each of p-hardening parameters of multiple yield surface model
H_{qi}	each of q-hardening parameters of multiple yield surface model
$\hat{H}$	hardening function of infinite yield surface model
$\hat{H}_p$	p-hardening function of infinite yield surface model
$\hat{H}_q$	q-hardening function of infinite yield surface model
I_1	first stress invariant
J	cross-coupling between shear and volumetric stress-strain
J_2	second stress invariant
J_3	third stress invariant
K	elastic bulk modulus
K	in-situ stress ratio ($K = \sigma_h / \sigma_v$)
K_0	coefficient of earth pressure at rest
K_a	coefficient of active pressure
$\mathbf{K}^{\mathbf{e}}$	elastic stiffness matrix
$\mathbf{K}_{\mathbf{G}}^{\ i}$	incremental global stiffness matrix

K_p	plastic bulk modulus
K_{sec}	secant bulk modulus at particular stress
K_T	tangential Young's modulus
KHMCC	kinematic hardening modified Cam-clay model
M	slope of critical state line
M_C	magnitude of critical state cone in compression side
M_E	magnitude of critical state cone in extension side
MCC	modified Cam-clay model
N	number of testing cycles
NCL	normal consolidated line
OCR	overconsolidated ratio
OXFEM	Oxford finite element program
P_a	active force
PS	plane strain condition
RR	recompression ratio
S	transverse settlement trough due to tunnel excavation
$S_{\max}$	maximum settlement above tunnel axis
SBS	state boundary surface
UU	unconsolidated undrained shear test
V_L	volume loss
α	internal variable
$\dot{\alpha}$	rate of change of internal variable
α_i	each of internal variables
$\hat{\alpha}_i$	each of internal variable functions
α_{ij}	internal variable tensor
$\dot{\alpha}_{ij}$	rate of change of internal variable tensor
$\hat{\alpha}_{ij}$	internal variable tensor function
α_p	internal variable for p term in triaxial model
α_{pi}	each of internal variables for p term in triaxial model
$\hat{\alpha}_p$	internal variable function for p term in triaxial model
α_q	internal variable for q term in triaxial model
α_{qi}	each of internal variables for q term in triaxial model
$\hat{\alpha}_q$	internal variable function for q term in triaxial model
β	modified isotropic hardening variable
γ	engineering shear strain
$\gamma_{xy}, \gamma_{xz}, \gamma_{yz}$	direction shear components in Cartesian coordinates
$\gamma_{rz}, \gamma_{r\theta}, \gamma_{\theta z}$	direction shear components in cylindrical coordinates
γ_{SA}	single amplitude shear strain
ε	one-dimensional strain
$\dot{\varepsilon}$	rate of change of strain
$\varepsilon_1, \varepsilon_2, \varepsilon_3$	major, intermediate, minor principal strain
$\varepsilon_h, \varepsilon_v$	horizontal and vertical strain
$\varepsilon_x, \varepsilon_y, \varepsilon_z$	direction strain components in Cartesian coordinates

$\varepsilon_z, \varepsilon_r, \varepsilon_\theta$	direction strain components in cylindrical coordinates
ε_v	volumetric strain
ε_{ij}	strain tensor
ε_v^e	elastic volumetric strain
ε_v^p	plastic volumetric strain
ε_s	shear strain
ε_s^e	elastic shear strain
ε_s^p	plastic shear strain
η	internal coordinate
η	stress ratio (q/p)
η^*	active internal coordinate
θ	temperature
θ	Lode's angle
κ	slope of swelling line (e – ln p plot)
κ^*	slope of swelling line (ln v – ln p plot)
κ'	slope of swelling line at half of maximum past stress
λ	slope of NCL (e – ln p plot)
λ	arbitrary non-negative multiplier for Legendre-Fenchel transformation
λ^*	slope of NCL (ln v – ln p plot)
$\hat{\lambda}$	λ function
μ	viscosity coefficient
υ	Poisson's ratio
υ'	angle of dilation
υ'	drained Poisson's ratio
υ_u	undrained Poisson's ratio
σ	total stress
$\dot{\sigma}$	rate of change of stress
σ'	effective stress
σ_0	reference stress
$\sigma_1, \sigma_2, \sigma_3$	major, intermediate, minor principal stress
σ'_h, σ'_v	horizontal and vertical effective stress
$\sigma'_{h0}, \sigma'_{v0}$	horizontal and vertical in-situ effective stress
$\sigma_x, \sigma_y, \sigma_z$	direction stress components in Cartesian coordinates
$\sigma_z, \sigma_r, \sigma_\theta$	direction stress components in cylindrical coordinates
σ_m	maximum past stress
σ_{ij}	total stress tensor
σ'_{ij}	effective stress tensor
ϕ'	friction angle parameter (Mohr-Coulomb failure criteria)
ϕ'_{TC}	critical state angle of shearing resistance in triaxial compression
ϕ'_{TE}	critical state angle of shearing resistance in triaxial extension
χ	dissipative generalised stress
$\overline{\chi}$	generalised stress

χ_{ij}	dissipative generalised stress tensor
$\overline{\chi}_{ij}$	generalised stress tensor
χ_p	dissipative generalised stress for p term in triaxial model
χ_q	dissipative generalised stress for q term in triaxial model
$\overline{\chi}_p$	generalised stress for p term in triaxial model
$\overline{\chi}_q$	generalised stress for q term in triaxial model
$\pi-$plane	deviatoric plane
Λ	arbitrary non-negative multiplier for constraint
$\langle\ \rangle$	Macaulay bracket
	Bounding surface model parameters, Dafalias and Herrmann (1982)
n	parameters for non-linear hardening
H	total stiffness
H_0	stiffness parameter
H_p	plastic stiffness at image point
δ	mapping distance
σ^*	image stress
	Kinematic hardening model parameters, Wood (1995)
b	distance from current stress to conjugate stress
k	parameter controlling rate of destructuration strain
$(p_0,0)$	centre of reference surface
(p_α,q_α)	centre of bubble
r	size of structure surface
r_0	initial degree of structure
rs	reference surface
ss	structure surface
A	destructuration parameter controlling influence of volumetric and distortion strain
$B,\ \psi$	soil constants controlling contribution and rate of change of hardening
M_θ	ratio of semi-axes of yield surface
R	size of bubble
ε_d	destructuration strain
η_0	dimensionless shear stress
σ_c	conjugate stress
	Three-surface kinematic hardening model, Atkinson and Stallebrass (1991)
b_1	dot product between movement vector from history surface to bounding surface and normal vector at bounding surface
b_2	dot product between movement vector from yield surface to history surface and normal vector at history surface
h	plastic stiffness
h_0	elastic stiffness
$(p_0,0)$	centre of bounding surface
(p_a,q_a)	centre of history surface
(p_b,q_b)	centre of yield surface
H_1	plastic stiffness parameter 1
H_2	plastic stiffness parameter 2

S	size of yield surface
T	size of history surface
β	movement vector from history surface to bounding surface
γ	movement vector from yield surface to history surface
ψ	hardening modulus parameter
	MIT-E3 model, Whittle (1993)
b	direction of yield surface axis
h	function of critical state cone
k	half range of critical state cone
(p_{rev}, q_{rev})	stress reversal point
r_c	parameter describing location of current stress state relative to failure surface
r_x	relative ratio between orientation of yield surface and critical state cone
C_c	friction angles parameter measured from triaxial compression tests
C_e	friction angles parameter measured from triaxial extension tests
C, n	material constant characterising non-linear behaviour in unloading
H	elasto-plastic modulus
(P_p, P_q)	plasticity flow direction
(Q_p, Q_q)	yield surface gradient
S_t	material parameter influencing strain softening behaviour
ξ	critical state cone axis
ξ_p, ξ_s	dimensionless parameters relating current stress state to stress reversal state
ζ	scalar obtained from the consistency requirement
κ_0	initial slope of swelling line in v-ln p plot
γ , h	dimensionless input parameter for non-linear hardening rule
$d\lambda$	plastic scalar multiplier
η_{K0NC}	stress ratio at K_0 normally consolidated condition
Ψ_0	material constant controlling rate yield surface's rotation
ω	parameter describing non-linearity at small strain due to undrained shearing
χ	magnitude of reversal strain

Chapter 1
Introduction

In soil mechanics research many constitutive models are currently built in terms of sophisticated mathematics which can be difficult to employ in geotechnical engineering practice. This research therefore aims to develop a new constitutive soil model for application in engineering practice and also to capture the main characteristics of soil behaviour.

There are many different groups of constitutive equations used to characterise the stress-strain-strength behaviour of materials. These constitutive models should be contrasted with the majority of conventional design methods, where much simpler representations of material behaviour are used. Examples of conventional design methods are stability analyses, typically assuming rigid perfectly plastic behaviour; while separate deformation calculations often assume linear elastic behaviour.

1.1 Real soil behaviour

Practical analyses of geotechnical problems at this time still often assume material behaviour to be linear elastic. However, real soils do not simply behave linear elastically. Real soil behaviour is highly nonlinear, with both strength and stiffness depending on stress and strain level. For realistic predictions, a more complex constitutive model is therefore required. Before delving into the constitutive theory, it is useful to consider real soils and identify some important aspects of their behaviour. Thus, the following section will begin by considering the behaviour of soils.

The stress-strain behaviour of soils can be divided into two categories: elastic and elasto-plastic behaviour. However, it is well established that this behaviour is controlled by strain amplitude. For instance, soils can be regarded as perfectly elastic (fully recoverable) only under extremely small strain levels, and as the strain amplitude increases the apparent stiffness decreases. The most challenging problem is how to describe, accurately, the smooth transition zone varying from the small strain level (elastic) to the large strain level (elasto-plastic). Several experimental researches show that the transition of the stiffness with strain level depends on the overconsolidation ratio (OCR) and the magnitude of the mean effective stress (p). An

example of the variation of stiffness with strain is presented by Soga *et al.* (1995), see Figure 1.1, where the result from four torsional tests on isotropically normally consolidated kaolin varied the stress level. Puzrin and Burland (1998) illustrate the small-strain behaviour of soils, dividing behaviour into three regions by means of strain level: linear elastic region (LER), small strain region (SSR) and large scale yield state. The initial stress-strain curve is linear in the LER and continues with logarithmic stress-strain relation in the SSR. This idea provides a good agreement with the small-strain behaviour of samples of Bothkennar clay.

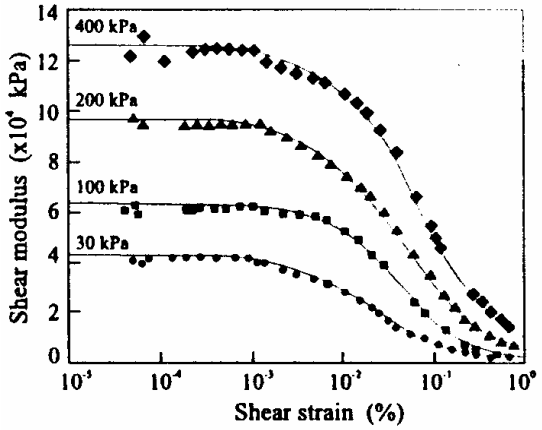

Figure 1.1 Dependence of shear stiffness on stress level (Soga *et al.*, 1995)

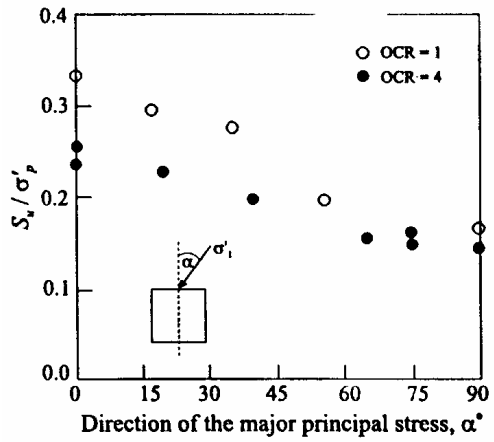

Figure 1.2 Undrained shear strength anisotropy of Boston Blue Clay (Seah, 1990)

Another feature of the stress-strain curve is that there is usually an unload-reload loop called a hysteresis loop. The openness of the hysteresis loop increases with strain amplitude. This behaviour is actually an effect of the immediate past history of the soil. Experimental observation shows that the tangential stiffness observed for a subsequent stress path depends on the immediate past history of the soil. Stress paths which represent a continuation of the immediate past stress path result in the lowest stiffness, and those which involve a complete reversal of direction result in the highest stiffness. Intermediate values are observed for stress paths that represent a sudden change of direction from the immediate past history. An example of the effect of immediate (or recent) stress history is given by Atkinson *et al.* (1990), and will be studied in more detail in chapter 2.

In recent years special testing devices such as true triaxial, directional shear cell and hollow cylinder apparatus have been developed. The effect of the magnitude of the intermediate principal stress (σ_2) can be investigated using this special

equipment. The relative magnitude of the intermediate principal stress (σ_2) is expressed by the value of $b = \frac{\sigma_2 - \sigma_3}{\sigma_1 - \sigma_3}$. For example, the undrained shear strength of undisturbed Haney clay in plane strain condition is some 10% higher than in triaxial compression, according to Vaid and Campanella (1974).

An anisotropic behaviour of soils is also observed by directional shear testing. In fact, soils are likely to be isotropic in the plane normal to its deposited direction, and are therefore called cross anisotropic or transversely isotropic. For instance, the data on the undrained shear strength of reconsolidated Boston Blue Clay varied the orientation of the major principal stress (σ_1) to the direction of deposition (Seah, 1990). It shows that the undrained shear strength drops by 50% as the angle of σ_1 to the deposited direction increases from 0^o-90^o as shown in Figure 1.2.

1.2 Problems associated with soil models

Due to the complexity of real soil behaviour, a single constitutive model that can describe all facets of behaviour, with a reasonable number of input parameters, has not been achieved. Consequently, there are many soil models available, each of which has different advantages and disadvantages. The constitutive soil models can be divided into two groups: elastic and elasto-plastic models.

Firstly, the elastic constitutive models are considered. The simple linear isotropic elastic models, which require only two material parameters, do not simulate any of important behaviour of real soil identified above, especially the change in stiffness. Although, the linear cross-anisotropic elastic models, which require 5 parameters, can reproduce anisotropic stiffness behaviour; they still do not describe the change in stiffness. Nonlinear elastic models, in which the material parameters vary with stress-strain level, give a substantial improvement on the shape of stress-strain curve; however, they still fail to model other behaviour. In particular, they never offer an irrecoverable or plastic strain along an unload-reload path.

Secondly, the elasto-plastic constitutive models are introduced. Tresca and Von Mises elastic perfectly plastic material models (Figure 1.3(a) and 1.3(b)), which require an extra input parameter than elastic models, are not suitable for all soils. This is because they assume that the stress-strain characteristic does not depend on the mean effective stress (p). Thus, the extended Von Mises yield function, known as a

Drucker-Prager (1952) yield function is considered instead (Figure 1.4(a)). However, the Von Mises model can be used to simulate the undrained behaviour of saturated clay, which the input parameter plays the role as the undrained shear strength (s_u).

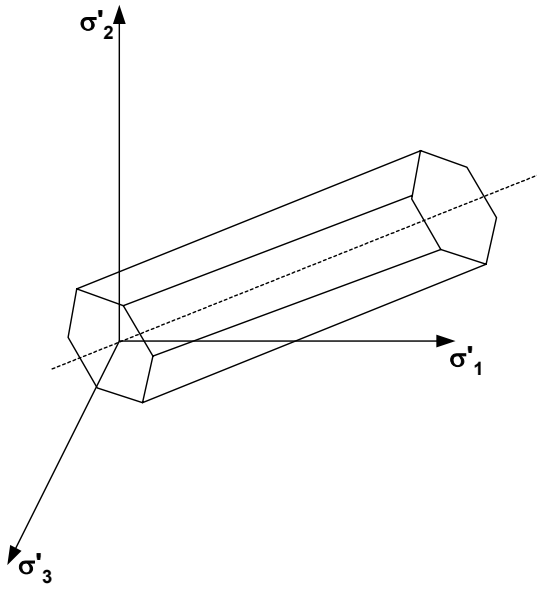

Figure 1.3 (a) Tresca yield surface in principal stress space

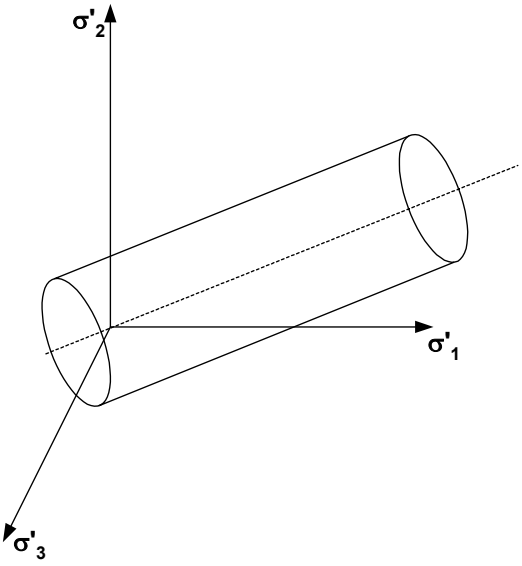

Figure 1.3 (b) Von Mises yield surface in principal stress space

The Mohr-Coulomb is the most well-known elastic perfectly plastic soil model (see Figure 1.4(b)). This still however has no requirement of hardening/softening law. The Mohr-Coulomb elastic perfectly plastic model needs at least two extra input parameters from elastic models: cohesion and friction angle (c', ϕ'). Furthermore, there are some modifications of the Mohr-Coulomb model such as:

(i) using two different friction angles based on conventional triaxial compression and extension results (ϕ'_{TC}, ϕ'_{TE}); and

(ii) adding the plastic potential function which requires the angle of dilation (υ') and non-associated flow rule to describe the dilation behaviour, especially for dense sands.

The problem with the Mohr-Coulomb model is a discontinuity of the expression at the corners in the deviatoric plane (π-plane) as shown in Figure 1.5. As a result, other failure surfaces have been suggested which are continuous and correlate more with experimental result in the π-plane. Matsuoka and Nakai's criteria is the most well known, see Figure 1.5.

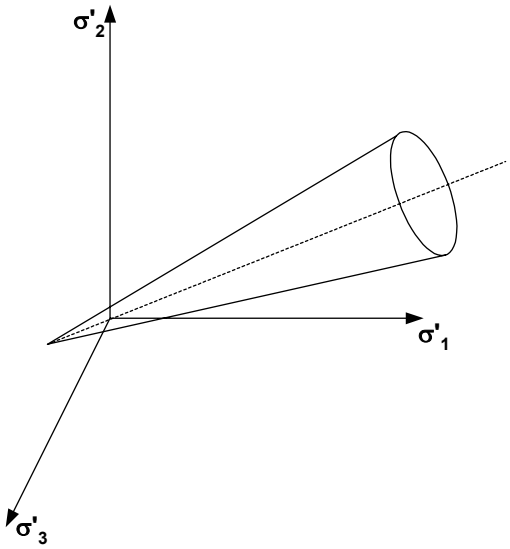

Figure 1.4(a) Drucker-Prager yield surface in principal stress space

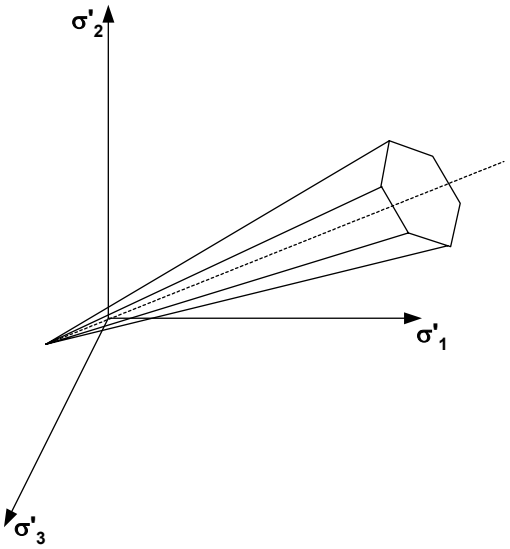

Figure 1.4(b) Mohr-Coulomb yield surface in principal stress space

However, the elastic perfectly plastic models behave as purely elastic when the stress state is inside the yield surface and purely plastic on the yield surface. This is far from the real soil behaviour. Hardening/softening plasticity formulations can be introduced to improve the stress-strain behaviour beyond the yield state. A simple possibility of the mathematic formulation is in the form of exponential function, which gradually increases/decreases from the yield strength until an asymptotic value is reaches, playing the role of a residual strength.

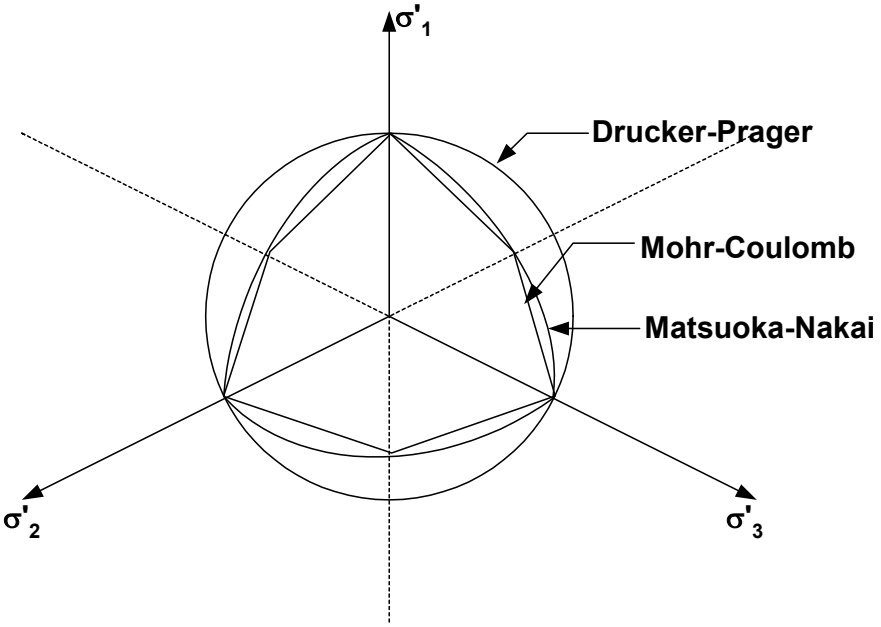

Figure 1.5 Failure surfaces in the deviatoric plane (π-plane)

In 1960's, the critical state models, which will be described in more detail in chapter 2, became the most successful models to describe normally consolidated soil behaviour. The models still have some drawbacks which should be improved such as:

(i) they behave as the purely elastic inside the yield surface,

(ii) they disregard the effect of immediate stress history; and

(iii) they ignore the anisotropic behaviour.

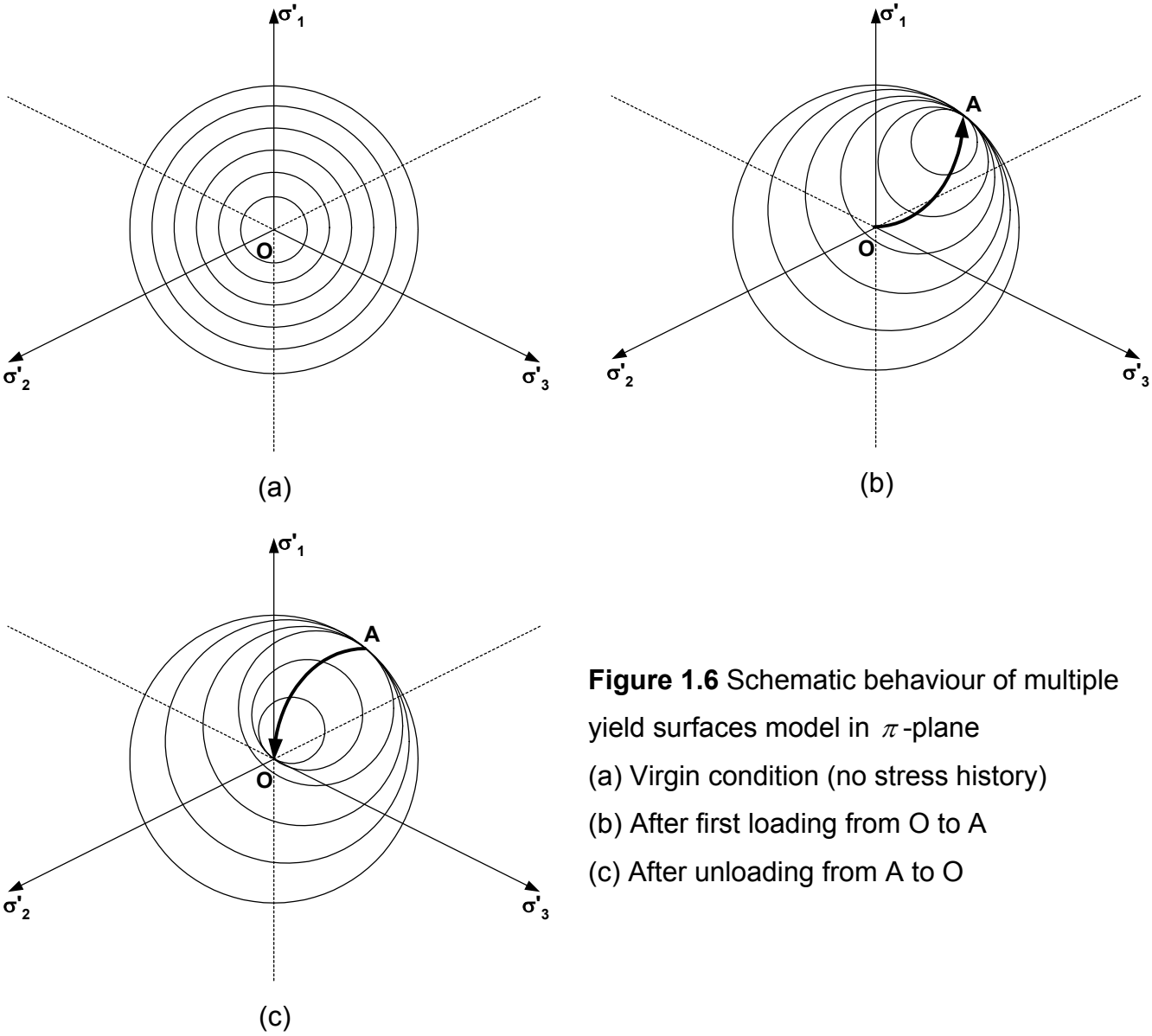

Figure 1.6 Schematic behaviour of multiple yield surfaces model in π-plane
(a) Virgin condition (no stress history)
(b) After first loading from O to A
(c) After unloading from A to O

Presently there are several plasticity theories which try to improve the problems of the critical state soil models. A multiple yield surface model is one possible approach that has been suggested to model the aforementioned effects (see Figure 1.6). The use of kinematic hardening plasticity with multiple yield surfaces has proved to be a convenient framework for modelling the pre-failure behaviour of

soils. This is because it can give a gradual change in stiffness, as more surfaces can be used to increase the smoothness of the change. Furthermore, it is capable of describing the effects of the immediate past history as well. The improvement of anisotropic behaviour can be further included in the model.

1.3 Research objectives and structure of the thesis

Many plasticity theories are used and combined together to predict the stress-strain response of soil in the overconsolidated state. The new constitutive model for soil currently being developed is the multi yield surface type of model. Chapter 2 presents the background of constitutive soil models. Three examples of recently developed soil models are illustrated; moreover, the model predictions and comparisons are addressed in chapter 2.

A new development of a soil model based on thermomechanics is introduced in chapter 3. The constitutive formulations in this chapter are developed based on the modified Cam-clay model, which are presented in triaxial stress-strain parameters. The incremental stress-strain calculation algorithms based on both rate-independence and rate-dependence are presented in chapter 3.

Chapter 4 illustrates the experimental data from Bangkok clay, carried out by Asian Institute of Technology (AIT) and Chulalongkorn University in Thailand. The geological background for Bangkok clay and the testing programmes are stated here. Prediction series of triaxial tests with the soil models are illustrated in chapter 5. Comparisons between predictions and the experimental data from Bangkok clay are also shown in chapter 5.

Chapter 6 explains the translation of the soil models from the triaxial stress-strain parameters to generalised stress-strain parameters. The two-dimensional soil models are implemented into the finite element program as new material subroutines. A series of tests, which simulate the triaxial condition to test the new subroutines, are carried out and presented in chapter 6. Two demonstrations using the models are described in chapter 7. The comparisons between the analysis result and monitoring data are also described in this chapter.

Finally, the conclusions on the development of new soil models are discussed in chapter 8. Developments for future research are stated in this last chapter.

Chapter 2
Constitutive model for soil

A simple elastic theory is used to model the basic features of the stress-strain behaviour of soils in routine engineering. An example is the calculation of final settlement of a rigid foundation, in which a single parameter for soil stiffness or flexibility (such as the coefficient of volume change, m_v) will be sufficient to provide the solution. However, additional predictions such as profiles of surface and subsurface settlement, horizontal and vertical movements and soil-structure interaction, require a relatively complex calculation and will usually need non-linear stress-strain theory.

2.1 Constitutive models for soil

A general constitutive soil model can be written in the following form:

$$d\varepsilon = F\left(d\sigma, dt\right) \tag{2.1}$$

Note that $d\sigma$ and dt represent changes in effective stresses (not total stresses as in other material models such as models for steel and concrete) and time respectively. However, most soil models have been developed from the results of laboratory tests with axi-symmetry condition (for example triaxial and oedometer tests). Consequently, and for simplicity, the Cambridge parameters for stress and strain are used to describe the stress-strain behaviour:

$$\begin{aligned} p &= \frac{\left(\sigma_a + 2\sigma_r\right)}{3}; \quad q = \left(\sigma_a - \sigma_r\right) \\ \varepsilon_v &= \left(\varepsilon_a + 2\varepsilon_r\right); \quad \varepsilon_s = \frac{2\left(\varepsilon_a - \varepsilon_r\right)}{3} \end{aligned} \tag{2.2}$$

where the subscripts *a* and *r* refer to axial and radial directions. The parameters *p* and ε_v are mean effective stress and volumetric strain, whereas *q* and ε_s are deviatoric stress and shear strain respectively. These parameters are related to the bulk modulus *K* and shear modulus *G* by

$$K = \frac{dp}{d\varepsilon_v}; \quad 3G = \frac{dq}{d\varepsilon_s} \tag{2.3}$$

Note that the multiplier 3 is needed to ensure that G corresponds to the general definition used in solid mechanics. Graham and Houlsby (1983) introduce a general constitutive equation for elastic anisotropic soil as

$$\begin{Bmatrix} dp \\ dq \end{Bmatrix} = \begin{bmatrix} K^* & J \\ J & 3G^* \end{bmatrix} \cdot \begin{Bmatrix} d\varepsilon_v \\ d\varepsilon_s \end{Bmatrix} \tag{2.4}$$

where J results in cross-coupling between shear and volumetric behaviour. In the case of naturally deposited soil, the stiffness depends on mode of deposition and its stress history. The superscript * is introduced to distinguish the anisotropic modulus from the isotropic modulus.

For a material which is elastic and isotropic, shear and volumetric stiffness are decoupled, that is, $J = 0$. The bulk modulus and shear modulus become elastic following Hooke's law, and the elastic constitutive equation can be written in the form:

$$\begin{Bmatrix} d\varepsilon_v^e \\ d\varepsilon_s^e \end{Bmatrix} = \begin{bmatrix} 1/K & 0 \\ 0 & 1/3G \end{bmatrix} \cdot \begin{Bmatrix} dp \\ dq \end{Bmatrix} \tag{2.5}$$

where K, G are elastic bulk modulus and elastic shear modulus respectively. Note that the elastic parameters can also be defined in the term of Young's modulus (E) and Poisson's ratio (υ) by the relations $G = \dfrac{E}{2 \cdot (1+\upsilon)}$ and $K = \dfrac{E}{3 \cdot (1-2\upsilon)}$.

2.2 Classical soil models

Many early developments of soil modelling are often referred to collectively as Critical State Soil Mechanics (CSSM), introduced by Schofield and Wroth (1968). CSSM combines three well-known concepts: the critical state line, normalisation with respect to pre-consolidation pressure, and the state boundary surface (SBS). Based on the critical state concept, a complete mathematical model of soil behaviour was created by Roscoe, et al. (1963) and called Cam-clay model. The original Cam-clay model developed for normally overconsolidated clay assumes that the energy is only dissipated due to plastic shear distortion. Roscoe and Burland (1968) subsequently developed the modified Cam-clay model (MCC), which considers both plastic volumetric strain and plastic shear distortion in the formulation of the energy dissipation equation.

The shape of modified Cam-clay yield locus is assumed to be elliptical, as shown in Figure 2.1(a). The equation of the yield locus is:

$$y = p^2 + \frac{q^2}{M^2} - pp_c = 0 \tag{2.6}$$

Making use of the state boundary surface as a yield surface and combining this with an associated flow rule, the constitutive equation of modified Cam-clay can be derived. The constitutive equation for plastic response may be expressed as:

$$\begin{Bmatrix} d\varepsilon_v \\ d\varepsilon_s \end{Bmatrix} = \begin{bmatrix} \frac{(\lambda-\kappa)(M^2p^2-q^2)}{pv(M^2p^2+q^2)} + \frac{\kappa}{pv} & \frac{2q(\lambda-\kappa)}{v(M^2p^2+q^2)} \\ \frac{2q(\lambda-\kappa)}{v(M^2p^2+q^2)} & \frac{4pq^2(\lambda-\kappa)}{v(M^4p^4-q^4)} + \frac{1}{3G} \end{bmatrix} \cdot \begin{Bmatrix} dp \\ dq \end{Bmatrix} \tag{2.7}$$

where v is a specific volume defined by $v = 1 + e$, e is a void ratio, p_c is the measure of size of the yield surface which depends on the stress history, and M, λ, as well as κ are the soil parameters that define the state boundary surface as shown in Figure 2.1. (Note that the elastic bulk modulus for the MCC model is defined as: $K = \frac{pv}{\kappa}$) Thus, the complete description of the model requires five parameters to specify the shape and size of the yield locus at a given pressure and specific volume, as well as the elastic properties of the material.

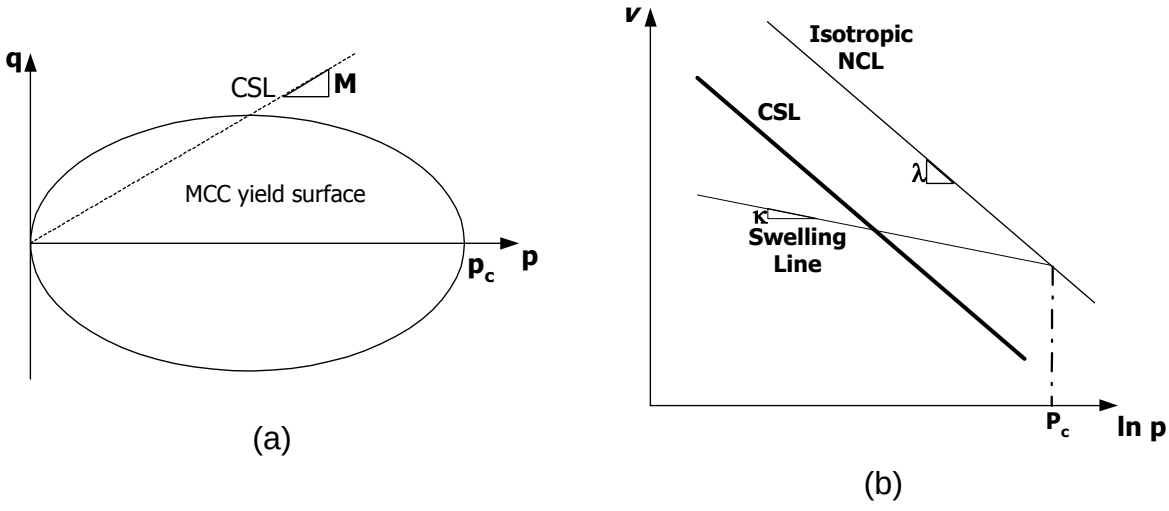

Figure 2.1 (a) Yield locus of Modified Cam-clay model; (b) Critical state soil parameters definition

The basic critical state model is particularly successful in describing the principal features of soft clay behaviour. The model provides good predictions of volumetric strain for normally consolidated soils subjected to isotropic consolidation.

However, it also has disadvantages. It does not describe anisotropic consolidation conditions because the shape of the modified Cam-clay yield surface is symmetric about the *p*-axis. It also gives poor predictions for heavily overconsolidated clay, in particular for shear strains, since it assumes purely elastic and reversible inside state boundary surface.

2.3 Development in soil models

In order to represent more realistic soil behaviour in a model, it is necessary to introduce plasticity within the SBS. To date, several approaches have been proposed. There are two main ideas that are often used to introduce plastic strain inside the SBS. The first involves mapping the stress inside the SBS to an image point on an extra surface usually known as the bounding surface. The plastic behaviour is obtained by relating the stress and the image points by means of the hardening rule. Examples are the bounding surface model by Dafalias and Herrmann (1982), the Hashiguchi model by Hashiguchi (1985); and the MIT-E3 model by Whittle (1993).

The other idea is to introduce multiple yield surfaces to give a smoother transition between elastic and plastic behaviour. This idea can also describe the effect of the recent past history. Illustrations of this idea include the multiple nested yield surface by Mroz et al. (1978), multiple surface model by Prevost (1978); and the continuous hyperplasticity model by Einav, Puzrin and Houlsby (2001).

2.3.1 The bounding surface concept

In the original bounding surface model by Dafalias and Herrmann (1982), there is a 'radial mapping rule', in which each stress state inside the SBS is mapped to a corresponding image point on the bounding surface. This idea can be applied to a soil model as shown in Figure 2.2(a). The SBS is defined as the MCC yield surface and a radial mapping rule is adopted to define the image stress $(\boldsymbol{\sigma}^*)$ from the current stress state $(\boldsymbol{\sigma})$.

A smooth transition between elastic and plastic behaviours is obtained by means of the hardening rule. The hardening rule can be written in the form:

$$H = H_p + H_0 \frac{\delta}{\delta_0 - \delta}\left[1 + \left|\frac{M}{\eta}\right|^n\right] \tag{2.8}$$

where H_p is plastic stiffness at the image point; δ and δ_0 are the distance between the current stress state and the SBS and the radial distance from SBS to the origin passing the current stress state; H_0 and n are parameters for non-linear hardening. The plastic strain increment at the current stress state is generated at a progressive rate which depends on how near the stress is to the SBS; the plastic strain increment is proportional to $1/\delta$. At $\delta = 0$, the value of H is equal to H_p, i.e., the model reduces to the MCC model at this stage.

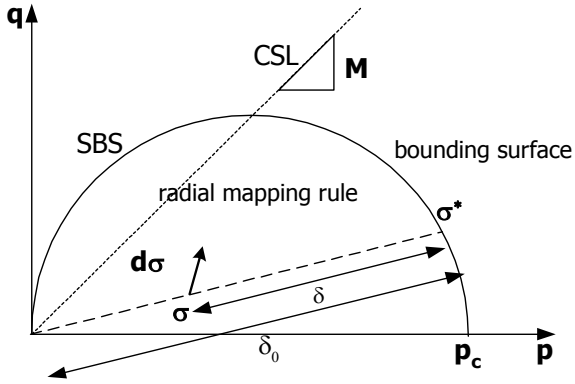

Figure 2.2(a) Bounding surface plasticity model

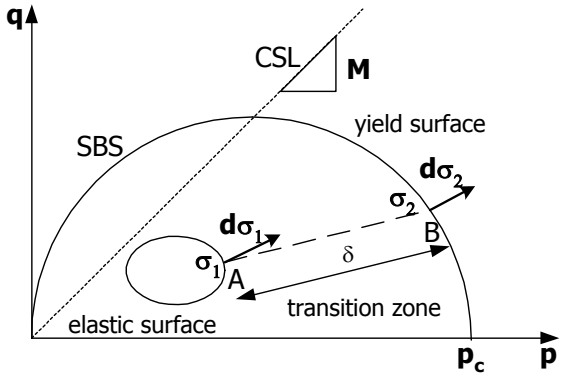

Figure 2.2(b) Kinematic yield surface model

The bounding surface models are efficient for computation, as they do not require the multiplicity of surfaces necessary in the multi yield surface models. There are however some drawbacks. A major deficiency of this concept is the requirement for the choice of a number of arbitrary functions (such as a mapping rule and a hardening rule) without obvious physical interpretation. For monotonic loading the model predictions are quite realistic and exhibit smooth transitions in response. However, on unloading-reloading or a sudden change in the loading path, the models are unrealistic. For example, in the case of 'small' strain levels, real soil is subjected to a loading-unloading-reloading path (ABCDE) as illustrated in Figure 2.3. From A to B, the stress-strain behaviour is plastic; next, the real soil behaves almost elastically under a 'small' unloading-reloading path (BCD) as shown in Figure 2.3(a). However, for reloading from C to D, the bounding surface model will produce a stiffness at the same stress level as the loading path (i.e. point A) as presented in Figure 2.3(b). When loading from D to E the real soil continuously shows a plastic stress-strain

response. For the MIT-E3 model using the bounding surface concept, it employs another rule called elastic hysteretic formulation (Hueckel and Nova, 1979) to solve this problem. However, these effects can be simply described in terms of 'recent stress history', Atkinson et al. (1990) and/or 'immediate past history', Houlsby (1999). A slight difference between these two terminologies is that the recent stress history considers either a sudden change in the direction of the stress path or the time spent at a constant stress state before an imposed change in stress, whereas the immediate past history relates only to the change of stress path direction.

Figure 2.3 Unloading-reloading response in the small strain region; (a) real soil behaviour, (b) bounding surface model behaviour

2.3.2 Kinematic yield surfaces concept

A more realistic response of overconsolidated soil can be described by means of the concept of kinematic hardening surface. A kinematic hardening surface is located within the SBS and the elastic nucleus is encircled by the surface. When the stress point touches the surface, then plastic strain will occur. The plastic strain increment can be evaluated by the flow rule. The surface is dragged by the stress point, following a kinematic hardening rule until the surface contacts the SBS. The simplest of these models, involving only two distinct yield surfaces, is depicted in Figure 2.2(b). This two-surface model can describe three types of behaviour:

(a) Fully elastic, for stress states within the inner yield surface (elastic surface).

(b) Transitional zone, with the stress point on the inner yield surface but inside the outer yield surface (point A)

(c) Fully plastic, when the inner yield and outer yield surface come into contact (point B). This is the normally consolidated state condition.

The original idea of the kinematic hardening model was introduced separately by Mroz (1967) and by Iwan (1967). Subsequently, the model has been extended to multiple surfaces models by Prevost (1978). The best known of this is the multiple "nested" yield surfaces model by Mroz et al. (1982). The multiple "nested" surfaces model is based on the assumption that the yield surfaces do not overlap. In some models overlapping is allowed, although this may occur only rarely.

The multiple yield surface models can successfully explain the effect of immediate past history. However, there are again some disadvantages. Firstly, the multiple surfaces model requires a considerable amount of calculation. This problem can be reduced by using a rate-dependent algorithm, which will be addressed later. Secondly, the multiple surfaces model requires a large number of hardening parameters. This problem can be eliminated by introducing a function to replace a large number of kinematic parameters.

2.4 Some recently developed soil models

This section will present some selected recent developments of constitutive models for soil. Based on the two different approaches for plasticity inside the SBS, the present research on constitutive models can be categorised into two groups as already described in the previous section. However, there are some models which merge the two ideas together and end up with somewhat complicated mathematical expressions, which are practicable. The following will explain the developments of some selected soil models which are a kinematic hardening model (Wood, 1995), three-surface kinematic hardening model (Atkinson and Stallebrass, 1991) and the MIT-E3 model (Whittle, 1993).

The first two models based on the kinematic hardening concept are selected to present here. Both models are modified from an original 'bubble' model (Al Tabbaa and Wood, 1989) to improve the transition zone between elastic behaviour and elastoplastic behaviour. The parametric study for the kinematic hardening model (Wood 1995) was done by Rouainia and Wood (2000) for Norrkoping clay. On the other hand, the three-surface kinematic hardening model (Atkinson and Stallebrass, 1991) was laboratory validated by using a centrifuge model foundation test at City University and also numerically implemented into a Finite Element analysis (Stallebrass and Taylor, 1997).

The MIT-E3 is the well known example based on the bounding surface concept. The parametric studies for MIT-E3 model were done by Whittle (1993) for Boston blue clay at MIT and Zdravkovic *et al.*(2001) for silt at Imperial College by using special equipment such as resonant column and large hollow cylindrical apparatus respectively.

2.4.1 A kinematic hardening model (Wood, 1995)

The kinematic hardening framework was applied to the MCC model to describe the behaviour of overconsolidated clay in a 'bubble' model, Al Tabbaa and Wood (1989). The underlying assumption is that soil 'structure' is seen as a strengthening contribution which is progressively removed by plastic strain. A 'bubble', hypothetically treated as a kinematically hardening yield surface, can describe small strain stiffness, degradation of stiffness with strain for overconsolidated clays and hysteretic behaviour due to the immediate stress history. In this model, a 'structure surface' is introduced to control the process of 'destructuration' through its interaction with the bubble, and this destructuration can capture strain softening effects.

The model consists of three elliptical yield surfaces (Figure 2.4(a)). A reference surface (*rs*) represents the intrinsic behaviour of the remoulded material. Its equation is defined as follows:

$$(p - p_0)^2 + \frac{q^2}{M_\theta^2} = p_0^2 \qquad (2.9)$$

where (p_0,0) is the centre of this surface ($p_0 = \frac{p_c}{2}$ in the MCC model). The parameter M_θ is the ratio of the semi-axes of the yield surface, as in the MCC model. Taking into account an unsymmetrical critical state cone between compression and extension, M_θ is further defined as: $M_\theta = \frac{2mM}{(1+m)-(1-m)\cdot\sin 3\theta}$, where θ is an angle on the π-plane related to the second and third stress invariants (J_2, J_3), that is $-\frac{\pi}{6} \le \theta = \sin^{-1}\left(\frac{-3\sqrt{3}J_3}{2J_2^{3/2}}\right) \le \frac{\pi}{6}$. For the triaxial compression case $\theta = \frac{\pi}{6}$, $M_\theta = M$;

whereas in the triaxial extension case $\theta = -\frac{\pi}{6}$, $M_\theta = mM$. Note that normally the *m* value should be between 1 and 0.7 for certain technical reasons.

A bubble with centre (p_α,q_α) and the size *R* times the size of the *rs* represents the boundary of elastic response and the bubble's equation can be written in the form:

$$(p - p_\alpha)^2 + \frac{(q - q_\alpha)^2}{M_\theta^2} = R^2 p_0^2 \tag{2.10}$$

A structure surface (*ss*) with size *r* times the size of the *rs* takes the place of the outer yield surface, or can be thought of as a bounding surface. The *ss* controls the process of destructuration, with its mathematical equation given by:

$$(p - rp_0)^2 + \frac{(q - (r-1)\eta_0 p_0)^2}{M_\theta^2} = r^2 p_0^2 \tag{2.11}$$

where η_0 is a dimensionless shear stress controlling the soil structure. The above equation indicates that both the size and location of the *ss* are affected by the process of destructuration through the variable *r*. Note that the centre of the *ss* is $(rp_0, (r-1)\cdot\eta_0 p_0)$.

The process of destructuration is controlled by the quantity *r*, which is assumed to be a monotonic decreasing function of the plastic strain. A simple exponential destructuration is then introduced as an example:

$$r = 1 + (r_0 - 1)\exp\left(\frac{-k\varepsilon_d}{\lambda^* - \kappa^*}\right) \tag{2.12}$$

where r_0 is the initial value of *r* (the initial degree of structure) probably related to the sensitivity of the soil, and a general destructuration strain, ε_d, is defined as $d\varepsilon_d = \sqrt{(1-A)d\varepsilon_v^{p\,2} + Ad\varepsilon_s^{p\,2}}$. The quantity $d\varepsilon_d$ increases whenever plastic strain $d\varepsilon_v^p$ or $d\varepsilon_s^p$ occurs; the parameter *A* controls the relative influence that volumetric and distortion effects have in causing destructuration. For *A* = 1, the destructuration is completely distortional, whereas for *A* = 0, the destructuration is fully volumetric. The parameter *k* controls the rate of destructuration with strain, and λ^* and κ^* represent the slope of the NCL and swelling lines in log *v*-log *p* space.

The elastic behaviour inside the bubble is assumed as behave as in the MCC model, with the elastic strain increments as given in equation (2.5). The plastic

strains occur when the stress state lies on the surface of bubble. The plastic strain increment vector is assumed to lie in the direction of outward normal to the bubble at the current stress. For the kinematic yield surface it is assumed that the size parameter R is constant but the reference pressure p_0 will be varying. Therefore, when a stress increment is applied, it will require the kinematic hardening bubble to translate. Since the bubble and *ss* have the same shape, a conjugate stress state $\boldsymbol{\sigma}_c$ can be determined on the *ss* in the same geometric position as the current stress state on the bubble:

$$\left(\boldsymbol{\sigma}_c - \begin{Bmatrix} rp_0 \\ (r-1)\eta_0 p_0 \end{Bmatrix}\right) = \frac{r}{R}\left(\boldsymbol{\sigma} - \begin{Bmatrix} p_\alpha \\ q_\alpha \end{Bmatrix}\right) \tag{2.13}$$

It is assumed that translation of the centre of the bubble occurs along the line joining the current stress state $\boldsymbol{\sigma}$ and the conjugate stress state $\boldsymbol{\sigma}_c$. This ensures that the bubble may touch the *ss* but can never intersect it. The constitutive equation can be written into the form given below.

$$\begin{Bmatrix} d\varepsilon_v^p \\ d\varepsilon_s^p \end{Bmatrix} = \frac{\lambda^* - \kappa^*}{Rpp_0 W}\begin{bmatrix} (p-p_b)^2 & (p-p_b)\dfrac{(q-q_b)}{M_\theta^2} \\ (p-p_b)\dfrac{(q-q_b)}{M_\theta^2} & \left(\dfrac{(q-q_b)}{M_\theta^2}\right)^2 \end{bmatrix} \cdot \begin{Bmatrix} dp \\ dq \end{Bmatrix} \tag{2.14}$$

where

$$W = (p-p_\alpha) + \frac{Bp_0}{Rp}\left(\frac{b}{b_{\max}}\right)^\psi \sqrt{(p-p_\alpha)^2 + \left(\frac{q-q_\alpha}{M_\theta^2}\right)^2} - \frac{k(r-1)}{r}\sqrt{(1-A)(p-p_\alpha)^2 + A\left(\frac{q-q_\alpha}{M_\theta^2}\right)^2}$$

and B, ψ are soil constants controlling the contribution and rate of change of hardening. The scalar quantity b is the dot product between the vector joining the stress state on the bubble $\boldsymbol{\sigma}$ and the conjugate stress state $\boldsymbol{\sigma}_c$ on the *ss* and the outward normal vector to the bubble. Because all the yield surfaces are elliptical in (p,q) space, the maximum value of b_{max} will occur when the bubble is touching the *ss* at a point diametrically opposite to the conjugate stress state (Figure 2.4(b)).

The model uses both the concepts of a kinematic hardening yield surface and a bounding surface. The elastic behaviour, when the stress state is inside the bubble, can be described by means of the MCC model. The bubble kinematic yield surface

can be used to describe the immediate stress history at the small strain level relatively well. However, due to the limitation of a single kinematic yield surface, the soil behaviour under a complex applied load history (such as cyclic loading) cannot be captured by the model. The introduction of the structure surface (or bounding surface) with the destructuration parameters can model aspects of the ansiotropic and strain softening behaviour by allowing the centre of the structure surface to move. All of the surfaces are elliptic in shape similar to the MCC yield surface. The model also modifies the value of semi-axis ratio of (*M*) by considering the asymmetry of the critical state cone in compression and extension. The plastic behaviour of overconsolidated clay can be described by a hardening rule using the bounding surface concept which uses a geometric mapping rule. The two hardening parameters are added in order to describe nonlinear plasticity behaviour.

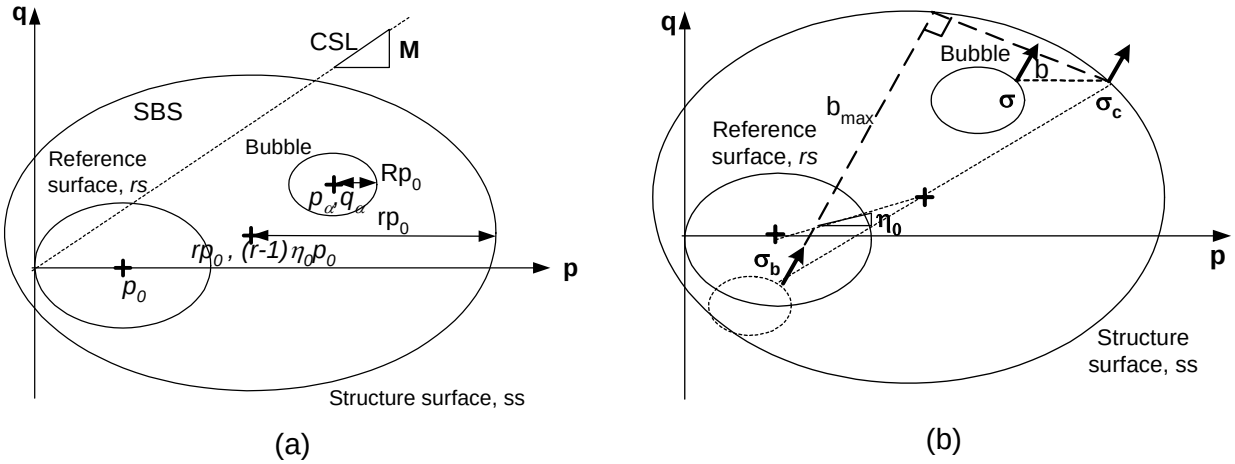

Figure 2.4 (a) Elastic bubble, reference surface (*rs*), and structure surface (ss) for destructration model in triaxial space; (b) Conjugate stress ($\boldsymbol{\sigma}_c$) and corresponding stress ($\boldsymbol{\sigma}_b$) on extreme bubble for definition of b_{max}, Wood (1995)

2.4.2 Three-surface kinematic hardening model (Atkinson and Stallebrass, 1991)

The three-surface kinematic hardening (3-SKH) soil model was formulated specifically to simulate the behaviour of clays in overconsolidated states and during early stages of loading. The model gives an improvement to the 'bubble' model of Al Tabbaa and Wood (1989), so that the effect of immediate stress history and yield at small strains or changes in the stresses can be modelled. The model is represented in *p*-*q* space in Figure 2.5(a). It requires three yield surfaces: Modified Cam-clay SBS (referred to as the bounding surface), and two nested kinematic surfaces (yield surface

and history surface), which are geometrically similar to the bounding surface. The surfaces are defined by the following equations:

Bounding surface: $$(p - p_0)^2 + \frac{q^2}{M^2} = p_0^2 \quad (2.15)$$

History surface: $$(p - p_a)^2 + \frac{(q - q_a)^2}{M^2} = T^2 p_0^2 \quad (2.16)$$

Yield surface: $$(p - p_b)^2 + \frac{(q - q_b)^2}{M^2} = T^2 S^2 p_0^2 \quad (2.17)$$

where $(p_0,0)$, (p_a,q_a) and (p_b,q_b) are the coordinates of the centre of the bounding surface ($p_0 = \frac{p_c}{2}$ in the MCC model), the history surface and the yield surface respectively, and (p,q) is the current stress state. The sizes of the history and yield surfaces are controlled by the two fixed ratios T and S.

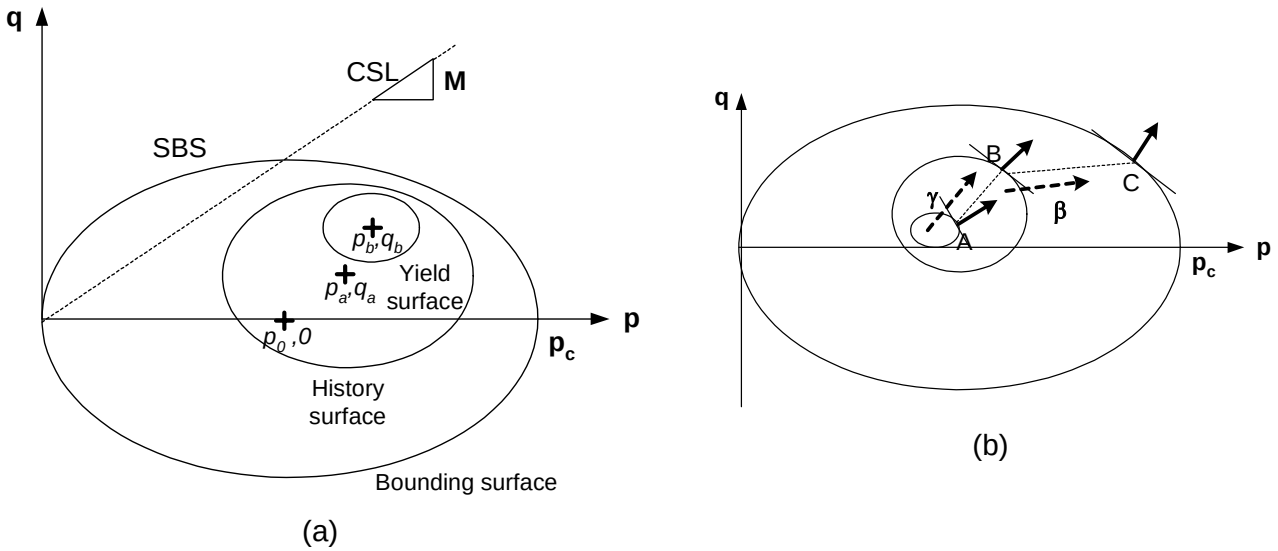

Figure 2.5 (a) The three-surface kinematic hardening model (3-SKH) in triaxial space; (b) Illustrating the principle of the translation rule for the kinematic surfaces, Atkinson and Stallebrass (1991)

The model can give three types of behaviour, which depend on where the stress state is in the yield surfaces, and the location of each yield surfaces themselves. If the stress state is within the inner yield surface, deformations are governed by the isotropic elastic constitutive equation (equation 2.5) as in the MCC model; however, elastic swelling is defined as a linear on the log v-log p space. Otherwise, the stress-strain behaviour is elastoplastic with the associated flow rule on all surfaces, and an appropriate hardening rule. The constitutive equation is of the form given below.

$$\begin{Bmatrix} d\varepsilon_v^p \\ d\varepsilon_s^p \end{Bmatrix} = \frac{1}{h}\begin{bmatrix} (p-p_b)^2 & (p-p_b)\dfrac{(q-q_b)}{M^2} \\ (p-p_b)\dfrac{(q-q_b)}{M^2} & \left(\dfrac{(q-q_b)}{M^2}\right)^2 \end{bmatrix} \cdot \begin{Bmatrix} dp \\ dq \end{Bmatrix} \qquad (2.18)$$

where $h = h_0 + H_1 + H_2$, and $h_0 = \dfrac{(p-p_b)}{\lambda^* - \kappa^*}\left(p(p-p_b) + q\dfrac{(q-q_b)}{M^2} \right)$.

λ^* and κ^* represent the slope of the NCL and swelling lines in the log *v*-log *p* space. The above equations can be reduced to the MCC constitutive equation when all the surfaces are in contact ($h = h_0$). Otherwise, the general case has to include H_1 and H_2 terms, which are functions of the position of the history and yield surfaces respectively. The functions H_1 and H_2 have to be added to ensure that they will give a smooth change in stiffness, so an exponent is introduced as a hardening modulus parameter, ψ. The general hardening function can be finally expressed in the form:

$$h = \frac{1}{\lambda^* - \kappa^*}\left[(p-p_b)\cdot\left(p(p-p_b) + q\frac{(q-q_b)}{M^2} \right) + \left(\frac{b_1}{b_{1\max}}\right)^{\psi} p_0^3 S^2 + \left(\frac{b_2}{b_{2\max}}\right)^{\psi} p_0^3 \right] \qquad (2.19)$$

where b_1 is the dot product of the normal vector at point B and vector $\boldsymbol{\beta}$ (the movement vector from the point B on the history surface to the point C on the bounding surface). b_2 is the dot product of the normal vector at point A and vector $\boldsymbol{\gamma}$ (the movement vector from the point A on the yield surface to the point B on the history surface). These can be illustrated in Figure 2.5(b).

The model adds another kinematic hardening yield surface to improve the variation of the elastoplastic stiffness; this make an improvement from the original 'bubble' model by Al Tabbaa and Wood (1989). The modifications on the effect of recent stress history and yield at small strains are obtained by means of the two kinematic and one outer yield surfaces with the same elliptical geometry. The size of each surface is controlled by two fixed ratios (*T*, *S*). The model captures three types of behaviour, depending on where the stress state is in the yield surfaces and the location of each yield surfaces themselves. The elastic behaviour occurs, when the stress state is inside the yield surface. The plastic behaviour of the overconsolidated clay can be described by the kinematic hardening rule. The hardening exponent (ψ) is adopted in order to explain the smooth transition of stiffness.

2.4.3 The MIT soil models (Whittle, 1993 and Pestana and Whittle, 1999)

Research at the Massachusetts Institute of Technology (MIT) has developed a series of generalised rate independent models for clays based on the theory of incremental linear elasto-plasticity. This model evolved from MIT-E1. Its key features are an anisotropic yield surface, kinematic plasticity and strain softening behaviour under undrained condition for normally consolidated clays. Subsequently, the further developments on model, MIT-E3, describe the rate independent behaviour of normally to moderately overconsolidated clays (OCR<8). The two additional features incorporated into MIT-E3 are small strain nonlinear elasticity using a closed hysteric loop and bounding surface plasticity.

The MIT-E3 model's conceptual framework can be subdivided into three components:

(a) an anisotropic yield surface with hardening rule and flow rule;

(b) a closed symmetric hysteresis loop; and

(c) a bounding surface plasticity formulation.

Table 2.1 Comparison between transformed variables for MIT-E3

Variables	Generalised space	Triaxial space
Effective stress	σ'_{ij}	(p,q)
Strain	ε_{ij}	$(\varepsilon_v,\varepsilon_s)$
Yield surface gradient	$\frac{\partial f}{\partial \sigma'_{ij}}$, where f is yield function	(Q_p,Q_q), where $Q_p=\frac{\partial f}{\partial p}$ and $Q_q=\frac{\partial f}{\partial q}$
Plasticity flow direction	$\frac{\partial g}{\partial \sigma'_{ij}}$, where g is plastic potential function	(P_p,P_q), where $P_p=\frac{\partial g}{\partial p}$ and $P_q=\frac{\partial g}{\partial q}$
Anisotropic axis	b_{ij}	$(1,b)$

The anisotropic model always has to deal with all six components of the stress-strain or some meaningful definitions. The constitutive relations have been presented in the

original paper in terms of generalised effective stresses. However, in order to be equivalent to other models, the MIT-E3 model equation will be expressed in triaixal stress-strain parameters. This will make the MIT-E3 model formulation slightly different from the original work. For more detail see Potts and Zdravkovic (1999). Table 2.1 presents a comparison between the transformed variables that are used in the original paper and variables in the triaxial case.

(a) An anisotropic yield surface

The yield function (Figure 2.6(a)) is assumed to be an anisotropic form of the elliptical modified Cam-clay yield written in the form:

$$f = (q - p \cdot b)^2 - M^2 p(p_c - p) = 0 \tag{2.20}$$

where b is the direction of the yield surface axis and M defines the ratio of the semi-axes of the ellipsoid, which is slightly different from the critical state definition.

The failure criterion, at which critical state behaviour is exhibited, is defined by an anisotropic conical surface:

$$h = (q - p \cdot \xi)^2 - k^2 p^2 = 0 \tag{2.21}$$

where h describes two boundaries of the critical state cone in compression and extension. Its axis of symmetry is on the direction ξ from p-axis, and a constant k parameter defines the half range of critical state cone. These two parameters (ξ, k) can be fully defined by the friction angles measured in triaxial compression and extension tests (ϕ'_{TC}, ϕ'_{TE} based on Mohr-Coulomb's failure criteria):

$$\xi = \frac{1}{2}(C_c - C_e);\ k = \frac{1}{2}(C_c + C_e)$$

where $C_c = \sqrt{\frac{2}{3}} \frac{6\sin\phi'_{TC}}{3 - \sin\phi'_{TC}}$; $C_e = \sqrt{\frac{2}{3}} \frac{6\sin\phi'_{TE}}{3 + \sin\phi'_{TE}}$.

Note that the direction of anisotropy of the yield surface (b) does not generally coincide with the direction of anisotropy of the critical state cone (ξ) as shown in Figure 2.6(a).

Flow rule

The model uses a non-associated flow rule with the flow direction defined as:

$$\begin{Bmatrix} d\varepsilon_v^p \\ d\varepsilon_s^p \end{Bmatrix} = d\lambda \begin{Bmatrix} P_p \\ P_q \end{Bmatrix} = d\lambda \begin{Bmatrix} M^2 p_c r_c \\ M^2 x \{Q_q + \langle r_c \rangle q\} \end{Bmatrix} \tag{2.22}$$

where $Q_q = \dfrac{\partial f}{\partial q} = 2(q - pb)$ is shear component of the yield surface gradient and $x = \left(\dfrac{\lambda}{\lambda - \kappa}\right)\left\{\dfrac{1}{\eta_{K_{0NC}}} - \dfrac{K}{3G}\left(\dfrac{\kappa}{\lambda}\right)\right\}$, $\eta_{K_{0NC}} = \dfrac{3 \cdot (1 - K_{0NC})}{1 + 2K_{0NC}}$ is the stress ratio at the K_0 normally consolidated condition. The parameter r_c describes the location of the current stress state relative to the failure surface (Figure 2.6(b)):

$$r_c = \frac{\overline{p_0 R_c}}{\overline{CR_c}} = \frac{a^* + b^* - d^*}{b^* - d^*}$$

where: $\overline{p_0 R_c}$ is the vector between p_0 and R_c, $\overline{p_0 R_c}$ is the vector between C and R_c

$a^* = M^2(p_c - p)$, $b^* = (b - \xi)(q - pb)$, $c^* = p\left[k^2 - (b - \xi)^2\right]$, and $d^* = \sqrt{\left(b^{*2} + a^* c^*\right)}$.

The value of r_c imply the following:

$r_c = 1$ the current stress state is on the axis of the bounding;

$0 < r_c < 1$ the current stress state lies inside the critical state cone;

$r_c = 0$ the current stress state is on the critical state cone;

$r_c < 0$ the current stress state is outside the critical state cone;

and $\langle\ \rangle$ is a Macaulay bracket to make a more robust expression for r_c.

The obtaining of the increment plastic volumetric and shear strains also needs plastic scalar multiplier ($d\lambda$), which is obtained from the standard plasticity equation. In this case $d\lambda = \dfrac{KQ_p d\varepsilon_v + 3GQ_q d\varepsilon_s}{H + KQ_p P_p + 3GQ_q P_q}$.

The elasto-plastic modulus H is selected to describe the slope λ in the v-ln p plot for all radial consolidation paths, strain hardening, peak strength, strain softening and critical state condition for undrained shearing of K_0 normally consolidated clays.

$$H = 2M^2\left(\frac{\kappa}{\lambda - \kappa}\right) \cdot K\left\{\frac{p_c P_p}{2} - S_t M^2 p_c x \langle r_c \rangle Q_q b\right\} \tag{2.23}$$

where S_t is a material parameter which influences the strain softening behaviour.

Hardening rule

The model assumes two hardening rules to describe changes in size and orientation of the yield surface respectively:

$$\frac{dp_c}{p_c} = \zeta \cdot d\varepsilon_v^p \tag{2.24}$$

$$db = \frac{2\Psi_0}{p_c}\langle r_x \rangle (q - pb) d\varepsilon_v^p \tag{2.25}$$

where ζ is a scalar, obtained from the consistency requirement $(df = 0)$. In this case: $\zeta = \frac{2}{p_c}\left\{\frac{1}{M^2 p_c}\cdot\frac{H}{P_p} - \Psi_0\langle r_x \rangle \frac{2p(p_c - p)}{p_c}\right\}$, with Ψ_0 being a material constant controlling the rate of rotation of the yield surface. r_x is a relative ratio between orientation of the yield surface and the critical state cone, which is graphically illustrated in Figure 2.6(b) and is defined as:

$$r_x = \frac{\overline{CR_x}}{\overline{O'R_x}} = \frac{k - |b - \xi|}{k}$$

The value of r_x imply the following:

$r_x = 1$ the axis of yield surface coincides with the axis of the critical state cone;

$0 < r_x < 1$ the axis of yield surface lies inside the critical state cone;

$r_x = 0$ the axis of yield surface is on the critical state cone;

$r_x < 0$ the axis of yield surface is outside the critical state cone.

The equation (2.25) describes rotational hardening of the yield surface and hence controls the rate of change of anisotropy of the clay. The variable r_x is controlled by the degree of anisotropy: $0 \le r_x < 1$ (If $r_x = 1$, the clay is an isotropic material). From the fact that the axes of anisotropy does not rotate outside the critical state cone, thus Macaulay bracket is introduced in the expression for r_x.

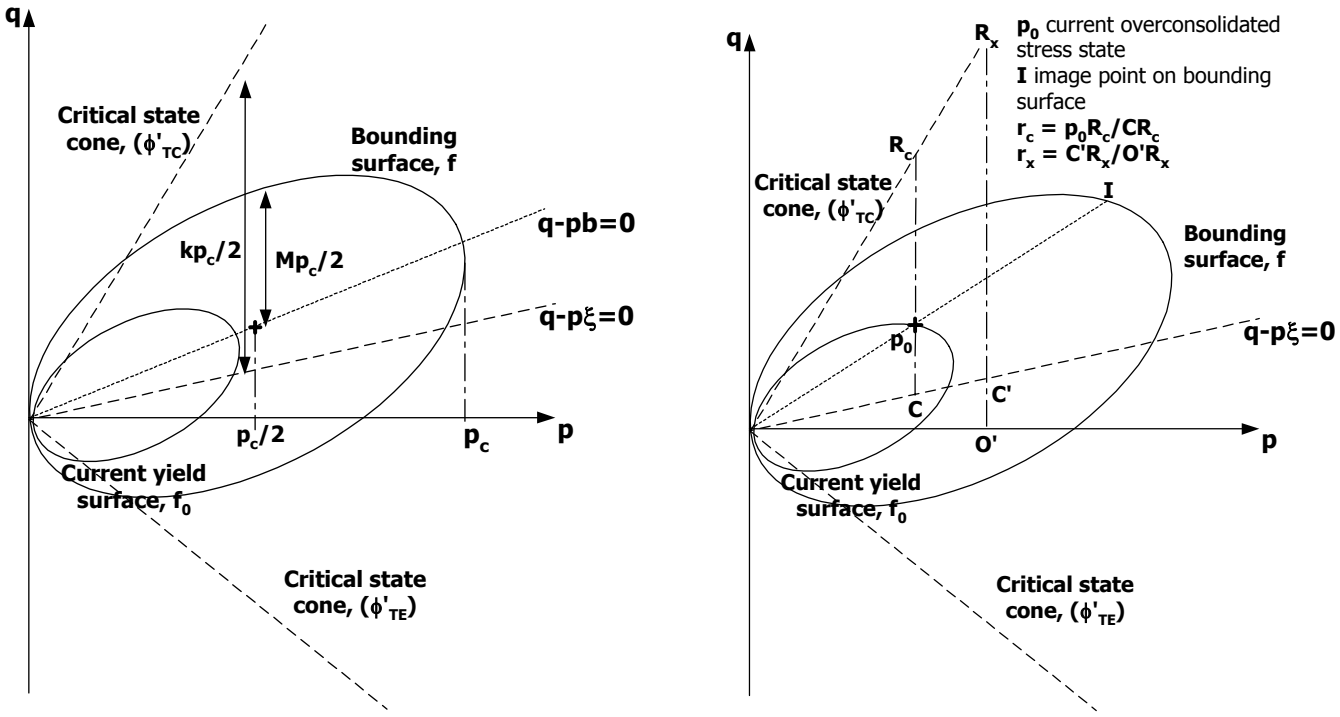

Figure 2.6 (a) MIT-E3 model in triaixal space; (b) Image stress point on the bounding surface and the radial mapping rule, Whittle (1993)

(b) Hysteretic behaviour

The hysteretic model describes a closed symmetric hysteresis loop. The elastic hysteretic formulation is based on Hueckel and Nova (1979) and consists of (i) a criterion for identifying the load reversal point and (ii) an expression of tangential stiffness, which is a function of the current stress state and the load reversal point. The nonlinear tangential bulk modulus inside the hysteresis loop is expressed by

$$K = \frac{vp}{\kappa_0 \cdot (1+\delta)} \tag{2.26}$$

$$\delta = Cn \cdot \left(\ln \xi_p + \omega \xi_s\right)^{n-1} \tag{2.27}$$

where κ_0 defines the initial slope in of the swelling line in v-ln p plot, C and n are material constants which characterise the non-linear behaviour in unloading, and ω describes non-linearity at small strain due to undrained shearing. The variables ξ_p and ξ_s are dimensionless parameters which relate the current stress state (p,q) to the stress reversal state (p_{rev}, q_{rev}):

$$\xi_p = \begin{cases} p/p_{rev} & \text{for} \quad p > p_{rev} \\ p_{rev}/p & \text{for} \quad p_{rev} > p \end{cases} \tag{2.28}$$

$$\xi_q = |\eta - \eta_{rev}| \tag{2.29}$$

where $\eta = q/p$ is the stress ratio. The major assumption of the perfectly hysteretic model is that the strains are fully recovered in a stress cycle. A further assumption is that there is uncoupling between volumetric and shear behaviour in the perfectly hysteretic model. Therefore, the elastic shear modulus (G) can be described by the elastic relation, in which a constant Poisson's ratio (or *K/G* constant) is used.

Another feature of this formulation is that the hysteretic behaviour is only a function of the last load reversal point and maintain no memory of any previous loading history. The definition of the load reversal point is achieved by introducing a scalar strain amplitude parameter which describes the strain history from the immediate stress reversal point as follows:

$$\chi = \begin{cases} |\varepsilon_v - \varepsilon_{v\,rev}| & \text{if} \quad \dot{\varepsilon}_v \neq 0 \\ |\varepsilon_s - \varepsilon_{s\,rev}| & \text{if} \quad \dot{\varepsilon}_v = 0 \end{cases} \tag{2.30a}$$

A load reversal point then occurs when the magnitude of χ reduces, i.e. $\Delta\chi < 0$. However, as the condition above is difficult to implement in an analysis, a more robust expression is presented by Potts and Zdravkovic (1999):

$$\chi = \sqrt{(\varepsilon_v - \varepsilon_{v\,rev})^2 + (\varepsilon_s - \varepsilon_{s\,rev})^2} \tag{2.30b}$$

(c) Bounding surface plasticity

In the case of normally consolidated clay, the bounding surface is described by the yield function; whereas, for overconsolidated clay, a radial mapping rule defines a unique image point on the bounding surface (Figure 2.6(b)). Plastic behaviour at the current stress state (p_0) is linked to the plastic behaviour at the image point *I*. The plastic strain increments at p_0 depend on the loading condition defined as:

$$KQ_p d\varepsilon_v + 3GQ_q d\varepsilon_s = \begin{cases} \geq 0 & \text{Loading} \\ < 0 & \text{Unloading} \end{cases} \tag{2.31}$$

where Q_p and Q_q are the yield surface gradients at the image stress point in the volumetric and deviatoric directions respectively.

The MIT-E3 model assumes separate mapping rules for the elasto-plastic modulus H and flow direction P_p, P_s at the current stress state p_0 inside the bounding surface. The flow direction and modulus are given in the forms:

$$\begin{Bmatrix} P_p \\ P_q \end{Bmatrix} = \begin{Bmatrix} P_{p_I} - P_{p_0} \cdot g_1^{\gamma} \\ P_{q_I} \end{Bmatrix} \tag{2.32}$$

$$H = H_I + H_0 \cdot g_2 \tag{2.33}$$

where $P_{p0} = \{M^2 p_c r_c + \eta_I Q_{q_I}\}$, $g_1 = \dfrac{p_c - p_{c0}}{p_c - p_{c0i}}$, $g_2 = \dfrac{p_c - p_{c0}}{p_{c0} - p_{c0i}}$, and $H_0 = \dfrac{v}{2\kappa_0}(p_c - p_{c0})hQ_{p_I}P_{p_I}$; in which p_{c0} and p_{c0i} are the reference pressure of the yield surface at the current stress state p_0 and at the first yield, and h and γ are dimensionless input parameters.

The MIT soil models have been developed based on experimental data, especially that on Boston Blue clay. The conceptual framework encompasses three concepts:

(a) K_0 normally consolidated yield surface, which allows yield surface distortion;

(b) a perfectly hysteretic model, which give a smooth changes of tangential stiffness during unloading; and

(c) a bounding surface model with the radial mapping rule, which describes the plastic behaviour inside yield surface by using the non-linear hardening rule.

2.5 Evaluation and Prediction of Models

In general, after the development of the model formulation, a parametric study is carried out mostly by an evaluation of model against laboratory data especially triaxial test. The simulation of a stress path triaxial test is carried out by using a computer program which models the test as a single element. A set of model parameters for any particular soil are obtained by using the procedure outlined above excepted some special model parameters which may require sophisticated apparatus such as resonant column and large hollow cylinder.

2.5.1 A kinematic hardening model (Rouainia and Wood, 2000)

The kinematic hardening model has been specifically tested for its ability to reproduce a series of triaxial test results for Norrkoping clay from Sweden (Rouainia and Wood, 2000). The thirteen model parameters have been estimated by using an automatic optimization procedure. The assumption that all samples from the same depth have the same initial conditions such as stress state, location of yield surface and structure surface is made. However, the value of κ^*, λ^*, r_0, and η_0 have been varied with depth in order to improve the match for the test concerned. The resulting set of model parameters, which has been used for matching the data at 5m depth, is shown in Table 2.2.

Table 2.2 Kinematic hardening model parameters for Norrkoping clay at depth 5m (After Rouainia and Wood, 2000)

Symbols	Physical meaning	Value
κ^*	Slope of swelling line in ln v–ln p plot	0.0297
υ	Poissons's ratio	0.22
λ^*	Slope of NCL in ln v–ln p plot	0.252
M	Critical state stress ratio	1.35
m	Ratio of extension and compression strength	0.85
R	Ratio of size of bubble and reference surface	0.145
b_{max}	Stiffness interpolation parameter	1.980
ψ	Stiffness interpolation exponent	1.547
k	Destructuration parameter	4.16
A	Destructuration strain parameter	0.494
p_{c0}	Initial centre of reference surface	13.28
r_0	Initial degree of structure	1.75
η_0	Anisotropy of initial structure	0.50

The simulations of the consolidation procedure for all tests follow the stress path in Figure 2.7. The optimization has been done using a K_0-consolidated undrained compression and extension triaxial test (CK_0UC and CK_0UE) with approximately the same effective stresses at the starting point (Figure 2.8). Other predictions based on the optimized parameters have been carried out, which are

(i) isotropic normally consolidated undrained compression tests with four different pressures of 40, 50, 58 and 100 kPa (Figure 2.9);

(ii) anisotropic normally consolidated undrained compression tests with four different initial stresses (Figure 2.10); and

(iii) isotropic overconsolidated undrained compression tests with three different overconsolidation ratios of 2, 5 and 9 (Figure 2.11).

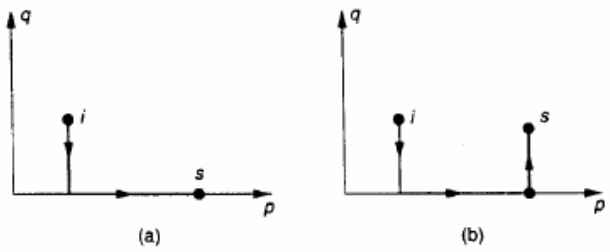

Figure 2.7 Stress path during consolidation procedure
(i = in-situ stress state; s = stress state at start of shearing);
(a) isotropic starting stress, (b) anisotropic starting stress,
Rouainia and Wood (2000)

It is not surprising that the normally consolidated undrained compression tests (Figure 2.8 and 2.9) can be predicted well by the kinematic hardening model. This is because the outer surface of the kinematic hardening model uses the MCC model yield surface that generally gives a good prediction for the normally consolidation clay. An improvement of the M value offers a slightly better prediction for anisotropic normally consolidated undrained compression tests. This model gives relatively accurate predictions for the overconsolidated sample, especially for the stress path direction (Figure 2.10). The model can also describe the softening behaviour due to the destructuration process (that allows the yield surface to relocate) as shown in Figure 2.10. When actually presenting the tests results, however, Rouainia and Wood changed some parameters including A, B, ψ, k and r_0 for two drained compression tests. It seems unreasonable to tune some parameters to offer a better prediction of drained shear behaviour.

However, the simulation still requires at least another set of experimental triaixal extension tests. The two predictions of drained shear tests are not enough to make a conclusion. Moreover, there is still no evidence on hysteretic behaviour,

especially the effects of immediate stress history on the unload-reload stress-strain response.

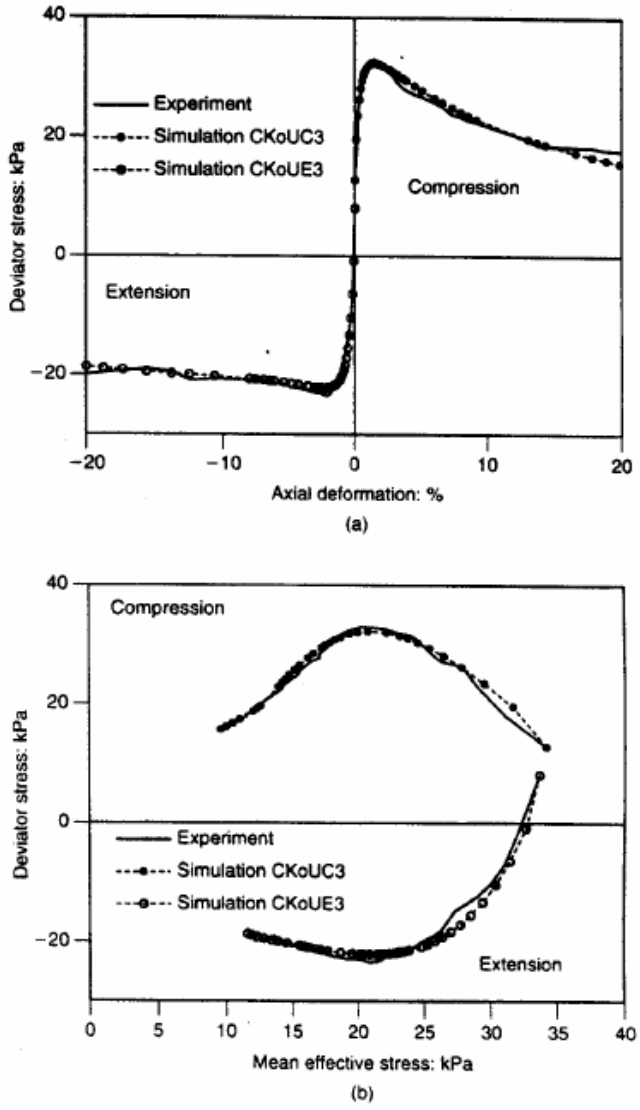

Figure 2.8 K_0-consolidated undrained triaxial compression and extension tests and KH-model predictions for Norrkoping Clay, Rouainia and Wood (2000)

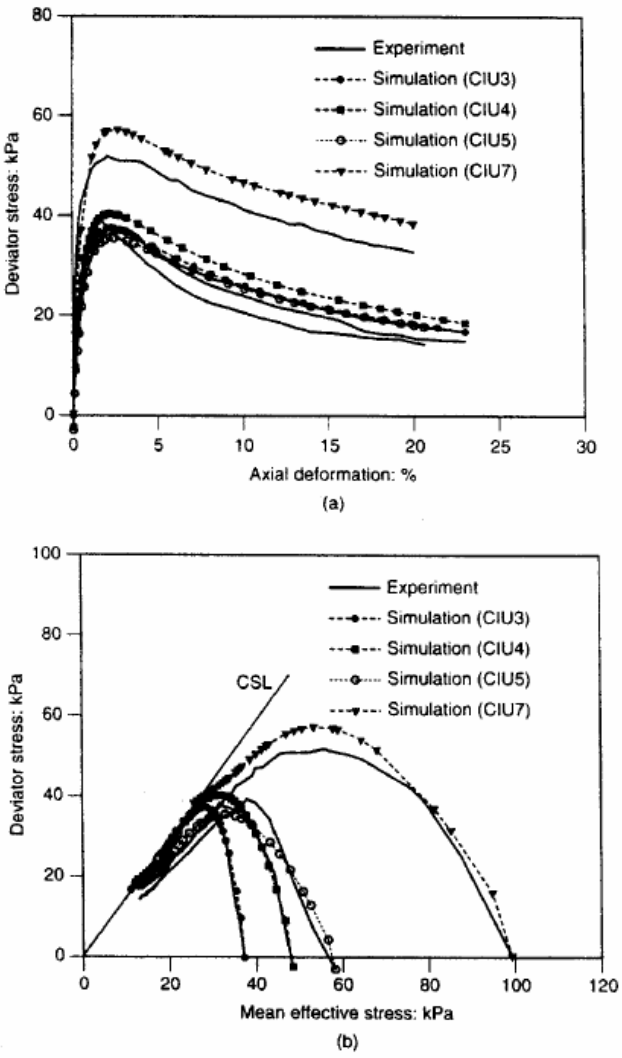

Figure 2.9 Isotropic normally consolidated undrained triaxial compression tests varied pressures of 40, 50, 58 and 100 kPa and KH-model prediction for Norrkoping Clay, Rouainia and Wood (2000)

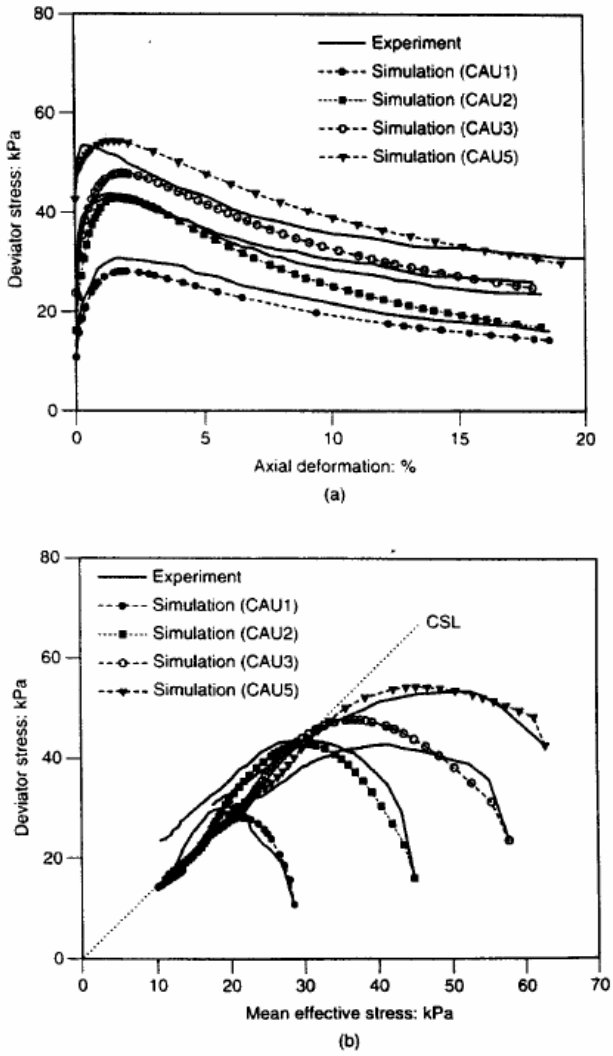

Figure 2.10 Anisotropic normally consolidated undrained triaxial compression tests varied initial pressures and KH-model prediction for Norrkoping Clay, Rouainia and Wood (2000)

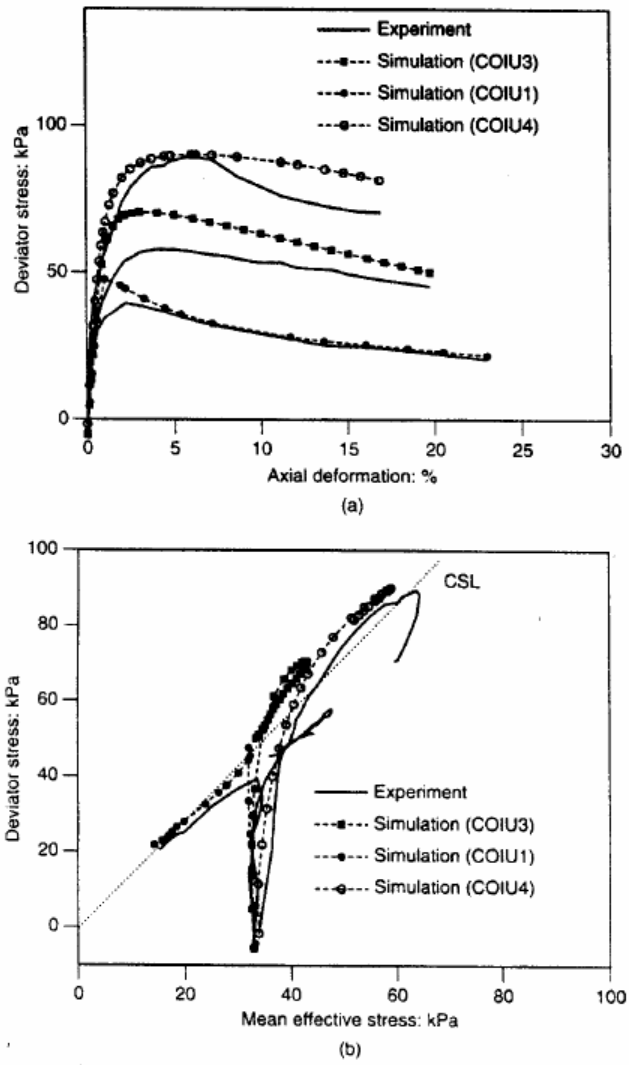

Figure 2.11 Isotropic overconsolidated undrained triaxial compression tests varied OCR of 2, 5, and 9 and KH-model prediction for Norrkoping Clay, Rouainia and Wood (2000)

2.5.2 Three-surface kinematic hardening model (Stallebrass and Taylor, 1997)

A set of 3-SKH model parameters is obtained for comparison with the experimental data from Speswhite kaolin as shown in Table 2.3 (Stallebrass and Taylor, 1997). All eight parameters in the model are assumed to be constant, except the elastic shear modulus (G), which varies with p and OCR according to the power function. Five of the parameters ($\kappa^*, \lambda^*, M, G, and\ e_{cs}$) carry the same meanings and significance as previously defined in the MCC model. T and S can be evaluated from two sets of isotropic consolidation stress paths (Figure 2.12(a)):

(i) a stress path after swelling from half of the maximum stress history (O-B-A); and

(ii) a stress path after one cycle of stress reversal (O-B-A-B-A).

The typical plots of secant bulk modulus (K_c) against p can be used to estimate T and S values (Figure 2.12(b)). However, the exponent for the hardening modulus, ψ is the only parameter that cannot be obtained directly from the experimental data; it has to be derived from parametric studies.

Table 2.3 3-SKH model parameter for Speswhite kaolin (After Stallebrass, 1990)

Symbols	Physical meaning	Value
κ^*	Slope of swelling line in ln v–ln p plot	0.005
λ^*	Slope of NCL in ln v–ln p plot	0.073
M	Critical state stress ratio	0.89
T	Ratio of size of history to bounding surface	0.25
S	Ratio of size of yield surface to history surface	0.08
ψ	Exponent in hardening modulus	2.5
e_{cs}	Void ratio of isotropically normally consolidated soil at reference pressure p_r=1kPa	1.994
G	Elastic shear modulus	60000*

*Calculate from $G = 1964\left(\frac{p}{p_r}\right)^{0.65} \cdot OCR^{0.2}$

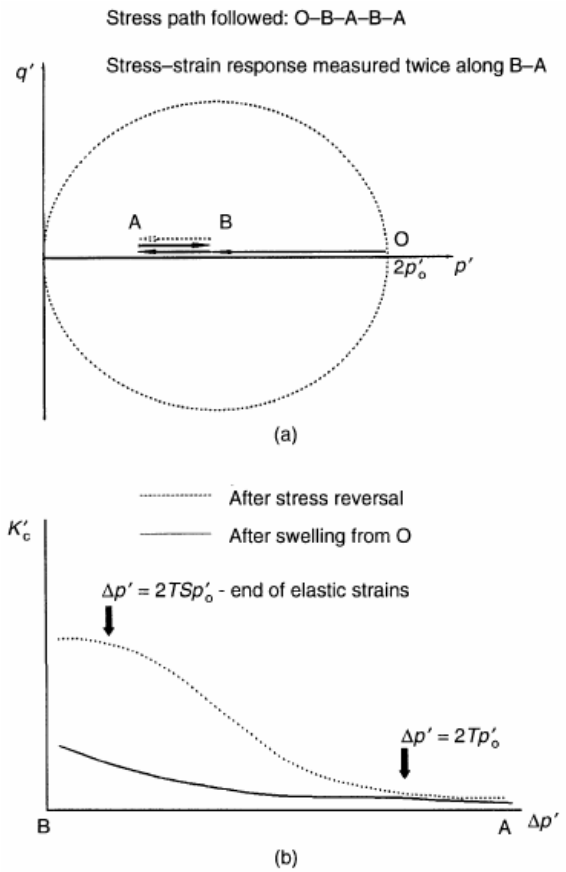

Figure 2.12 Sketch showing (a) isotropic stress path required to determine values for parameters *T* and *S*; (b) typical stiffness plots from *T* and *S* can be estimated, Atkinson, *et al.* (1991)

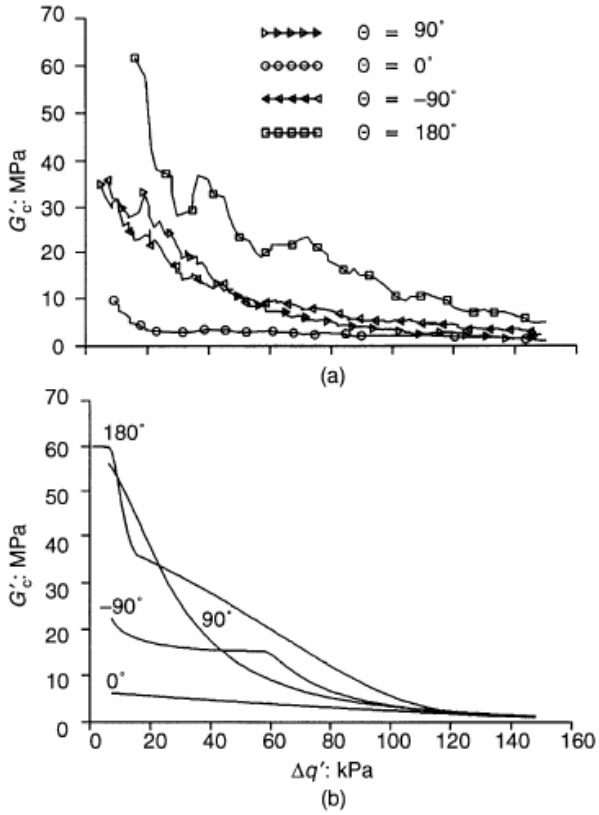

Figure 2.14 Comparison between stiffness data computed from a single element simulation and measured data, Atkinson, *et al.* (1991)

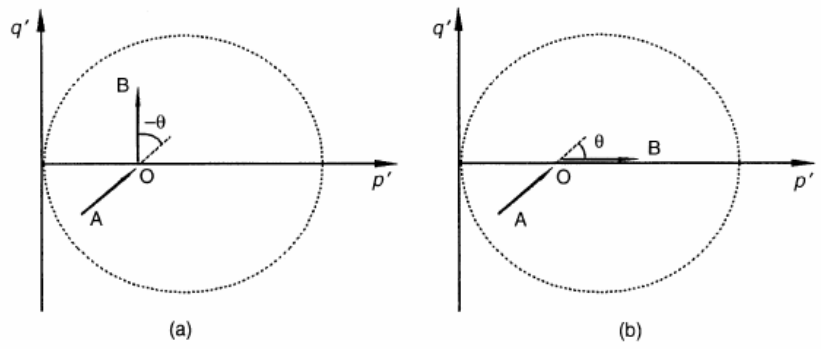

Figure 2.13 Typical stress path showing the recent stress history (AO) and its sudden change of direction; (a) Anticlockwise direction (negative θ), (b) Clockwise direction (positive θ), Atkinson, *et al.* (1991)

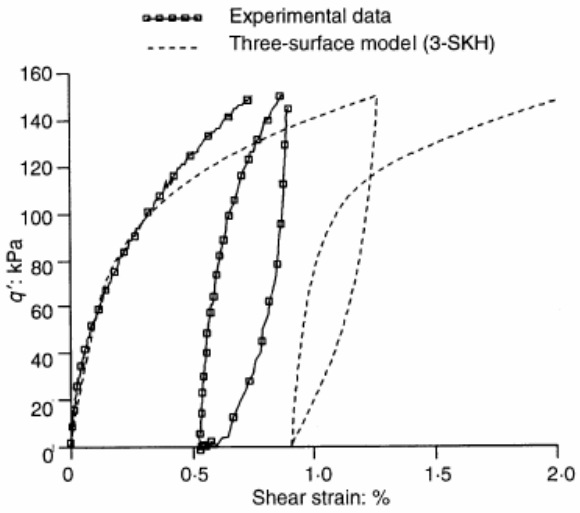

Figure 2.15 Cycle of loading during test, p_{ini} = 300 kPa, p_{max} = 720 kPa: comparison between predicted and measured stress-strain response, Atkinson, *et al.* (1991)

A study of the effect of recent stress history has been experimentally carried out by Atkinson *et al*. (1991), who use test procedures as illustrated in Figure 2.13. The simulations of tests have been numerically reproduced by following the same stress paths. Figure 2.14 shows a comparison between experimental secant shear modulus data and the model predictions. A study of the hysteresis loop has been done by means of unload-reload shear stress at constant p. The comparison between the model prediction and experimental data is shown in Figure 2.15.

The 3-SKH model is developed with the purpose of describing the effect of recent stress history. Therefore, the presented paper emphasises only this effect. Although the 3-SKH model can explain the variation of shear modulus due to a sudden change of stress path direction during shearing process, the curve is still not smooth. This might be a result of the fact that number of the kinematic yield surfaces is limited to only two. The 3-SKH model could show two sudden changes of elastoplastic behaviour when the inner surface touches the outer surface. For the hysteretic behaviour, the prediction of the unload-reload shear stress-strain shape is correct. The magnitude still needs improvement nevertheless.

A yield surface shape that uses the elliptic modified Cam-clay yield surface can explain the normally consolidated behaviour. The model still needs a proof of anisotropic behaviour particularly on K_0-consolidated undrained/drained compression and extension tests.

2.5.3 The MIT-E3 model (Whittle et al., 1994)

The fifteen input parameters for the MIT-E3 model can be evaluated directly or indirectly based on laboratory tests, as presented in Table 2.4. The parameters that can be directly measured from standard laboratory tests are: e_0, K_{0NC}, K/G, ϕ'_{TC}, ϕ'_{TE}, λ and κ_0. The remaining input constants must be determined from parametric studies:

(i) *C, n* are the parameters for the nonlinear in perfect hysteretic volumetric response and *h* is the controlling parameter for the amount of irreversible volumetric strain, which can be selected to match swelling curves from the CRS consolidometer (Figure 2.16);

(ii) S_t and M are established from the K_0-consolidated undrained shear compression and extension (CK_0UC and CK_0UE) at OCR = 1.0, which control the shape of the undrained path in both compression and extension (Figure 2.17);

(iii) ω and γ are nonlinear secant shear modulus at small strain level and shear-induced pore pressure at large strain level during undrained shear condition respectively, which can be measured from the secant modulus and excess pore pressure; and

(iv) ψ_0 controls the rate of change of the anisotropic direction (yield surface rotation), which suggested the reasonable values between 75 to 200 based on the parametric studies (Figure 2.18).

Table 2.4 MIT-E3 parameters for Boston Blue Clay and their requirement of laboratory tests, (Whittle, 1993)

Test type	OCR	Test detail and measurement	Input parameter	
			Direct	Indirect
Odeometer or Constant Rate of Strain consolidometer (CRS) Test	–	- initial void ratio, e_0 - slop of NCL line on e-ln p plot - swelling at two levels include two unload-reload cycles	e_0, λ (1.12, 0.184)	C, n, h (22.0, 1.60, 0.20)
K_0-consolidation triaxial test	1-4	effective stress path during K_0 consolidation and swelling	K_{0NC}, K/G (0.48, 1.90)	–
Undrained shear test	1, 2	- two tests in different modes at OCR =1 (e.g. CK_0UC, CK_0UE) - one CK_0UC test at OCR=2	ϕ'_{TC}, ϕ'_{TE} (33.4°, 45.9°)	S_t, M ω, γ (4.5, 0.866 0.07, 0.5)
Resonant column or in-situ cross hole test	–	Direct measurement of G_{max} from elastic shear wave velocity	κ_0 (0.001)	–
Special tests	1	drained triaxial strain path test	–	ψ_0 (100)

Remark: Figures in brackets are the model parametric values for Boston Blue Clay

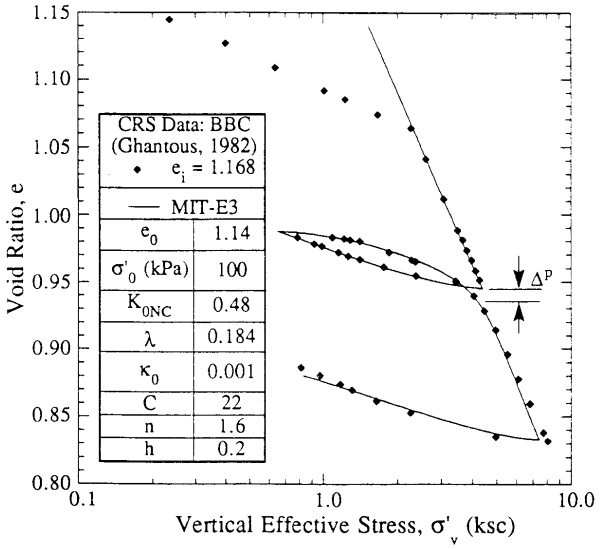

Figure 2.16 Consolidation data and MIT-E3 prediction for Boston Blue Clay, Whittle, *et al*. (1994)

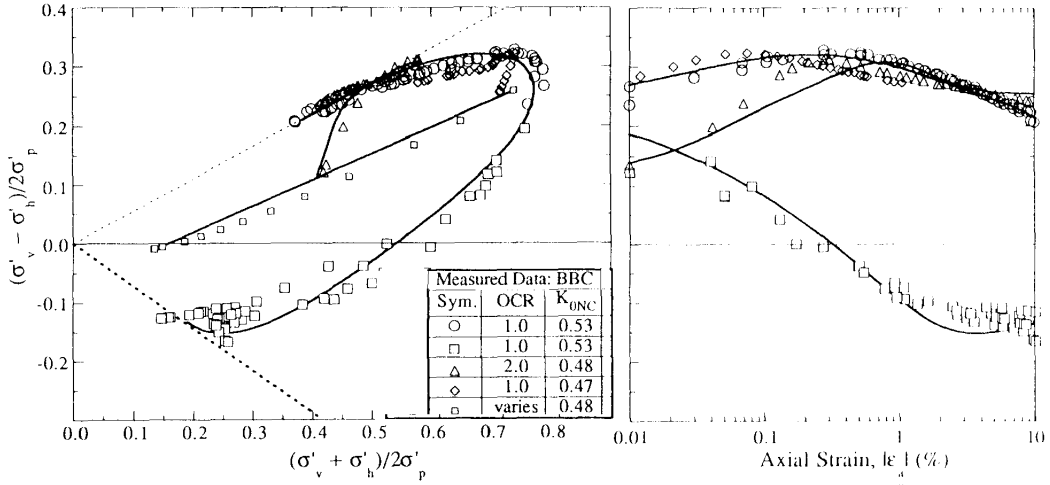

Figure 2.17 K_0-consolidated undrained triaxial compression and extension shear data and MIT-E3 prediction for Boston Blue Clay, Whittle, *et al*. (1994)

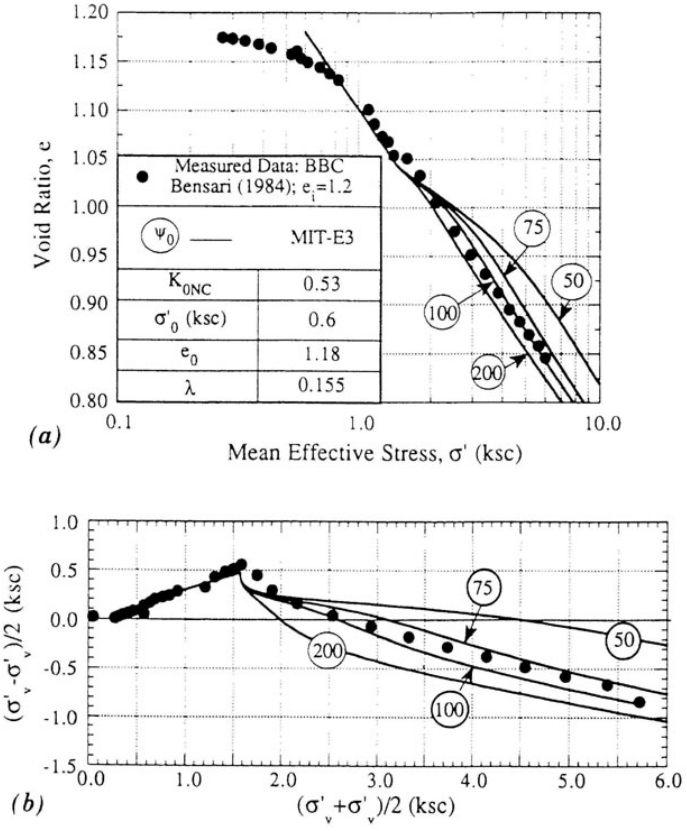

Figure 2.18 Parametric studies of ψ_0 value and MIT-E3 prediction of drain strain path triaxial test, Whittle, *et al*. (1994)

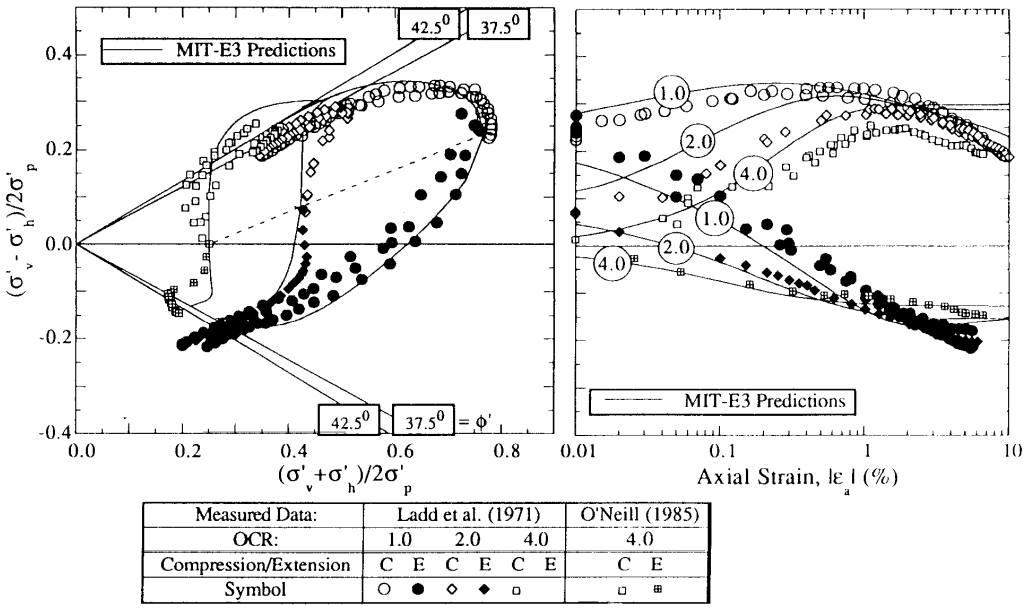

Measured Data:	Ladd et al. (1971)						O'Neill (1985)	
OCR:	1.0		2.0		4.0		4.0	
Compression/Extension	C	E	C	E	C	E	C	E
Symbol	○	●	◇	◆	□		□	⊞

Figure 2.19 K_0-consolidated undrained plan strain compression and extension shear data varied OCR = 1-4 and MIT-E3 prediction for Boston Blue Clay, Whittle, *et al*. (1994)

The MIT-E3 model offers accurate predictions for Boston Blue Clay as shown in Figures 2.16, 2.17 and 2.19. This is because the model contains many advantages of theories such as the bounding surface theory (Dafalias and Herrmann, 1982), the elastic hysteretic formulation (Hueckel and Nova, 1979) and the anisotropic yield surface and critical state cone. In particular, the stress path of anisotropic consolidated tests can be simulated by the MIT-E3 model as presented in Figures 2.17 and 2.19. Although the hysteresis loop can be reproduced by the MIT-E3 model, it is controlled by the stress reversal point. This cannot be used to explain the complicated unloading response; for instance the three different unloading paths from A to B in the generalised stress space as illustrated in Figure 2.20. The elastic hysteretic formulation (Hueckel and Nova, 1979) cannot be used to distinguish the responses from these three different unloading paths because they are unloaded from the same reversal stress point (i.e. point A).

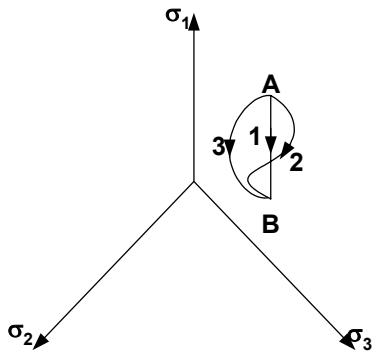

Figure 2.20 Three different unloading paths in generalised stress space

2.6 Comparison of models

Table 2.5 Evaluation of some selected soil models

Model Behaviour	Evaluation			
	MCC, Roscoe and Burland 1968	**KH, Wood 1995**	**3-SKH, Atkinson, *et al.* 1991**	**MIT-E3, Whittle 1993**
Normally consolidated line	Linear on *v*-log *p* plot	Linear on log *v*-log *p* plot	Linear on log *v*-log *p* plot	Linear on *v*-log *p* plot
Elastic behaviour	Linear	Linear	Linear	Non-linear
Smooth transition of stiffness during unloading	No	Yes	Yes	Yes
Variation of stiffness at small strain level	No	Yes	Yes	Yes
Hysteretic behaviour	No	Yes	Yes	Yes
Immediate past history	No	Yes	Yes	No
Flow rule	Associated	Associated	Associated	Non-associated
Hardening rule	Isotropic	Kinematic	Kinematic	Isotropic
Anisotropy	No	Yes	No	Yes
Strain softening	No	Yes	No	Yes
Rate dependent	No	No	No	No
Law of Thermodynamics	Satisfied	?	?	?
Number of model parameters	5	13	8	15
Physical meanings of model parameters	Good	Poor	Fair	Poor
Laboratory testing to evaluate model parameters	Good	Poor	Fair	Poor
Mathematic equations	Easy	Complicated	Fair	Complicated
Implementation on computer program	Easy	Fair	Fair	Complicated

Each soil model described above tries to explain the behaviour of overconsolidated soil with the aim of generating plastic behaviour inside the SBS which could not be previously achieved by a conventional plasticity model. Of the several frameworks of plasticity theory with mathematically sophisticated equations, most are based on two different concepts: bounding surface models (Dafalias and Herrmann, 1982) and kinematic hardening models (Mroz, 1967 and Iwan, 1967). There are some advantages and disadvantages in relation to both concepts. The models introduced previously are compared in Table 2.5. The author's comments in Table 2.5 present not only the facts but also the author's views especially in the last four lines. For instance physical meanings of model parameters: 'good' for the MCC model means that the author is of the opinion that all the physical meanings of the parameters are well defined; however, 'poor' for the MIT-E3 model refers to a lack of clear definition for the physical meanings of some of the model parameters.

Table 2.6 Comparison of physical meaning of soil model parameters

Physical meaning of parameter	Symbols			
	MCC, Roscoe and Burland 1968	**KH, Wood 1995**	**3-SKH, Atkinson, *et al.* 1991**	**MIT-E3, Whittle 1993**
Normally consolidated line	λ,κ	λ^*,κ^*	λ^*,κ^*	λ,κ_0
Reference of yield surface	p_c	p_0	P_0	p_c (2α)
Elastic parameter	G^* or ν	G^* (ν)	G^*	K/G
Critical state parameter	M	M_θ	M	M (c)
Anisotropic parameters	-	$m,\ \eta_0$	-	$K_{0NC},\ \phi'_{TC},\ \phi'_{TE}$
Non-linear hardening parameter	-	B,ψ	ψ	$h,\ \gamma,\ \Psi_0$
Non-linear at small strain	-	r_0,A,k,ψ	T,S,ψ	C,n,ω
Parameters describe the effect of immediate history	-	R,r_0	T,S	-
Strain softening parameter	-	r_0	-	S_t
Total no. of parameter	5	13	8	15

Remark: symbols in brackets are those used in the original papers

The nature of the model parameters is an important factor in indicating the laboratory testing requirements to define the constitutive equations. Table 2.6 summarises the physical meanings of model parameters used in each model.

The MIT model was developed strictly based on the bounding surface theory. The considerable experimental research on Boston Blue Clay was used to validate the model. The MIT-E3 model is developed from the MCC model, but their features are distinctively different. Firstly, the elliptic modified Cam-clay yield surface is replaced by a twisted elliptic shaped yield surface. The unsymmetrical critical state cone is defined using two different values of compression and extension Mohr-Coulomb's friction angles. Although these two modifications enable the model to exhibit the anisotropic behaviour relatively well, a few criteria (such as the change of yield surface direction, b and the location of the critical state cone axis, ξ) have to be carefully defined. The MIT-E3 model uses the non-associated flow rule which has to assume another arbitrary function for plastic flow potential. The two hardening rules which describe the changes in size and orientation of the yield surface are also assumed. The hysteresis behaviour based on only one point of stress reversal state could not sufficiently describe the effect of the immediate stress history especially the complicated stress path (such as cyclic loading). The irrecoverable strain from each loading cycle could not be captured by the model. The MIT-E3 bounding surface uses two different radial mapping rules for the gradient of plastic flow and hardening modulus at image stress point. As a result, the final model employs many complicated mathematic expressions as well as model parameters. The most important shortcoming of the MIT model is the implementation in numerical calculations. This is because the model is not a standard elastic-plastic model, thus some special techniques are required such as hystersis formulation and mapping algorithm for bounding surface plasticity.

On the other hand, the 3-SKH model, Atkinson, *et al.* (1991) and the kinematic hardening model, Wood (1995) are based on the same original idea of the 'bubble' model, Al Tabbaa and Wood (1989). These tried to improve the original bubble model by adding an extra intermediate yield surface in order to deal with moderate strain levels. The bubble surface (or inner surface) covers the elastic behaviour at small strain, whereas the bounding surface (or outer surface), which acts as the modified Cam-clay yield surface, gives the prediction of strength near failure. As a result, they can give a smoother transition response from small strain level (elastic) to large strain level (near failure). However, there is still a question whether

it is logical to limit the numbers of multiple yield surfaces to 3 surfaces. The models cannot produce the response to cyclic loading behaviour which has a small change of stress amplitude. These models could be extended to an infinite number of yield surfaces. However, the infinite yield surface must be based on a theoretical basis if unwarranted complexity is to be avoided.

All three examples of the recent soil models are originally modified from the MCC model and add somewhat considerable arbitrary changes. This is because they aim to generate plasticity behaviour inside the SBS which could not be achieved by the MCC model. Some models contain many advantages of theories such as anisotropic yield surface, hysteretic formulation and process of destructuration. Thus, they give a better quality in terms of laboratory prediction. However, they express the models too complicatedly, thereby making it impracticable. This research tries to bridge between the theoretical and practical aspects. Although the new model may not give better prediction qualities than those three models, the new model can address some of the weak points that can not be achieved by other models. The developing process of the new model will be explained in the next section.

Chapter 3
Hyperplasticity Theory

The specification of a conventional plasticity model requires the definition of the incremental stress-strain response, which consists of the following: (i) the elastic response, (ii) the yield surface, (iii) the flow rule or plastic potential and (iv) the hardening rule including strain hardening and yield surface translation rules. Plasticity models for the prediction of the behaviour of realistic soil usually employ a non-associated flow rule. Although many variants of plasticity theory have been proposed for soil, they are flexible enough to disobey the Laws of Thermodynamics. In contrast plasticity theories rigorously based on thermodynamic frameworks have also been developed over the years such as thermodynamics of internal variables (Coleman and Gurtin, 1967 and Lubliner, 1972). Ziegler (1983) has shown that a constitutive model of a deformable solid may be completely defined by the use of two potential functions: energy and dissipation. This is a unique characteristic that means that the constitutive model could be written in a compact and consistent framework for the computation of the stress-strain response. Collins and Houlsby (1997) recently developed an approach called "hyperplasticity" theory which adopts Ziegler's concept.

It is important to clarify that an alternative plasticity approach termed "hypoplasticity" originally proposed by Kolymbas (1977) has no thermodynamic basis and fundamentally ignores the Law of Thermodynamics. It is totally different and not related to the hyperplasticity theory; therefore, the author will not consider to this concept.

3.1 Hyperplasticity theory

Houlsby and Puzrin (1999) illustrate an approach to plasticity based on generalised thermodynamics, which is called hyperplasticity theory. In that approach, the entire constitutive model is specified by two scalar potential functions: an energy function and a dissipation function (or yield function).

The energy function can be defined by using one of four alternative forms, which are internal energy (u), Helmholtz free energy (f), Gibbs free energy (g) or enthalpy (h). They are not independent, but related by Legendre transformations.

An assumption that the dissipation is a function of the thermodynamic state and the rate of change of material state is introduced. In fact it is sufficient to consider that the dissipation function depends only on the rate of change of the internal variable, $\dot{\alpha}_{ij}$. The dissipation function can be written in four possible ways, depending on which form of the energy function is specified:

$$d = d^e\left(\sigma_{ij} \text{ or } \varepsilon_{ij}, \alpha_{ij}, s \text{ or } \theta, \dot{\alpha}_{ij}\right) \geq 0 \tag{3.1}$$

where the thermodynamic state of the material depends not only on strain (ε_{ij}), stress (σ_{ij}), temperature (θ) or specific entropy (s), but also kinematic internal variables (α_{ij}) and e represents one of the four energy functions.

A yield function is defined as a degenerate special case of the Legendre transformation of the dissipation function:

$$y = y^e\left(\sigma_{ij} or \varepsilon_{ij}, \alpha_{ij}, s or \theta, \chi_{ij}\right) = 0 \tag{3..2}$$

where the dissipative generalised stress can be given as $\chi_{ij} = \dfrac{\partial d^e}{\partial \dot{\alpha}_{ij}}$.

Due to the fact that the dissipation is homogeneous and first order in the rate of internal variables, the relation for the Legendre-Fenchel transformation is written in this special case as

$$\lambda y^e = \chi_{ij}\dot{\alpha}_{ij} - d^e = 0 \tag{3.3}$$

The flow rule, following the Legendre-Fenchel transformation, becomes $\dot{\alpha}_{ij} = \lambda \dfrac{\partial y^e}{\partial \chi_{ij}}$,

where λ is an arbitrary non-negative multiplier.

Therefore, a constitutive framework for materials can be fully defined by using two potential functions: energy function and dissipation function. Table 3.1 summarises the formulations that define the constitutive law based on Gibbs free energy (g) and Helmholtz free energy (f). Note that thermal effects will be ignored in this research.

3.2 Hyperplasticity model for rate-dependent material

Houlsby and Purzin (2002) derived a rate-dependent plasticity model from two potential functions. The energy function does not change from the rate-independent model, but the dissipation function is no longer a potential. Instead, two potentials are used that are force potential (z) and flow potential (w). They are related by a

Legendre-Fenchel transformation, and the sum of these two potentials is equal to the dissipation function (*d*). Table 3.2 presents the comparison between rate-dependent and rate-independent formulas.

Table 3.1 Basic formulations for hyperplasticity theory

	Gibbs free energy (*g*)	**Helmholtz free energy (*f*)**
Energy function	$g = g\left(\sigma_{ij}, \alpha_{ij}\right)$	$f = f\left(\varepsilon_{ij}, \alpha_{ij}\right)$
Dissipation function	$d = d^{g}\left(\sigma_{ij}, \alpha_{ij}, \dot{\alpha}_{ij}\right) \geq 0$	$d = d^{f}\left(\varepsilon_{ij}, \alpha_{ij}, \dot{\alpha}_{ij}\right) \geq 0$
Generalised stress	$\overline{\chi}_{ij} = -\dfrac{\partial g}{\partial \alpha_{ij}}$	$\overline{\chi}_{ij} = -\dfrac{\partial f}{\partial \alpha_{ij}}$
Formula for stress and strain	$\varepsilon_{ij} = -\dfrac{\partial g}{\partial \sigma_{ij}}$	$\sigma_{ij} = \dfrac{\partial f}{\partial \varepsilon_{ij}}$
Dissipative generalised stress	$\chi_{ij} = \dfrac{\partial d^{g}}{\partial \dot{\alpha}_{ij}}$	$\chi_{ij} = \dfrac{\partial d^{f}}{\partial \dot{\alpha}_{ij}}$
Yield function	$y = y^{g}\left(\sigma_{ij}, \alpha_{ij}, \chi_{ij}\right) = 0$	$y = y^{f}\left(\varepsilon_{ij}, \alpha_{ij}, \chi_{ij}\right) = 0$
Formula for flow rule	$\dot{\alpha}_{ij} = \lambda \dfrac{\partial y^{g}}{\partial \chi_{ij}}$	$\dot{\alpha}_{ij} = \lambda \dfrac{\partial y^{f}}{\partial \chi_{ij}}$

Table 3.2 Comparison of formulations between rate-independent and rate-dependent hyperplasticity

Definition	**Rate-independent model**	**Rate-dependent model**
First potential	The same definition of energy functions (*g, f, h, u*)	
Second potential	dissipation function (*d*) and yield function (*y*)	force potential (*z*) and flow potential (*w*)
Dissipative generalised stress	$\chi_{ij} = \dfrac{\partial d}{\partial \dot{\alpha}_{ij}}$	$\chi_{ij} = \dfrac{\partial z}{\partial \dot{\alpha}_{ij}}$
Legendre-Fenchel transformation	$\lambda y = \chi_{ij}\dot{\alpha}_{ij} - d = 0$	$w = \chi_{ij}\dot{\alpha}_{ij} - z = d - z$
Formula for flow rule	$\dot{\alpha}_{ij} = \lambda \dfrac{\partial y}{\partial \chi_{ij}}$	$\dot{\alpha}_{ij} = \dfrac{\partial w}{\partial \chi_{ij}}$

An example of a simple elastic-viscoplastic model is presented by Houlsby and Puzrin (2002). The simplest form of one-dimensional viscosity model is the linear viscosity model, which is given in terms of dissipation function as: $d = \mu\dot{\alpha}^2$. Combing the elastic perfectly plastic model of $d = c|\dot{\alpha}|$, the dissipation function of the simple elastic-viscoplastic model becomes:

$$d = c|\dot{\alpha}| + \mu\dot{\alpha}^2 \tag{3.4}$$

Following the definition of rate-dependent formulations expressed in Table 3.2, the linear viscosity formula can be calculated as summarised in Table 3.3.

The linear viscosity model is sufficient and may be suitable to simulate the conventional triaxial experiment data, since the strain rate is not too high. However, for other complicated geotechnical problems, the more sophisticated rate process theory may be required. Houlsby and Purzin (2002) also produce the rate-dependent formula based on a rate process theory, Mitchell (1976).

This following considers a more sophisticated form of rate-dependence for soil behaviour. The rate process theory is regarded as a thermally activated process, providing a useful theory for soil mechanics. The final result of the theory is that the rate of change of state depends on the driving force in the form of exponential function. Denoting the rate of change of state as $\dot{\alpha}$ and the driving force as χ, the expected relation of rate process is $\dot{\alpha} \propto \exp\left(\frac{\chi}{B}\right) - \exp\left(-\frac{\chi}{B}\right)$. This can be rewritten in the form: $\dot{\alpha} = A\sinh\left(\frac{\chi}{B}\right)$, where A and B are functions of the temperature. Therefore, the viscous dissipation is defined as $d = \chi\dot{\alpha} = \frac{\dot{\alpha}}{B}\sinh^{-1}\left(\frac{\dot{\alpha}}{A}\right)$. Finally, adding a dissipative plasticity term and changing the constants, the dissipation function is expressed as:

$$d = c|\dot{\alpha}| + \mu r\dot{\alpha}\sinh^{-1}\left(\frac{\dot{\alpha}}{r}\right) \tag{3.5}$$

Following the definition of rate-dependent formulations expressed in Table 3.2, the rate process viscosity formula can be produced as shown in Table 3.3.

Table 3.3 Summary of the formulations of the rate-dependent models (After Houlsby and Purzin, 2002)

Definition	**Linear viscosity model**	**Rate process theory**
Dissipation function	$d = c\lvert\dot{\alpha}\rvert + \mu\dot{\alpha}^2$	$d = c\lvert\dot{\alpha}\rvert + \mu r\dot{\alpha}\sinh^{-1}\left(\frac{\dot{\alpha}}{r}\right)$
Force potential	$z = c\lvert\dot{\alpha}\rvert + \frac{\mu\dot{\alpha}^2}{2}$	$z = c\lvert\dot{\alpha}\rvert + \mu r\left[\dot{\alpha}\sinh^{-1}\left(\frac{\dot{\alpha}}{r}\right) + r - \sqrt{r^2+\dot{\alpha}^2}\right]$
Flow potential	$w = \frac{\langle\lvert\chi\rvert - c\rangle^2}{2\mu}$	$w = \mu r^2\cdot\left[\cosh\left(\frac{\langle\lvert\chi\rvert - c\rangle}{\mu r}\right) - 1\right]$
Formula for flow rule	$\dot{\alpha} = \frac{\langle\lvert\chi\rvert - c\rangle}{\mu} sg(\chi)$	$\dot{\alpha} = r\cdot\sinh\left(\frac{\langle\lvert\chi\rvert - c\rangle}{\mu r}\right)\cdot sg(\chi)$

Note that, for small strain rate, ($\dot{\alpha}$ approach to small value); the flow potential function can be approximated to be of the linear viscous type: $w \approx \frac{\langle\lvert\chi\rvert - c\rangle^2}{2\mu}$ (because $\cosh(x) \approx 1 + \frac{x^2}{2} + \cdots$).

3.3 Multiple internal variables and continuous internal function

Puzrin and Houlsby (2001b) describe the idea of extending the single yield surface to multiple yield surface hyperplasticity. It still based on the concept that the entire constitutive response is the product of the derivative of two scalar potential functions. Finally, these are further extended to be internal functions, which represent infinite number of internal variables. The principal advantage of this development is that it provides realistic modelling of kinematic hardening and smooth transitions between elastic and elastic-plastic behaviour.

The multiple internal variables approach is developed to be applied to a more complex case. For instance, the case of *N* internal variables would mean that the function for the Gibbs free energy $g(\sigma_{ij}, \alpha_{ij}, \theta)$ is simply generalised to $g(\sigma_{ij}, \alpha_{ij}^{(1)}, ..., \alpha_{ij}^{(N)}, \theta)$. The corresponding differentiation $\overline{\chi}_{ij} = -\frac{\partial g}{\partial \alpha_{ij}}$ is replaced

by $\overline{\chi}_{ij}^{(n)} = -\dfrac{\partial g}{\partial \alpha_{ij}^{(n)}}$ where $n = 1...N$. The formulae of the multiple internal variables hyperplasticity are presented in Table 3.4. Although the use of multiple internal variables allows these changes to be divided into a number of smaller steps, a completely smooth transition can only be achieved by introducing an infinite number of internal variables. Such an idea leads to the concept of an internal function rather than internal variables.

Table 3.4 Examples of comparisons between different formulations

	Single internal variable	**Multiple internal variables**	**Internal function**
Variables	$\sigma_{ij}, \varepsilon_{ij}$ α_{ij}, χ_{ij}	$\sigma_{ij}, \varepsilon_{ij}$ $\alpha_{ij}^{(n)}, \chi_{ij}^{(n)}$	$\sigma_{ij}, \varepsilon_{ij}$ $\hat{\alpha}_{ij}(\eta), \hat{\chi}_{ij}(\eta)$
Typical energy function(al)	$g(\sigma_{ij}, \alpha_{ij})$	$g(\sigma_{ij}, \alpha_{ij}^{(1)}, \ldots, \alpha_{ij}^{(N)})$	$\int_Y \hat{g}(\sigma_{ij}, \hat{\alpha}_{ij}(\eta), \eta) d\eta$
Typical dissipation function(al)	$d^g\left(\sigma_{ij}, \alpha_{ij}, \dot{\alpha}_{ij}\right)$	$d^g(\sigma_{ij}, \alpha_{ij}^{(1)}, \ldots, \alpha_{ij}^{(N)},$ $\dot{\alpha}_{ij}^{(1)}, \ldots, \dot{\alpha}_{ij}^{(N)})$	$d^g = \int_Y \hat{d}^g(\sigma_{ij}, \hat{\alpha}_{ij}(\eta), \dot{\hat{\alpha}}_{ij}(\eta), \eta) d\eta$
Typical yield function(al)	$y^g\left(\sigma_{ij}, \alpha_{ij}, \chi_{ij}\right) = 0$	$y^g(\sigma_{ij}, \alpha_{ij}^{(1)}, \ldots, \alpha_{ij}^{(N)},$ $\chi_{ij}^{(1)}, \ldots, \chi_{ij}^{(N)}) = 0$	$y^g = \int_Y \hat{y}^g(\sigma_{ij}, \hat{\alpha}_{ij}(\eta), \hat{\chi}_{ij}(\eta), \eta) d\eta = 0$
Typical derivatives	$\varepsilon_{ij} = -\dfrac{\partial g}{\partial \sigma_{ij}}$ $\overline{\chi}_{ij} = -\dfrac{\partial g}{\partial \alpha_{ij}}$	$\varepsilon_{ij} = -\dfrac{\partial g}{\partial \sigma_{ij}}$ $\overline{\chi}_{ij}^{(n)} = -\dfrac{\partial g}{\partial \alpha_{ij}^{(n)}}$	$\varepsilon_{ij} = -\dfrac{\partial g}{\partial \sigma_{ij}} = -\int_Y \dfrac{\partial \hat{g}}{\partial \sigma_{ij}} d\eta$ $\hat{\overline{\chi}}_{ij}(\eta) = -\dfrac{\partial g}{\partial \hat{\alpha}_{ij}(\eta)}$

In general, the internal function will be expressed in terms of an internal co-ordinate η, so the internal function can be written as $\hat{\alpha}_{ij}(\eta)$. The "hat" notation is used to distinguish any variable which is a function of the internal co-ordinate, from a previously used variable with the same name. As an example of the Gibbs free energy, the free energy *function* will now become a free energy *functional* $g[\sigma_{ij}, \hat{\alpha}_{ij}(\eta), \theta]$. Note: the square brackets [ ] distinguishes a functional from a

function. In loose terms, a functional may be defined as a "function of a function". It is assumed that the expression for the functional can be written in the particular form: $g[\sigma_{ij}, \hat{\alpha}_{ij}, \theta] = \int_Y \hat{g}(\sigma_{ij}, \hat{\alpha}_{ij}(\eta), \theta, \eta) d\eta$, where Y is the domain of η. For other formulas of the continuous internal variable hyperplasticity are also concluded in Table 3.4.

However, the conventional partial derivative of a function with respect to a variable cannot accommodate the Legendre formula for the continuous internal function. In order to deal with the derivative of a funtional with respect to a function, a concept of Frechet derivative is requied. The Frechet differential is explained in Puzrin and Houlsby (2001d) and is used in derivation of incremental response of material behaviour.

3.4 Strain hardening model

There are two explanations for the strain hardening behaviour of material after yield. One is the translation of the yield surface, known as kinematic hardening and the other is the change of yield surface size, known as isotopic hardening. Puzrin and Houlsby (2001b) develop the fundamentals of kinematic hardening for hyperplasticity, in which the hardening terms are introduced into the energy function. In contrast, for isotropic hardening, the hardening terms enter the dissipation function. Real material behaviour may involve both isotropic and kinematic hardening. This leads to the idea of merging the two hardening approaches together.

The one-dimensional hardening model can be illustrated simply by using the frictional slip and linear spring model (Figure 3.1). The linear spring component represents a stored energy term in the internal energy function (u) (equivalent to the Helmholtz free energy function (f), by neglecting the thermal term). The dissipative energy can be generated in a frictional slip component, and will always give a positive dissipated energy for both slip directions.

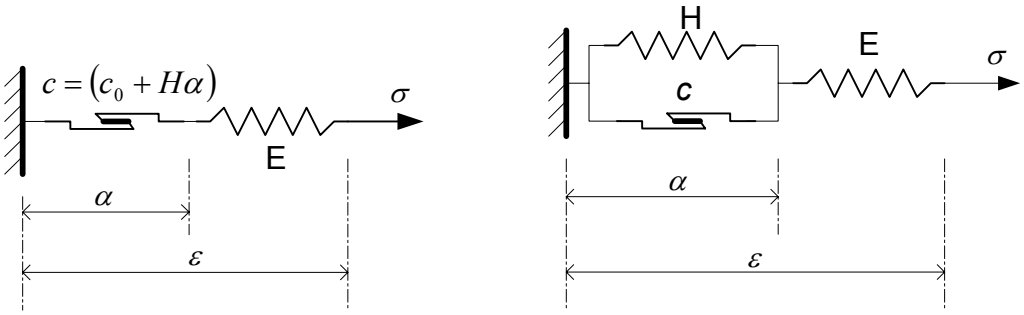

(a) (b)

Figure 3.1 Friction slip and spring model for illustration
(a) Isotropic hardening; (b) Kinematic hardening

3.4.1 Isotropic hardening model

The conventional one-dimensional isotropic hardening model can be illustrated by using the friction slip and spring model (Figure 3.1(a)). The constitutive equation expressed in the product of the derivative of the two potential functions is shown in Table 3.5.

Table 3.5 Comparisons of constitutive formulations for hardening behaviour

	Conventional isotropic hardening	**Modified isotropic hardening**	**Kinematic hardening**
Helmholtz free energy, f	$f = \frac{E}{2}(\varepsilon - \alpha)^2$		$f = \frac{E}{2}(\varepsilon - \alpha)^2 + \frac{H\alpha^2}{2}$
Gibbs free energy, g	$g = -\frac{\sigma^2}{2E} - \sigma\alpha$		$g = -\frac{\sigma^2}{2E} + \frac{H\alpha^2}{2} - \sigma\alpha$
Dissipation function, d	$d = (c_0 + H\alpha)\cdot\lvert\dot{\alpha}\rvert$	$d = (c_0 + H\beta)\cdot\lvert\dot{\alpha}\rvert$ $c^* = \dot{\beta} - \lvert\dot{\alpha}\rvert = 0$	$d = c\cdot\lvert\dot{\alpha}\rvert$
Generalised stress, $\overline{\chi}$	$\overline{\chi} = \sigma$	$\overline{\chi}_\alpha = \sigma, \quad \overline{\chi}_\beta = 0$	$\overline{\chi} = \sigma - H\alpha$
Dissipative generalised stress, χ	$\chi = (c_0 + H\alpha)\cdot sg(\dot{\alpha})$	$\chi_\alpha = (c_0 + H\beta)\cdot sg(\dot{\alpha})$ $-\Lambda\cdot sg(\dot{\alpha})$ $\chi_\beta = \Lambda$	$\chi = c\cdot sg(\dot{\alpha})$
Yield function, y	$y = \lvert\sigma - (c_0 + H\alpha)\rvert = 0$	$y = \lvert\sigma - (c_0 + H\beta)\rvert = 0$	$y = \lvert\sigma - H\alpha\rvert - c = 0$

However, the conventional isotropic hardening model faces a problem of an unrealistic unloading curve (Figure 3.2(a)). As a result, the proper way to solve this problem is by adding an extra constraint condition into the dissipation function by introducing a new parameter β. The physical meaning of parameter β is the cumulative magnitude of internal variable α. Thus, the yield range of modified isotropic hardening model will expand, even when loading (positive α) or unloading (negative α). This phenomenon has been investigated quite often in the cyclic loading response. An example of one-dimensional loading and unloading response is presented in Figure 3.2(b).

3.4.2 Kinematic hardening model

The kinematic hardening model for hyperplasticity was fully developed by Puzrin and Houlsby (2001b). The hardening term is expressed in the energy function rather than the dissipation function as in the case of isotropic hardening (Table 3.5). An example of a one-dimensional kinematic hardening is also shown in Figure 3.1(b) and its stress-strain response in Figure 3.2(c).

The kinematic hardening model is a key stage in developing a model with multiple internal variables and its extension to a continuous internal functional. Only the continuous kinematic hardening functional model can accommodate a smooth transition of stiffness during unloading and reloading under the cyclic stress history.

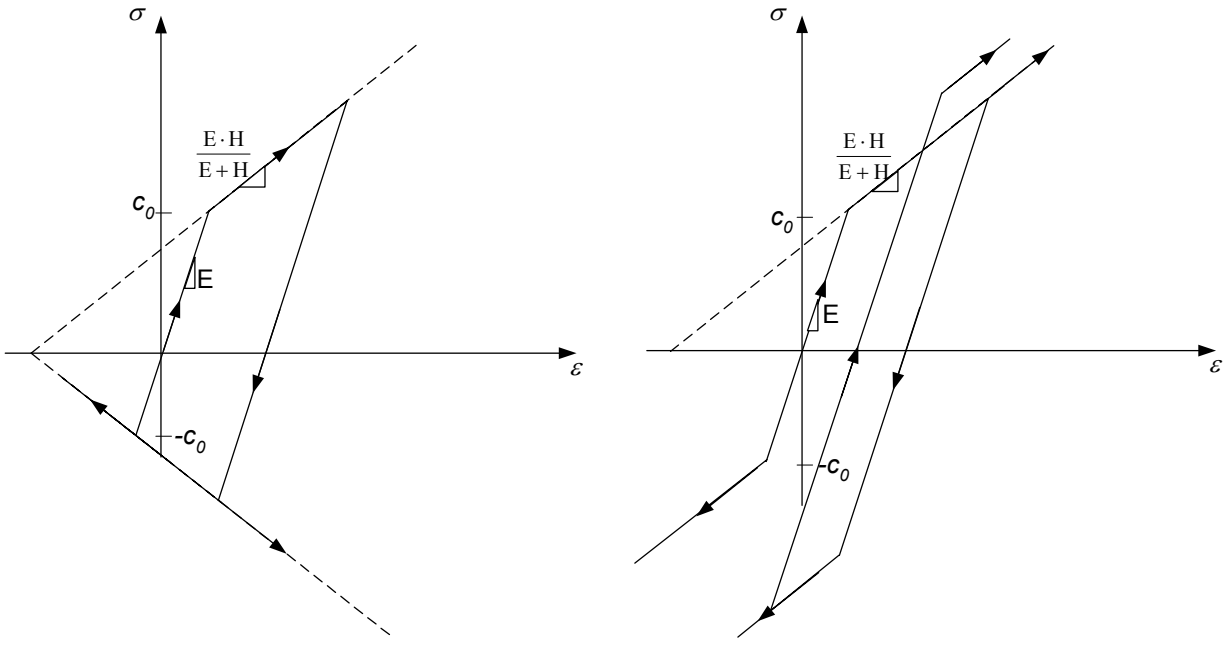

(a) (b)

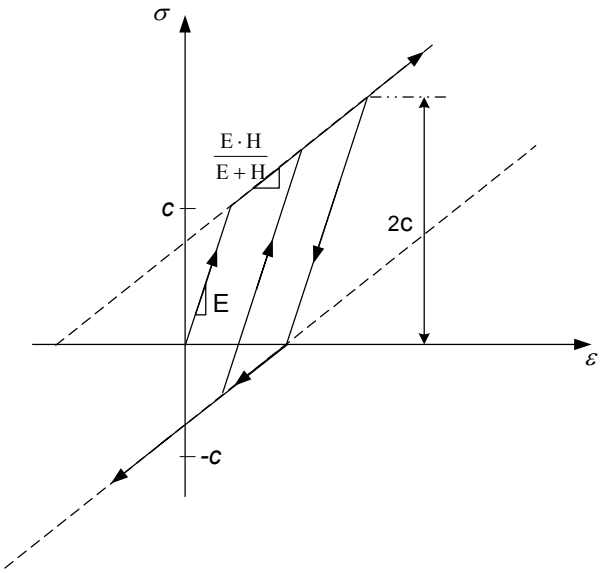

(c)

Figure 3.2 One-dimensional plot of loading and unloading response
(a) Conventional isotropic hardening
(b) Modified isotropic hardening
(c) Kinematic hardening

3.5 Kinematic hardening function for a continuous hyperplasticity model

Based on the kinematic hardening function in section 3.4.2, the bilinear stress-strain behaviour can be described by a single internal variable. By using the multiple internal variables, this idea can be extended to explain a piecewise linear stress-strain behaviour. Finally, for non-linear stress-strain behaviour, a continuous internal function is required. The comparison of the bilinear, piecewise and non-linear stress-strain behaviours is illustrated in Figure 3.3.

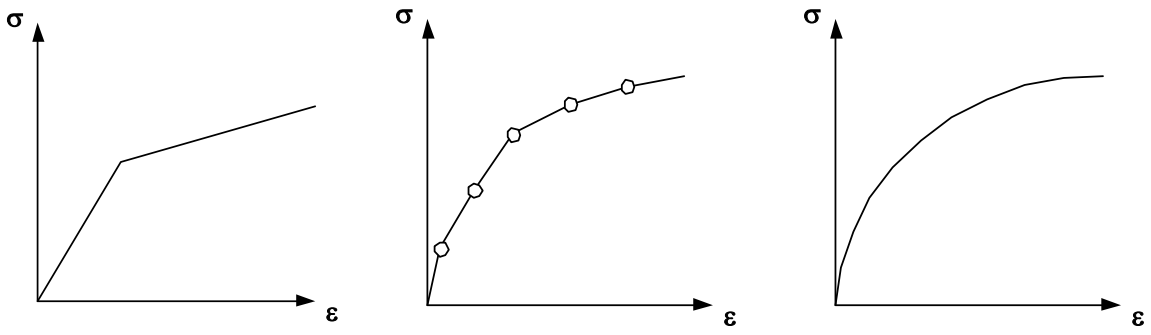

(a) (b) (c)

Figure 3.3 Stress-strain relationships
(a) Bilinear; (b) Piecewise linear; (c) Non-linear

The concept of kinematic hardening hyperplasticity with a continuous internal function can be employed to describe a continuous smooth transition from elastic to plastic behaviour, including the case of a small finite area of the truly elastic region.

The stress history is memorised within the internal variables function $\hat{\alpha}_{ij}(\eta)$, expressed in terms of an internal co-ordinate η.

Research on the determination of the suitable kinematic hardening function is needed to construct a complete stress-strain curve. Starting from the definition of total strain: $\varepsilon = \frac{\sigma}{E} + \int_0^{\eta} \hat{\alpha}(\eta) d\eta$ and combining with the yield function for kinematic hardening: $\hat{y} = \left|\sigma - \hat{H}\hat{\alpha}\right| - \hat{c} = 0$. These leads to $\varepsilon = \frac{\sigma}{E} + \int_0^{\sigma/c} \frac{\sigma - \hat{c}}{\hat{H}} d\eta$.

The following method is presented by Puzrin and Houlsby (2001d) to produce the kinematic hardening function. Assuming the $\hat{c}$ function is independent with time, then

Derivative with respect to time: $\dot{\varepsilon} = \frac{\dot{\sigma}}{E} + \int_0^{\sigma/c} \frac{\dot{\sigma}}{\hat{H}} d\eta + \frac{\sigma - \hat{c}(\sigma/c)}{\hat{H}(\sigma/c)} \cdot \frac{\dot{\sigma}}{c}$, but the last term becomes zero since $\sigma - \hat{c}(\sigma/c) = 0$.

First derivative with respect to stress: $\frac{d\varepsilon}{d\sigma} = \frac{1}{E} + \int_0^{\sigma/c} \frac{1}{\hat{H}} d\eta$

Second derivative with respect to stress: $\frac{d^2\varepsilon}{d\sigma^2} = \frac{1}{c} \frac{1}{\hat{H}(\sigma/c)}$

Therefore, the hardening function can be expressed as:

$$H\left(\frac{\sigma}{c}\right) = \frac{1}{c \dfrac{d^2\varepsilon}{d\sigma^2}} \tag{3.6}$$

As an example, the hyperbolic stress-strain relationship (Figure 3.4) can be written in the form: $\varepsilon = \frac{c}{E} \cdot \frac{\sigma}{c - \sigma}$. Thus, $\frac{d^2\varepsilon}{d\sigma^2} = \frac{1}{E} \cdot \frac{2c^2}{(c-\sigma)^3}$. By substituting it into equation (3.19), the hardening function becomes $H\left(\frac{\sigma}{c}\right) = \frac{1}{c} \cdot \frac{E(c-\sigma)^3}{2c^2}$. It can thus be expressed in the terms of internal co-ordinate:

$$H(\eta) = \frac{E(1-\eta)^3}{2} \tag{3.7}$$

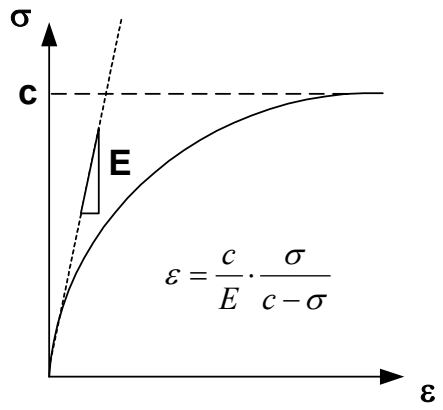

Figure 3.4 Hyperbolic stress-strain relationship

The continuous hyperplasticity approach allows the definition of a material model, which gives a continuous smooth stress-strain response. However, in applying this numerically, the continuous non-linear function has to be replaced by a piecewise linear function. The implementation details will be given in the next section.

3.6 Hyperplasticity models for soil mechanics

The hyperplasticity model for soil behaviour was first introduced by rewriting the modified Cam Clay equation in the form of the dissipation function using a single kinematic variable (Collins and Houlsby, 1997). Further development has continued leading to the latest version called "kinematic hyperplasticity modified Cam-clay model (KHMCC)" by Houlsby (2001).

In general, the development of a new material model starts from a simple formula. Further mathematic expressions are then added to better predict stress-strain behaviour. The model formulae and parameters should have physical meaning. Finally, the model parameters also need tuning to correspond with experimental results.

The following section describes the development of a new constitutive model for soil mechanics, which begins with the one-dimensional elasticity model. The model is then manipulated into the elasto-plastic model with a single internal variable, multiple internal variables and a continuous internal function respectively. In addition, the model will extend to two-dimension including triaxial stress-strain parameters. This is useful for validation of the model with the triaxial experimental data. The research aims to develop a soil model which will address some of the weak

points of the MCC model, specifically the fact that it cannot model small strain stiffness or the effect of immediate stress history. All expressions thus need to be consistent with the CSSM terminology. Lastly, summaries of the new constitutive model will be presented in tables. The description of the development can be illustrated as a diagram shown in Figure 3.5.

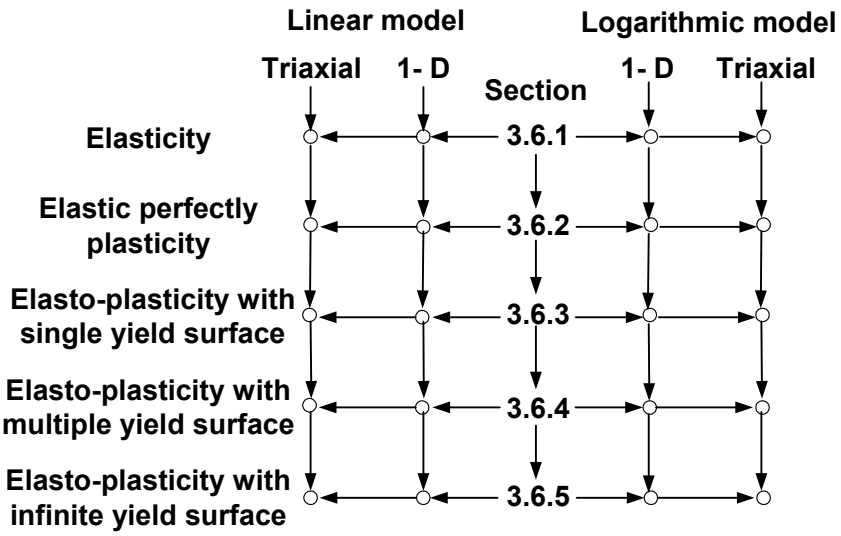

Figure 3.5 Diagram illustrate the development of kinematic hardening models

3.6.1 Elastic model

A basic one-dimensional elastic model (linear spring model) gives a linear relationship between stress and strain ($\varepsilon = \frac{\sigma}{E}$), where E represents a modulus of elasticity. From the formulation in Table 3.1, the relations can be reduced to

Relationship of two potentials: $$f = g + \sigma\varepsilon \qquad (3.8a)$$

Stress-strain definition: $$\sigma = \frac{\partial f}{\partial \varepsilon},\ \varepsilon = -\frac{\partial g}{\partial \sigma} \qquad (3.8b)$$

Stiffness and flexibility definition: $$d\sigma = \frac{\partial^2 f}{\partial \varepsilon^2} d\varepsilon,\ d\varepsilon = -\frac{\partial^2 g}{\partial \sigma^2} d\sigma \qquad (3.8c)$$

Following the relations in equation 3.8(b), the Helmholtz free energy (f) and the Gibbs free energy (g) can be calculated as:

$$f = \int \sigma \cdot d\varepsilon = \int E\varepsilon \cdot d\varepsilon = \frac{E\varepsilon^2}{2} \text{ and } g = -\int \varepsilon \cdot d\sigma = -\int \frac{\sigma}{E} \cdot d\sigma = -\frac{\sigma^2}{2E}$$

Thus, the one-dimensional linear elastic model can be written in the form of energy functions, which are presented in equation 3.9.

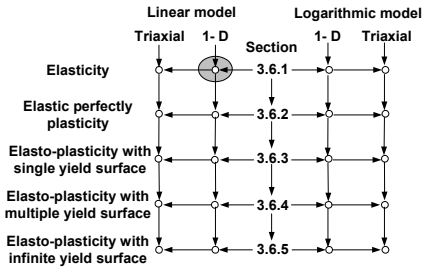

$$f = \frac{E\varepsilon^2}{2},\ g = -\frac{\sigma^2}{2E} \tag{3.9}$$

The physical meaning of the Helmholtz free energy can be thought of as an amount of stored energy in a spring. On the other hand, the Gibbs free energy is known as a (negative) complementary energy in solid mechanics terminology.

In soil mechanics, a logarithmic elastic stress-strain relation can be used to fit consolidation behaviour, Butterfield (1979). The one-dimensional logarithmic elastic relation is $\varepsilon = \kappa \log\left(\frac{\sigma}{\sigma_0}\right)$, where σ_0 (arbitrary constant) and κ represent the reference-stress and logarithmic elastic flexibility. From the relation in equation 3.8(b), the Helmholtz free energy (f) and the Gibbs free energy (g) can be worked out as:

$$f = \int \sigma \cdot d\varepsilon = \int \sigma_0 \exp\left(\frac{\varepsilon}{\kappa}\right) \cdot d\varepsilon = \kappa\sigma_0 \exp\left(\frac{\varepsilon}{\kappa}\right) \text{ and}$$

$$g = -\int \varepsilon \cdot d\sigma = -\int \kappa \log\left(\frac{\sigma}{\sigma_0}\right) = -\kappa\sigma\left[\log\left(\frac{\sigma}{\sigma_0}\right) - 1\right]$$

Therefore, the energy functions of the one-dimensional logarithmic elastic model become:

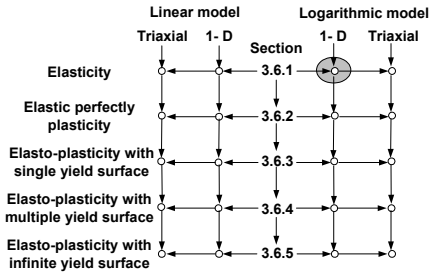

$$f = \kappa\sigma_0 \exp\left(\frac{\varepsilon}{\kappa}\right),$$
$$g = -\kappa\sigma_0 \operatorname{ilog}\left(\frac{\sigma}{\sigma_0}\right) \tag{3.10}$$

Note the definition $\operatorname{ilog}(x) = x\log(x) - x$, so that $\frac{d}{dx}\operatorname{ilog}(x) = \log(x)$.

From the definition of stiffness equation 3.8(c), it becomes $K = \frac{\partial^2 f}{\partial \varepsilon^2} = \frac{\sigma}{\kappa}$. This leads to the idea that the elastic modulus is linear proportional to the stress.

For the triaxial stress-strain model, the definition of the triaxial stress-strain parameters and elastic bulk modulus (K) and shear modulus (G) are presented in

equation 2.2 and 2.3 respectively. Since, it is a fact that the elastic moduli of soils is non-linear, i.e. the tangent moduli depend on the stress level, the bulk and shear moduli may be written in the form of a power function of mean stress *p*:

$$\frac{K}{p_a} = k\left(\frac{p}{p_a}\right)^n, \quad \frac{G}{p_a} = g_x\left(\frac{p}{p_a}\right)^n \tag{3.11}$$

where p_a and n represent the reference mean stress and power order. This expression can be reduced to simple linearity where n is equal to unity (i.e. $K \propto p, G \propto p$). In this research an assumption that the shear modulus (G) vary linearly with pressure (i.e. $G = g_x p$)[1] is made.

The formulation in Table 3.1 for the triaxial stress-strain case is slightly more complicated than for the one-dimensional case. It can be expressed in the form as

Relationship of two potentials: $$f = g + (p\varepsilon_v + q\varepsilon_s) \tag{3.12a}$$

Triaxial stress-strain parameter definition:

$$p = \frac{\partial f}{\partial \varepsilon_v}, q = \frac{\partial f}{\partial \varepsilon_s}; \ \varepsilon_v = -\frac{\partial g}{\partial p}, \varepsilon_s = -\frac{\partial g}{\partial q} \tag{3.12b}$$

Stiffness and flexibility matrix for triaxial stress-strain parameter:

$$\begin{Bmatrix} dp \\ dq \end{Bmatrix} = \begin{bmatrix} \frac{\partial^2 f}{\partial \varepsilon_v^2} & \frac{\partial^2 f}{\partial \varepsilon_v \partial \varepsilon_s} \\ \frac{\partial^2 f}{\partial \varepsilon_v \partial \varepsilon_s} & \frac{\partial^2 f}{\partial \varepsilon_s^2} \end{bmatrix} \begin{Bmatrix} d\varepsilon_v \\ d\varepsilon_s \end{Bmatrix}, \begin{Bmatrix} d\varepsilon_v \\ d\varepsilon_s \end{Bmatrix} = \begin{bmatrix} -\frac{\partial^2 g}{\partial p^2} & -\frac{\partial^2 g}{\partial p \partial q} \\ -\frac{\partial^2 g}{\partial p \partial q} & -\frac{\partial^2 g}{\partial q^2} \end{bmatrix} \begin{Bmatrix} dp \\ dq \end{Bmatrix} \tag{3.12c}$$

The linear elastic modulus is displayed in equation 2.3 which are $dp = Kd\varepsilon_v$ and $dq = 3g_x p d\varepsilon_s$. Thus, following the relation in equation 3.12(b), the Gibbs free energy (g) can be worked out as

$$g = -\int \varepsilon_v \cdot dp + g_1(q) = -\frac{p^2}{2K} + g_1(q), \text{ and } g = -\int \varepsilon_s \cdot dq + g_2(p) = -\frac{q^2}{6g_x p} + g_2(p)$$

Assuming there is no coupling term between p and q, g can then be expressed in equation 3.13.

For the Helmholtz free energy (f), the assumption that p depends on not only ε_v but also ε_s is made, and can be written in the form: $p = K\left(\varepsilon_v + \frac{3g_x\varepsilon_s^2}{2}\right)$. The

[1] The subscript x is introduced to distinguish g_x from g of the Gibbs free energy

$\frac{3g_x\varepsilon_s^2}{2}$ term is added in order to generate the complete mathematic relation between g and f as in equation 3.12, which introduces a small change from the original definition. Following the same procedure for defining g, f can also be evaluated and presented as in equation 3.13.

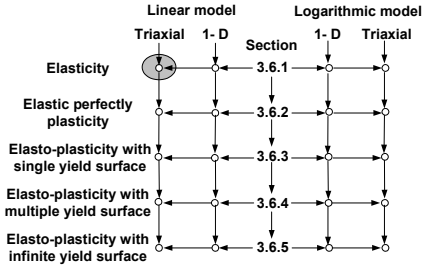

$$f = \frac{K}{2}\left(\varepsilon_v + \frac{3g_x\varepsilon_s^2}{2}\right)^2, \qquad g = -\frac{p^2}{2K} - \frac{q^2}{6g_x p} \tag{3.13}$$

For example, from equation 3.12(c) the linear elastic stiffness matrix can be expressed as:

$$\mathbf{K}^e = \begin{bmatrix} -\frac{\partial^2 g}{\partial p^2} & -\frac{\partial^2 g}{\partial p \partial q} \\ -\frac{\partial^2 g}{\partial p \partial q} & -\frac{\partial^2 g}{\partial q^2} \end{bmatrix} = \begin{bmatrix} \frac{1}{K} + \frac{q^2}{3g_x p^3} & -\frac{q}{3g_x p^2} \\ -\frac{q}{3g_x p^2} & \frac{1}{3g_x p} \end{bmatrix}$$

Comparing this matrix with the elastic stiffness matrix for anisotropic soil in equation 2.4 (Graham and Houlsby, 1983), the cross-coupling term $\left(-\frac{q}{3g_x p^2}\right)$ comes from the second differentiation. This term also represents "stress-induced anisotropy".

For the triaxial stress-strain parameters, the energy function can be calculated based on the logarithmic elasticity in volumetric behaviour, which is $d\varepsilon_v = \frac{\kappa}{p}dp$. Conversely, the deviatoric term is still linear elasticity: $d\varepsilon_s = \frac{dq}{3g_x p}$. Thus, following the equation 3.12(b), the Gibbs free energy (g) is calculated:

$$g = -\int \varepsilon_v dp + g_1(q) = -\kappa p_0 \cdot \mathrm{ilog}\left(\frac{p}{p_0}\right) + g_1(q), \text{ and}$$

$$g = -\int \varepsilon_s dq + g_2(p) = -\frac{q^2}{6g_x p} + g_2(p)$$

and the final g expression is shown in equation 3.14. Similar to the linear case, p should be modified and written in the form: $p = p_0 \exp\left(\frac{\varepsilon_v + 3g_x\varepsilon_s^2/2}{\kappa}\right)$. The term

$3g_x\varepsilon_s^2/2$ is added in order to generate the complete mathematic solution of equation 3.12, which introduces an insignificant modification from the original definition. The Helmholtz free energy (*f*) can be evaluated in the same way as procedure for defining *g* and it is presented in equation 3.14.

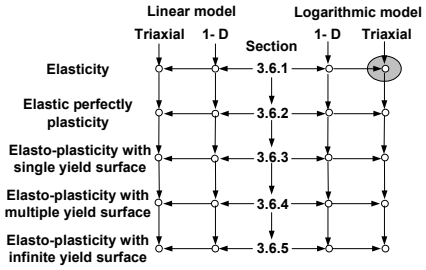

$$f = \kappa p_0 \exp\left(\frac{\varepsilon_v + 3g_x\varepsilon_s^2/2}{\kappa}\right),$$
$$g = -\kappa p_0 \cdot \mathrm{ilog}\left(\frac{p}{p_0}\right) - \frac{q^2}{6g_x p} \qquad (3.14)$$

For example, from equation 3.12(c) the logarithmic elastic stiffness matrix can be expressed as:

$$\mathbf{K}^{\mathbf{e}} = \begin{bmatrix} -\frac{\partial^2 g}{\partial p^2} & -\frac{\partial^2 g}{\partial p \partial q} \\ -\frac{\partial^2 g}{\partial p \partial q} & -\frac{\partial^2 g}{\partial q^2} \end{bmatrix} = \begin{bmatrix} \frac{\kappa}{p} + \frac{q^2}{3g_x p^3} & -\frac{q}{3g_x p^2} \\ -\frac{q}{3g_x p^2} & \frac{1}{3g_x p} \end{bmatrix}$$

where the cross-coupling term $\left(-\frac{q}{3g_x p^2}\right)$ comes from the second differentiation and introduces the stress-induced anisotropy to the material.

3.6.2 Elasto-plastic model with single internal variable

The linear elasto-plastic model has been mentioned in section 3.5; while, the logarithmic elasto-plasticity model will be stated in this section. A single internal variable model offers a sudden change of modulus at yield. It behaves as purely elastic under the yield surface and plastic once yield is reached. The stress-strain curve is composed of two straight lines (i.e. linear elastic and perfect plastic), and it is sometimes called the bi-linear model.

A perfectly plastic model is a special case of the elasto-plastic model, in which there is an absence of hardening or softening. The stress-strain relations are $\varepsilon = \frac{\sigma}{E} + \alpha$ and $\varepsilon = \kappa \log\left(\frac{\sigma}{\sigma_0}\right) + \alpha$ for linear and logarithmic elasticity respectively, which α refers to the plastic strain. Following the stress-strain relation in equation 3.8(b), the calculation of energy functions can be processed as:

Linear model:

$$f = \int E(\varepsilon - \alpha) \cdot d\varepsilon = \frac{E(\varepsilon - \alpha)^2}{2} \text{ and}$$

$$g = -\int \left(\frac{\sigma}{E} + \alpha \right) \cdot d\sigma = -\frac{\sigma^2}{2E} - \sigma\alpha$$

Logarithmic model:

$$f = \int \sigma_0 \exp\left(\frac{\varepsilon - \alpha}{\kappa} \right) \cdot d\varepsilon = \sigma_0 \kappa \exp\left(\frac{\varepsilon - \alpha}{\kappa} \right) \text{ and}$$

$$g = -\int \left(\kappa \log\left(\frac{\sigma}{\sigma_0} \right) + \alpha \right) \cdot d\sigma = -\sigma_0 \kappa \operatorname{ilog}\left(\frac{\sigma}{\sigma_0} \right) - \sigma\alpha$$

The energy functions of the linear and logarithmic perfect plastic model are in equations 3.15 and 3.16 respectively.

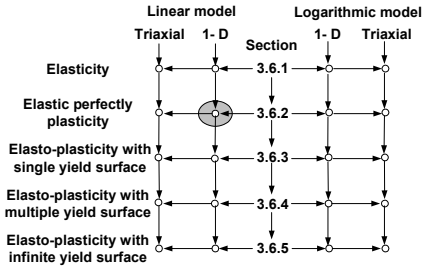

$$f = \frac{E(\varepsilon - \alpha)^2}{2}, \qquad g = -\frac{\sigma^2}{2E} - \sigma\alpha \tag{3.15}$$

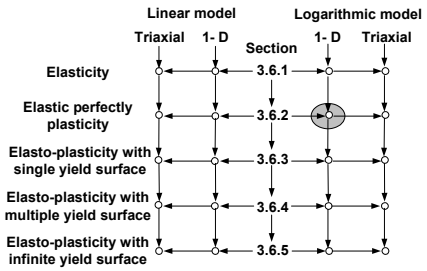

$$f = \sigma_0 \kappa \exp\left(\frac{\varepsilon - \alpha}{\kappa} \right), \qquad g = -\sigma_0 \kappa \operatorname{ilog}\left(\frac{\sigma}{\sigma_0} \right) - \sigma\alpha \tag{3.16}$$

The plasticity can be modelled by using the friction slip component which generates the dissipative energy in form the $d = c|\dot{\alpha}|$, where c is a friction stress in the slip component. The yield function can be calculated using Legendre transformation ($\chi = \frac{\partial d}{\partial \dot{\alpha}} = c \cdot sg(\dot{\alpha})$), thus the dissipation and yield function are written in the form as in equation 3.17.

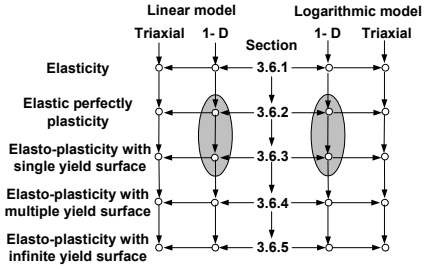

$$d = c|\dot{\alpha}|, \; y = |\chi| - c = 0 \tag{3.17}$$

Note that the generalised stress is defined by $\overline{\chi} = -\dfrac{\partial e}{\partial \alpha}$, where e represents one of the four choices of the energy function. Thus, the yield surface in the case of one-dimensional elastic perfectly plastic becomes $y = |\sigma| - c = 0$, and can be drawn as in Figure 3.6(a). If the hardening term is addressed by replacing the slip friction component (c) with the linear hardening term ($H\alpha$), the yield function becomes $y = |\sigma| - H\alpha = 0$. For this case the yield surface can be plotted as in Figure 3.6(b). If the hardening term is also added into the energy function, the yield surface might be illustrated as in Figure 3.6(c). This could be a benefit for developing a model to describe the consolidation behaviour. To deal with this, the model with a kinematic hardening function is considered in the next section.

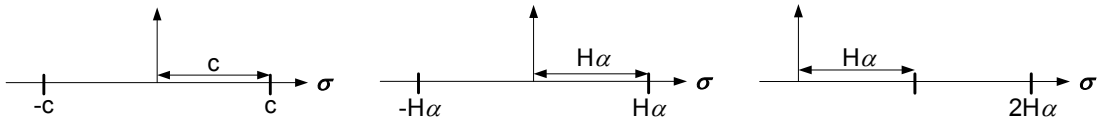

(a) (b) (c)

Figure 3.6 One-dimensional yield surfaces;
(a) Elasto-plasticity, (b) Elasto-plasticity with linear hardening term,
(c) Elasto-plasticity with hardening function in the energy potential

For triaxial stress-strain parameters, the energy function has been referred to in equation 3.13 and 3.14, but the plasticity terms (α_p, α_q) have been not yet considered. Following the formulas in equation 3.12(b), the energy potential can be expressed as equation 3.18 for the linear model and equation 3.19 for the logarithmic model.

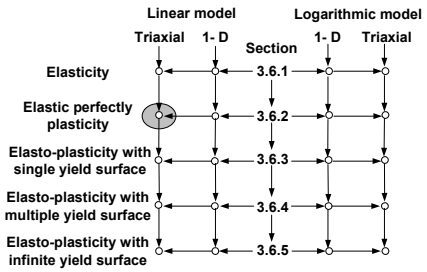

$$f = \frac{K}{2}\left(\left(\varepsilon_v - \alpha_p\right) + \frac{3g_x\left(\varepsilon_s - \alpha_q\right)}{2}\right)^2,$$
$$g = -\frac{p^2}{2K} - \frac{q^2}{6g_x p} - \left(p\alpha_p + q\alpha_q\right) \qquad (3.18)$$

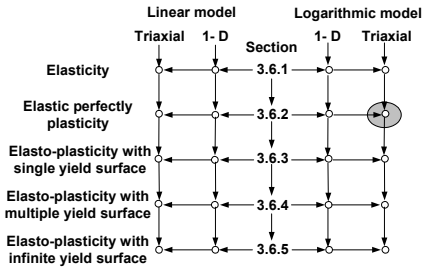

$$f = \kappa p_0 \exp\left(\frac{\left(\varepsilon_v - \alpha_p\right) + 3g_x\left(\varepsilon_s - \alpha_q\right)^2/2}{\kappa}\right),$$
$$g = -\kappa p_0 \cdot \mathrm{ilog}\left(\frac{p}{p_0}\right) - \frac{q^2}{6g_x p} - \left(p\alpha_p + q\alpha_q\right) \tag{3.19}$$

The dissipation potential has to be chosen in order to correspond with the elliptical yield surface of the MCC model $y = \chi_p^2 + \frac{\chi_q^2}{M^2} - c^2 = 0$, where c is half of the major axis of the elliptical yield surface. The reader should be reminded that the definition of the generalised stress ($\overline{\chi}$), the two generalised stresses are defined as: $\overline{\chi}_p = -\frac{\partial e}{\partial \alpha_p}$, $\overline{\chi}_q = -\frac{\partial e}{\partial \alpha_q}$, where e represents one of the four choices of the energy function.

Firstly, assuming the dissipation is proportional to the rate of internal variables, which is in the form of $d \propto \sqrt{\dot{\alpha}_p^2 + M^2\dot{\alpha}_q^2}$. Next, by using the Legendre transformation, we get $\chi_p = \frac{\partial d}{\partial \dot{\alpha}_p}$, $\chi_q = \frac{\partial d}{\partial \dot{\alpha}_q}$. Thus, the dissipation function and the yield function become as in equation 3.20.

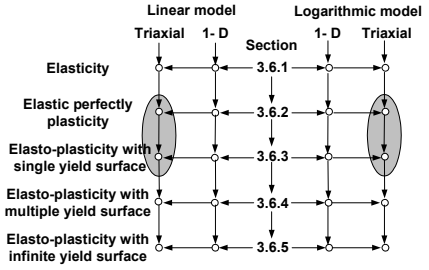

$$d = c \cdot \sqrt{\dot{\alpha}_p^2 + M^2\dot{\alpha}_q^2} = 0,$$
$$y = \sqrt{\chi_p^2 + \chi_q^2/M^2} - c = 0 \tag{3.20}$$

Note that the shape of yield surface depends on the definition of generalised stresses (χ_p, χ_q).

The shape of yield function in the case of triaxial elastic perfectly plastic becomes $y = p^2 + \frac{q^2}{M^2} - c^2 = 0$, and can be drawn as in Figure 3.7(a). Similar to the one-dimensional case, a development for the consolidation model requires an modification of the yield function. If the slip friction component (c) is replaced by the linear hardening term ($H\alpha_p$), the yield function becomes $y = p^2 + \frac{q^2}{M^2} - \left(H\alpha_p\right)^2 = 0$.

For this case, the elliptic yield surface can be plotted as in Figure 3.7(b). If the hardening term is also added in the energy function, the yield surface may be illustrated as in Figure 3.7(c). This may also be described with the model with a kinematic hardening function which will be considered in the next section.

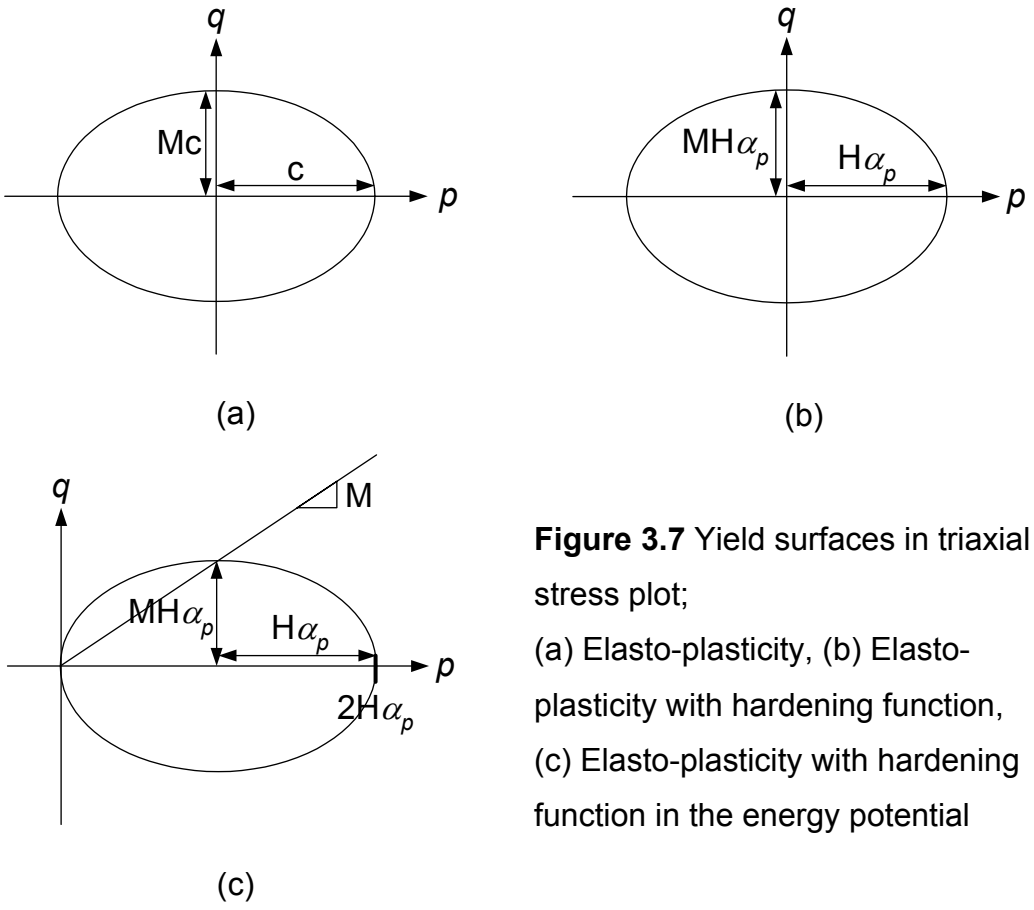

Figure 3.7 Yield surfaces in triaxial stress plot;
(a) Elasto-plasticity, (b) Elasto-plasticity with hardening function,
(c) Elasto-plasticity with hardening function in the energy potential

3.6.3 Elasto-plastic model with single kinematic internal variable

The single kinematic hardening model is similar to the perfect plasticity model. The slight difference is that a hardening term is added in the energy potential function. For the linear elasticity model, the hardening term in the energy function is calculated by integration of $H\alpha$ term, which is $\int H\alpha \cdot d\alpha = \frac{H\alpha^2}{2}$. The linear energy potentials are stated in the equation 3.21.

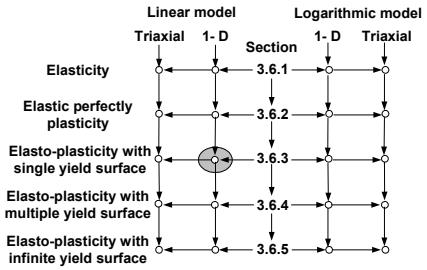

$$f = \frac{E(\varepsilon-\alpha)^2}{2} + \frac{H\alpha^2}{2}, \qquad g = -\frac{\sigma^2}{2E} - \sigma\alpha + \frac{H\alpha^2}{2} \tag{3.21}$$

In contrast, the logarithmic model uses an exponential hardening term, which is calculated from $\int \sigma_0 \exp\left(\frac{\alpha}{\lambda}\right)\cdot d\alpha = \sigma_0\lambda\exp\left(\frac{\alpha}{\lambda}\right)$, to be included in the energy function as in equation 3.22.

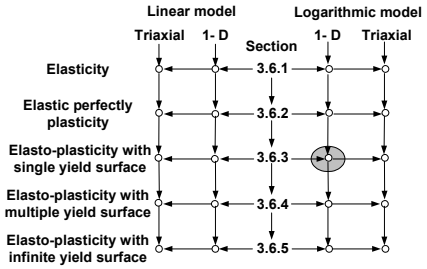

$$f = \sigma_0\kappa\exp\left(\frac{\varepsilon-\alpha}{\kappa}\right) + \sigma_0\lambda\exp\left(\frac{\alpha}{\lambda}\right), \qquad g = -\sigma_0\kappa\,\mathrm{ilog}\left(\frac{\sigma}{\sigma_0}\right) - \sigma\alpha + \sigma_0\lambda\exp\left(\frac{\alpha}{\lambda}\right) \tag{3.22}$$

Nevertheless, for the dissipation and yield function, the expressions used are likewise the same as in equation 3.17.

A special feature of the consolidation behaviour of soil is that when the stress state is touching the yield surface, the yield surface will translate and expand along the *p*-axis (in triaixal stress space) as illustrated in Figure 3.6(c). This leads to the idea of controlling the amount of the yield surface expansion to equal the amount of the translation of yield surface's centre, i.e. substituting $c = H\alpha$ or $c = \sigma_0\exp\left(\frac{\alpha}{\lambda}\right)$ into equation 3.17. Thus, the yield surface becomes $y = |\chi| - H\alpha = 0$ for linear model, and $y = |\chi| - \sigma_0\exp\left(\frac{\alpha}{\lambda}\right) = 0$ for logarithmic model.

The triaxial stress-strain models for the elasto-plastic model with the kinematic internal variable are now considered. The hardening terms are required in the equations 3.18 and 3.19 for explication of the kinematic hardening behaviour. For the linear elastic model, the separated linear hardening terms of volumetric and shear behaviour are used in the energy potential, which are calculated from

$\int H_p \alpha_p \cdot d\alpha_p = \dfrac{H_p \alpha_p^2}{2}$ and $\int H_q \alpha_q \cdot d\alpha_q = \dfrac{H_q \alpha_q^2}{2}$ respectively. The use of the dissipation function and yield function are the same as in equation 3.20.

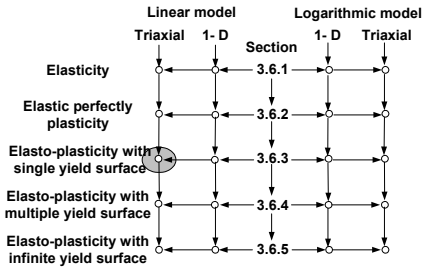

$$
\begin{aligned}
f &= \frac{K}{2}\left(\left(\varepsilon_v - \alpha_p\right) + \frac{3g_x\left(\varepsilon_s - \alpha_q\right)}{2}\right)^2 \\
&\quad + \frac{H_p \alpha_p^2}{2} + \frac{H_q \alpha_q^2}{2} \\
g &= -\frac{p^2}{2K} - \frac{q^2}{6g_x p} - \left(p\alpha_p + q\alpha_q\right) \\
&\quad + \frac{H_p \alpha_p^2}{2} + \frac{H_q \alpha_q^2}{2}
\end{aligned}
\tag{3.23}
$$

Note that for the consolidation behaviour, the term *c* is replaced by $H_p \alpha_p$ as in equation 3.20. The yield function becomes $y = \sqrt{\chi_p^2 + \chi_q^2 / M^2} - H_p \alpha_p = 0$ as illustrated in Figure 3.7(c).

For the logarithmic relation, the hardening term (p_x) is assumed in terms of an exponential function. We know from the one-dimensional model that the hardening function of α_p is $\lambda p_0 \cdot \exp\left(\dfrac{\alpha_p}{\lambda}\right)$. The hardening function of the triaxial model (in terms of α_p, α_q) is assumed as following the elastic term in the Helmholtz free energy (*f*), which is $\lambda p_0 \cdot \exp\left(\dfrac{\alpha_p + 3g\varepsilon_s^2/2}{\lambda}\right)$. Therefore, the final energy potentials end up with the form as in equation 3.24.

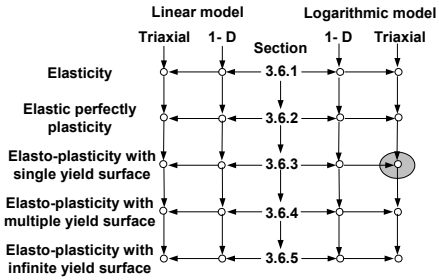

$$
\begin{aligned}
f &= \kappa p_0 \exp\left(\frac{\left(\varepsilon_v - \alpha_p\right) + 3g_x\left(\varepsilon_s - \alpha_q\right)^2/2}{\kappa}\right) \\
&\quad + \lambda p_0 \cdot \exp\left(\frac{\alpha_p + 3g\varepsilon_s^2/2}{\lambda}\right) \\
g &= -\kappa p_0 \cdot \mathrm{ilog}\left(\frac{p}{p_0}\right) - \frac{q^2}{6g_x p} - \left(p\alpha_p + q\alpha_q\right) \\
&\quad + \lambda p_0 \cdot \exp\left(\frac{\alpha_p + 3g\varepsilon_s^2/2}{\lambda}\right)
\end{aligned}
\tag{3.24}
$$

For the consolidation behaviour $c = p_x = \lambda p_0 \cdot \exp\left(\frac{\alpha_p + 3g\,\varepsilon_s^2/2}{\lambda}\right)$ is replaced into equation 3.20. This idea is employed to control the expansion of yield surface and translation of yield surface's centre occurring simultaneously.

In Collins and Houlsby, (1997), the MCC model was displayed in the thermomechanics framework, in which the two potentials are defined as:

$$g = -\kappa p\left(\log\left(\frac{p}{p_c}\right) - 1\right) - \frac{q^2}{6G} - \left(p\alpha_p + q\alpha_q\right) + (\lambda - \kappa)p_{x0}\exp\left(\frac{\alpha_p}{\lambda - \kappa}\right)$$

$$d = p_{x0}\exp\left(\frac{\alpha_p}{\lambda - \kappa}\right)\sqrt{\dot{\alpha}_p^2 + M^2\dot{\alpha}_q^2}$$

This model is an application of the single kinematic hardening model, in which the shear modulus (G) is constant and the kinematic hardening term is defined following the MCC model. The elastic and plastic bulk modulus are related to κ and λ values as $K = \frac{p}{\kappa}$ and $K_p = \frac{p}{\lambda}$ respectively, where κ and λ are defined as two constant slopes of the consolidation curve in $\ln v - \ln p'$ plot. This model is one type of the elasto-plastic model with a single kinematic hardening yield surface, in which one of its main drawbacks is that it is purely elastic inside the yield surface and plastic on the yield surface.

3.6.4 Elasto-plastic model with multiple kinematic internal variables

Combining the idea of kinematic hardening and multiple internal variables together, the piecewise linear stress-strain response can be built. This model can be thought as a series of spring and friction slip components in the multiple yield surfaces model, Iwan (1967). Following this approach, the one-dimensional linear model with multiple kinematic internal variables can be formulated as shown in equation 3.25 for the energy functions and equation 3.26 for the dissipation and the yield function, Puzrin and Houlsby (2001b).

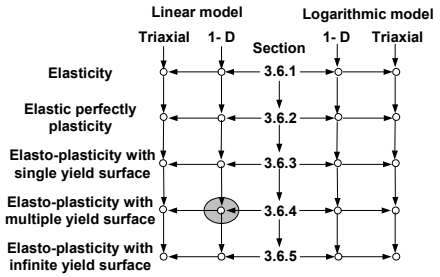

$$f = \frac{E(\varepsilon-\alpha)^2}{2} + \sum_{i=1}^{n}\frac{H_i\alpha_i^2}{2}, \qquad g = -\frac{\sigma^2}{2E} - \sigma\alpha + \sum_{i=1}^{n}\frac{H_i\alpha_i^2}{2} \tag{3.25}$$

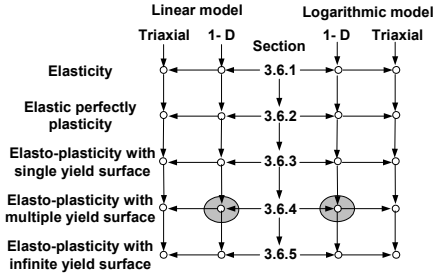

$$d = \sum_{i=1}^{n} c_i\left|\dot{\alpha}_i\right|,\ y_i = \left|\chi_i\right| - c_i = 0 \quad \text{and } c^* = \alpha - \sum_{i=1}^{n}\alpha_i = 0 \tag{3.26}$$

Note that the total of an internal variable is the sum of each kinematic internal variable, which plays the role of the plastic strain. This may be thought of as a constraint condition, i.e. $c^* = \alpha - \sum_{i=1}^{n}\alpha_i = 0$.

The dissipation function is computed from the summation of the dissipative energy of each slip friction element, where c_i is the friction stress of the ith element. The Legendre-Fenchel transformation is used for the evaluation of the yield functions. A simple form of the friction stress is linearly proportional to the maximum friction stress (or size of outer yield surface). Thus, c_i is generally defined as $c_i = \left(\frac{i}{n}\right)c + c_0$, where n, c_0 represent the number of the internal variable and an amount of elastic region (for simplicity sometimes c_0 is set to zero). In this research, c_i is defined as $c_i = \left(\frac{i}{n}\right)c$. Furthermore, for consolidation behaviour the size of each yield surface is simply defined as $c_i = \left(\frac{i}{n}\right)H_i\alpha_i$.

For the logarithmic relation, based on equation 3.22, the energy function of the one-dimensional logarithmic model with multiple kinematic internal variables can be written into the equation 3.27.

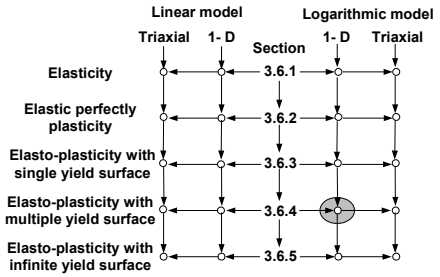

$$f = \kappa\sigma_0 \cdot \exp\left(\frac{\varepsilon - \alpha}{\kappa}\right) + \sigma_0 \cdot \sum_{i=1}^{n} \lambda_i \exp\left(\frac{\alpha_i}{\lambda_i}\right)$$
$$g = -\kappa\sigma_0 \cdot \text{ilog}\left(\frac{\sigma}{\sigma_0}\right) - \sigma\alpha + \sigma_0 \cdot \sum_{i=1}^{n} \lambda_i \exp\left(\frac{\alpha_i}{\lambda_i}\right) \quad (3.27)$$

The dissipation function and the yield function of the logarithmic multiple internal variables model also uses equation 3.26. In addition, for consolidation behaviour the size of each yield surface is defined as $c_i = \sigma_0 \exp\left(\frac{\alpha_i}{\lambda_i}\right) \cdot \left(\frac{i}{n}\right)$.

For the triaxial stress-strain parameters, the energy functions of linear and logarithmic multiple kinematic hardening models are evaluated and presented in equation 3.28 and 3.29 respectively.

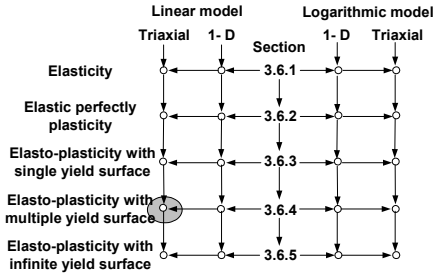

$$f = \frac{K}{2}\left(\left(\varepsilon_v - \alpha_p\right) + \frac{3g_x\left(\varepsilon_s - \alpha_q\right)}{2}\right) + \sum_{i=1}^{n} \frac{H_{p,i}\alpha_{p,i}^2}{2} + \frac{H_{q,i}\alpha_{q,i}^2}{2}$$
$$g = -\frac{p^2}{2K} - \frac{q^2}{6G} - \left(p\alpha_p + q\alpha_q\right) + \sum_{i=1}^{n} \frac{H_{p,i}\alpha_{p,i}^2}{2} + \frac{H_{q,i}\alpha_{q,i}^2}{2} \quad (3.28)$$

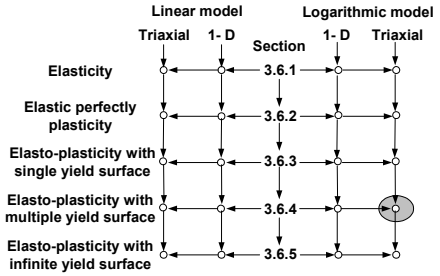

$$f = \kappa p_0 \exp\left(\frac{\left(\varepsilon_v - \alpha_p\right) + 3g_x\left(\varepsilon_s - \alpha_q\right)^2/2}{\kappa}\right) + \sum_{i=1}^{n} \lambda_i p_0 \cdot \exp\left(\frac{\alpha_{p,i} + 3g_i\alpha_{q,i}^2/2}{\lambda_i}\right)$$
$$g = -\kappa p_0 \cdot \text{ilog}\left(\frac{p}{p_0}\right) - \frac{q^2}{6G} - \left(p\alpha_p + q\alpha_q\right) + \sum_{i=1}^{n} \lambda_i p_0 \cdot \exp\left(\frac{\alpha_{p,i} + 3g_i\alpha_{q,i}^2/2}{\lambda_i}\right) \quad (3.29)$$

For the second potentials, the dissipation function and the yield surface are modified from equation 3.20, taking into account the multiple internal variables. The final expressions are shown in equation 3.30.

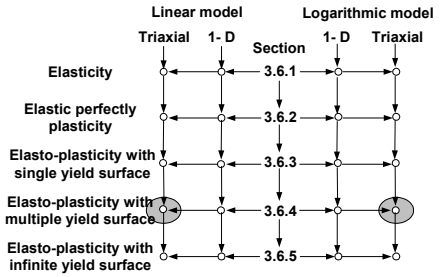

$$d = \sum_{i=1}^{n} c_i \cdot \sqrt{\dot{\alpha}_{p,i}^2 + M^2 \dot{\alpha}_{q,i}^2} = 0\,,$$

$$y_i = \sqrt{\chi_{p,i}^2 + \chi_{q,i}^2 / M^2} - c_i = 0$$

$$\text{and } c_p^* = \alpha_p - \sum_{i=1}^{n} \alpha_{p,i} = 0\,, \tag{3.30}$$

$$c_q^* = \alpha_q - \sum_{i=1}^{n} \alpha_{q,i} = 0$$

Note that the total of an internal variable is the sum of each kinematic internal variable, which plays the role of the plastic strain. These may be thought of as two constraint conditions, which are $c_p^* = \alpha_p - \sum_{i=1}^{n} \alpha_{p,i} = 0$, $c_q^* = \alpha_q - \sum_{i=1}^{n} \alpha_{q,i} = 0$ for α_p and α_q. In addition, for consolidation behaviour in the triaxial case the size of each yield surface can be defined as: $c_i = \left(\frac{i}{n}\right) H_{p,i} \alpha_{p,i}$ and $c_i = p_0 \exp\left(\frac{\alpha_{p,i} + 3 g_i \alpha_{q,i}^2 / 2}{\lambda_i}\right) \cdot \left(\frac{i}{n}\right)$ for the linear and logarithmic model respectively.

3.6.5 Elasto-plastic model with continuous kinematic internal function

Following the idea of the continuous kinematic internal function $\hat{\alpha}_{ij}(\eta)$, a smooth stress-strain curve can be generated. This idea is further developed from the multiple kinematic hardening model, in which the summation of finite internal variables is replaced by the integral of the internal function, Puzrin and Houlsby (2001b). The energy functions of the one-dimensional models are shown in equations 3.31 and 3.32 for the linear and logarithmic models respectively.

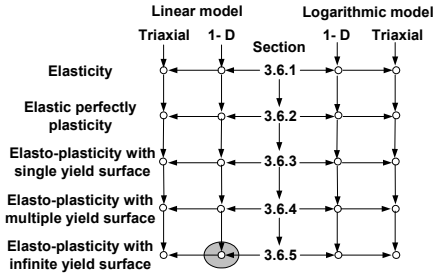

$$f = \frac{E(\varepsilon - \alpha)^2}{2} + \int_0^1 \frac{\hat{H}\hat{\alpha}^2}{2} d\eta\,,$$

$$g = -\frac{\sigma^2}{2E} - \sigma\alpha + \int_0^1 \frac{\hat{H}\hat{\alpha}^2}{2} d\eta \tag{3.31}$$

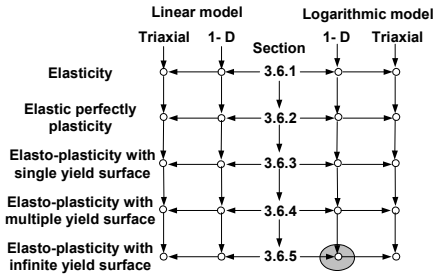

$$f = \kappa\sigma_0 \cdot \exp\left(\frac{\varepsilon - \alpha}{\kappa}\right) + \int_0^1 \hat{\lambda}\sigma_0 \cdot \exp\left(\frac{\hat{\alpha}}{\hat{\lambda}}\right) d\eta,$$
$$g = -\kappa\sigma_0 \cdot \mathrm{ilog}\left(\frac{\sigma}{\sigma_0}\right) - \sigma\alpha + \int_0^1 \hat{\lambda}\sigma_0 \cdot \exp\left(\frac{\hat{\alpha}}{\hat{\lambda}}\right) d\eta \qquad (3.32)$$

The continuous dissipation energy and yield function are additionally shown in equation 3.33 by Puzrin and Houlsby (2001b).

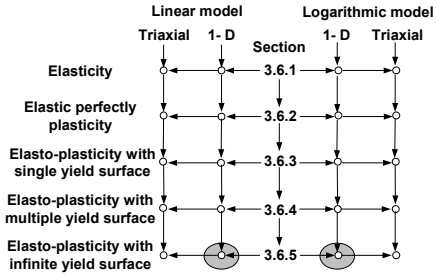

$$d = \int_0^1 \hat{c}\left|\dot{\hat{\alpha}}\right| d\eta,\ \hat{y} = \left|\hat{\chi}\right| - \hat{c} = 0$$
$$\text{and } c^* = \alpha - \int_0^1 \hat{\alpha} d\eta = 0 \qquad (3.33)$$

Note that the total of an internal variable constraint condition is $c^* = \alpha - \int_0^1 \hat{\alpha} d\eta = 0$.

A simple form of the $\hat{c}$ function can be defined as a linear function in the internal coordinate. Thus, the $\hat{c}$ is generally defined as $\hat{c} = c\eta + c_0$, where c, c_0 are arbitrary constants. In this research, for simplicity c_0 is set to zero, thus $\hat{c}$ becomes $c\eta$. Moreover, for consolidation behaviour of the infinite yield surface model it is simply defined as $\hat{c} = \hat{H}\hat{\alpha}\eta$ and $\hat{c} = p_0 \exp\left(\frac{\hat{\alpha}_p}{\hat{\lambda}}\right) \cdot \eta$ for linear and logarithmic model respectively.

For triaxial stress-strain parameters model, the energy formulations are expressed by equations 3.34 and 3.35 for the linear and logarithmic models respectively.

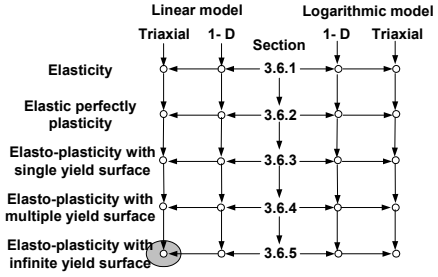

$$f = \frac{K\left(\varepsilon_v - \alpha_p\right)^2}{2} + \frac{3G\left(\varepsilon_s - \alpha_q\right)^2}{2} + \int_0^1 \frac{\hat{H}_p\hat{\alpha}_p^2}{2} + \frac{\hat{H}_q\hat{\alpha}_q^2}{2} d\eta$$
$$g = -\frac{p^2}{2K} - \frac{q^2}{6G} - \left(p\alpha_p + q\alpha_q\right) + \int_0^1 \frac{\hat{H}_p\hat{\alpha}_p^2}{2} + \frac{\hat{H}_q\hat{\alpha}_q^2}{2} d\eta \qquad (3.34)$$

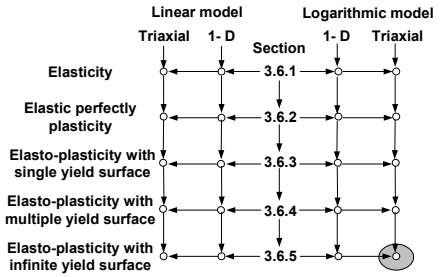

$$
\begin{aligned}
f &= \kappa p_0 \cdot \exp\left(\frac{\varepsilon_v - \alpha_p}{\kappa}\right) + \frac{3G\left(\varepsilon_s - \alpha_q\right)^2}{2} \\
&\quad + \int_0^1 \hat{\lambda} p_0 \cdot \exp\left(\frac{\hat{\alpha}_p + 3\hat{g}\hat{\alpha}_q^2/2}{\hat{\lambda}}\right) d\eta \\
g &= -\kappa p_0 \cdot \mathrm{ilog}\left(\frac{p}{p_0}\right) - \frac{q^2}{6G} - \left(p\alpha_p + q\alpha_q\right) \\
&\quad + \int_0^1 \hat{\lambda} p_0 \cdot \exp\left(\frac{\hat{\alpha}_p + 3\hat{g}\hat{\alpha}_q^2/2}{\hat{\lambda}}\right) d\eta
\end{aligned}
\tag{3.35}
$$

The dissipation and yield function can be modified based on the multiple yield surfaces model in equation 3.30, and thus the formulations become as in equation 3.36.

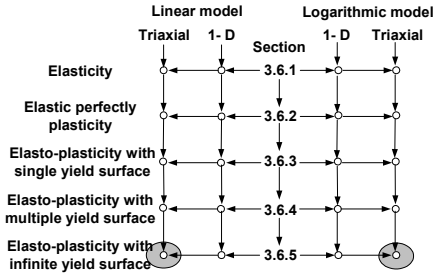

$$
\begin{aligned}
& d = \int_0^1 \hat{c} \cdot \sqrt{\dot{\hat{\alpha}}_p^2 + M^2 \dot{\hat{\alpha}}_q^2}\, d\eta = 0, \\
& \hat{y} = \sqrt{\hat{\chi}_p^2 + \hat{\chi}_q^2 / M^2} - \hat{c} = 0 \\
& \text{and } c_p^* = \alpha_p - \int_0^1 \hat{\alpha}_p d\eta = 0, \\
& c_q^* = \alpha_q - \int_0^1 \hat{\alpha}_q d\eta = 0
\end{aligned}
\tag{3.36}
$$

Note that the total internal variables are calculated from the integration of the kinematic internal variable, which plays the role of the plastic strain. The particular case of the $\hat{c}$ function is simply defined as a liner function with an internal coordinate, which is $\hat{c} = c\eta$. In addition, for consolidation behaviour of the triaxial case it can be defined as: $\hat{c} = \hat{H}_p \hat{\alpha}_p \eta$ and $\hat{c} = p_0 \exp\left(\frac{\hat{\alpha}_p + 3\hat{g}\hat{\alpha}_q^2/2}{\hat{\lambda}}\right) \cdot \eta$ for the linear and logarithmic model respectively.

The models, however, need an expression of the kinematic hardening function which corresponds to the observed stress-strain curve. This process involves much trial and error in order to define the mathematic formulae. Some selected hardening functions, which are suitable for soil behaviour, will be presented in the next section.

3.7 Continuous hardening function

In the previous section, the continuous hardening functions are required to define the stress-strain response for the continuous hyperplasticity model. The continuous function provides a smooth transition of the stiffness from elastic stiffness (when $\eta = 0$) to plastic stiffness (when $\eta = 1$). In order to construct the stress-strain curve, some components of the curve must be decided upon such as the initial slope, the asymptotic slope, and the secant or tangential slope at particular stress. This is because a particular hardening function is able to define only one particular stress-strain curve, for example the kinematic hardening function in equation 3.7 is used to generate the curve in Figure 3.4. The research is conducted separately for linear and logarithmic stress-strain relations.

3.7.1 Linear volumetric stress-strain relation

Puzrin and Houlsby (2001d) showed how to define a new hardening function based on a particular curve (backbone curve). An example of a specific form of the hyperbolic curve is also given in that paper. A more general hyperbolic curve, which can control the asymptote (c) and the rate of change of slope by adjusting two additional parameters (a, b), is shown in Figure 3.8(a). A hardening function for the general hyperbolic curve is in the form:

$$\hat{H} = \frac{E \cdot (1-\eta)^b}{2(a-1)} \tag{3.37}$$

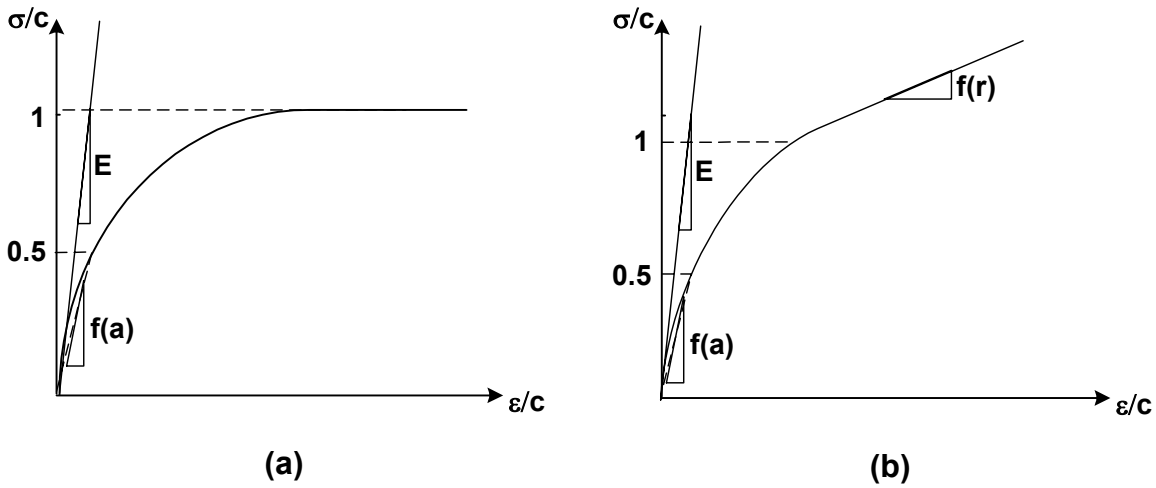

Figure 3.8 Hyperbolic stress-strain backbone curve
(a) Horizontal asymptote (b) Sloping asymptote

This following section shows a mathematic proof of the hyperbolic hardening function (equation 3.37) based on work by Puzrin and Houlsby (2001a).

General hyperbolic curve (Backbone curve)

Now, consider the first loading from $\hat{\chi} = \hat{c}$, and $\hat{\bar{\chi}} = \sigma - \hat{H}\hat{\alpha}$ thus, $\hat{\alpha} = \dfrac{\sigma - \hat{c}}{\hat{H}}$

For the case $\hat{c} = c\eta$ and assuming the hardening function as in equation 3.37, we obtain:

$$\varepsilon = \frac{\sigma}{E} + \int_0^{\sigma/c} \frac{\sigma - c\eta}{\hat{H}} d\eta = \frac{\sigma}{E} + \frac{2(a-1)}{E} \int_0^{\sigma/c} \frac{\sigma - c\eta}{(1-\eta)^b} d\eta$$

$$= \frac{\sigma}{E} + \frac{2(a-1)}{(b-1)(b-2)E} \left(\frac{c^{b-1}}{(c-\sigma)^{b-2}} - (b-2)\sigma - c \right)$$

Next, following the method presented by Puzrin and Houlsby (2001d) for general $\hat{H}(\eta)$, we obtain:

$$\frac{d^2\varepsilon}{d\sigma^2} = \frac{2(a-1)}{E} \left(\frac{1}{c(1-\sigma/c)^b} \right) = \frac{1}{c\hat{H}(\sigma/c)}$$

Thus, the loading curve can be defined by $\dfrac{d^2\varepsilon}{d\sigma^2} = \dfrac{1}{c\hat{H}(\sigma/c)}$, which is exactly the same as equation 3.6.

The modified version of the hyperbolic hardening function is shown in equation 3.38.

$$\hat{H} = \frac{E \cdot (1 - r \cdot \eta)^b}{2(a-1)} \tag{3.38}$$

The modification gives a sloping asymptote (when η approaches to 1), which is controlled by the parameter *r*, see Figure 3.8(b). The *r*-value should be between 0 (asymptote approaches vertical) and 1 (horizontal asymptote).

Consolidation loading curve

Now, we consider the loading curve of the consolidation model.

From $\hat{\chi} = \hat{c} = \hat{p}_x \eta = \hat{H}\hat{\alpha}\eta =$, and $\hat{\bar{\chi}} = \sigma - \hat{H}\hat{\alpha}$ thus, $\hat{\alpha} = \dfrac{\sigma}{\hat{H} \cdot (1-\eta)}$.

So, $\varepsilon = \frac{\sigma}{E} + \int_0^{\sigma/c} \frac{\sigma}{\hat{H}\cdot(1-\eta)} d\eta$

Differential with respect to time: $\dot{\varepsilon} = \frac{\dot{\sigma}}{E} + \int_0^{\sigma/c} \frac{\dot{\sigma}}{\hat{H}\cdot(1-\eta)} d\eta$

First derivative with respect to stress: $\frac{d\varepsilon}{d\sigma} = \frac{1}{E} + \int_0^{\sigma/c} \frac{1}{\hat{H}\cdot(1-\eta)} d\eta$

Second derivative with respect to stress: $\frac{d^2\varepsilon}{d\sigma^2} = \frac{1}{\hat{H}(\sigma/c)\cdot(c-\sigma)}$

Swelling unloading curve

For the unloading curve, unloading from σ_m (maximum stress history) and yield up to σ, we get $\sigma_m = \hat{p}_x(1+\eta^*)$, and $\sigma = \hat{p}_x(1-\eta^*)$ (see Figure 3.9), where $\hat{p}_x = \hat{H}\hat{\alpha}$ for the consolidation model.

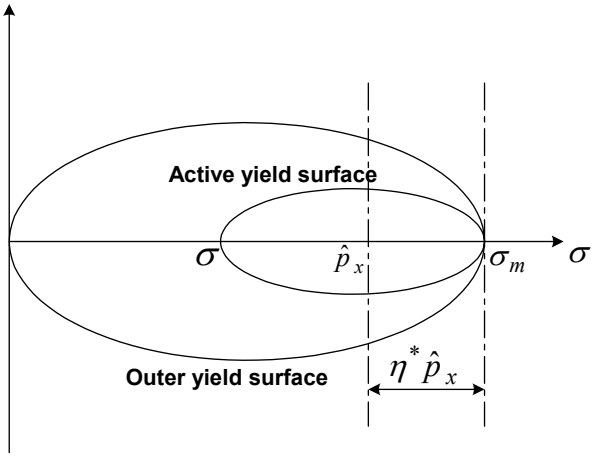

Figure 3.9 Illustration of the yield surfaces during on unloading from σ_m and yield up to σ

The results are $\eta^* = \frac{\sigma_m - \sigma}{\sigma_m + \sigma}$, $\frac{d\eta^*}{d\sigma} = \frac{-2\sigma_m}{(\sigma_m+\sigma)^2}$, and $\frac{\sigma}{\sigma_m} = \frac{1-\eta^*}{1+\eta^*}$.

So, $\varepsilon = \frac{\sigma}{E} + \int_0^{\eta} \frac{\sigma}{\hat{H}(1-\eta)} d\eta = \frac{\sigma}{E} + \int_0^{\eta^*} \frac{\sigma}{\hat{H}(1-\eta)} d\eta + \int_{\eta^*}^{1} \frac{\sigma_m}{\hat{H}(1+\eta)} d\eta$

Differential with respect to time:

$$\dot{\varepsilon} = \frac{\dot{\sigma}}{E} + \int_0^{\eta^*} \frac{\dot{\sigma}}{\hat{H}(1-\eta)} d\eta + \left(\frac{\sigma}{\hat{H}^*(1-\eta^*)} - \frac{\sigma_m}{\hat{H}^*(1+\eta^*)} \right) \dot{\eta}^* = \frac{\dot{\sigma}}{E} + \int_0^{\eta^*} \frac{\dot{\sigma}}{\hat{H}(1-\eta)} d\eta$$

First derivative with respect to stress: $\frac{d\varepsilon}{d\sigma} = \frac{1}{E} + \int_0^{\eta^*} \frac{1}{\hat{H}(1-\eta)} d\eta$

Second derivative with respect to stress: $\frac{d^2\varepsilon}{d\sigma^2} = \frac{1}{\hat{H}^*(1-\eta^*)}\frac{d\eta^*}{d\sigma} = \frac{-\sigma_m}{\hat{H}^*\sigma(\sigma_m+\sigma)}$

Thus, the swelling unloading curve is defined by $\frac{d^2\varepsilon}{d\sigma^2} = \frac{-\sigma_m}{\hat{H}^*\sigma(\sigma_m+\sigma)}$.

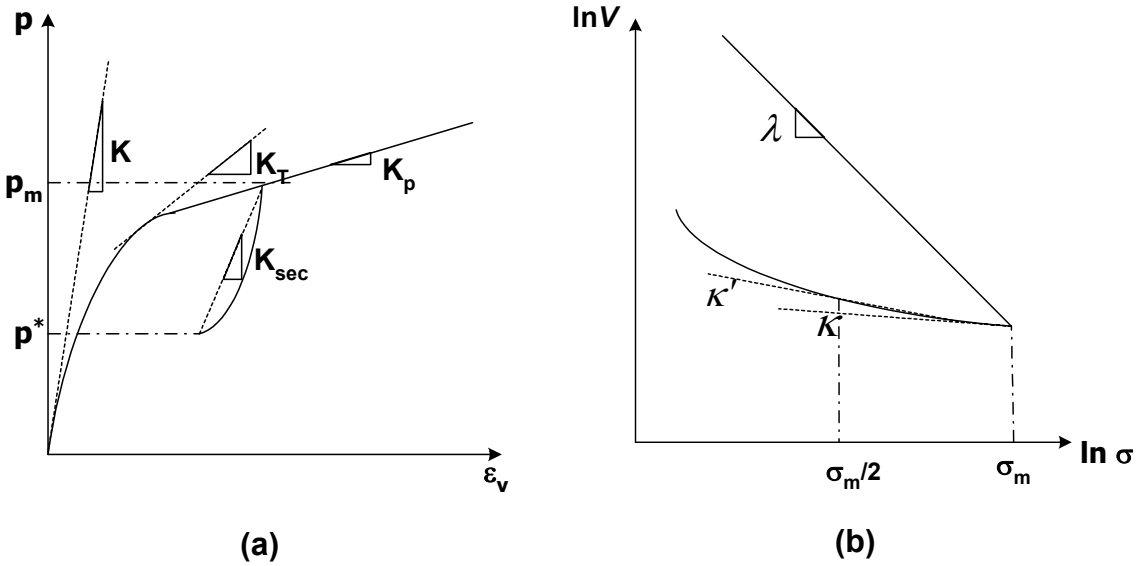

Figure 3.10 Consolidation loading and unloading curve
(a) Linear stress-strain relation, (b) Logarithmic stress-strain relation

Evaluation of the hardening parameter

Using the hardening function in equation 3.38, the linear consolidation hardening function can be written as $\hat{H}_p = \frac{K\cdot(1-r\cdot\eta)^{b_p}}{2(a_p-1)}$, which has four parameters (K, a_p, b_p and r) in total. The following are four conditions defining the components of the consolidation curve (see Figure 3.10(a)):

1. Initial bulk modulus K, $K = \left.\frac{dp}{d\varepsilon_v}\right|_{\varepsilon_v\to 0}$

2. Tangential bulk modulus K_T at particular p, $\frac{1}{K_T} = \frac{1}{K} + \int_0^{p/c}\frac{1}{\hat{H}_p(1-\eta)}d\eta$

3. Plastic modulus K_P (or asymptotic slope), $\frac{1}{K_P} = \frac{1}{K} + \int_0^{1}\frac{1}{\hat{H}_p(1-\eta)}d\eta$

4. Secant modulus K_{sec} at particular p^*,

$$\frac{1}{K_{\sec}} = \frac{1}{K} + \frac{1}{p_m - p^*}\int_0^{p^*/c}\left(\frac{p_m}{\hat{H}_p(1+\eta)} - \frac{p}{\hat{H}_p(1-\eta)}\right)d\eta$$

Thus, the above four conditions are adequate to estimate the linear consolidated parameters.

On the shearing behaviour, the shear modulus (G) is assumed to be linearly proportional to the mean stress that is $G = g_x p$. The shear hardening function is assumed by equation 3.37, which is $\hat{H}_q = \frac{3g_x p \cdot (1-\eta)^{b_q}}{2(a_q - 1)}$. The additional three parameters (g_x, a_q, b_q) are evaluated by using the shear stress-strain curve. Firstly, the g_x value can be obtained from the initial shear modulus (shearing after the consolidation process), which is $G_{ini} = g_x p_c$, where p_c represents consolidation pressure. The a_q and b_q parameters are observed using the parametric study based on experimental results.

3.7.2 Logarithmic volumetric stress-strain relation

Consolidation loading curve

Consider first loading from $\hat{\chi} = \hat{c} = \eta\sigma_0 \exp\left(\frac{\hat{\alpha}}{\hat{\lambda}}\right)$, and $\hat{\bar{\chi}} = \sigma - \sigma_0 \exp\left(\frac{\hat{\alpha}}{\hat{\lambda}}\right)$

thus, $\hat{\alpha} = \hat{\lambda}\log\left(\frac{\sigma}{\sigma_0(1+\eta)}\right)$

$\varepsilon = \kappa\log\left(\frac{\sigma}{\sigma_0}\right) + \int_0^{\eta^*}\hat{\lambda}\log\left(\frac{\sigma}{\sigma_0(1+\eta)}\right)d\eta$, where $\eta*$ is the largest active internal coordinate.

Differentiating with respect to time:

$\dot{\varepsilon} = \kappa\frac{\dot{\sigma}}{\sigma} + \int_0^{\eta^*}\hat{\lambda}\frac{\dot{\sigma}}{\sigma}d\eta + \hat{\lambda}\log\left(\frac{\sigma}{\sigma_0(1+\eta^*)}\right)\dot{\eta}^* = \kappa\frac{\dot{\sigma}}{\sigma} + \int_0^{\eta^*}\hat{\lambda}\frac{\dot{\sigma}}{\sigma}d\eta$, since $1+\eta^* = \frac{\sigma}{\sigma_0}$.

First derivative with respect to stress: $\frac{d\varepsilon}{d\sigma} = \frac{\kappa}{\sigma} + \int_0^{\eta^*}\frac{\hat{\lambda}}{\sigma}d\eta$

It is noteworthy that the definition of the conventional slope of the consolidation line is $\frac{d\varepsilon}{d(\log\sigma)} = \sigma\frac{d\varepsilon}{d\sigma}$. Thus, $\frac{d\varepsilon}{d(\log\sigma)} = \kappa + \int_0^{\eta^*}\hat{\lambda}d\eta$. The slope of the consolidation line should go to λ, when η approaches to 1, and equal to κ, when $\eta = 0$.

As a result, a possible function $\hat{\lambda}$ is assumed in the form of the power function:

$$\hat{\lambda} = (\lambda - \kappa)(n+1)\eta^n \tag{3.39}$$

where *n* is the degree of power function and κ, λ are the slope of the swelling line and normally consolidated line.

Swelling unloading curve

The form of $\hat{\lambda}$ is probably best determined from the unloading curve.

$$\varepsilon = \kappa \log\left(\frac{\sigma}{\sigma_0}\right) + \int_0^{\eta^*} \hat{\lambda} \log\left(\frac{\sigma}{\sigma_0(1-\eta)}\right) d\eta + \int_{\eta^*}^{1} \hat{\lambda} \log\left(\frac{\sigma_m}{\sigma_0(1+\eta)}\right) d\eta ,$$

where σ_m represents the stress history.

Differential with respect to time:

$$\dot{\varepsilon} = \kappa \frac{\dot{\sigma}}{\sigma} + \int_0^{\eta^*} \hat{\lambda} \log\left(\frac{\dot{\sigma}}{\sigma_0(1-\eta)}\right) d\eta + \left(\hat{\lambda}^* \log\left(\frac{\sigma}{\sigma_0(1-\eta^*)}\right) - \hat{\lambda}^* \log\left(\frac{\sigma_m}{\sigma_0(1+\eta^*)}\right)\right) \cdot \dot{\eta}^*$$

$$\dot{\varepsilon} = \kappa \frac{\dot{\sigma}}{\sigma} + \int_0^{\eta^*} \hat{\lambda} \frac{\dot{\sigma}}{\sigma} d\eta$$

First derivative with respect to stress: $\frac{d\varepsilon}{d\sigma} = \frac{\kappa}{\sigma} + \int_0^{\eta^*} \frac{\hat{\lambda}}{\sigma} d\eta$, so $\frac{d\varepsilon}{d(\log\sigma)} = \kappa + \int_0^{\eta^*} \hat{\lambda} d\eta$.

This leads to the same equation as derived from the loading curve.

Evaluation of the hardening parameter

There are three parameters (κ, λ, and *n*) for the logarithmic hardening function (equation 3.39). The κ and λ are the conventional soil parameters, which respectively represent the slope of swelling line and normally consolidated line. The *n* value can be obtained using the measure of the slope at half of the maximum past pressure ($\sigma_m/2$).

Let $\kappa' = \frac{d\varepsilon}{d(\log\sigma)}$ at $\frac{\sigma}{\sigma_m} = \frac{1}{2}$ (see Figure 3.10(b)),

then from Figure 3.9, $\eta^* = \frac{\sigma_m - \sigma}{\sigma_m + \sigma} = \frac{1}{3}$.

Thus, $\frac{\lambda - \kappa}{\kappa' - \kappa} = 3^{n+1}$, in which the *n* value can be obtained.

For the shearing behaviour, the assumption of the shear modulus which is linearly proportional to pressure is still used ($G = g_x p$). The shear hardening function also uses the form of equation 3.37, which is $\hat{g} = \frac{g_x \cdot (1-\eta)^b}{2(a-1)}$. The three shear hardening parameters (g_x, a, b) are evaluated by using the same methodology described in the linear model.

3.8 Summarised table of the hyperplaticity soil model

One-dimensional model

Table 3.6 The development of formulae for one-dimensional model

Model	Linear stress-strain	Logarithmic elastic stress-strain
1. Elasticity model	$g = -\frac{\sigma^2}{2E}$	$g = -\kappa\sigma_0 \operatorname{ilog}\left(\frac{\sigma}{\sigma_0}\right)$
2. Perfect plasticity model	$g = -\frac{\sigma^2}{2E} - \sigma\alpha$ $y = \lvert\chi\rvert - c = 0$	$g = -\sigma_0\kappa \operatorname{ilog}\left(\frac{\sigma}{\sigma_0}\right) - \sigma\alpha$ $y = \lvert\chi\rvert - c = 0$
3. Work hardening plasticity model	$g = -\frac{\sigma^2}{2E} - \sigma\alpha + \frac{H\alpha^2}{2}$ $y = \lvert\chi\rvert - c = 0$	$g = -\sigma_0\kappa \operatorname{ilog}\left(\frac{\sigma}{\sigma_0}\right) - \sigma\alpha + \sigma_0\lambda \exp\left(\frac{\alpha}{\lambda}\right)$ $y = \lvert\chi\rvert - c = 0$
4. Multi work hardening plasticity model	$g = -\frac{\sigma^2}{2E} - \sigma\alpha + \sum_{i=1}^{n} \frac{H_i\alpha_i^2}{2}$ $y_i = \lvert\chi_i\rvert - c_i = 0$	$g = -\kappa\sigma_0 \cdot \operatorname{ilog}\left(\frac{\sigma}{\sigma_0}\right) - \sigma\alpha + \sigma_0 \cdot \sum_{i=1}^{n} \lambda_i \exp\left(\frac{\alpha_i}{\lambda_i}\right)$ $y_i = \lvert\chi_i\rvert - c_i = 0$
5. Continuous work hardening plasticity model	$g = -\frac{\sigma^2}{2E} - \sigma\alpha + \int_0^1 \frac{\hat{H}\hat{\alpha}^2}{2} d\eta$ $\hat{y} = \lvert\hat{\chi}\rvert - \hat{c} = 0$	$g = -\kappa\sigma_0 \cdot \operatorname{ilog}\left(\frac{\sigma}{\sigma_0}\right) - \sigma\alpha + \int_0^1 \hat{\lambda}\sigma_0 \cdot \exp\left(\frac{\hat{\alpha}}{\hat{\lambda}}\right) d\eta$ $\hat{y} = \lvert\hat{\chi}\rvert - \hat{c} = 0$

Note: the definition $\operatorname{ilog}(x) = x\log(x) - x$, so that $\frac{d}{dx}\operatorname{ilog}(x) = \log(x)$

This section will summarise all the developed models, based on hyperplasticity theory. Each model is defined by two potentials (energy function and dissipation or yield function). The following section will present the model by using the Gibbs free energy (g) and the yield function (y).

The study begins with the elasticity model, followed by the perfectly plastic model, the kinematic work hardening plasticity model, and the multi work hardening plasticity model respectively. The development ends with the continuous work hardening plasticity model (plus the consolidation variant for consolidation behaviour). The above development is applied to both the linear and logarithmic type of stress-strain behaviour as summarised in Table 3.6.

Triaxial stress-strain model

Table 3.7 The development formulae of triaixal model

Model	Linear volumetric stress-strain	Logarithmic volumetric stress-strain
1. Elasticity model	$g = -\frac{p^2}{2K} - \frac{q^2}{6g_x p}$	$g = -\kappa p_0 \cdot \text{ilog}\left(\frac{p}{p_0}\right) - \frac{q^2}{6g_x p}$
2. Perfect plasticity model	$g = -\frac{p^2}{2K} - \frac{q^2}{6g_x p} - \left(p\alpha_p + q\alpha_q\right)$ $y = \sqrt{\chi_p^2 + \chi_q^2 / M^2} - c = 0$	$g = -\kappa p_0 \cdot \text{ilog}\left(\frac{p}{p_0}\right) - \frac{q^2}{6g_x p} - \left(p\alpha_p + q\alpha_q\right)$ $y = \sqrt{\chi_p^2 + \chi_q^2 / M^2} - c = 0$
3. Work hardening plasticity model	$g = -\frac{p^2}{2K} - \frac{q^2}{6g_x p} - \left(p\alpha_p + q\alpha_q\right) + \frac{H_p\alpha_p^2}{2} + \frac{H_q\alpha_q^2}{2}$ $y = \sqrt{\chi_p^2 + \chi_q^2 / M^2} - c = 0$	$g = -\kappa p_0 \cdot \text{ilog}\left(\frac{p}{p_0}\right) - \frac{q^2}{6g_x p} - \left(p\alpha_p + q\alpha_q\right) + \lambda p_0 \cdot \exp\left(\frac{\alpha_p + 3g\varepsilon_s^2/2}{\lambda}\right)$ $y = \sqrt{\chi_p^2 + \chi_q^2 / M^2} - c = 0$
4. Multi work hardening plasticity model	$g = -\frac{p^2}{2K} - \frac{q^2}{6g_x p} - \left(p\alpha_p + q\alpha_q\right) + \sum_{i=1}^{n} \frac{H_{p,i}\alpha_{p,i}^2}{2} + \frac{H_{q,i}\alpha_{q,i}^2}{2}$ $y_i = \sqrt{\chi_{p,i}^2 + \chi_{q,i}^2 / M^2} - c_i = 0$	$g = -\kappa p_0 \cdot \text{ilog}\left(\frac{p}{p_0}\right) - \frac{q^2}{6g_x p} - \left(p\alpha_p + q\alpha_q\right) + \sum_{i=1}^{n} \lambda_i p_0 \cdot \exp\left(\frac{\alpha_{p,i} + 3g_i\alpha_{q,i}^2/2}{\lambda_i}\right)$ $y_i = \sqrt{\chi_{p,i}^2 + \chi_{q,i}^2 / M^2} - c_i = 0$
5. Continuous work hardening plasticity model	$g = -\frac{p^2}{2K} - \frac{q^2}{6g_x p} - \left(p\alpha_p + q\alpha_q\right) + \int_0^1 \frac{\hat{H}_p\hat{\alpha}_p^2}{2} + \frac{\hat{H}_q\hat{\alpha}_q^2}{2} d\eta$ $\hat{y} = \sqrt{\hat{\chi}_p^2 + \hat{\chi}_q^2 / M^2} - \hat{c} = 0$	$g = -\kappa p_0 \cdot \text{ilog}\left(\frac{p}{p_0}\right) - \frac{q^2}{6g_x p} - \left(p\alpha_p + q\alpha_q\right) + \int_0^1 \hat{\lambda} p_0 \cdot \exp\left(\frac{\hat{\alpha}_p + 3\hat{g}\hat{\alpha}_q^2/2}{\hat{\lambda}}\right) d\eta$ $\hat{y} = \sqrt{\hat{\chi}_p^2 + \hat{\chi}_q^2 / M^2} - \hat{c} = 0$

This section summarises the triaxial stress-strain models; the model formulae are expressed in two types of stress-strain relation. The triaxial model development is concluded in Table 3.7 in a similar pattern to that of the one-dimensional model.

Continuous kinematic hardening model with consolidation variant

The final soil models developed, which are used in this research, are summarised in Tables 3.8 and 3.9 for linear and logarithmic models, respectively. The ultimate models require eight parameters (for linear), or seven parameters (for logarithmic) plus one parameter (μ) for rate-dependent. They describe a smooth change of response between elastic to elastic-plastic, a hystersis loop due to the immediate stress history, and can accurately predict the strength as well as the rate-dependence process. The significant advantage of this model is that it tries to compensate for the separate prediction of small strain level (e.g. cyclic behaviour) and large strain level problem (e.g. strength). The implementation of the model will be presented in the next section.

Table 3.8 Triaxial linear volumetric stress-strain model with continuous kinematic hardening plasticity plus consolidation variant

Constants	K, g_x, M, a_p, b_p, r, a_q, b_q
Potential functions	$g = -\frac{p^2}{2K} - \frac{q^2}{6g_x p} - \left(p\alpha_p + q\alpha_q\right) + \int_0^1 \frac{\hat{H}_p \hat{\alpha}_p^2}{2} + \frac{\hat{H}_q \hat{\alpha}_q^2}{2} d\eta$ $\hat{y} = \sqrt{\hat{\chi}_p^2 + \hat{\chi}_q^2 / M^2} - \hat{H}_p \hat{\alpha}_p \eta = 0$ $c_p^* = \alpha_p - \int_0^1 \hat{\alpha}_p d\eta = 0$, $c_q^* = \alpha_q - \int_0^1 \hat{\alpha}_q d\eta = 0$
Basic derivatives	$\varepsilon_v = -\frac{\partial g}{\partial p} = \frac{p}{K} - \frac{q^2}{6g_x p^2} + \alpha_p$, $\varepsilon_s = -\frac{\partial g}{\partial q} = \frac{q}{3g_x p} + \alpha_q$
Hardening functions	$\hat{H}_p(\eta) = \frac{(1-r\eta)^{b_p}}{2(a_p - 1)} K$, $\hat{H}_q(\eta) = \frac{(1-\eta)^{b_q}}{2(a_q - 1)} 3g_x p$
Notes	$\hat{c}$ replaced by $\hat{p}_x \eta = \hat{H}_p \hat{\alpha}_p \eta$ for consolidation variant

Table 3.9 Triaxial logarithmic volumetric stress-strain model with continuous logarithmic work hardening plasticity plus consolidation variant

Constants	p_0 (reference pressure), κ, λ, M, g_x, a, b
Definitions	Note the definition $\mathrm{ilog}(x) = x\log(x) - x$, so that $\frac{d}{dx}\mathrm{ilog}(x) = \log(x)$
Potential functions	$g = -\kappa p_0 \mathrm{ilog}\left(\frac{p}{p_0}\right) - \frac{q^2}{6g_x p} - \left(p\alpha_p + q\alpha_q\right) + p_0\int_0^1 \hat{\lambda}\exp\left(\frac{\hat{\alpha}_p + 3\hat{g}\hat{\alpha}_q^2/2}{\hat{\lambda}}\right)d\eta$ $\hat{y} = \sqrt{\hat{\chi}_p^2 + \hat{\chi}_q^2/M^2} - p_0\exp\left(\frac{\hat{\alpha}_p + 3\hat{g}\hat{\alpha}_q^2/2}{\hat{\lambda}}\right)\eta = 0$ $c_p^* = \alpha_p - \int_0^1 \hat{\alpha}_p d\eta = 0$, $c_q^* = \alpha_q - \int_0^1 \hat{\alpha}_q d\eta = 0$
Basic derivatives	$\varepsilon_v = -\frac{\partial g}{\partial p} = \kappa\log\left(\frac{p}{p_0}\right) - \frac{q^2}{6g_x p^2} + \alpha_p$, $\varepsilon_s = -\frac{\partial g}{\partial q} = \frac{q}{3g_x p} + \alpha_q$
Hardening functions	$\hat{\lambda}(\eta) = (\lambda - \kappa)(n+1)\eta^n$, where $n = \left[\log\left(\frac{\lambda - \kappa}{\kappa' - \kappa}\right)/\log(3)\right] - 1$ $\hat{g}(\eta) = \frac{(1-\eta)^b}{2(a-1)}g_x$
Notes	Replaced $\hat{c}$ by $\hat{p}_x\eta = p_0\exp\left(\frac{\hat{\alpha}_p + 3\hat{g}\hat{\alpha}_q^2/2}{\hat{\lambda}}\right)\eta$ for consolidation variant

3.9 Calculation algorithms

The potentials to define the constitutive model for soil behaviour have been proposed in the previous section. In order to develop the stress-strain response, the incremental response is introduced. One of the benefits of the hyperplasticity theory is that the rate-dependent plasticity can be derived from two potential functions. The following section will show two separate algorithms used to provide the stress-strain increment.

3.9.1 Rate independent formulation

Calculation

The derivation of the incremental response begins with the differentiation of the energy function. For example, based on Gibbs free energy function, the further differential, which gives the rate of the variables, can be shown below.

$$d\varepsilon_{ij} = \int\left(-\frac{\partial^2 \hat{g}}{\partial\sigma_{ij}\partial\sigma_{kl}} d\sigma_{kl} - \frac{\partial^2 \hat{g}}{\partial\sigma_{ij}\partial\hat{\alpha}_{kl}} d\hat{\alpha}_{kl} \right) d\eta \tag{3.40}$$

$$d\hat{\chi}_{ij} = -\frac{\partial^2 \hat{g}}{\partial\hat{\alpha}_{ij}\partial\sigma_{kl}} d\sigma_{kl} - \frac{\partial^2 \hat{g}}{\partial\hat{\alpha}_{ij}\partial\hat{\alpha}_{kl}} d\hat{\alpha}_{kl} \tag{3.41}$$

In addition to flow rule $d\hat{\alpha}_{ij} = \hat{\Lambda}(\eta)\frac{\partial \hat{y}^g}{\partial \hat{\chi}_{ij}}$ and combing it with the consistency equation $d\hat{y}^g = \frac{\partial \hat{y}^g}{\partial \sigma_{ij}} d\sigma_{ij} + \frac{\partial \hat{y}^g}{\partial \hat{\alpha}_{ij}} d\hat{\alpha}_{ij} + \frac{\partial \hat{y}^g}{\partial \hat{\chi}_{ij}} d\hat{\chi}_{ij} = 0$, the final constitutive equation, which eliminates the $d\hat{\chi}_{ij}$ term, becomes

$$d\hat{y}^g = \frac{\partial \hat{y}^g}{\partial \sigma_{ij}} d\sigma_{ij} + \frac{\partial \hat{y}^g}{\partial \hat{\alpha}_{ij}} d\hat{\alpha}_{ij} + \frac{\partial \hat{y}^g}{\partial \hat{\chi}_{kl}} \cdot \left(-\frac{\partial^2 \hat{g}}{\partial\hat{\alpha}_{kl}\partial\sigma_{ij}} d\sigma_{ij} - \frac{\partial^2 \hat{g}}{\partial\hat{\alpha}_{kl}\partial\hat{\alpha}_{ij}} d\hat{\alpha}_{ij} \right) = 0 \tag{3.42}$$

The overall increment response can be represented together in matrix form:

$$\begin{Bmatrix} \Delta\varepsilon_{ij} \text{ or } \Delta\sigma_{ij} \\ 0 \\ 0 \\ 0 \end{Bmatrix} = \begin{bmatrix} 1 \text{ or } 0 & 1 \text{ or } 0 & 0 & 0 \\ -\frac{\partial^2 \hat{g}}{\partial\sigma_{kl}\partial\sigma_{ij}} & -1 & \int -\frac{\partial^2 \hat{g}}{\partial\sigma_{kl}\partial\hat{\alpha}_{ij}} d\eta & 0 \\ 0 & 0 & -1 & \frac{\partial \hat{y}^g}{\partial \hat{\chi}_{ij}} \\ \frac{\partial \hat{y}^{g^*}}{\partial \sigma_{ij}} & 0 & \frac{\partial \hat{y}^{g^*}}{\partial \hat{\alpha}_{ij}} & 0 \end{bmatrix} \cdot \begin{Bmatrix} d\sigma_{ij} \\ d\varepsilon_{ij} \\ d\hat{\alpha}_{ij} \\ \hat{\Lambda} \end{Bmatrix} \tag{3.43}$$

where $y^*\left(\sigma_{ij},\hat{\alpha}_{ij}\right)=y\left(\sigma_{ij},\hat{\alpha}_{ij},\hat{\chi}_{ij}\left(\sigma_{ij},\hat{\alpha}_{ij}\right)\right)$, thus $\frac{\partial \hat{y}^{g^*}}{\partial \sigma_{ij}}=\frac{\partial \hat{y}^{g}}{\partial \sigma_{ij}}-\frac{\partial \hat{y}^{g}}{\partial \hat{\chi}_{kl}}\cdot\frac{\partial^2 \hat{g}}{\partial \hat{\alpha}_{kl}\partial \sigma_{ij}}$, and $\frac{\partial \hat{y}^{g^*}}{\partial \hat{\alpha}_{ij}}=\frac{\partial \hat{y}^{g}}{\partial \hat{\alpha}_{ij}}-\frac{\partial \hat{y}^{g}}{\partial \hat{\chi}_{kl}}\cdot\frac{\partial^2 \hat{g}}{\partial \hat{\alpha}_{kl}\partial \hat{\alpha}_{ij}}$.

Included in the total strain definition is $d\varepsilon_{ij}=d\varepsilon_{ij}^{e}+d\alpha_{ij}$, where $d\varepsilon_{ij}^{e}=-\frac{\partial^2 \hat{g}}{\partial \sigma_{kl}\partial \sigma_{ij}}$ from the hyperelasticity theory and $d\alpha_{ij}=\int \hat{\Lambda}\frac{\partial \hat{y}^{g}}{\partial \hat{\chi}_{ij}}d\eta$ from flow rule. Note that: the last row (consistency equation) in equation 3.43 must be modified to be $\hat{\Lambda}(\eta)=0$ when the stress state is inside yield surface (elastic).

Error control

In a numerical calculation, with the stress state approaching to the yield surface, the update stress routine at this point will not necessary give the exactly response on the yield surface. This error will bring the calculation result outside the yield surface, and the error may accumulate in every step of the calculation. The following error control routines named “alpha” and “beta” techniques (following the Greek alphabet), are consequently introduced. The former brings the yield value back to the actual yield surface after use of a large increment step. The value of zero on the right-hand side of the consistency equation is replaced by $-\alpha y_{old}$, where y_{old} represents the value of previous step of yield function and $\alpha=0$ to 1 (depending on how much the stress state will be moved back to actual yield surface, where $\alpha=1$ for moving stress state to actual yield surface).

The principle of the second technique is that a tolerance on the yield surface, β is allowed. This tolerance makes the yield surface into a zone (rather than a boundary as usual). The zone should be not too large (usually around 0.1 or 0.01 % of yield surface size). The yield condition should therefore be replaced by some figures, which are a function of the tolerance β (i.e. $y=f(\beta)$) rather than $y=0$ as usual.

Flow chart

The flow chart of calculation is illustrated in Figure 3.11(a)

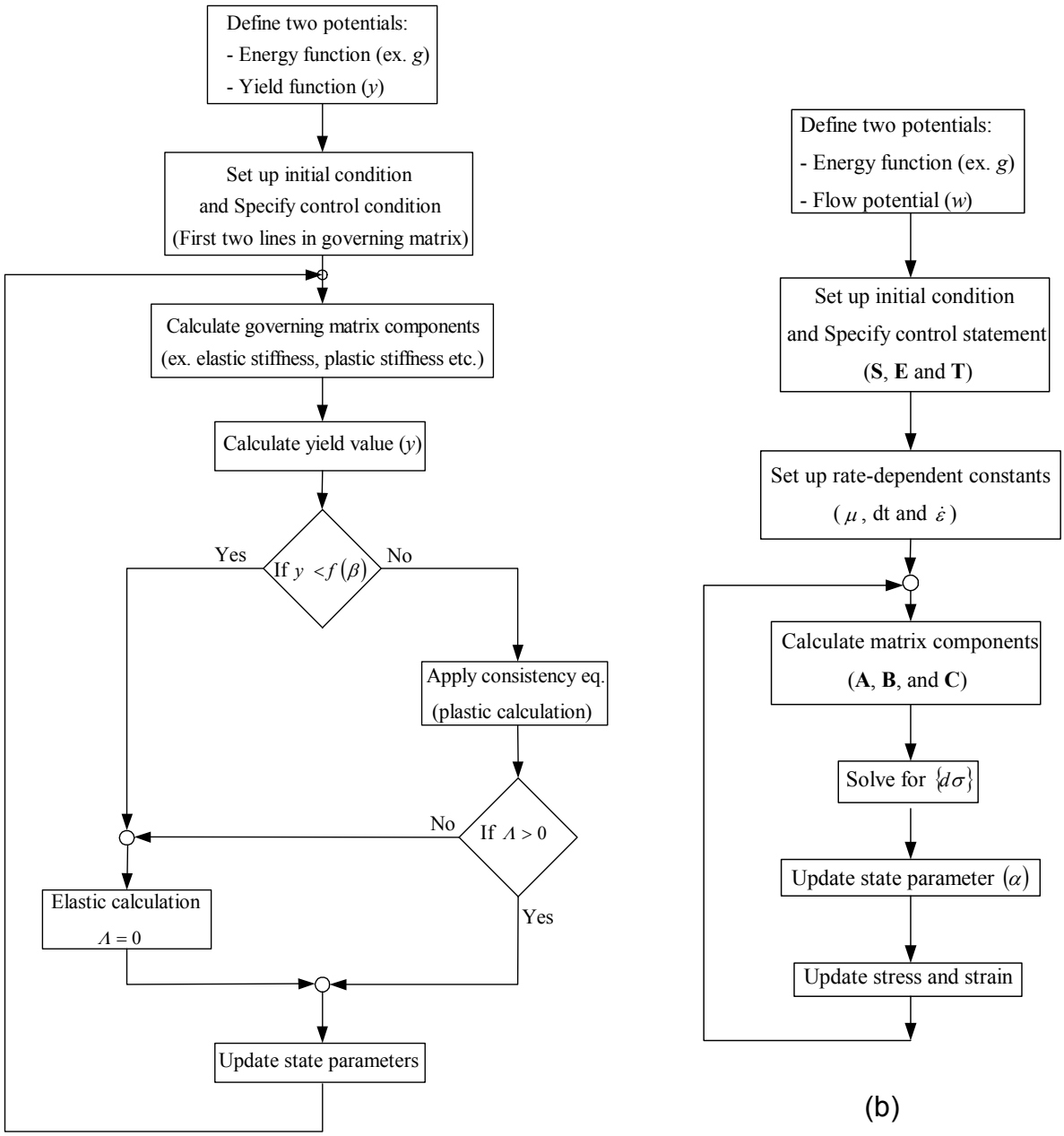

Figure 3.11 Calculation flow chart

(a) Rate-independent algorithm, (b) Rate-dependent algorithm

3.7.2 Example of rate-independent triaxial test

An example of triaxial stress-strain parameters for the rate-independent calculation algorithm is presented. Assuming that there are n numbers of yield surfaces, the governing matrix size becomes $[(2+n)nv]+1$, where nv is a number of

stress-strain parameters (*nv* = 2 for triaxial case). The governing matrix for strain controlled triaxial undrained test is :-

$$\begin{Bmatrix} \Delta\varepsilon \\ 0 \\ 0 \\ 0 \\ 0 \\ 0 \\ -\alpha \cdot y_{1old} \\ \vdots \\ 0 \\ 0 \\ -\alpha \cdot y_{nold} \end{Bmatrix} = \begin{bmatrix} 0 & 0 & 0 & 1 & 0 & 0 & 0 & \cdots & 0 & 0 & 0 \\ 0 & 0 & 1 & 0 & 0 & 0 & 0 & \cdots & 0 & 0 & 0 \\ -\frac{\partial^2 g}{\partial p^2} & -\frac{\partial^2 g}{\partial p \partial q} & -1 & 0 & 1 & 0 & 0 & \cdots & 0 & 0 & 0 \\ -\frac{\partial^2 g}{\partial q \partial p} & -\frac{\partial^2 g}{\partial q^2} & 0 & -1 & 0 & 1 & 0 & \cdots & 0 & 0 & 0 \\ 0 & 0 & 0 & 0 & -1 & 0 & \frac{\partial y_1}{\partial \chi_{p1}} & \cdots & 0 & 0 & 0 \\ 0 & 0 & 0 & 0 & 0 & -1 & \frac{\partial y_1}{\partial \chi_{q1}} & \cdots & 0 & 0 & 0 \\ \frac{\partial y_1^*}{\partial p} & \frac{\partial y_1^*}{\partial q} & 0 & 0 & \frac{\partial y_1^*}{\partial \alpha_p} & \frac{\partial y_1^*}{\partial \alpha_q} & 0 & \cdots & 0 & 0 & 0 \\ \vdots & \vdots & \vdots & \vdots & \vdots & \vdots & \vdots & \cdots & \vdots & \vdots & \vdots \\ 0 & 0 & 0 & 0 & -1 & 0 & \frac{\partial y_n}{\partial \chi_{pn}} & \cdots & 0 & 0 & 0 \\ 0 & 0 & 0 & 0 & 0 & -1 & \frac{\partial y_n}{\partial \chi_{qn}} & \cdots & 0 & 0 & 0 \\ \frac{\partial y_n^*}{\partial p} & \frac{\partial y_n^*}{\partial p} & 0 & 0 & \frac{\partial y_n^*}{\partial \alpha_p} & \frac{\partial y_n^*}{\partial \alpha_q} & 0 & \cdots & 0 & 0 & 0 \end{bmatrix} \cdot \begin{Bmatrix} dp \\ dq \\ dv \\ d\varepsilon \\ d\alpha_{p1} \\ d\alpha_{q1} \\ \Lambda_1 \\ \vdots \\ d\alpha_{pn} \\ d\alpha_{qn} \\ \Lambda_n \end{Bmatrix} \tag{3.44}$$

where, $\frac{\partial y_n^*}{\partial p} = \frac{\partial y_n}{\partial p} - \left(\frac{\partial y_n}{\partial \chi_{pn}} \cdot \frac{\partial^2 g}{\partial \alpha_{pn} \partial p} + \frac{\partial y_n}{\partial \chi_{qn}} \cdot \frac{\partial^2 g}{\partial \alpha_{qn} \partial p} \right)$,

$\frac{\partial y_n^*}{\partial q} = \frac{\partial y_n}{\partial q} - \left(\frac{\partial y_n}{\partial \chi_{pn}} \cdot \frac{\partial^2 g}{\partial \alpha_{pn} \partial q} + \frac{\partial y_n}{\partial \chi_{qn}} \cdot \frac{\partial^2 g}{\partial \alpha_{qn} \partial q} \right)$,

$\frac{\partial y_n^*}{\partial \alpha_{pn}} = \frac{\partial y_n}{\partial \alpha_{pn}} - \left(\frac{\partial y_n}{\partial \chi_{pn}} \cdot \frac{\partial^2 g}{\partial \alpha_{pn}^2} + \frac{\partial y_n}{\partial \chi_{qn}} \cdot \frac{\partial^2 g}{\partial \alpha_{qn} \partial \alpha_{pn}} \right)$,

$\frac{\partial y_n^*}{\partial \alpha_{qn}} = \frac{\partial y_n}{\partial \alpha_{qn}} - \left(\frac{\partial y_n}{\partial \chi_{pn}} \cdot \frac{\partial^2 g}{\partial \alpha_{pn} \partial \alpha_{qn}} + \frac{\partial y_n}{\partial \chi_{qn}} \cdot \frac{\partial^2 g}{\partial \alpha_{qn}^2} \right)$

3.9.3 Rate dependent formulation

Calculation

The incremental response for rate-dependence can be derived in the same way as the rate-independence except that the internal kinematic variable rate $\left(\dot{\hat{\alpha}}_{ij}\right)$ is calculated from the flow potential. For example, assuming that the model is defined

based on the Gibbs free energy function, the incremental relations in equation 3.40 and incorporates the derivative of flow potential $\dot{\hat{\alpha}}_{ij} = \frac{\partial w}{\partial \hat{\chi}_{ij}}$, the incremental response can be re-expressed in the form:

$$d\varepsilon_{ij} = -\frac{\partial^2 \hat{g}}{\partial \sigma_{ij} \partial \sigma_{kl}} d\sigma_{kl} - \int \left(\frac{\partial^2 \hat{g}}{\partial \sigma_{ij} \partial \hat{\alpha}_{kl}} \cdot \frac{\partial w}{\partial \hat{\chi}_{kl}} \right) d\eta \cdot dt \tag{3.45}$$

$$d\hat{\chi}_{ij} = -\frac{\partial^2 \hat{g}}{\partial \hat{\alpha}_{ij} \partial \sigma_{kl}} d\sigma_{kl} - \frac{\partial^2 \hat{g}}{\partial \hat{\alpha}_{ij} \partial \hat{\alpha}_{kl}} \cdot \frac{\partial w}{\partial \hat{\chi}_{kl}} dt \tag{3.46}$$

In addition the boundary conditions during the calculation (ex. undrained condition, stress control etc.) are introduced by the controlling statement:

$$S_{ijkl} \cdot d\sigma_{kl} + E_{ijkl} \cdot d\varepsilon_{kl} = T_{ij} \cdot dt \tag{3.47}$$

where **S** and **E** are stress and strain control matrices, and **T** is the strain or stress rate vector.

Substituting $d\varepsilon_{ij}$ into equation (3.47), the equation becomes:

$$\left(S_{ijkl} + E_{ijmn} \left(-\frac{\partial^2 \hat{g}}{\partial \sigma_{mn} \partial \sigma_{kl}} \right) \right) \cdot d\sigma_{kl} = \left[T_{ij} - E_{ijmn} \int \left(-\frac{\partial^2 \hat{g}}{\partial \sigma_{mn} \partial \hat{\alpha}_{kl}} \cdot \frac{\partial w}{\partial \hat{\chi}_{kl}} \right) d\eta \right] \cdot dt \tag{3.48a}$$

or, in the matrix form: $$\left(\mathbf{S} + \mathbf{E} \cdot \mathbf{A}\right) \cdot \mathbf{d\sigma} = \left\{ \mathbf{T} - \mathbf{E} \cdot \int \left(\mathbf{B} \cdot \mathbf{C}\right) \cdot d\eta \right\} \cdot dt \tag{3.48b}$$

where $\mathbf{A} = -\frac{\partial^2 \hat{g}}{\partial \sigma_{ij} \partial \sigma_{kl}}$, $\mathbf{B} = -\frac{\partial^2 \hat{g}}{\partial \sigma_{ij} \partial \hat{\alpha}_{kl}}$, and $\mathbf{C} = \frac{\partial w}{\partial \hat{\chi}_{ij}}$.

Error control

The accuracy of the rate-dependent calculation algorithm mainly depends on the time step and the viscosity coefficient (μ). The artificial rate-independent process can be approached by assuming a small value of viscosity. This would lead to a numerical problem in the calculation of $\dot{\hat{\alpha}}_{ij}$, because of the factor $1/\mu$ in the $\dot{\hat{\alpha}}_{ij}$ term. A reasonable time step and strain rate must be tuned to correspond to the viscosity value, otherwise errors from rate process would dominate.

Flow chart

The flow chart of rate-dependent algorithm is illustrated in Figure 3.11(b).

3.9.4 Example of rate-dependent triaxial test

An example of triaxial stress-strain parameters for the rate-dependent calculation algorithm will also be presented. Assume that there are *n* numbers of yield surface; the governing matrix for strain controlled triaxial undrained test as follows:

$$\begin{aligned}&\left[\begin{bmatrix}0 & 0\\ 0 & 0\end{bmatrix}+\begin{bmatrix}0 & 1\\ 1 & 0\end{bmatrix}\cdot\begin{bmatrix}-\dfrac{\partial^2 g}{\partial p^2} & -\dfrac{\partial^2 g}{\partial p\partial q}\\ -\dfrac{\partial^2 g}{\partial q\partial p} & -\dfrac{\partial^2 g}{\partial q^2}\end{bmatrix}\right]\cdot\begin{Bmatrix}dp\\ dq\end{Bmatrix}\\ &=\left\{\begin{Bmatrix}\dot{\varepsilon}\\ 0\end{Bmatrix}-\begin{bmatrix}0 & 1\\ 1 & 0\end{bmatrix}\cdot\frac{1}{n}\sum_{i=1}^{n}\left(\begin{bmatrix}-\dfrac{\partial^2 g}{\partial p\partial \alpha_{p_i}} & -\dfrac{\partial^2 g}{\partial p\partial \alpha_{q_i}}\\ -\dfrac{\partial^2 g}{\partial q\partial \alpha_{p_i}} & -\dfrac{\partial^2 g}{\partial q\partial \alpha_{q_i}}\end{bmatrix}\cdot\begin{Bmatrix}\dfrac{\partial w}{\partial \chi_{p_i}}\\ \dfrac{\partial w}{\partial \chi_{q_i}}\end{Bmatrix}\right)\right\}\cdot dt\end{aligned} \tag{3.49}$$

3.9.5 Comparison between two approaches

The most obvious benefit of the rate-dependent calculation is the including rate dependency for materials which can exhibit any significant rate effects. Another advantage of the rate-dependent procedure is that it is not necessary to stick with the consistency condition (during the plasticity condition, the state always stays on the yield surface). Thus, the higher complexity of numerical calculation is not required for the rate-dependence. This may not require some error controlling by special procedures that the rate-independent does. From the mathematic viewpoint, the algorithm for rate-independence has to deal with the large size of the governing matrix; on the other hand, the rate-dependent algorithm operates on smaller sized matrices. As a result, it is logically shown that the computing time is reduced.

Chapter 4
Review of experimental work

In order to develop a constitutive soil model, relevant experimental soil data are required. Two separate sets of experimental data for Bangkok clay have been obtained from the Asian Institute of Technology (AIT), and Chulalongkorn University in Bangkok, Thailand. The data set from AIT was gathered for the purpose of studying the stress-strain behaviour of Bangkok clay inside the State Boundary Surface (SBS). The experimental data set from Chulalongkorn University is focused on the cyclic behaviour of Bangkok Clay, which is mostly concentrated on exploring the undrained cyclic shear strength. The main purpose of this chapter is to present and reproduce some key results from the experimental work on Bangkok clay. The test data has been locally published as Masters theses at AIT and Chulalongkorn University, the original copies of which are difficult for the reader to access. Therefore, this chapter summarises the experimental techniques and conditions from which the data is obtained. This chapter starts with a description of Bangkok clay properties followed by the experimental programs, testing conditions and finally an illustration of the experimental results. The advantages and disadvantages of these experimental data are also discussed.

4.1 Geology Condition

The Central Plain of Thailand consists of a flat, marine delta deposit about 300km measured north to south and about 200km east to west. These sediments comprise alternate layers of stiff clay and dense sand aquifers down to 500m depth. Generally, the topmost layer contains 2m thick weathered clay underlain by about 9m of very soft clay, and followed by about 4m of soft to medium clay. Stiff clay is encountered starting from a depth of about 15m. The thick deposit of soft clay is the cause of substructure problems associated with low strength and high compressibility. As a result, research on the stress-strain-strength of Bangkok clay has been significantly developing for some time in Thailand.

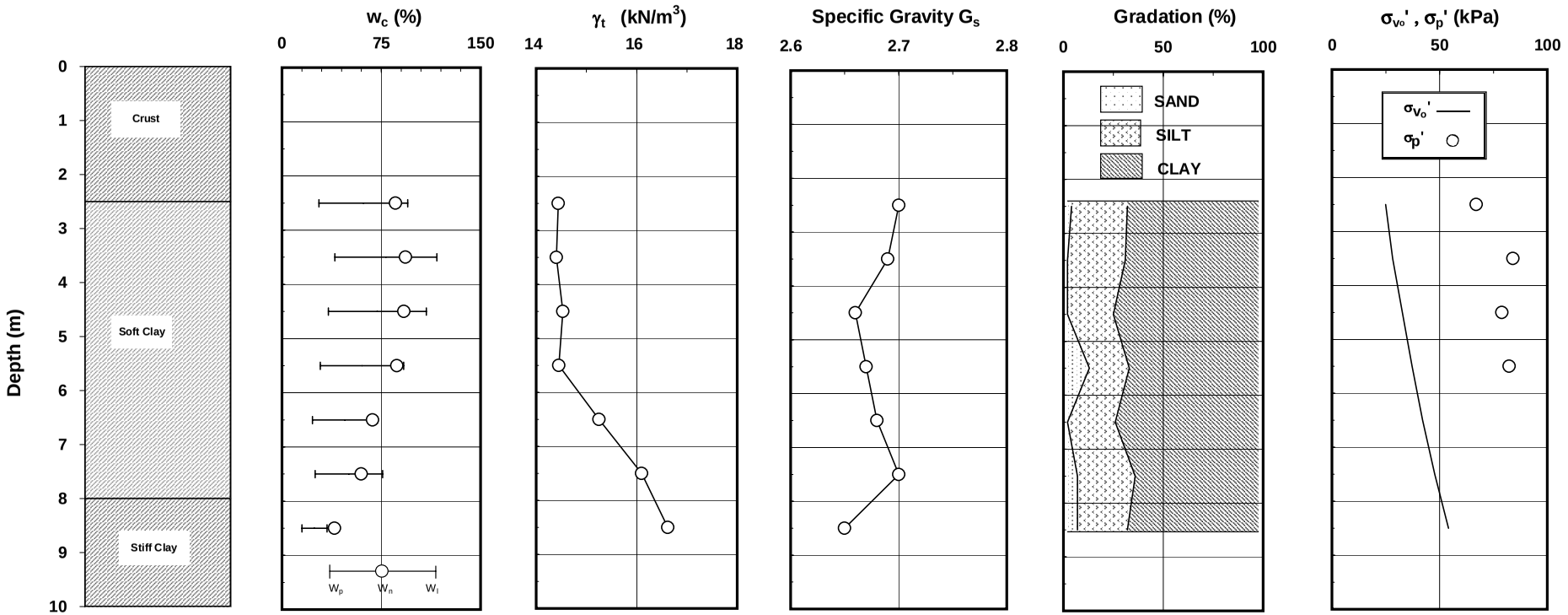

Fig. 4.1 Profile of physical properties of AIT soil sample (Seah, 1998)

4.2 Experimental program

Experimental tests from AIT were carried out mainly by triaxial test in a comprehensive manner, by controlled stress and strain. The studies involving a ten-year research programme, were primarily intended to investigate the state boundary surface for Bangkok clay. Details of each experimental program were stated in the author's master thesis, Likitlersuang (2000). Other experimental programs have also been active at AIT, including the study of the consolidation behaviour of Bangkok clay with constant rate of strain consolidation testing (CRS).

For cyclic data, Teachavorasinskun and Thongchim (2001) studied the cyclic behaviour of clay by two testing procedures (staged cyclic loading test, SC, and continuous cyclic loading test, CC). The shear modulus and damping ratio during undrained cyclic loading at varying stress amplitude were obtained. The stress rate effect on the stiffness of clay was pointed out, Teachavorasinskun and Thongchim (2002).

4.2.1 Sample preparation

The AIT clay samples used in the following analysis are undisturbed soft Bangkok clay taken from a site within the AIT campus. Samples are collected by using 7.5cm diameter, 90cm long thin-walled piston samplers from depth of 3 to 4m. The observation of ground conditions underlying the site is shown in Figure 4.1. By assuming the soil profile as shown, the pre-consolidation pressure can be roughly estimated. The pre-consolidation pressure varies with depth in the deposit; this may result from the combination of effects of the river deposition and the oscillation of ground water level.

After sampling, the tube containing the soil sample, is immediately sealed with paraffin wax and the samples are kept in a cold wet room to prevent the loss of moisture content. Before testing, the index properties: particle distribution, specific gravity and Atterberg limits are carried out according to the ASTM (1965) standard procedure. The general index properties of soil samples are presented in Table 4.1.

The cyclic tests are performed on undisturbed samples collected at depth of about 6m from a site in Chulalongkorn University. The natural water content, and plasticity index of the tested samples vary in the ranges 65-70%, and 39-40%

respectively. The maximum past stresses vary with depth, which can be approximated from in-situ stress based on OCR values of about 1.00-1.30 (lightly overconsolidated clay).

Table 4.1 General Bangkok soft clay index properties

Property	Value
Natural water content (%)	80-90
Liquid Limit (%)	95-110
Plastic Limit (%)	35-40
Plasticity Index	55-75
Liquidity Index	0.7-0.8
Average unit weight (kN/m^3)	14.8
Specific gravity	2.7
Sand content (%)	5
Silt content (%)	25
Clay content (%)	75

4.2.2 Equipment accuracy

The triaxial equipment is made up of three main parts: triaxial cell, loading device and readout unit. The triaxial cell can accommodate the soil specimen which has the nominal dimensions of 50mm diameter and 100mm length. To allow drainage to occur during the saturation and consolidation processes, saturated porous stones and circular filter papers are placed at both ends of the specimen. In extension tests the filter paper strips are added around the specimen spirally. The specimen is also enclosed in a rubber membrane and sealed with two O-rings on each end.

For loading, the cell pressure is applied by self-compensating mercury columns and dead weight suspended from a hanger. The Bourden type of pressure gauge with an accuracy of 1kPa (0.01kg/cm^2) is used. The axial load is applied by a one-ton capacity frame and measured using a load cell. The change in volume is measured through a 10 or 25cm^3 capacity burette. The pore pressure and axial displacement are measured by a pressure transducer of 1,000kPa (10kg/cm^2) capacity and displacement transducer respectively. Some of the experimental work was done ten years ago, when the electronic transducers were not so common as now. A dial gauge with an accuracy of 0.01mm was used for measuring axial displacement at that

time. The accuracy achieved for load and displacement measurements varies between the different theses cited here as different calibration procedures were used by different authors. However, the accuracy of strain measurement of these data sets can be estimated, based on the accuracy of the devices and dimensions of the specimen. It is of the order of 10^{-4} for axial strain and 10^{-3} for volumetric strain.

4.2.3 Testing program

The triaxial program consists of three main processes: sample preparation, consolidation and shearing process. The essential process of sample preparation is to ensure that entire specimen is fully saturated, because of the simplicity of pore pressure measurement and analysis. The specimen is saturated by balancing cell pressure and back pressure, and then leaving the specimen for at least 24 hours before testing.

After fully saturating the specimen, the consolidation process is implemented. This consolidation process is done by two different approaches: isotropic consolidation and K_0-consolidation. In the first approach, the loading increment ratio[1] is set to unity for the sample. The next incremental load will apply after leaving the previous load 24 hours for ensuring fully drainage occur. The latter approach is more complicated because cell pressure and axial stress must be applied simultaneously in order to maintain the absence of lateral strain for K_0-consolidation or other anisotropic consolidation condition. The reduction of pressure is required for preparation of overconsolidated samples. The overconsolidated ratio (OCR) is defined as the ratio between the maximum past mean effective normal stress (p_{max}) and the current mean effective normal stress (p).

The shearing process begins after 24 hours of consolidation or swelling to ensure full dissipation of excess pore pressure. For stress controlled tests (only the CID-0, CID-180, CK_0D-0, CK_0D-180, CAD-0 and CAD-180 tests), a mean normal stress increment of 10kPa is used and the sample is left for 24 hours to allow the drainage to occur. For strain controlled tests (all directions of the CID, CK_0D and CAD tests except 0^o and 180^o directions), the displacement rate applied for drained tests was 0.0024mm/min and the cell pressure was continuously adjusted to maintain

[1] Loading increment ratio is defined as the next load increment divided by the current applied load

the stress direction. Undrained tests (CIU tests) were conducted with constant cell pressure and involved increasing the axial load for compression and increasing the cell pressure for extension during undrained shearing. The sample was sheared at a displacement rate of 0.009mm/min.

For cyclic undrained tests, the samples are firstly saturated and then consolidated to the prescribed initial isotropic consolidation pressures: 50kPa and 100kPa. The samples tested were in a lightly overconsolidated state. The shearing under undrained conditions was performed as stress controlled with varying rate of loading. The shear stress amplitudes are varied from small, and moderate to large stress levels: 0.3, 0.5 and 0.8 times unconsolidated undrained shear strength, q_u (measured from UU-test, where $q_u = 2s_u$). In order to keep the load frequencies constant at 0.1Hz and 1Hz, the rates of loading applied have to be automatically adjusted corresponding with amplitude level. The testing schemes are summarised in Table 4.2.

Table 4.2 Test scheme for cyclic undrained tests

Initial consolidation stress, (p_{ini})	Load frequency (Hz)	Stress amplitude, (q/p_{ini})
50	0.1, 1.0	0.24, 0.40
	0.1, 1.0	0.40, 0.60
	0.1, 1.0	0.60, 0.83
100	0.1, 1.0	0.32, 0.34
	0.1, 1.0	0.56, 0.52
	0.1, 1.0	0.80, 0.74

4.3 AIT experimental data

The available triaxial experimental data from AIT are briefly summarised in Table 4.3. The triaxial experimental data can be categorised into three groups: consolidation data, undrained shear data and drained shear data. The detail of each group is explained and illustrated as follows.

Table 4.3 Available triaxial experimental test data from AIT

Author	Year	Test	OCR[2]	η [3]	Direction[4]	Number of tests.
Kim	1991	CIU	1.00-4.25	0	-	9
		CK_0UC	1.00-2.75	0.49-0.09	-	7
		CK_0UE	1.00-2.75	0.49-0.09	-	7
Gurung	1992	CIP	1.00-16.00	0	-	10
		CIU	1.00-16.00	0	-	10
Uchaipichat	1998	CIDC	2.75	0	0-180	15
Navaneethan	1999	CIDE	2.75	0	180-360	15
Khan	1999	CK_0DC	1.85	0.23	0-180	8
		CK_0DE	1.85	0.23	180-360	8
		CK_0UC	1.85	0.23	-	1
		CK_0UE	1.85	0.23	-	1
Tuladhar	2000	CADC	1.00	-0.27	0-180	8
		CADE	1.00	-0.27	180-360	8
		CAUC	1.00	-0.27	-	1
		CAUE	1.00	-0.27	-	1

4.4 Consolidation data

Though there are several tests on consolidation, only some data on consolidation hysteresis behaviour can be used. The complete load-unload-reload loops are required for capturing the behaviour due to immediate stress history. The consolidation data are divided into four types based on testing equipment and condition.

4.4.1 Isotropic consolidation data from triaxial test

The isotropic consolidation data are achieved from the consolidation stage of the isotropic fan tests that were done by Uchipichat (1998) and Navaneethan (1999). These two investigations prepared every specimen as an overconsolidated sample at constant OCR value in isotropic consolidation condition; the consolidation stress path

[2]The definition of OCR-value is based on mean effective stress (p) rather than the original work that use the definition based on vertical effective stress (σ'_v)

[3] η is initial stress ratio (p/q) before shearing the samples

[4] The direction of stress paths is measured from the p-axis in a counter clockwise direction

is shown in Figure 4.2(a). The data on consolidation stage can be used to construct a consolidation curve. Furthermore, the CID-0 and CID-180 tests, equivalent to isotropic reload and unload consolidation respectively, can provide further information on the consolidation curve to obtain the effect of immediate stress history as shown in Figures 4.3(a) and (b).

However, there are two disadvantages with the isotropic consolidation data. Firstly, according to the large load increment in the consolidation process, only one data point on swelling back curve was observed. As a result, an accurate hysteresis loop cannot be built. However, there are still enough data points to form completely a reload and unload curve from CID-0 and CID-180 tests. Although, from this data it is not possible to generate the hysteresis loop, the behaviour on changing of tangent stiffness due to immediate stress past history of soil can be observed.

Another, rather insignificant, problem is the discontinuity of the consolidation curve, caused by the use of different samples. Every specimen does not necessarily have the same specific volume or void ratio. The consolidation curve between two samples on unloading and reloading therefore might not coincide. In order to reduce this complication on analysis, the assumption that every specimen has the same specific volume after the consolidation process finished is proposed. This assumption will not affect the actual behaviour of soil; it merely shifts the starting point of every test to coincide as shown in Figure 4.3(c).

4.4.2 Anisotropic consolidation data from triaxial test

The anisotropic consolidation or K_0-consolidation conditions involve zero lateral strain during the consolidation process. Since the K_0 value of Bangkok clay is less than unity, the slope of consolidation stress path will be positive as shown in Figure 4.2(a).

The K_0-consolidation data can be obtained from the consolidation process for the K_0 fan tests, studied by Khan (1999). The thesis investigated the behaviour of Bangkok clay varying stress path from 0^o to 360^o. During the consolidation phase, every specimen was consolidated in K_0-consolidation condition along both loading and swelling paths, depicted in Figure 4.2(a). However, after back-calculation to establish the K_0 condition, it is found that there are small radial strains on the

swelling paths. This mean that the K_0-consolidation condition occurs only on the loading paths, whereas on the swelling paths should be treated as a stress path control.

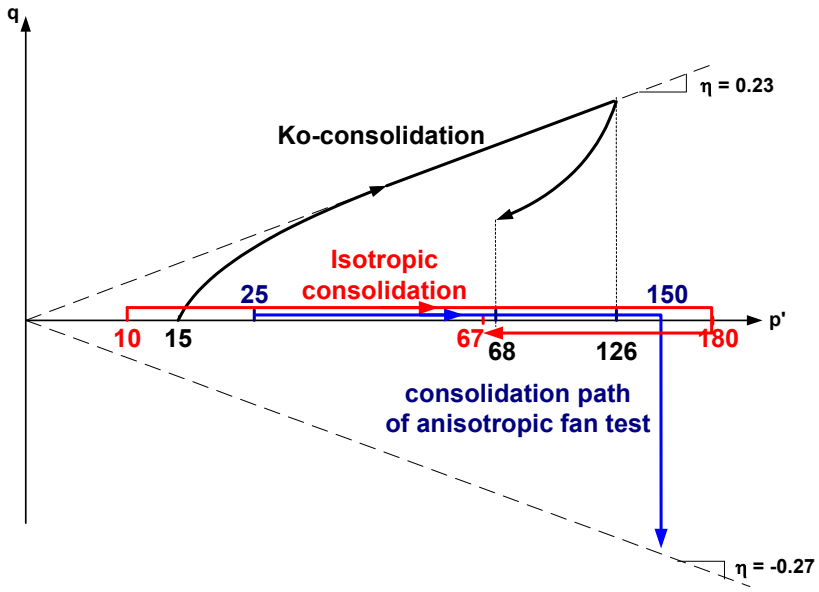

(a)

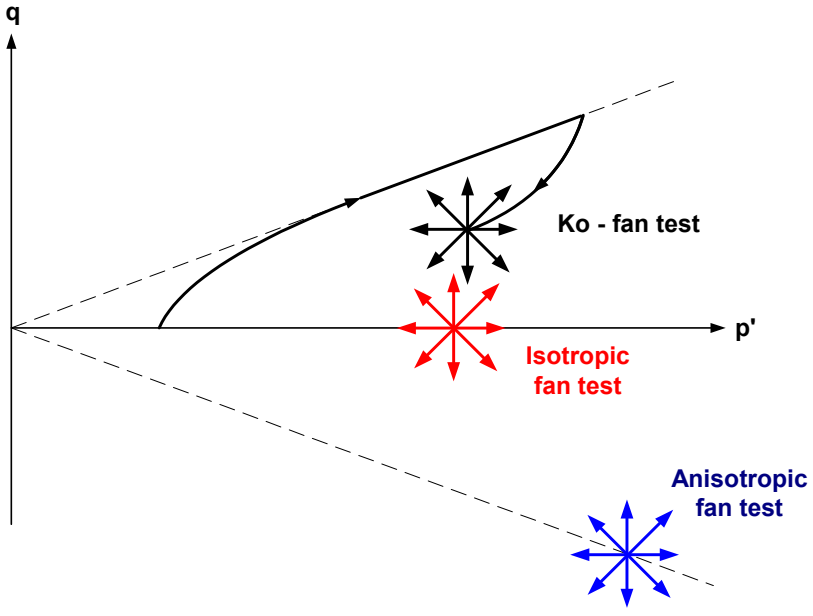

(b)

Figure 4.2 (a) Consolidation stress path, (b) Drained shear stress path
(i) Isotropic fan test, Uchipichat (1998) and Navaneethan (1999),
(ii) K_0 fan test, Khan (1999),
(iii) Anisotropic fan test, Tuladhar (2000)

Unlike the K_0 fan tests, in the anisotropic fan test, investigated by Tuladhar (2000), the samples were not prepared in an anisotropic consolidation condition. To eliminate the complicated process on anisotropic consolidation, the samples were first consolidated to a certain value of p on the isotropic condition, then sheared vertically until they reached a certain negative q value. The consolidation stress path is also shown in Figure 4.2(a).

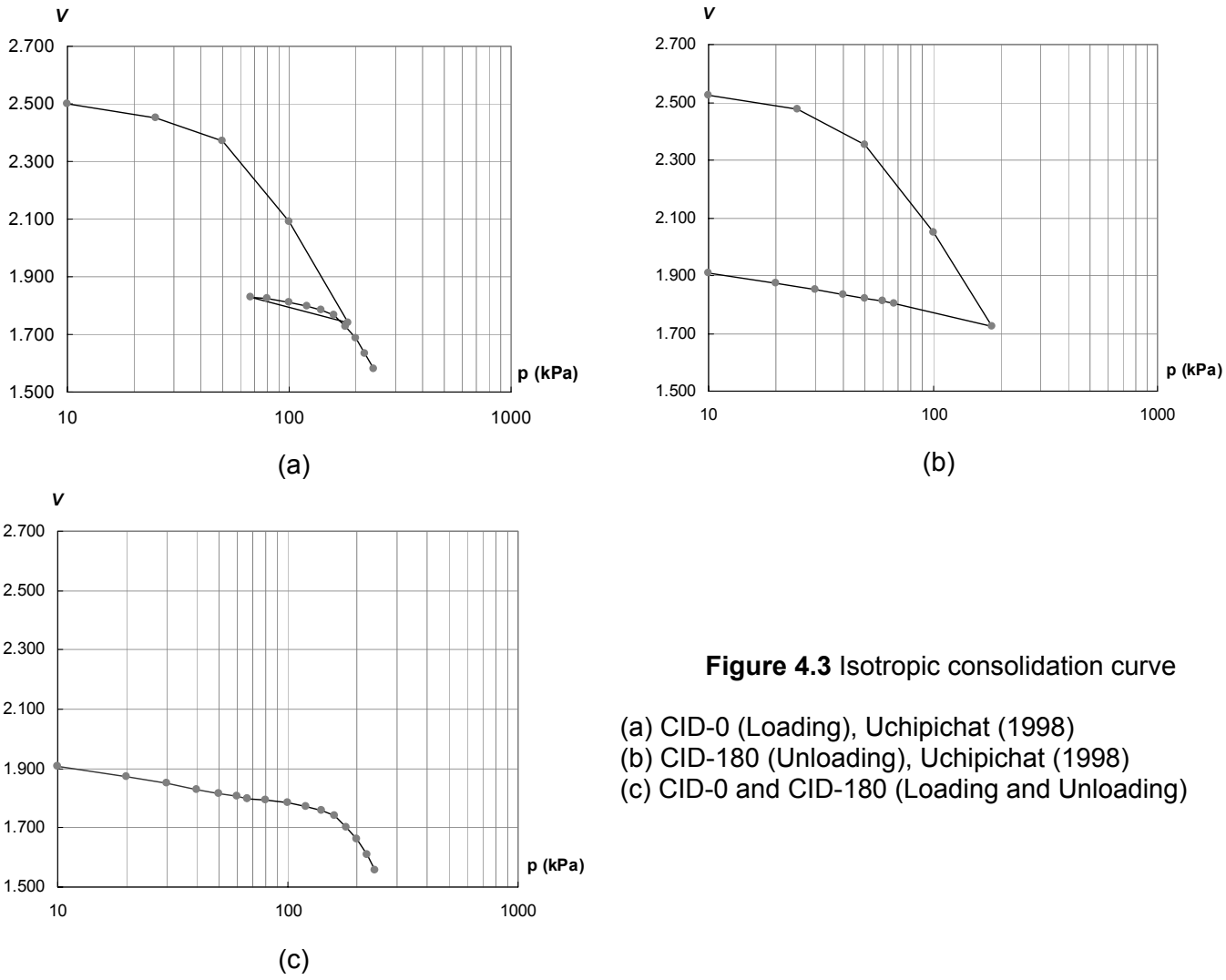

Figure 4.3 Isotropic consolidation curve

(a) CID-0 (Loading), Uchipichat (1998)
(b) CID-180 (Unloading), Uchipichat (1998)
(c) CID-0 and CID-180 (Loading and Unloading)

4.4.3 Consolidation data from Oedometer

An oedometer or one-dimensional consolidometer was first introduced by Terzaghi. This test is performed to measure one-dimensional consolidation behaviour of soil, since the soil specimen is placed inside a constraining metal ring, allowing only vertical compression and swelling to occur. The nominal size of the specimen is 63.5mm in diameter and 25.4mm thick. The load is applied by a lever arm, and

compression is measured by a dial gauge with an accuracy 0.01mm. The specimen is kept under water to maintain the saturation of the soil sample. The load increment ratio is set to unity, and remains at this level for at least 24 hours until the next load increment applied.

The consolidation data from oedometer can be simplified as a K_0-consolidation condition, because there is no lateral strain occuring during the compression. Data interpretation on the logarithmic or square root of time plot are required to evaluate the end of primary consolidation. The calculated effective stress is based on the assumption of a parabolic pore water pressure distribution and if the tests are slow enough there will be zero pore pressure at the end of each stage. The analysis must be repeated at every data point to generate the complete consolidation curve. The oedometer test data were obtained by Seah and Hassan (1999). The oedometer tests were conducted with one loading increment per day up to a maximum vertical pressure of 1,600kPa. The tests were performed on samples from 3.5m and 4.5m. The oedometer results at 3.5m are shown in Figure 4.4(a).

The weak point of the data comes from the limitation of the oedometer itself. Firstly, there are fewer data points on the consolidation curve, particularly during the swelling curve. This is because the assumption of pore pressure distribution cannot be applied to the water absorbed during the swelling process. Thus, the data interpretation procedure (logarithmic or square root time plot) cannot be processed on the unloading curve correctly. The data point was therefore observed only at the end of the testing program. Moreover, due to the inconstant strain rate during the testing programme, the effect of viscosity is included in the consolidation result.

4.4.4 Consolidation data from CRS test

In order to improve the one-dimensional consolidometer test, the constant rate of strain (CRS) consolidometer is introduced. This is because the conventional consolidometer usually applies the load increment ratio equal to one for the duration of one day, giving a total testing period consisting of one to two weeks. The resulting compression curve may be poorly defined, especially near the maximum past stress. For example, in sensitive clay, it is frequently recommended to use a low strain rate in order to capture the behaviour near the maximum past stress. However, a small strain

rate test will make the data interpretation difficult because it may not see a distinct break (end of primary consolidation) due to the creep effect.

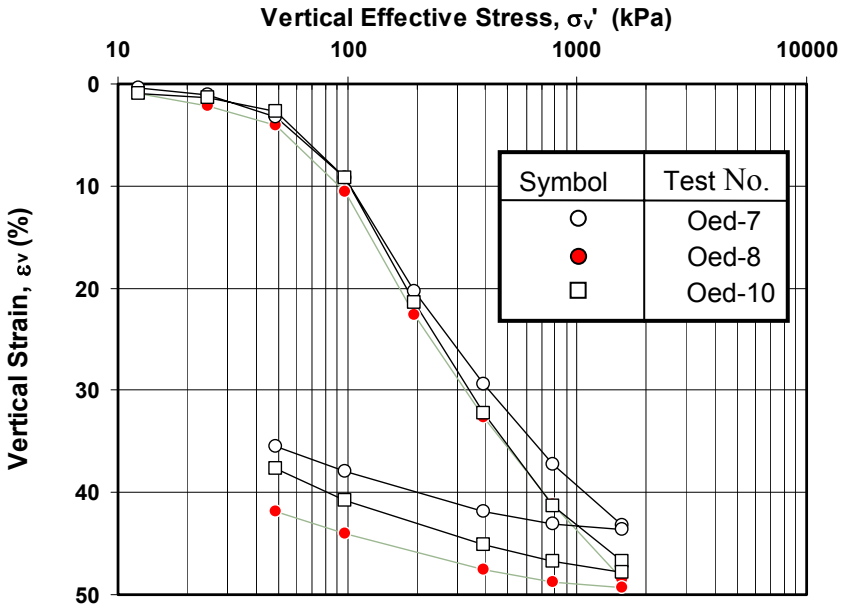

(a)

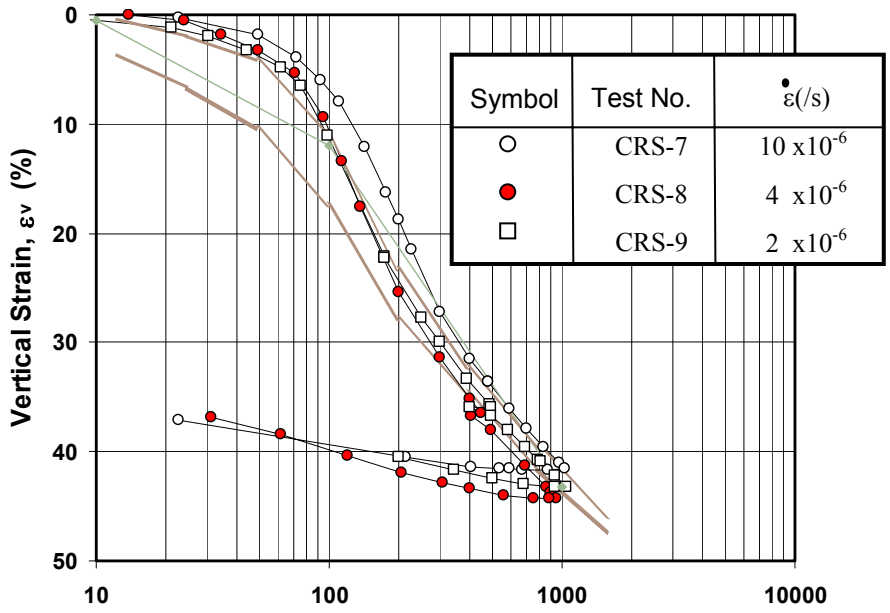

(b)

Figure 4.4 One-dimensional Consolidation data at 3.5m (Seah and Hassan, 1993) (a) Oedometer tests, (b) CRS tests

In the CRS consolidometer test, the soil sample is loaded continuously, rather than incrementally, at the rate required to produce a desired constant rate of strain one dimensionally with one end drainage at the top. Back pressure can be applied on the sample to improve the degree of saturation. The pore water pressure develops at the lower end of the sample. During the test, continuous reading of the loads corresponding to the strain and the pore water pressure at the base are obtained. These data allow a continuous compression curve to be produced with greater objectivity.

The CRS consolidometer used consists of base plate from a triaxial cell, sample-retaining ring from oedometer and loading cell at a constant speed. The sample size is the same as the oedometer sample, and the pressure transducer is connected at the base plate to measure the pore water pressure. In order to achieve the single drainage condition, a coarse porous stone is attached to the top cap.

The CRS tests were carried out by Seah and Hassan (1999), and Seah and Juirnarongrit (1999). The CRS tests were conducted with three different strain rates between 10^{-5} and $2x10^{-6}$ /s. The tests were performed up to a maximum vertical pressure of 1,600kPa on samples from 3.5 and 4.5m. The CRS results, at depth of 3.5m, are shown in Figure 4.4(b).

4.5 Undrained shear data

The undrained shear data can be divided into two groups based on the consolidation process.

The isotropic consolidation undrained shear (CIU) data come from two studies which were done by Kim (1991) and Gurung (1992). Kim's CIU tests were done by varying the OCR value from 1.00 to 4.25, but each specimen was not consolidated to the same pre-consolidation pressure. To reduce the complexity of analysis, the data was normalised by the maximum past value of mean stress, which is equal to the vertical pre-consolidation stress in this case. The normalised undrained stress path of the OCR value varying from 1.00 to 4.25 is shown in Figure 4.5(a). Another source of CIU data is obtained from Gurung (1992). The CIU tests were carried out by varying the OCR value from 1.00 to 16.00, consolidated to the same value of maximum past pressure.

The K_0-consolidation undrained shear (CK_0U) data has also been obtained from Kim (1991). These CK_0U tests were done by varying the OCR value from 1.00 to 4.25, in which each specimen was consolidated under K_0-swelling conditions at the same maximum past pressures. There are two sets of data, namely compression (CK_0UC) and extension (CK_0UE) as shown in Figure 4.5(b).

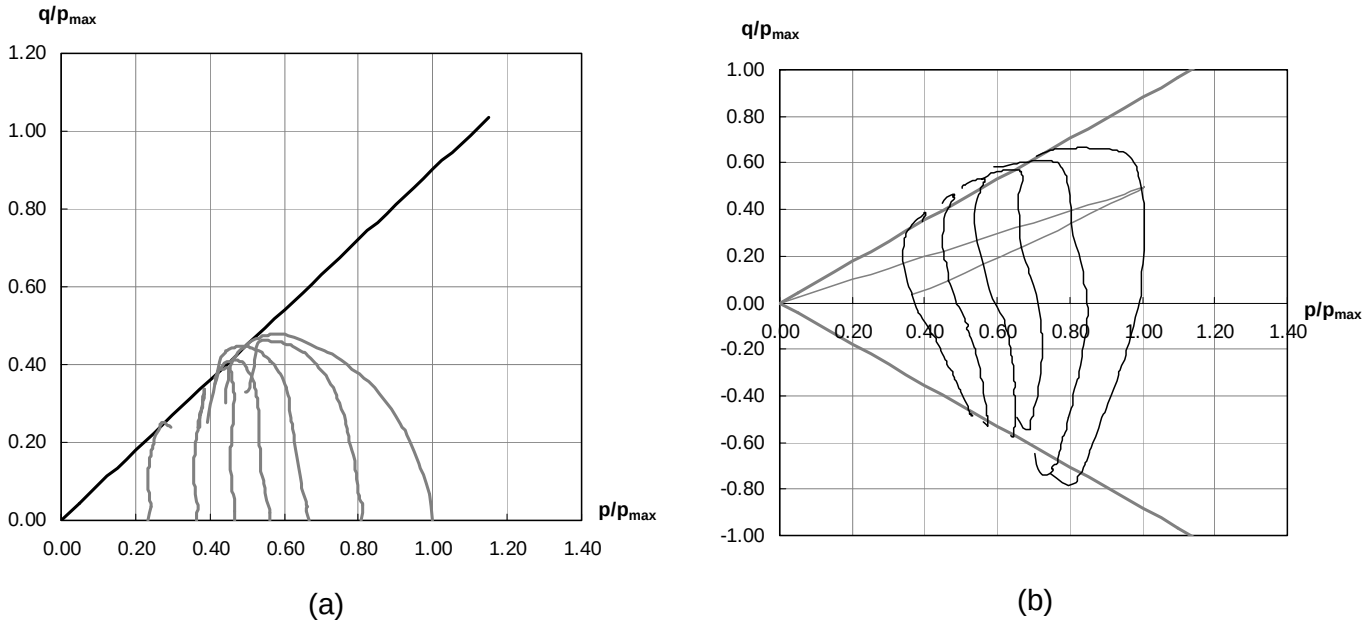

Figure 4.5 Undrained shear test (Kim, 1990)
(a) CIU test (b) CKU test

A possible weak point of Kim's undrained shear data is its unreliability due to the fact that the research investigation took a total of four years. Every soil sample was collected from the site at the same time and kept for more than two years. Therefore, the in-situ stress and moisture content might decrease due to aging effects. The specimen may be stiffer than its original behaviour. For Gurung's data, the electronic data is not supplied directly, however the secondary data were measured from the stress-strain curve by Likitlersuang (2000). As a result, an error from human measurement is added into these data.

4.6 Drained shear data

There are three complete sets of investigations on the triaxial drained behaviour of overconsolidated clay. Each study program consists of two phases: the consolidation phase and shearing phase. For the consolidation phase, each study

consolidated the specimens using different consolidation conditions, namely the isotropic, K_0, and anisotropic condition. The different consolidation stress paths are already described in the consolidation data section as illustrated in Figure 4.2(b). For the shearing phase, all studies sheared the specimens varying the stress path direction from 0^o to 360^o as presented in Figure 4.2(b).

The isotropic fan tests (CID) were carried out by Uchaipichat (1998) and Navaneethan (1999), (compression and extension drained shear tests respectively). A total of 30 tests were sheared in a comprehensive manner which spread from the centre point in a fan shape and all have the same stress history from the isotropic overconsolidated stage. Therefore, the isotropic data can be used to validate the soil model efficiently; by using the soil model to generate the numerical stress-strain data in each shearing direction, a comparison with experimental data can be obtained. A plot of volumetric and shear strain parameter $(\sqrt{\varepsilon_v^2 + \varepsilon_s^2})$ contour can be constructed as shown in Figure 4.6.

However, the stress-strain data, which were tested under different rates of strain conditions, can be observed from the contour plot. The CID-0 and CID-180 tests were carried out by stress controlled conditions which use the load increment equal to 20kPa and 10kPa per step for loading and unloading respectively, and takes 24 hours allowing for the drainage. Thus, the CID-0 and CID-180 tests have taken 9 days and 6 days respectively. For other strain controlled tests, the strain increment of 0.0024mm/min have been used. The average time of strain controlled tests is roughly 3 days. The result of the using of two different rates is implied in Figure 4.6, where the contour points of CID-0 and CID-180 tests are very close together than others. The viscosity effects or rate effects have to be considered, as a result.

The K_0 fan test (CKD) and anisotropic fan test (CAD) were carried out by Khan (1999), and Tuladhar (2000), respectively. The CKD and CAD tests were sheared in a comprehensive manner, which spread from the centre point in a fan shape. However, in the consolidation process, the CKD tests were consolidated with the K_0-condition, the CAD tests on the other hand were consolidated by the isotropic condition first and then constant-p shearing until they reach the anisotropic line as already described in consolidation data. The CKD and CAD test data can be used to

validate the model on anisotropy behaviour. Nevertheless, the difference of testing rate can be observed in these test data as well.

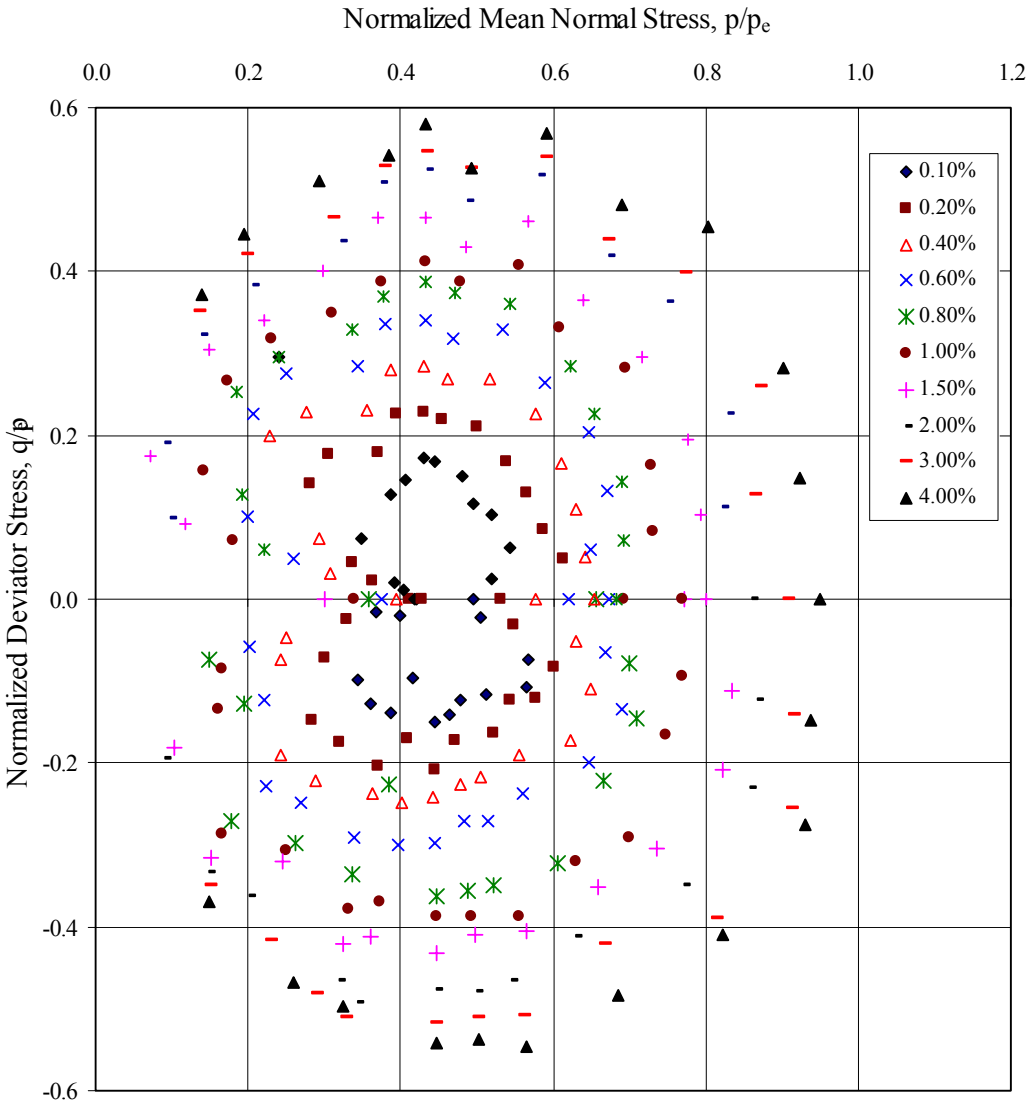

Figure 4.6 Contour plot of volumetric and shear strain parameter ($\sqrt{\varepsilon_v^2 + \varepsilon_s^2}$) of CID-tests (after Uchaipichat, 1998 and Navaneethan, 1999)

4.7 Cyclic undrained data

Research on the cyclic behaviour of Bangkok clay from Chulalongkorn University mainly focused on exploring the undrained cyclic shear strength. An assumption is stated that there are some links between the cyclic shear strength and several physical parameters such as stress amplitude, rate of loading, strain level and

number of load cycles. The shear stress amplitude was defined, based on the unconsolidated undrained (UU-Test) shear strength ($q_u = 2s_u$), as small, moderate, and large amplitude levels. The cyclic tests data were carried out under initial isotropic consolidation stress: 50kPa and 100kPa. The rate of loading was at two constant frequencies of 0.1Hz and 1.0Hz.

The cyclic undrained shear strength behaviour can be determined by the values of secant shear modulus (G_{sec}) and damping ratio (h_c) as shown in Figure 4.7. The initial shear modulus obtained at a small strain level of about 0.02-0.05% were measured for all samples and compared with the shear wave velocity measurement at field, which gave a reasonable agreement value about 13-15MPa. Moreover, the semi-log plot of the shear modulus (G) with the single amplitude shear strain (γ_{SA}) is illustrated. The calculation of the damping ratio, which can represent the shape of hystersis loop, was performed in this research. The relationship between the damping ratio and the single amplitude shear strain is shown in Figure 4.7. Moreover, the effect of rate of loading on cyclic properties was investigated. Because of the small frequency difference between 0.1Hz and 1Hz, it does not show a significant effect on shear modulus and damping ratio.

Due to the lack of the information on stress history of tested samples, estimations of maximum stress past are required. Based on the other research on Bangkok clay, there is some evidence showing that the top Bangkok clay soil layer is lightly overconsolidated (approximated OCR value about 1.20). The maximum past stress can be roughly estimated from the OCR value and in-situ stress. However, the research pointed out that the in-situ stress of tested samples is around 90-100kPa.

These experimental data on cyclic load are particularly useful for the validation of the model, because they consider the variation of stiffness at small strain level. However, some significant information about testing procedure such as sampling procedure, maximum past stress and also the parameter definitions used in this research is not available. The confusion of stress-strain parameters has to be eliminated by using Cambridge triaxial stress-strain parameters. The evidence on the monotonic undrained compression test found that Chulalongkorn's clay samples are slightly stiffer than AIT's samples. The natural water content and plasticity index are

also illustrated this same trend. However, this is not a significant issue for the parametric evaluation and will be discussed in the next chapter.

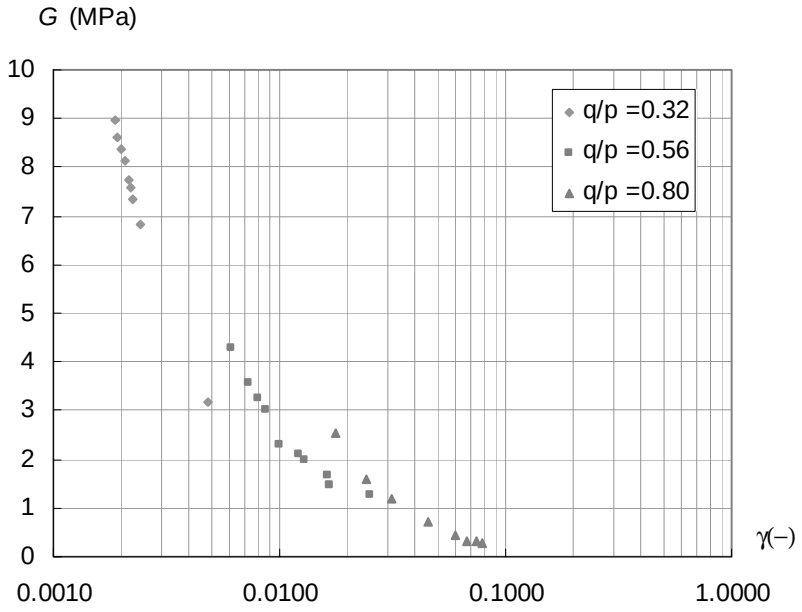

(a)

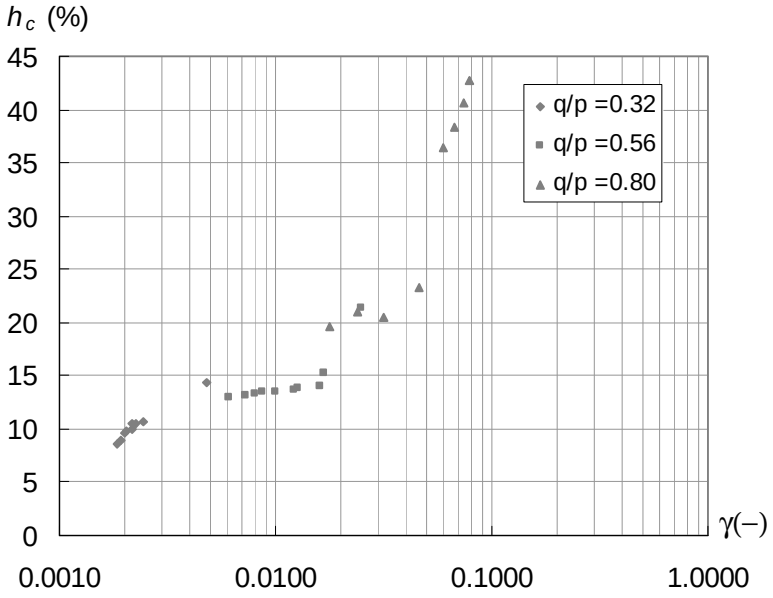

(b)

Figure 4.7 Cyclic Undrained Shear Test varying shear stress magnitude (*q/p*) at confining pressure (p_c) = 100kPa (Teachavorasinskun and Thongchim, 2001)
(a) Plot of shear modulus (G) vs. single amplitude shear strain (γ_{SA})
(b) Plot of damping ration (h_c) vs. single amplitude shear strain (γ_{SA})

4.8 Conclusion

Almost all soil models focus on either large strain (near failure) or small strain behaviour. It is rarely the case that a soil model can describe both behaviours. In order to develop a model, the experimental data at both small strain and large strain behaviours, which are carried out on the same material, are required.

A series of experimental investigations on stress-strain-strength behaviour of Bangkok clay were carried out at AIT and Chulalongkorn University. There are several categories of testing programs: consolidation test, undrained shear test and drained shear test as well as cyclic loading test.

Consolidation data can be divided into four types, based on the testing equipment and conditions: isotropic triaxial consolidation, anisotropic triaxial consolidation, oedometer test and CRS consolidometer test. The triaxial consolidation data is mainly obtained from of the consolidation phase of undrained shear and drained shear tests. The research on one-dimensional consolidation was investigated widely at AIT, employing an improved consolidometer called a CRS consolidometer. Although, there are many sets of consolidation data available, only some of them can be used to construct the hysteresis loop, which is important for the current research.

The undrained and drained shear data can be divided into two groups based on the consolidation process: isotropic and anisotropic consolidation. The accuracy of the undrained shear data is subjected to the testing programme which took about four years. This makes the sample stiffer than its original behaviour due to aging effects. The drained shear data are obtained from the three series of the fan test. The major disadvantage of drained shear data is the usage of different testing conditions, namely the stress-controlled test on the horizontal direction and the strain-controlled test in the other directions. These two different testing conditions also used two different rates of loading, which is significant for the analysis using rate-dependent calculation. The result is implied in the plot of strain contour as illustrated in Figure 4.6.

The experimental data at small strain levels can be achieved from the research on cyclic undrained shear at Chulalongkorn University. This research provides the information on the variation of shear modulus and damping ratio. However, although the rate of loading was studied in the research, it does not point out that different rates

of loading would produce significantly different effects. Due to the lack of stress history information, reasonable values have to be estimated. Moreover, evidence on monotonic undrained compression test found that Chulalongkorn's samples are slightly stiffer than those of AIT.

Chapter 5
Comparisons, Results and Discussion

A hyperplasticity model in terms of triaxial stress-strain parameters has been developed as presented in chapter 3. The experimental data for Bangkok clay have been obtained from AIT and Chulalongkorn University. All experimental programs have been already described in the previous chapter. In this chapter, some comparisons between experimental data and model predictions based on a particular set of parameters will be presented. The comparisons can be categorised into four types based on the type of data: consolidation, undrained, drained, and cyclic undrained data.

The predictions of the KHMCC model are compared with all experimental data. Both linear and logarithmic stress-strain relations are used. The linear model, however, seems to provide a better result than the logarithmic model, especially on swelling data from consolidation tests. Another advantage of using the linear model is the simplicity of the calculation. Nevertheless, from the CSSM viewpoint, the definition of compression parameters (λ, κ) is defined based on v-log p plot. The log v-log p plot introduced by Butterfield (1979) shows that it is not necessary to retain with the v-log p plot in describing the consolidation behaviour. The compression curve can be defined in other ways, and one possible stress-strain relation is a simple linear one. As a result, the simple linear stress-strain relation is used to define the soil behaviour in this research.

Tables 5.1(a) and (b) summary all parameters and their physical meaning based on Bangkok clay experimental data for the linear model and the MCC model respectively.

Table 5.1(a) Summary of KHMCC parameters for Bangkok clay

Parameter	Value	Physical meaning
K	5200 (kPa)	Initial bulk modulus
a_p	2.0	Non-linear kinematic hardening parameter for p-direction
b_p	2.5	
r	0.8	
g_x	60	Elastic shear modulus gradient
a_q	3.5	Non-linear kinematic hardening parameter for q-direction
b_q	2.5	
M	0.9	Slope of critical state line in q-p plane
μ	-	Viscosity coefficient (for rate-dependent calculation)

Table 5.1(b) Summary of MCC parameters for Bangkok clay

Parameter	Value	Physical meaning
κ^*	0.045	Slope of swelling consolidation line on log v-log p plot
λ^*	0.38	Slope of virgin consolidation line on log v-log p plot
g_x	60	Elastic shear modulus gradient
M	0.9	Slope of critical state line in q-p plane
μ	-	Viscosity coefficient (for rate-dependent calculation)
p_{x0}	-	Reference pressure of initial yield surface (kPa)

5.1 Implementation in FORTRAN code

The linear continuous kinematic hardening plasticity model (Table 3.8) is incorporated into the computer software. Firstly, the research takes advantage of the smooth continuous response which is obtained using the multiple yield surfaces model. The implementation is achieved using the symbolic calculation software, Maple 7. Although, the Maple 7 code provides a smooth response following the large number of the kinematic internal variables, the calculation time is considerable (2-3 hours per 1000 calculation cycles). This result comes from the fact that a large

amount of computer memory is needed for symbolic calculation, and an experiment has revealed that the symbolic calculation is 100 times more time-consuming than arithmetic calculation.

In order to make the smooth continuous plasticity model more practical, the multiple yield surfaces model is considered. The numerical approach for the multiple yield surfaces model is implemented in FORTRAN 90. This will give an advantage in the next stage of the research on application into the OXFEM program, because OXFEM was written in FORTRAN. Numerical problems such as rounding error can be controlled by using double precision numbers (10^{-16} accuracy) rather than single precision (10^{-8}). The calculation accuracy also depends on other factors (eg. number of yield surfaces, time step, and viscosity coefficient). The greater the number of yield surfaces used, the smoother the response generated. Use of too many yield surfaces, however, may lead to a computation time problem. This study uses fifty yield surfaces for comparisons with triaxial experimental data and ten yield surfaces for cyclic data. The effect of viscosity will be described in the next section.

5.2 Consolidation behaviour prediction

The consolidation behaviour prediction is calculated from the KHMCC model, however, the model can be reduced to the one-dimensional model as shown in Table 3.6. The evaluation based on a rate-dependent algorithm assumes the set of viscosity parameters to have no effect. This seems to be artificial rate-independence, which use a small viscosity value μ. The study on the viscosity effect on the stress-strain behaviour has found that the strength of material depends on a product of coefficient of viscosity and strain rate $(\mu\dot{\varepsilon})$ as shown in Figure 5.1(a). This relationship is in terms of an exponential function, i.e. the material strength will grow rapidly with increasing of $\mu\dot{\varepsilon}$ value (see Figure 5.1(b)). However, at small values $\mu\dot{\varepsilon}$, the rate effect will not be significant. This leads to an approximation of the rate-independent response.

The predicted results compare isotropic consolidation along unloading-reloading curves in term of mean stress (p). The evaluation has found that the linear model gives a more reasonable volumetric strain on the swelling path than the logarithmic model. This continuous kinematic hardening model results comply

strictly with the Masing rules. It always gives a symmetric closed hysteresis loop when the stress path returns to the same maximum past stress. In reality, some investigations into cyclic loading often find that there is a small drift (Δ_p) of strain occurring in every cycle as illustrated in Figure 5.2(a). As a result, the research has considered this effect by introducing a special mechanism called a ratchetting[1] mechanism. It is biased in one direction by adding an "engine" (Figure 5.2(b)). However, this idea has not been implemented in the final model yet. This model leads to a complicated yield condition.

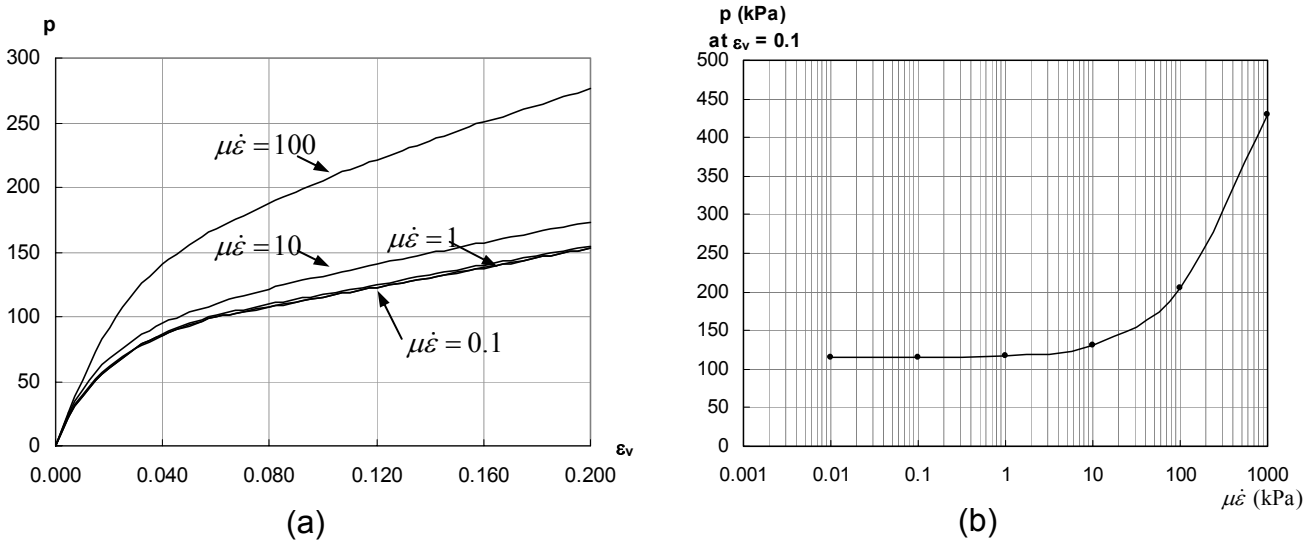

(a) (b)

Figure 5.1 The effect of viscosity coefficient of rate-dependent material (a) Stress-strain curves with varying viscosity coefficient; (b) Plot of predicting solution of rate-dependent material with Logarithmic of $\mu\dot{\varepsilon}$ value

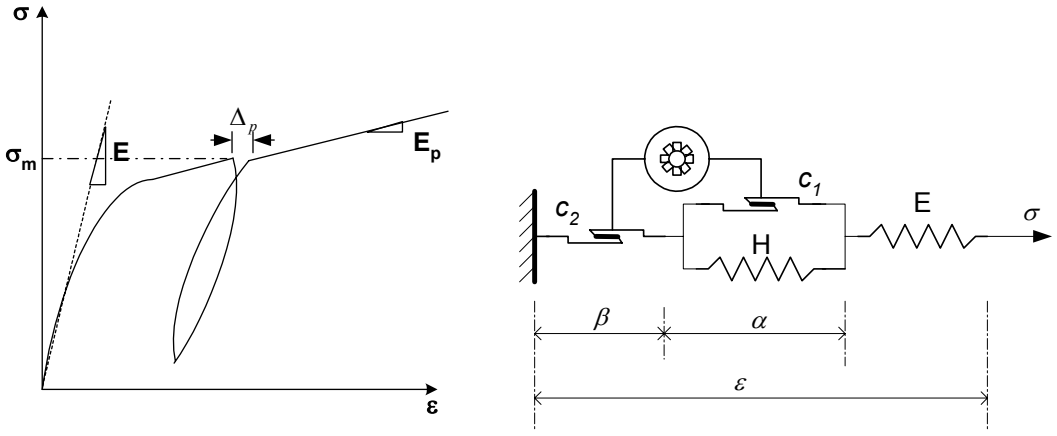

(a) (b)

Figure 5.2 (a) A small drift during a cyclic loading; (b) Rachetting mechanism model

[1] This word comes from the ratchet in bicycle that always gives a rotation in only the forward direction.

The comparison between model prediction and isotropic consolidation data is presented in Figure 5.3. There are four tests with two different strain rates, i.e. isotropic consolidation unload and reload with average displacement rate $1.0\text{x}10^{-4}$ mm/min (curve A, B) and controlled stress path test at 14^{o} and 194^{o} with rate $2.4\text{x}10^{-3}$ mm/min (curve C, D). The model prediction uses two different values of strain rates (i.e. $1.67\text{x}10^{-7}\text{s}^{-1}$ and $4\text{x}10^{-6}\text{s}^{-1}$). Note that the viscosity coefficient[2] is assumed to be in the order of $10^{4}\,\text{kPa}\cdot\text{s}$, thus $\mu\dot{\varepsilon}$ values are approximately 0.005kPa and 0.1kPa respectively. These two values do not significant affect the analysis result (see Figure 5.1(b)). Although, the volumetric behaviour given by the controlled stress path tests at 14^{o} and 194^{o} does not conform to the condition of isotropic consolidation, they are very close to the *p*-axis, thus the volumetric behaviour can be approximately treated as isotropic consolidation.

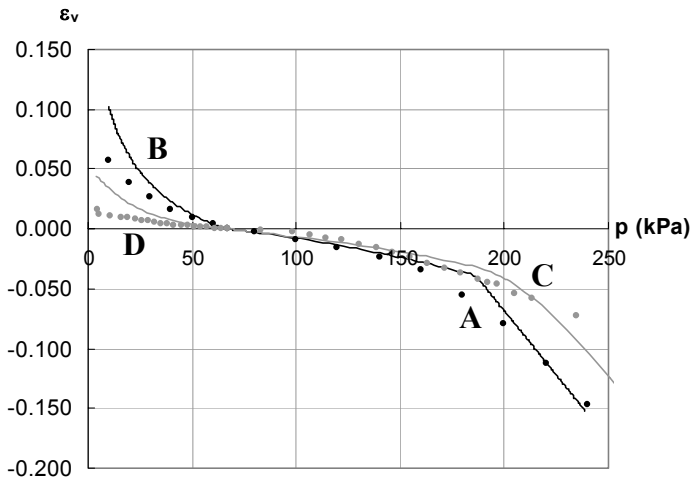

Figure 5.3 Isotropic consolidation prediction

A – isotropic consolidation loading (1.0×10^{-4}mm/min)
B – isotropic consolidation unloading (1.0×10^{-4}mm/min)
C – controlled stress path 14^{o} (2.4×10^{-4}mm/min)
D – controlled stress path 194^{o} (2.4×10^{-4}mm/min)

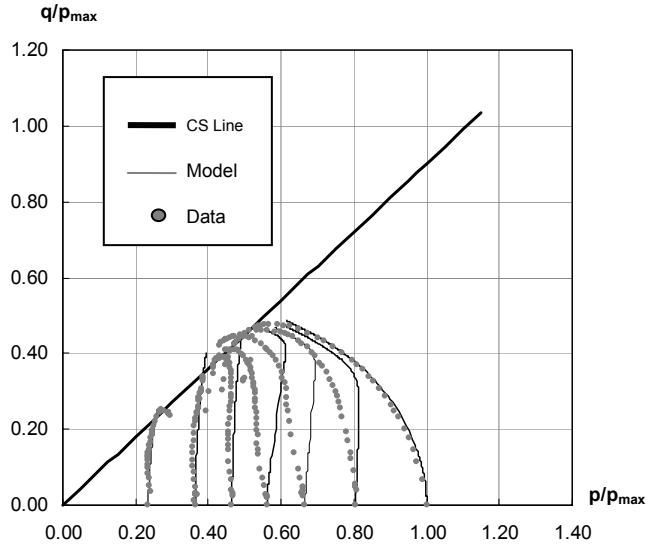

Figure 5.4 Prediction of isotropic consolidation undrianed shear stress paths varying OCR from 1.00 to 4.25

The KHMCC model prediction of consolidation behaviour seems to be in good agreement with experimental evidence. The KHMCC model is sufficient to explain the behaviour of the consolidation paths for both reloading and unloading and to describe the rate-effect on consolidation. Nevertheless, it does not accurately

[2] Dynamic viscosity (kPa s)

predict behaviour in the heavily overconsolidated zone. This can be replaced by a more suitable hardening function that requires further research.

5.3 Isotropic behaviour prediction

The model which has its yield surface centre located on the *p*-axis will show an isotropic behaviour (e.g. symmetry of stress paths on *p*-axis; same magnitude of shear strengths between compression and extension etc). The simply isotropic yield criteria such as the von-Mises yield criterion will produce a symmetric stress-strain response. However, the fact is that the critical state cone is not symmetric on the hydrostatic axis (*p*-axis). The magnitude of the critical state cone (*M*) depends on where the state is in stress space. Although, the Matsuoka-Nakai yield criterion can continuously predict the variation of the critical state cone magnitude, it involves a complicated mathematical expression. In developing a model for triaxial data, the two different *M* values are needed (M_C for compression and M_E for extension). Note that the relation of *M*-value can be linked with the friction angle (Mohr-Coulomb yield criteria): $M_C = \dfrac{6\sin\phi'_{TC}}{3-\sin\phi'_{TC}}$; $M_E = \dfrac{6\sin\phi'_{TE}}{3+\sin\phi'_{TE}}$, where ϕ'_{TC}, ϕ'_{TE} denote triaxial compression and extension friction angles respectively. Thus, the modification of the yield function becomes $\hat{y} = \sqrt{\hat{\chi}_p^2 + \dfrac{\langle \hat{\chi}_q \rangle^2}{M_C^2} + \dfrac{\langle -\hat{\chi}_q \rangle^2}{M_E^2}} - \hat{H}_p \hat{\alpha}_p \eta = 0$.

The triaxial form of the KHMCC model (Table 3.8) is written in FORTRAN code to predict the isotropic consolidation tests. The multi yield surfaces are dragged in the line of stress history on the *p*-axis, and the centres of all yield surfaces are located on this axis. It guarantees that the model will respond isotropically. After the consolidation stage, the tested samples are sheared under two conditions (undrained shear and specific stress direction drained shear tests). The results and comparison details will be illustrated in the following section.

5.3.1 Isotropic undrained behaviour

The KHMCC model was used to simulate a set of isotropic consolidation triaxial undrained compression tests for OCR-values varying from 1.00 to 4.25. The normalised stress paths are shown in Figure 5.4. Figures 5.5 to 5.8 present the

KHMCC model predictions of the isotropic undrained compression tests with OCR values of 1.00, 1.24, 2.15 and 2.75 respectively. The figures also show a comparison between the KHMCC model and the MCC model. It shows that the normally overconsolidated clay (Figure 5.5) is fully predicted by both the MCC model and the KHMCC model, but the KHMCC model gives a slightly better prediction than the MCC model. The undrained stress-strain response of normally consolidated clay exhibits only plastic behaviour because the stress path drags along the yield surface boundary, which is in the plastic region. Thus, the MCC model can capture this special behaviour.

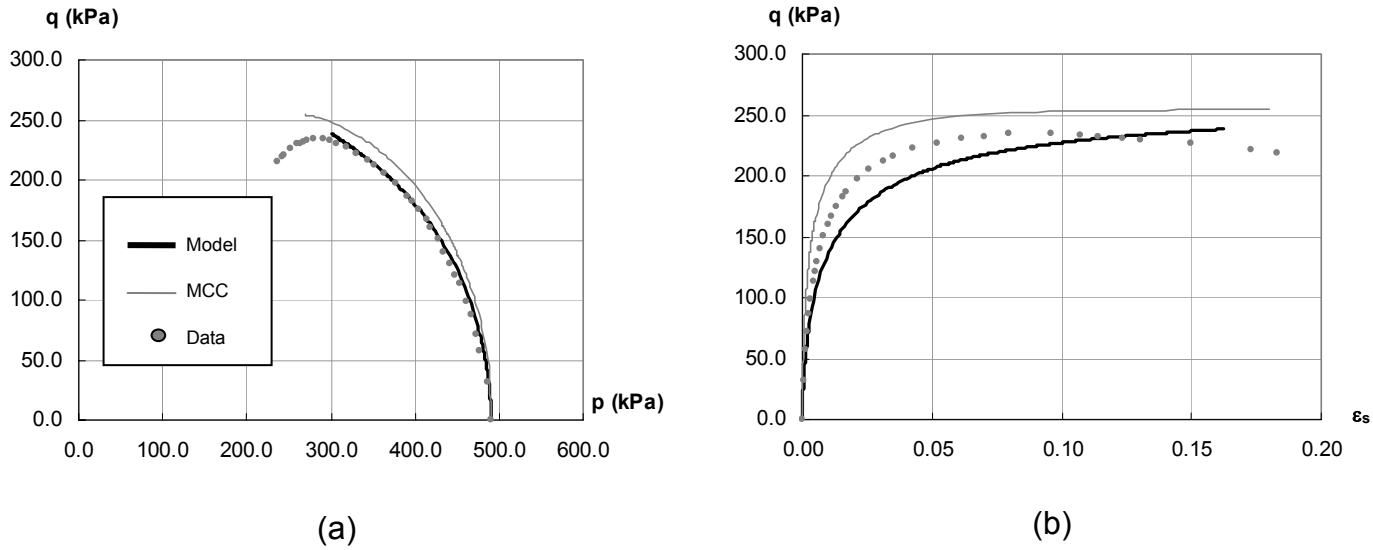

Figure 5.5 Prediction of isotropic consolidation undrained test at OCR = 1.00
(a) Stress path; (b) Shear stress-strain curve

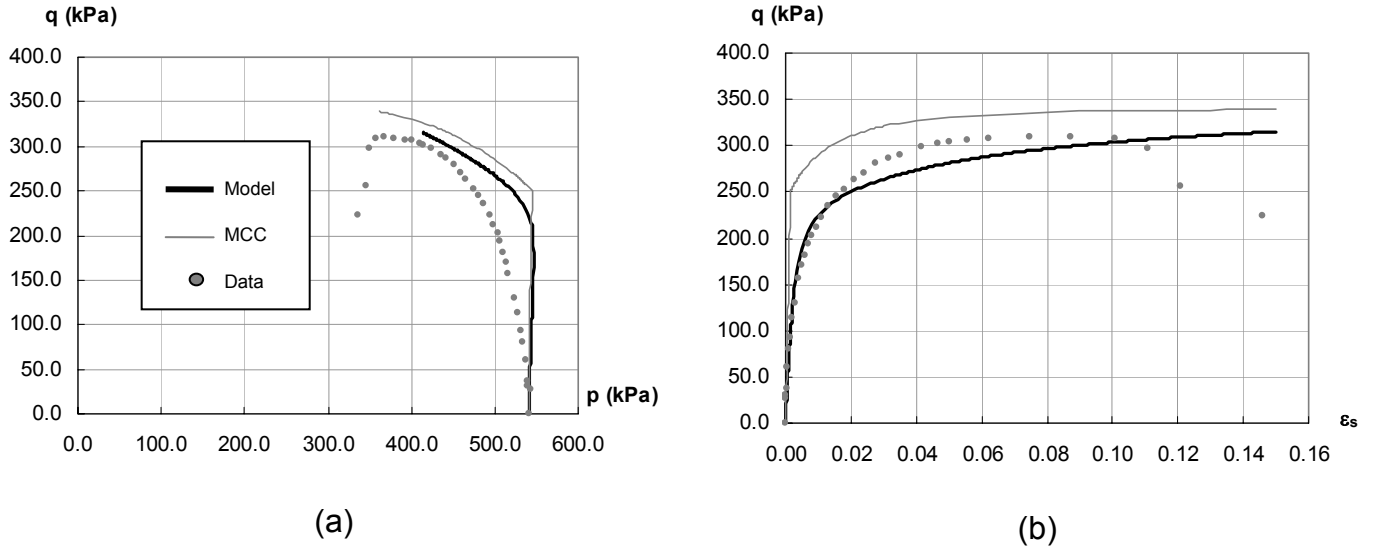

Figure 5.6 Prediction of isotropic consolidation undrained test at OCR = 1.24

(a) Stress path; (b) Shear stress-strain curve

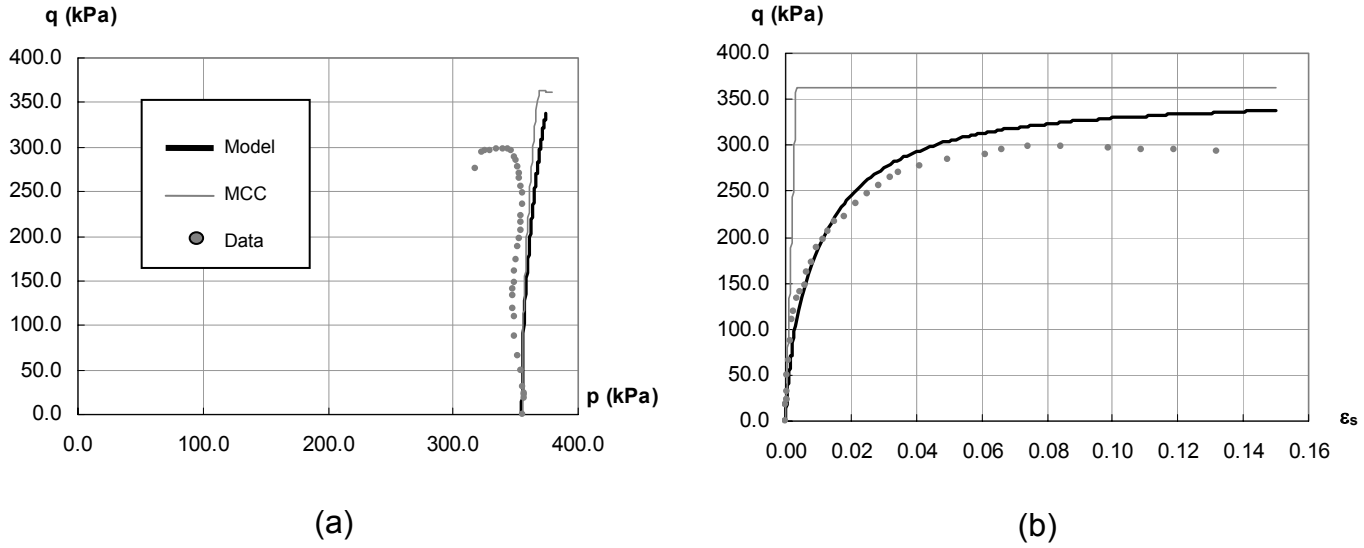

(a) (b)

Figure 5.7 Prediction of isotropic consolidation undrained test at OCR = 2.15
(a) Stress path; (b) Shear stress-strain curve

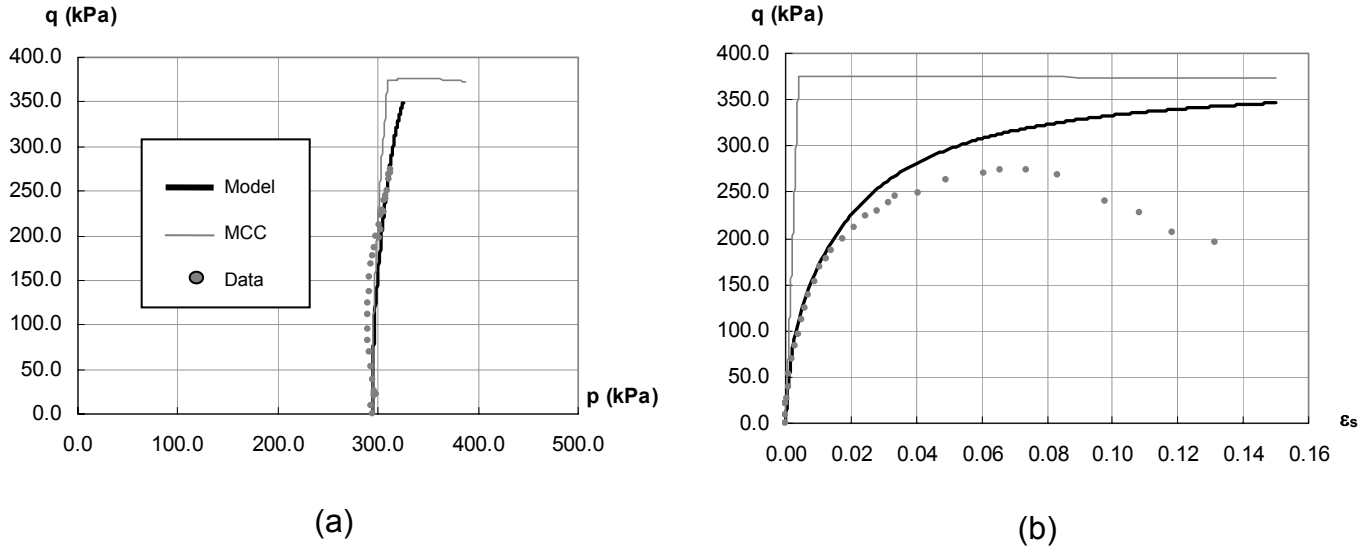

(a) (b)

Figure 5.8 Prediction of isotropic consolidation undrained test at OCR = 2.75
(a) Stress path; (b) Shear stress-strain curve

On the other hand, the lightly and moderately overconsolidated samples (Figures 5.6, 5.7 and 5.8) can still use the MCC model to predict their behaviour; however it does not fit very well for both stress path and stress-strain responses. This is due to the limitation that the MCC model only gives the elastic response for the stress state inside the yield surface. The multiple yield surface model can accommodate the smooth transition change from elastic stiffness to elastic-plastic

stiffness. Figures 5.6, 5.7 and 5.8 show that the KHMCC model can capture the transition of shear stiffness. However, the undrained stress path pattern (Figure 5.4) does not fit well with all tests, especially heavily overconsolidated samples. This is because the KHMCC model is strictly based on the CSSM assumption, i.e. every sheared sample must reach the same final state called "critical state". The experimental data, however, did not show a unique critical state. This may be due to localisation in which each element of the sample does not yield at the same time. Another way of explaining the phenomenon is the introduction of a strain softening function, an agenda for further research.

The final version of the KHMCC model cannot accurately give the prediction of the undrained shear strength especially for the heavily overconsolidated sample. The most significant advantage over the MCC model is that it can give a smooth transition of stiffness without any additional expression. This benefit can be applied for the cyclic loading response, the details of which are in the following section.

5.3.2 Isotropic drained behaviour

A set of data for isotropic consolidation triaxial drained tests has been obtained in the testing program with variation of stress path direction from 0^o-360^o. The data are compared with the prediction for the models and some selected results are presented in Figures 5.9, 5.10 and 5.11. The figures also show a comparison between the KHMCC model and the MCC model.

The stress history is simplified in the testing program which is illustrated in Figure 4.4(a). Every sample is in the moderately overconsolidated state (OCR = 2.75) after the isotropic consolidation history path. The samples are then sheared in the particular direction with strain being controlled. The artificial rate-dependent process is used for this prediction, using a $\mu\dot{\varepsilon}$ value equal to 0.1kPa. This value has a very small effect on the result following the rate-effect in the consolidation behaviour prediction section (see Figure 5.1(b)).

Figures 5.9(a) and (b) show the volumetric and shear stress-strain curves of the CID-56 and CID-236 tests as illustrated by the small diagram. There are three stress-strain curves, i.e. data, MCC model prediction and KHMCC model prediction.

Figures 5.10(a) and (b) present the volumetric and shear stress-strain curves of the CID-135 and CID-315 tests.

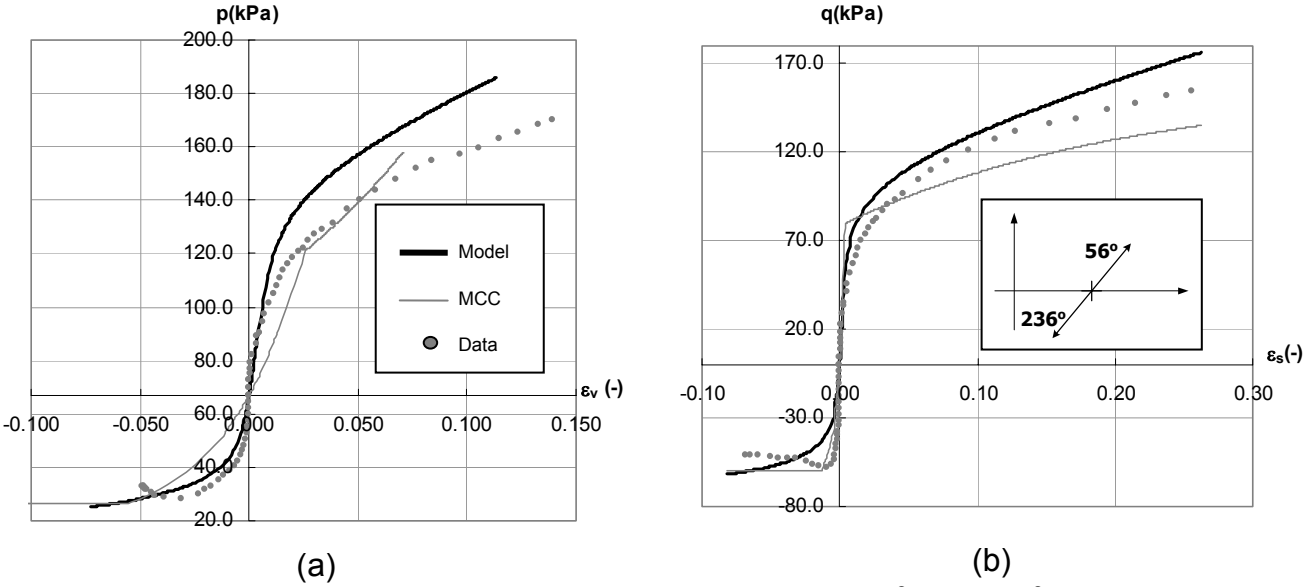

(a) (b)

Figure 5.9 Prediction of isotropic consolidation drained test at 56° and 236° direction of OCR = 2.75; (a) Volumetric stress-strain curve; (b) Shear stress-strain curve

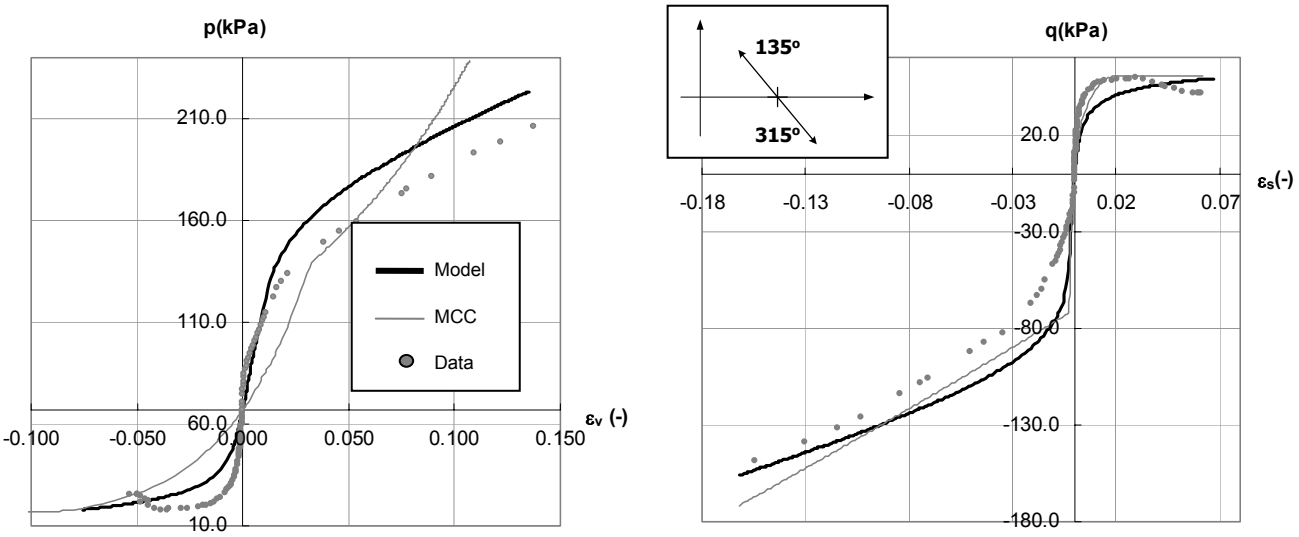

(a) (b)

Figure 5.10 Prediction of isotropic consolidation drained test at 135° and 315° direction of OCR = 2.75; (a) Volumetric stress-strain curve; (b) Shear stress-strain curve

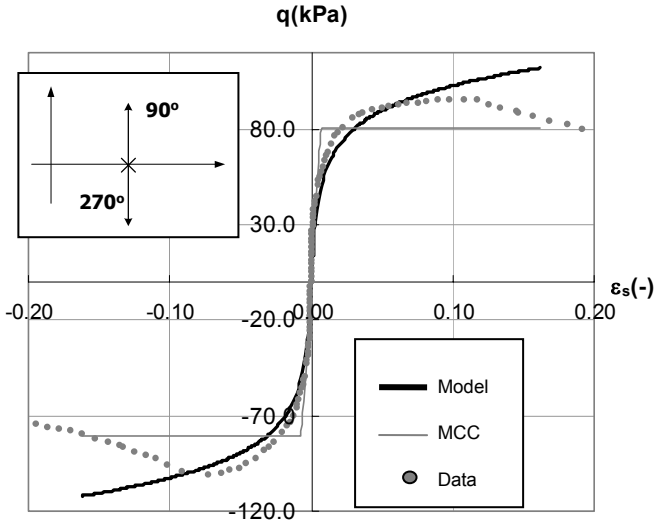

Figure 5.11 Prediction of shear stress-strain curve of isotropic consolidation drained test at 90^{o} and 270^{o} direction of OCR = 2.75

Figure 5.11 presents the shear stress-strain curve of the CID-90 and CID-270 tests. Due to the fact that the MCC model does not describe the transition of stiffness, the stress-strain response from the MCC prediction gives a sudden change of stiffness from elastic to plastic. The KHMCC model not only accommodates the change of stiffness, but also gives a better prediction of shear strength as shown in Figure 5.11. However, the prediction of KHMCC model exhibits a symmetric stress-strain response about the *p*-axis. This limitation of the KHMCC model will be tackled in the next section which deals with the prediction of the stress-strain behaviour with an anisotropic stress history.

5.4 Anisotropic behaviour prediction

Following the stress history, the anisotropic consolidation stress path will make the yield surface centres move from the *p*-axis. This leads to the observation of an unsymmetric behaviour about the *p*-axis. Although, the KHMCC model does not have a rotated yield surface shape, the KHMCC model with multi yield surface can be sufficient to describe the anisotropy phenomenon. The benefit of the multi yield surfaces model is that, after any stress history, each of the yield surface will memorise its location following the stress path. Then, during the next loading, the stress-strain response will exhibit the behaviour according to the past stress history. The

prediction of the shear strength can be improved using the inequality of critical state cone magnitude (M). In this stage, however, the two different M values are used for the triaxial model (in p-q space).

Incorporating the KHMCC model (Table 3.8) into the FORTRAN code, the prediction of anisotropic consolidation tests is processed. Firstly, the multi yield surfaces are dragged following the anisotropic consolidation stress history as shown in Figure 4.5. After the consolidation stage, the tested samples are sheared into two conditions (undrained shear condition and some specific stress direction drained shear condition). The results and comparison details will be described in the following section.

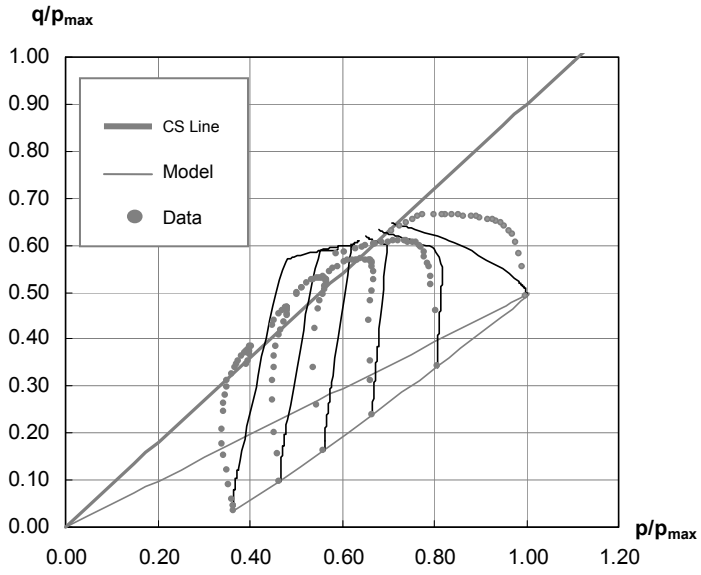

Figure 5.12 Prediction of K_0 consolidation undrained compression shear stress paths varying OCR from 1.00 to 2.75

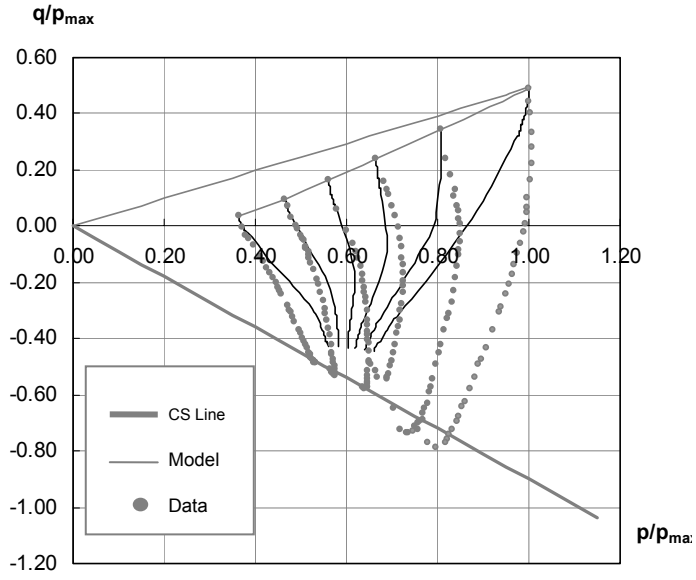

Figure 5.13 Prediction of K_0 consolidation undrained extension shear stress paths varying OCR from 1.00 to 2.75

5.4.1 Anisotropic undrained behaviour

The KHMCC model is used to simulate two sets of K_0 consolidation triaxial undrained tests with varying OCR-values from 1.00 to 2.75, both in compression and extension tests. The normalised stress paths are shown in Figures 5.12 and 5.13 for compression and extension tests respectively. Figures 5.14 to 5.17 present the model predictions of the K_0 undrained compression tests with OCR values 1.00, 1.24, 2.15

and 2.75 respectively, and Figures 5.18 to 5.21 exhibit the model predictions of the K_0 undrained extension tests with varying the OCR values 1.00, 1.24, 2.15 and 2.75 respectively. These plots show the comparison between the experimental data, the MCC model and the KHMCC model prediction.

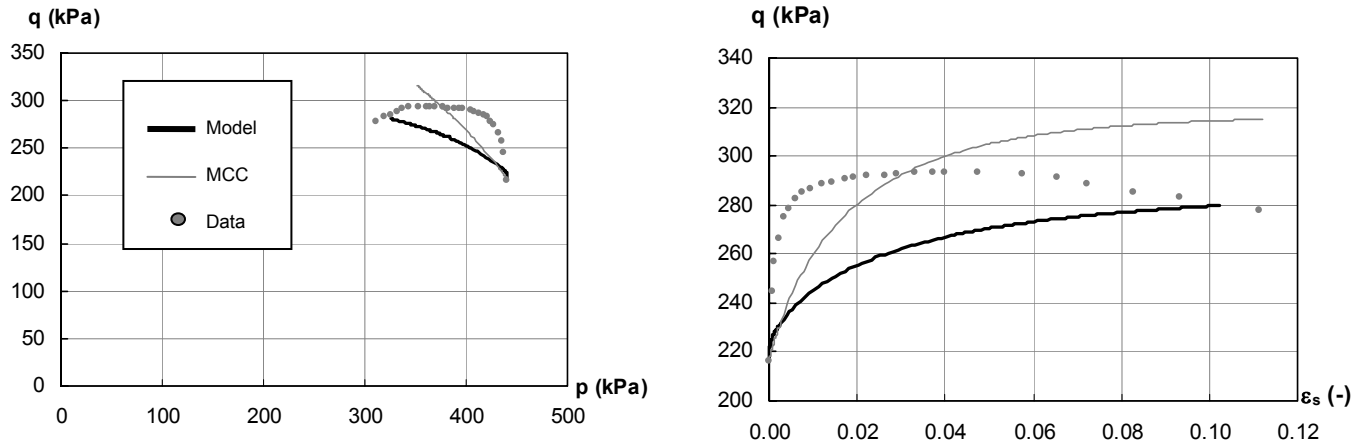

(a) (b)

Figure 5.14 Prediction of K_0 consolidation undrained compression test at OCR = 1.00
(a) Stress path; (b) Shear stress-strain curve

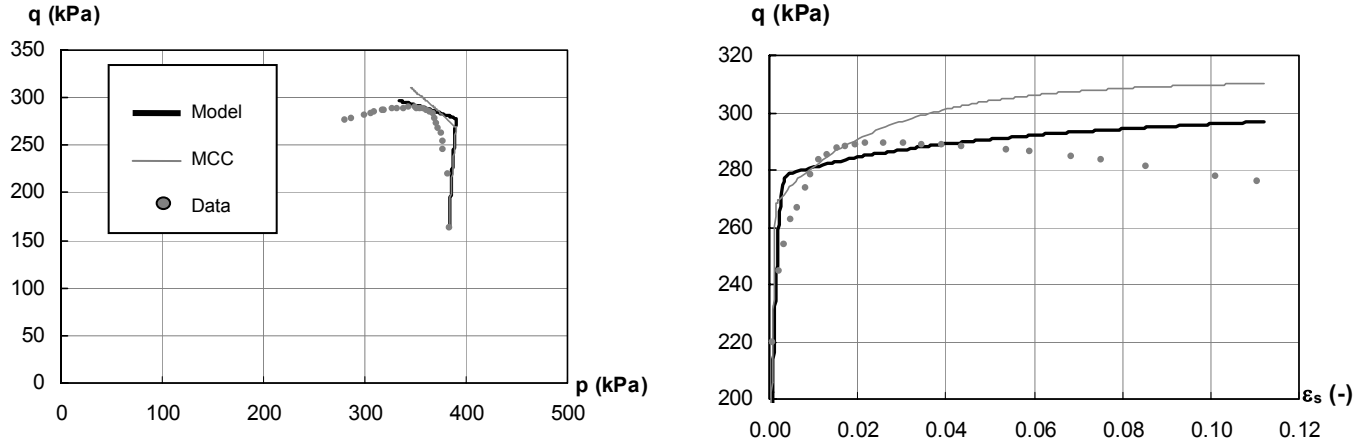

(a) (b)

Figure 5.15 Prediction of K_0 consolidation undrained compression test at OCR = 1.24
(a) Stress path; (b) Shear stress-strain curve

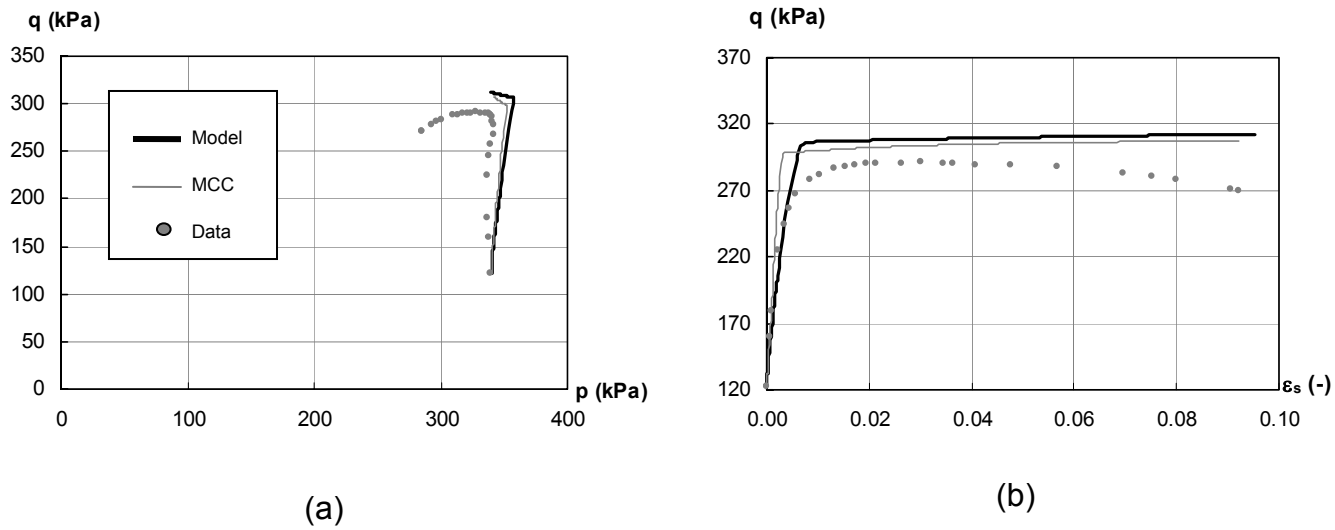

(a) (b)

Figure 5.16 Prediction of K_0 consolidation undrained compression test at OCR = 1.50
(a) Stress path; (b) Shear stress-strain curve

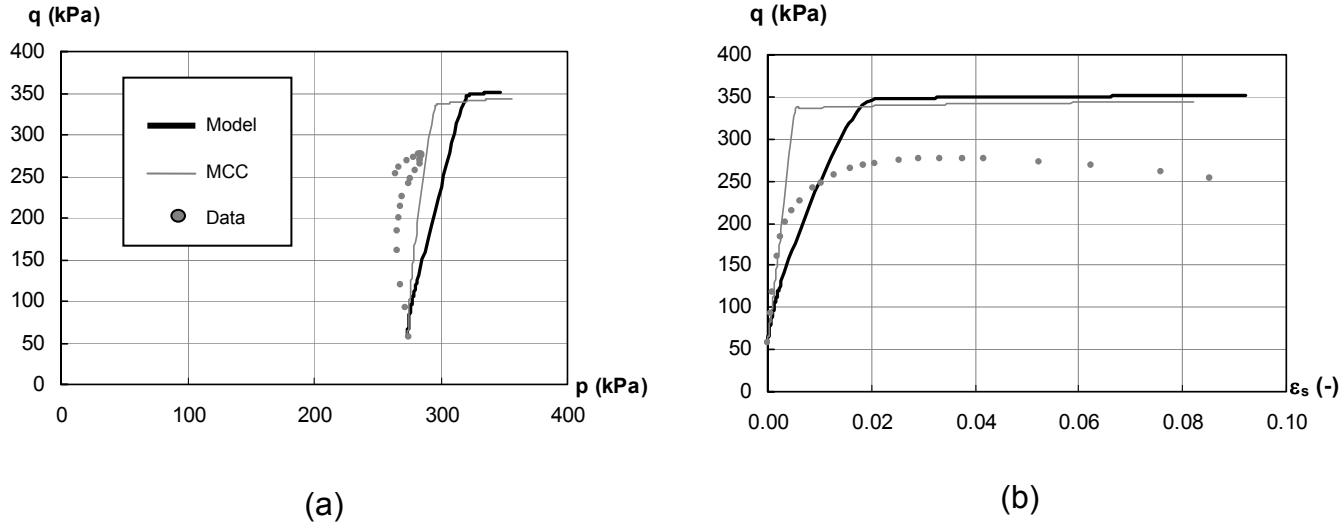

(a) (b)

Figure 5.17 Prediction of K_0 consolidation undrained compression test at OCR = 2.15
(a) Stress path; (b) Shear stress-strain curve

For the K_0 undrained compression test, the KHMCC model provides a better prediction of shear strength and variation of shear stiffness than the MCC model. Considering the normally consolidated sample (Figure 5.14), the KHMCC model gives a poor result for stress path and variation of stiffness. This may be due to the fact that the undrained stress path of the normally overconsolidated sample is dragged

along the yield surface boundary. Thus the yield surface shape could be improved by, for example, deforming the yield surface shape or rotating the yield surface axis around the *p*-axis. Moreover, there is also the problem for the heavily overconsolidated sample (Figure 5.17, OCR = 2.15), which is the same as presented in the isotropic undrained test. It is not necessary to reach the exact same point when shearing approaches its final stage. This may be described by introducing the concept of localisation or strain softening function.

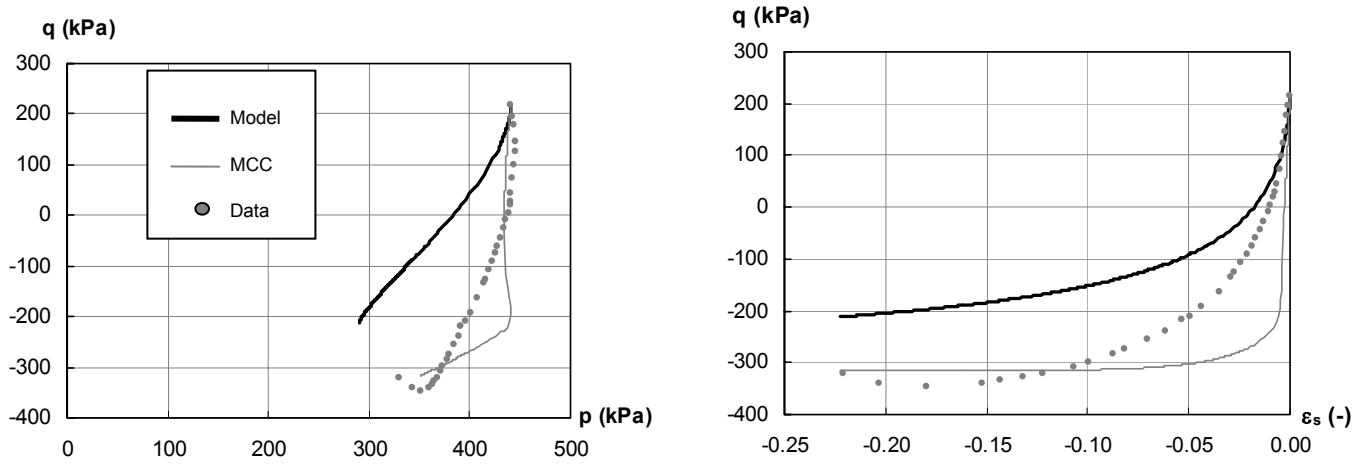

(a) (b)

Figure 5.18 Prediction of K_0 consolidation undrained extension test at OCR = 1.00
(a) Stress path; (b) Shear stress-strain curve

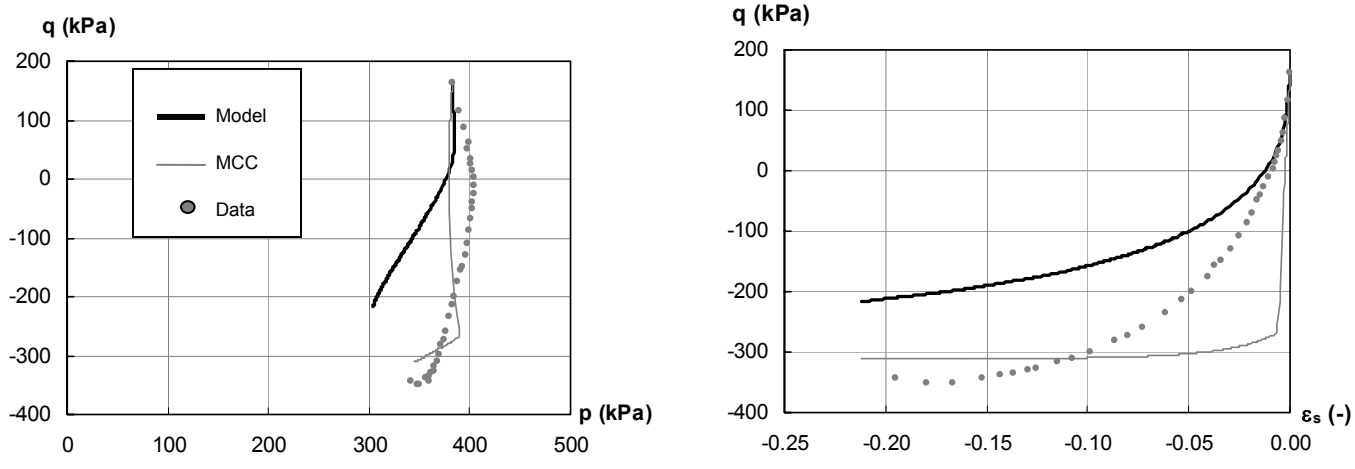

(a) (b)

Figure 5.19 Prediction of K_0 consolidation undrained extension test at OCR = 1.24
(a) Stress path; (b) Shear stress-strain curve

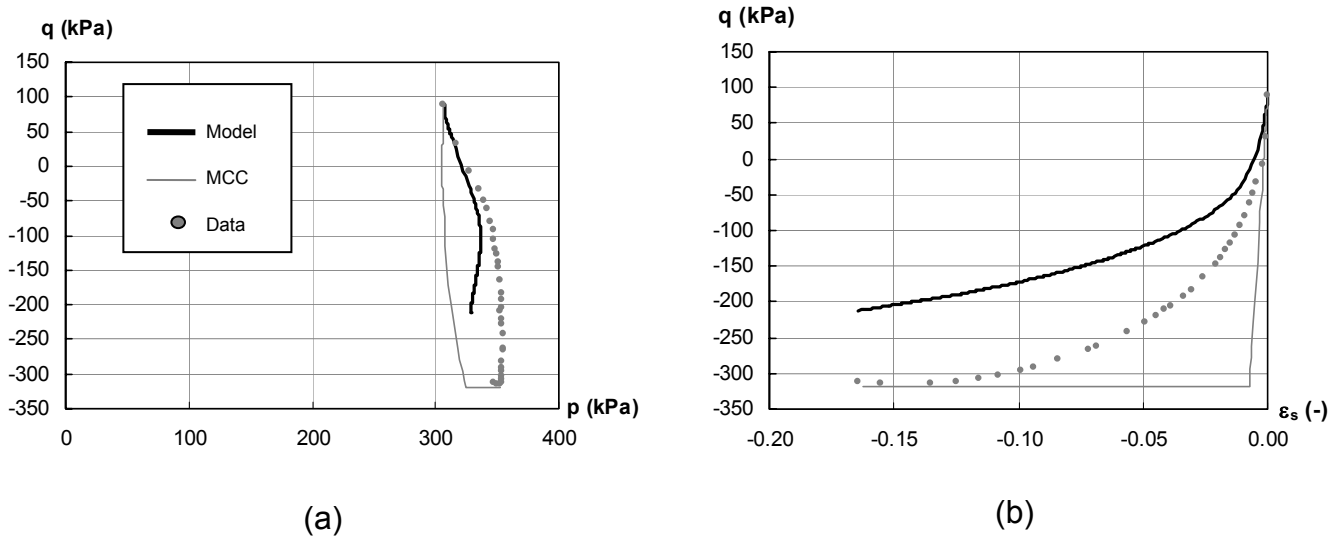

(a) (b)

Figure 5.20 Prediction of K_0 consolidation undrained extension test at OCR = 1.78
(a) Stress path; (b) Shear stress-strain curve

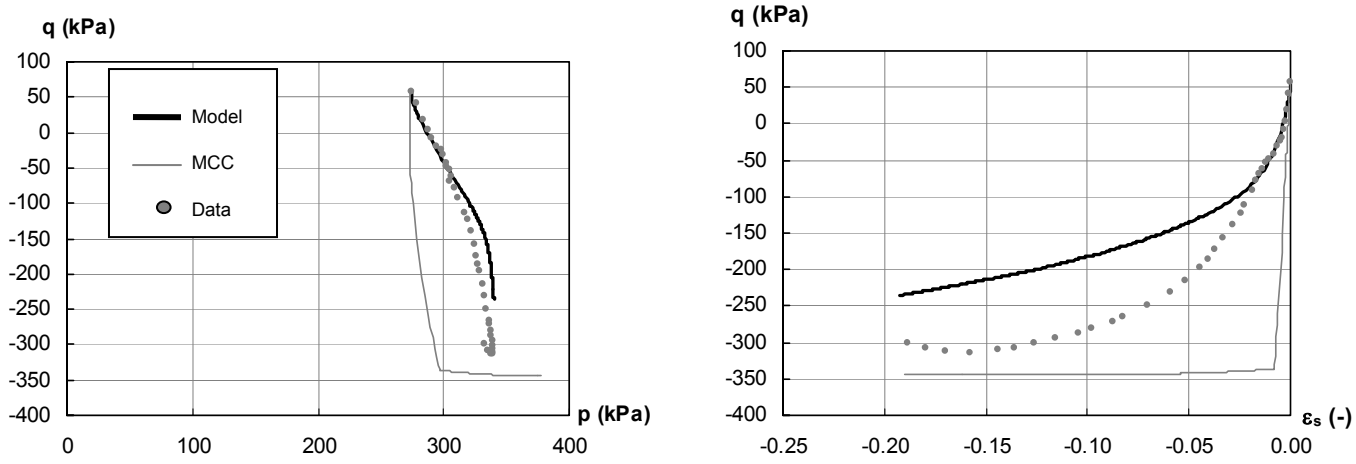

(a) (b)

Figure 5.21 Prediction of K_0 consolidation undrained extension test at OCR = 2.15
(a) Stress path; (b) Shear stress-strain curve

For the K_0 undrained extension test, the prediction exhibits the same trend as the compression tests except for the prediction of shear strength. The KHMCC model underestimates the shear strength value, compared to the MCC model. This may be due to the effect of the M-value, i.e. M_C is more than M_E, when keeping $\phi'_{TC} = \phi'_{TE}$ as a

material constant. However, this seems to be unsuitable for the explanation of the experimental data from AIT because the data shows that the extension shear strength is slightly higher than the compression shear strength. The KHMCC model allows the use of the same M-value for both compression and extension, $M_C = M_E$ (as shown in Table 5.1). The prediction of shear stiffness on the extension side is reasonably accurate, compared with the compression side. This simplification to the model reasonably compensates for the shortfall of the model.

5.4.2 Anisotropic drained behaviour

Like the isotropic consolidation data, the data for the anisotropic consolidation triaxial drained test are provided by the varying stress path directions from 0^o-360^o. Figures 5.22 to 5.25 show the comparison of the prediction of the KHMCC model and the MCC model with experimental data from AIT. Figures 5.22(a) and (b) show the volumetric and shear stress-strain curves of the CKD-45 and CKD-225 tests as shown in the small diagram. Figures 5.23(a) and (b) present the similar curves of CKD-135 and CKD-315 tests. Figures 5.24(a) and (b) exhibit the volumetric stress-strain plots of CKD-0 and CKD-180 tests respectively; on the other hand, Figure 5.25 presents the shear stress-strain curve of CKD-90 and CKD-270 tests.

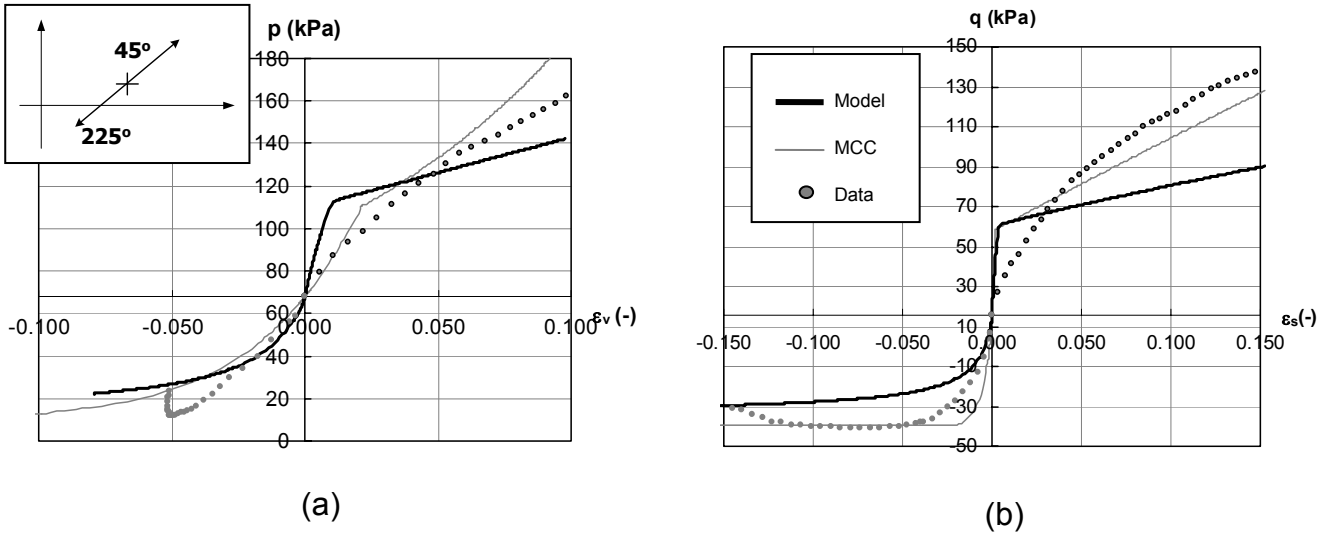

Figure 5.22 Prediction of K_0 consolidation drained test at 45^o and 225^o direction of OCR = 2.75; (a) Volumetric stress-strain curve; (b) Shear stress-strain curve

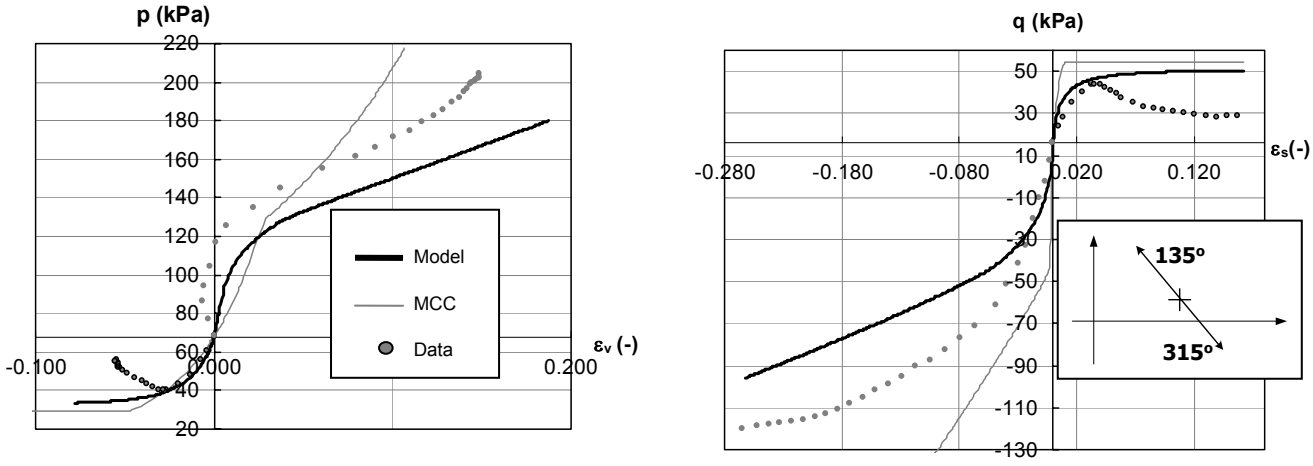

(a) (b)

Figure 5.23 Prediction of K_0 consolidation drained test at 135^o and 315^o direction of OCR = 2.75; (a) Volumetric stress-strain curve; (b) Shear stress-strain curve

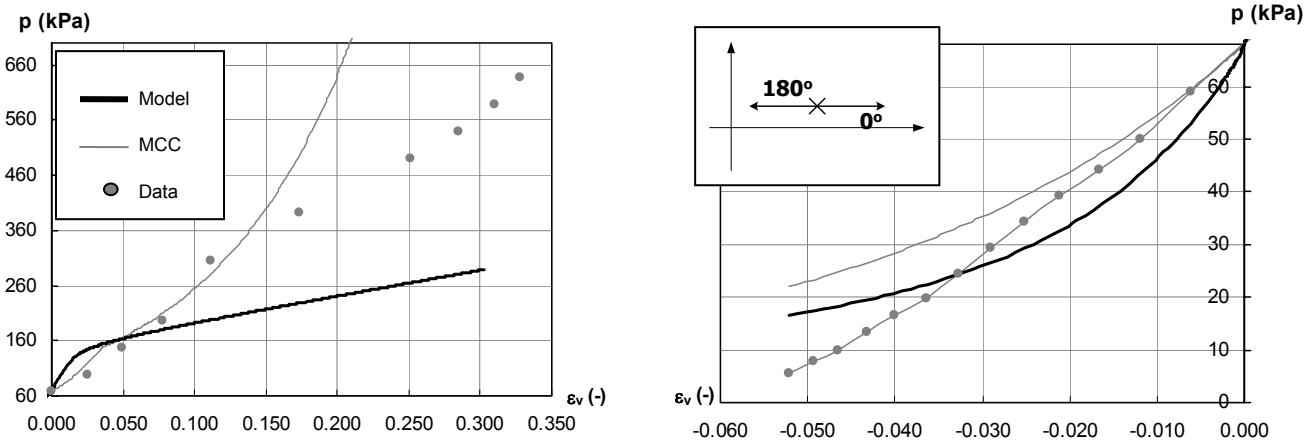

(a) (b)

Figure 5.24 Prediction of volumetric stress-strain curve of K_0 consolidation drained test of OCR = 2.75; (a) 0^o direction; (b) 180^o direction

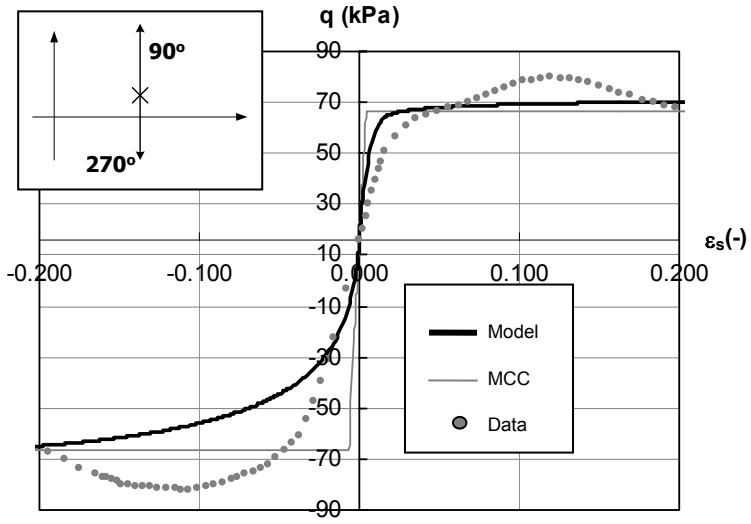

Figure 5.25 Prediction of shear stress-strain curve of K_0 consolidation drained test at 90° and 270° direction of OCR = 2.75

From Figures 5.22 to 5.25, the model behaves in the same way as predicted in the isotropic drained tests except in Figure 5.22. This may due to the fact that CKD-45 path is close to the K_0-line representing the past stress history direction. The KHMCC model therefore responds suddenly to a change of stiffness. The prediction of shear stress-strain behaviour (Figure 5.25) is accurate. On the other hand, the predictions of consolidation behaviour (Figures 5.24(a) and (b)) are not efficient. This is because the CKD-0 and CKD-180 data was obtained using a different rate of loading to the other CKD tests. This leads to the problem of how to select the appropriate viscosity coefficient to represent all tests. However, the overall predictions are seen to describe the main characteristics both for shear and consolidation stress-strain behaviour (Figures 5.22 and 5.23).

5.5 Cyclic behaviour prediction

The most important advantage of the KHMCC model is that it can simulate the smooth transition of stiffness before failure occurs. This advantage is crucial in construction work, because the stress-strain behaviour is actually limited under a certain value (i.e. the strength divided by a safety factor), which is much lower than the peak strength. In recent years, models for the small strain behaviour of soils have been developed independent of the model of prediction of strength behaviour, as there

is no theoretical framework to describe both behaviours in an uncomplicated way. However, hyperplasticity with a continuous kinematic hardening function can explain both.

The data on cyclic loading from Bangkok clay can be used to validate the hyperplasticity model. The testing program concerns the undrained cyclic behaviour whose details have been described in section 4.7. However, the original paper (Teachavorasinskun *et. al*, 2001 and 2002) uses a slightly confusing concept that mixes up the definition between two-dimensional (MIT) and three-dimensional (Cambridge) stress-strain parameters. To avoid this, all definitions are transferred to the terms of three-dimensional stress-strain parameters. Table 5.2 represents the definitions of the cyclic stress-strain parameters used in this research.

For the simulation of cyclic tests, the shear modulus gradient (g_x) is taken at a slightly higher value than for static tests, i.e. g_x = 150 in cyclic tests, while g_x = 60 in static tests. The evidence from the monotonic undrained compression test found that Chulalongkorn's clay samples are slightly stiffer than AIT's samples.

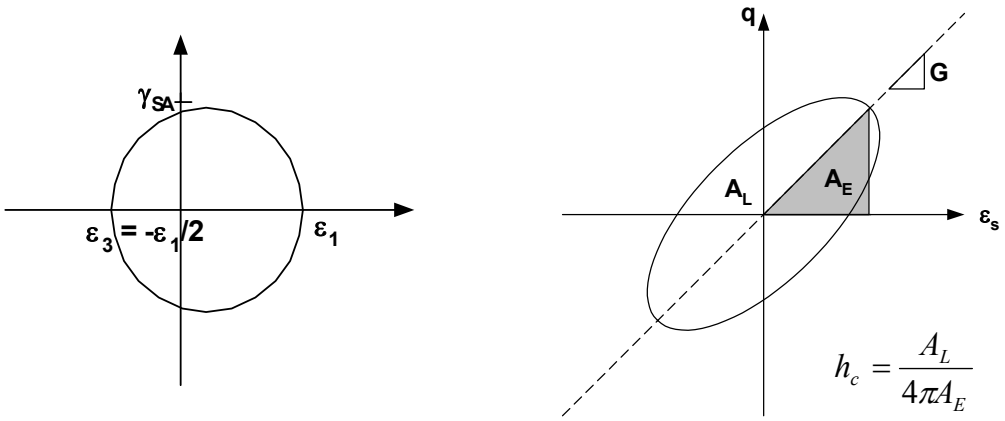

Figure 5.26 (a) Mohr's circle represents the strain parameters for undrained condition; (b) Definition of damping ratio

Table 5.2 The definitions of cyclic stress-strain parameters

Definition	Description
$\frac{\gamma_{SA}}{2} = \frac{(\varepsilon_1 - \varepsilon_3)}{2}$; in undrained condition $\gamma_{SA} = 1.5\varepsilon_s$	Single amplitude shear strain
$G = \frac{E}{2(1-\nu)}$; in undrained condition $G = \frac{q}{\varepsilon_s}$	Secant shear modulus
$h_c = \frac{A_L}{4\pi A_E}$; where A_L and A_E represent the area of hysterisis loop and the area of elastic zone (show in Figure 5.26)	Damping ratio

Figures 5.27 and 5.28 present the simulated result of cyclic undrained shear tests with varying confining pressure (p_c) of 50 and 100kPa respectively. The results exhibit the variation of shear modulus and damping ratio with single amplitude shear strain. The prediction of cyclic undrained triaxial tests are good for both the normally consolidated sample (p_c = 100kPa) and lightly overconsolidated sample (p_c = 50kPa). The *N*-value in Figures 5.27 and 5.28 represent the number of testing cycles. Although, the testing program has not been continued until failure (excess pore pressure develops due to the cyclic load), the first ten cycles are sufficient to represent the cyclic behaviour. The effect of viscous behaviour on cyclic properties can actually be investigated by the KHMCC model. However, because of the inconsiderable amount of the frequency difference in the data, it does not show a significant effect.

The prediction of the cyclic test at small strains is the most important advantage of the multiple yield surface model. In particular, the rate-dependent model shows the deformed elliptical shape of hysteresis loops during the cyclic load. The area of the hysteresis loop becomes larger when the number of cycles increases. This evidence is exhibited on the damping ratio Figures 5.27(b) and 5.28(b).

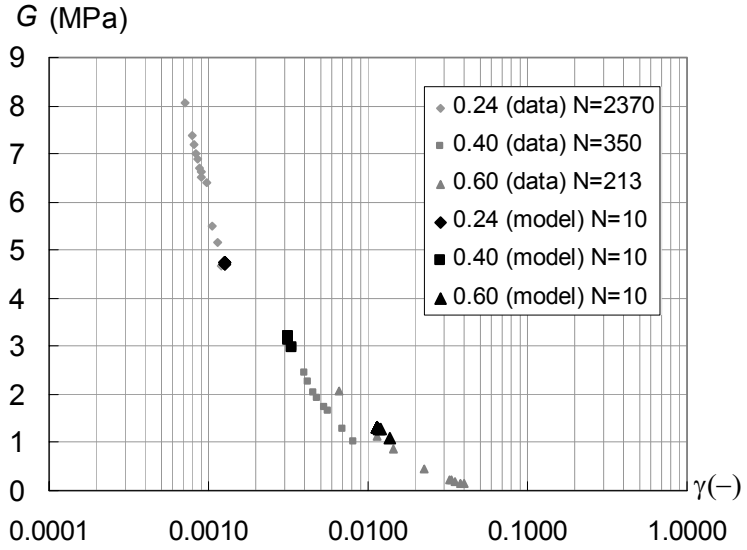

(a)

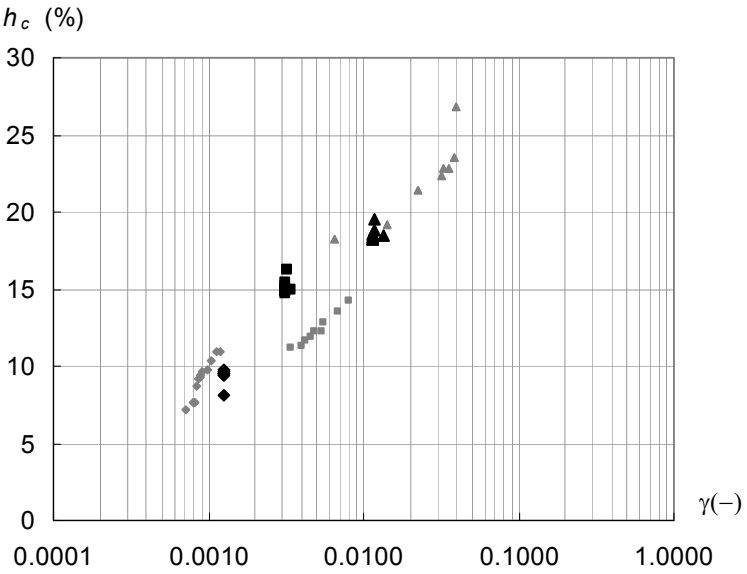

(b)

Figure 5.27 Prediction of cyclic undrained shear test varying shear stress magnitude (q/p) at confining pressure (p_c) = 50kPa, N = number of cycles

(a) Plot of shear modulus (G) vs. single amplitude shear strain (γ_{SA})

(b) Plot of damping ratio (h_c) vs. single amplitude shear strain (γ_{SA})

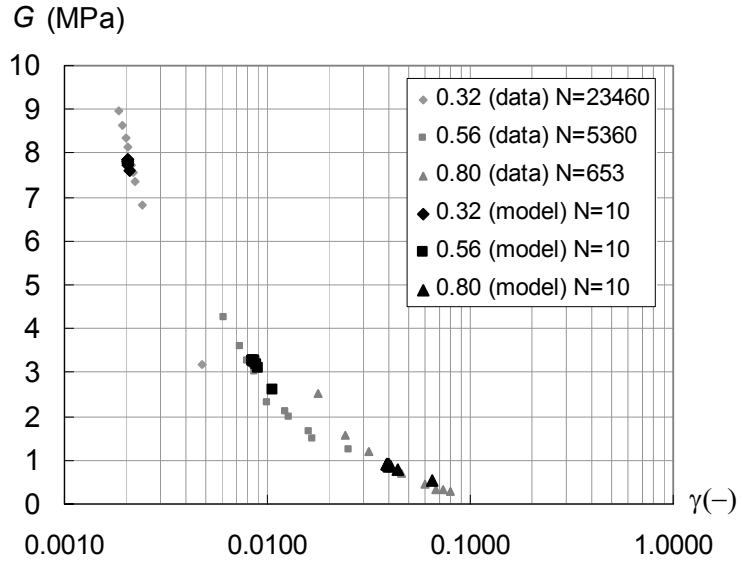

(a)

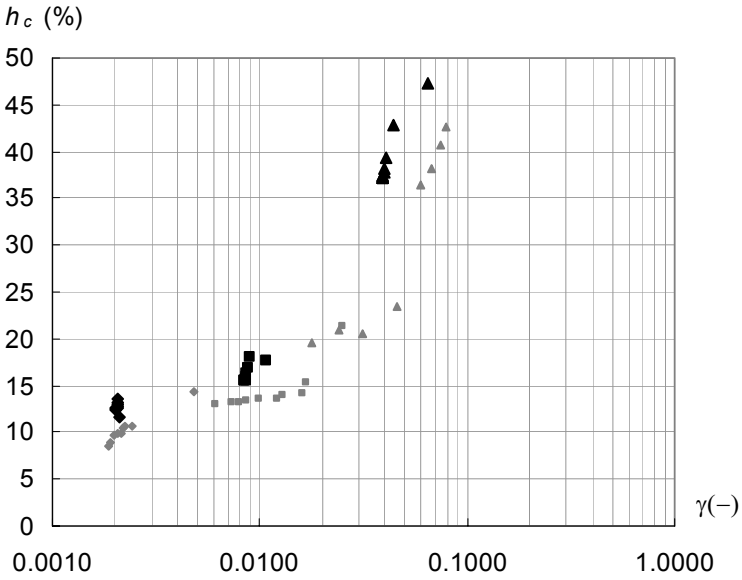

(b)

Figure 5.28 Prediction of cyclic undrained shear test varying shear stress magnitude (q/p) at confining pressure (p_c) = 100kPa, N = number of cycles

(c) Plot of shear modulus (G) vs. single amplitude shear strain (γ_{SA})

(d) Plot of damping ratio (h_c) vs. single amplitude shear strain (γ_{SA})

5.6 Conclusion and Future work

The hyperplasticity model based on two potential functions can define the constitutive law for an engineering material, especially soil. The advantage is that a continuous kinematic hardening function can exhibit a continuous stress-strain response. The KHMCC model with a linear stress-strain relationship has been finally proposed for the implementation. A parametric study on Bangkok clay is based on two sources of research. All predictions of the experimental result have been processed by FORTAN 90 with the assumption that stress-strain is uniformly distributed under the triaxial condition (axi-symmetry condition). Every sample is consolidated following its stress history and sheared in its specific condition such as undrained, drained or cyclic undrained condition.

The prediction for consolidation behaviour is more accurate than shear behaviour. Since, the consolidation prediction only acts on the p term of the model, there is no p-q coupling term that affects the stress-strain response. The real-time analysis can be done by means of adjusting the viscosity coefficient and the rate in the rate-dependent analysis.

The prediction for pure shear behaviour can be determined from the CID-90 and CID-270 tests. These two tests are used to evaluate the magnitude of the critical state cone both on the compression and extension sides. The evidence on anisotropic tests, however, shows that the extension strength is slightly higher than compression. Thus, for simplicity for the downside of the model, the assumption that $M_C = M_E$ has been proposed in this study.

The isotropic consolidated tests are accurately predicted in terms of stress path and shear strength. On the other hand, the anisotropic consolidated samples are slightly inaccurate, especially the stress path. The variation of shear stiffness is relatively well fitted for both isotropic and anisotropic consolidated tests. However, the prediction of the shear strength of the heavily overconsolidated sample should be improved.

The simulation of the cyclic undrained tests gives an accurate result. The variation of the shear modulus is simulated by the model accurately all shear strain amplitudes. The damping ratio is also well predicted at all shear strain amplitudes.

This leads to the significant benefit of the model that it can simulate both the monotonic loading and the cyclic loading behaviour by a unique constitutive law.

However, this version of the hyperplasticity model still has to be improved. The suggested information is summarised below:

1. Because the model is based strictly on the Masing rule; it always gives a symmetric closed hysteresis loop when the stress path returns to the same maximum past stress. Further research has to introduce a ratchetting mechanism that will provide an unsymmetrical hysteresis loop and a small drift after one load cycle.

2. The investigation shows that it is not necessary to strictly enforce the CSSM assumption that every sheared sample must reach the same critical state. Further research should consider either the concept of localisation or the strain softening phenomenon. The localisation idea assumes that material consists of two zones i.e. elastic and plastic zones[3], where the ratio of these two zone's volume controls the material behaviour. This idea implies that all material elements do not necessarily reach the yield state at the same time. In contrast, the strain softening will result in a softening behaviour after material yield. The yield surface will move inward or shrink when the stress state touches the yield surface. These two concepts might be used to explain the behaviour of heavily overconsolidated clay.

3. The fact that the magnitude of the critical state cone (M) depends on where the stress state is in stress space. For the generalised stress-strain model, the general expression to evaluate the shape of critical state cone has to be considered.

4. For the better prediction of anisotropy, the yield surface shape may be improved by, for example, deforming the yield surface shape or rotating the yield surface axis around the p-axis. These ideas are believed to be able to generate anisotropy.

[3] the plastic zone is sometimes called the shear band

Chapter 6
Implementation into Finite Element Code

In recent times, the finite element method has been used in engineering practice including for the analysis of geotechnical problems. A finite element program OXFEM has been developed at the University of Oxford over the last ten years. The nested yield surface model, a multi yield surface soil model, has been implemented into OXFEM (Augarde, 1997). Based on the hyperplasticity approach (Collins and Houlsby, 1997, and Houlsby and Puzrin, 2000), rate independent plasticity is not difficult apply in OXFEM. Nonetheless, the rate-dependent calculation is distinctively different from the classical plasticity theory. The rate-dependent stress-strain algorithm must be further developed and included in the OXFEM code.

This chapter focuses on the implementation of the new constitutive law using the finite element method, and the two-dimensional finite element formulation for geotechnical problems is summarised. The KHMCC and MCC models are represented in terms of generalised stress-strain parameters. The models are also reduced for the analysis of the two-dimensional problem.

6.1 Stress-strain definition

The formulation of an element stiffness matrix is based on the isoparametric method used in the derivation of small strain finite element equations. If deformations are defined by continuous functions *u, v* and *w* in the *x, y* and *z* directions respectively, the strains (assuming small strain theory and a compression positive sign convention) are defined as (Howatson, Lund and Todd, 1991):

$$\varepsilon_x = -\frac{\partial u}{\partial x};\quad \varepsilon_y = -\frac{\partial v}{\partial y};\quad \varepsilon_z = -\frac{\partial w}{\partial z}$$
$$\gamma_{xy} = -\frac{\partial v}{\partial x} - \frac{\partial u}{\partial y};\quad \gamma_{yz} = -\frac{\partial w}{\partial y} - \frac{\partial v}{\partial z};\quad \gamma_{xz} = -\frac{\partial w}{\partial x} - \frac{\partial u}{\partial z} \tag{6.1}$$

As the six strains are a function of only three displacements, they are not independent.

However, to analyse a real geotechnical problem, some assumptions and idealisations must be made. Due to the special geometric characteristics of many problems such as retaining walls, continuous footings and stability of slopes, they can

be treated in soil mechanics as *plane strain* problems. If the z dimension of the problem is large, the conditions consistent with these approximations are defined as:

$$\varepsilon_z = -\frac{\partial w}{\partial z} = 0; \quad \gamma_{yz} = -\frac{\partial w}{\partial y} - \frac{\partial v}{\partial z} = 0; \quad \gamma_{xz} = -\frac{\partial w}{\partial x} - \frac{\partial u}{\partial z} = 0 \tag{6.2}$$

Some special geometries, for example circular footings, single piles or caissons and cylindrical triaxial specimens, have rotational symmetry about a vertical axis through the centre. These types regularly use a cylindrical coordinate r (radial direction), z (axial direction) and θ (circumferential direction). Due to the symmetry, there is no displacement in the θ direction and the displacement in r and z directions are independent of θ. This is called the *axi-symmetry* condition. The strains can be reduced to (Timoshenko, 1951):

$$\varepsilon_r = -\frac{\partial u}{\partial z}; \quad \varepsilon_z = -\frac{\partial v}{\partial z}; \quad \varepsilon_\theta = -\frac{u}{r}; \quad \gamma_{rz} = -\frac{\partial v}{\partial r} - \frac{\partial u}{\partial z}; \quad \gamma_{r\theta} = \gamma_{z\theta} = 0 \tag{6.3}$$

For these two cases, the strain variables are reduced to three and four unknowns respectively for the plane strain and axi-symmetric cases.

6.2 Generalised soil model

The constitutive models explained in the previous chapter are in the form of triaxial stress-strain parameters. In the finite element method, however, generalised stress-strain (three-dimensional) parameters are required. The following table shows comparisons between triaxial, generalised and two-dimensional stress-strain parameters.

Table 6.1 Comparisons between triaxial and generalised stress-strain parameters

Variables	Generalised stress-strain	Two-dimensional stress-strain	Triaxial stress-strain
Stress parameters	σ_{ij} where $i, j = 1 \ldots 6$	$\{\sigma_1, \sigma_2, \sigma_3, \sigma_4\}^T$ equivalent to $\{\sigma_{11}, \sigma_{22}, \sigma_{33}, \sigma_{12}\}^T$	$\{\sigma_r, \sigma_r, \sigma_z\}^T$
Mean stress	$\frac{\sigma_{kk}}{3}$	$p = \frac{(\sigma_1 + \sigma_2 + \sigma_3)}{3}$	$p = \frac{2\sigma_r + \sigma_z}{3} = \frac{\sigma_{kk}}{3}$
Deviatoric stress	$\sigma'_{ij} = \sigma_{ij} - \frac{\sigma_{kk}}{3}\delta_{ij}$	$\sigma'_i = \sigma_i - p \cdot \delta_i$ where $i = 1 \ldots 4$ and	$q = \sigma_z - \sigma_r$ $= \sqrt{\frac{3}{2}\sigma'_{ij} \cdot \sigma'_{ij}}$

		$\delta_i = \begin{cases} 1, & i = 1-3 \\ 0 & i = 4 \end{cases}$	
Strain parameters	ε_{ij} where $i, j = 1 \ldots 6$	$\{\varepsilon_1, \varepsilon_2, \varepsilon_3, \varepsilon_4\}^T$ equivalent to $\{\varepsilon_{11}, \varepsilon_{22}, \varepsilon_{33}, 2\varepsilon_{12}\}^T$	$\{\varepsilon_r, \varepsilon_r, \varepsilon_z\}^T$
Volumetric strain	ε_{kk}	$\varepsilon_v = \varepsilon_1 + \varepsilon_2 + \varepsilon_3$	$\varepsilon_v = 2\varepsilon_r + \varepsilon_z = \varepsilon_{kk}$
Deviatoric strain	$\varepsilon'_{ij} = \varepsilon_{ij} - \frac{\varepsilon_{kk}}{3}\delta_{ij}$	$\varepsilon'_i = \varepsilon_i - \frac{v}{3}\delta_i$ where $i = 1 \ldots 4$	$\varepsilon_s = \frac{2}{3}(\varepsilon_z - \varepsilon_r)$ $= \sqrt{\frac{2}{3}\varepsilon'_{ij} \cdot \varepsilon'_{ij}}$
Bulk modulus (K)	$3K = \frac{\sigma_{kk}}{\varepsilon_{kk}}$	$K = \frac{p}{\varepsilon_v}$	$K = \frac{p}{\varepsilon_v}$
Shear modulus (G)	$2G = \frac{\sigma'_{ij}}{\varepsilon'_{ij}}$	$2G = \frac{\sigma'_i}{\varepsilon'_i}$	$3G = \frac{q}{\varepsilon_s}$

The MCC model and KHMCC model can be transformed into the generalised stress-strain parameters shown in Table 6.2. The simplicity of the generalisation from triaxial conditions is a feature of the approach in which the model is defined entirely by scalar functions.

Table 6.2 Generalised soil models

MCC model	$g = -\kappa \frac{\sigma_{0kk}^2}{3} \cdot \text{ilog}\left(\frac{\sigma_{kk}}{\sigma_{0kk}}\right) - \frac{3}{4} \cdot \frac{\sigma'_{ij}\sigma'_{ij}}{g_x \sigma_{kk}} - \sigma_{ij}\alpha_{ij} + (\lambda - \kappa) \cdot \frac{\sigma_{0kk}}{3} \cdot \exp\left(\frac{\alpha_{kk}}{\lambda - \kappa}\right)$ $y = \sqrt{\frac{\chi_{kk}^2}{9} + \frac{3}{2} \cdot \frac{\chi'_{ij}\chi'_{ij}}{M^2}} - \frac{\sigma_{x0kk}}{3} \cdot \exp\left(\frac{\alpha_{kk}}{\lambda - \kappa}\right) = 0$ where subscript *0*, *x* represent the reference (initial) and the reference point of yield surface
KHMCC model	$g = -\frac{\sigma_{kk}^2}{18K} - \frac{3}{4} \cdot \frac{\sigma'_{ij}\sigma'_{ij}}{g_x \sigma_{kk}} - \sigma_{ij}\alpha_{ij} + \int_0^1 \left(\frac{\hat{H}_p \hat{\alpha}_{kk}^2}{2} + \frac{\hat{H}_q \hat{\alpha}'_{ij}\hat{\alpha}'_{ij}}{3}\right) d\eta$ $\hat{y} = \sqrt{\frac{\hat{\chi}_{kk}^2}{9} + \frac{3}{2} \cdot \frac{\hat{\chi}'_{ij}\hat{\chi}'_{ij}}{M^2}} - \hat{H}_p \hat{\alpha}_{kk} \eta = 0$

6.3 Two-dimensional soil model for OXFEM

Taking advantage of the special geometry arising in many geotechnical problems, some assumptions are made to reduce the amount of calculation in the finite element analysis. In this research, the two-dimensional analysis, such as plane strain and/or axi-symmetry is used. However, a transformation from generalised stress-strain parameters to two-dimensional stress-strain parameters is required and is shown in Table 6.2. The two-dimensional version of the MCC model and KHMCC model defined by two scalar functions is presented in Table 6.3.

Table 6.3 Two-dimensional soil models

MCC model	$g = -\frac{\kappa\sum_{i=1}^{3}\sigma_{0i}}{3}\cdot \mathrm{ilog}\left(\frac{\sum_{i=1}^{3}\sigma_i}{\sum_{i=1}^{3}\sigma_{0i}}\right) - \frac{3}{4}\cdot\frac{\sum_{i=1}^{3}\left(\sigma_i'^2\right)+2\sigma_4'^2}{g_x\left(\sum_{i=1}^{3}\sigma_i\right)} - \left(\sum_{i=1}^{3}\left(\sigma_i\cdot\alpha_i\right)+2\sigma_4\cdot\frac{\alpha_4}{2}\right)$ $+\left(\lambda-\kappa\right)\cdot\frac{\sum_{i=1}^{3}\sigma_{x0i}}{3}\cdot\exp\left(\frac{\sum_{i=1}^{3}\alpha_i}{\lambda-\kappa}\right)$ $y = \sqrt{\frac{\left(\sum_{i=1}^{3}\chi_i\right)^2}{9}+\frac{3}{2}\cdot\frac{\left(\sum_{i=1}^{3}\left(\chi_i'^2\right)+2\chi_4'^2\right)}{M^2}} - \frac{\sum_{i=1}^{3}\sigma_{x0i}}{3}\cdot\exp\left(\frac{\sum_{i=1}^{3}\alpha_i}{\lambda-\kappa}\right) = 0$
KHMCC model	$g = -\frac{\left(\sum_{i=1}^{3}\sigma_i\right)^2}{18K} - \frac{3}{4}\cdot\frac{\sum_{i=1}^{3}\left(\sigma_i'^2\right)+2\sigma_4'^2}{g_x\left(\sum_{i=1}^{3}\sigma_i\right)} - \left(\sum_{i=1}^{3}\left(\sigma_i\cdot\alpha_i\right)+2\sigma_4\cdot\frac{\alpha_4}{2}\right)+$ $\int_0^1\left(\frac{\hat{H}_p\left(\sum_{i=1}^{3}\hat{\alpha}_i\right)^2}{2}+\frac{\hat{H}_q\left(\sum_{i=1}^{3}\left(\hat{\alpha}_i'^2\right)+2\left(\frac{\hat{\alpha}_4'}{2}\right)^2\right)}{3}\right)d\eta$ $\hat{y} = \sqrt{\frac{\left(\sum_{i=1}^{3}\hat{\chi}_i\right)^2}{9}+\frac{3}{2}\cdot\frac{\left(\sum_{i=1}^{3}\left(\hat{\chi}_i'^2\right)+2\hat{\chi}_4'^2\right)}{M^2}} - \hat{H}_p\left(\sum_{i=1}^{3}\hat{\alpha}_i\right)\cdot\eta = 0$

6.4 Solution scheme

There are two levels for the calculation of the stress-strain relationship, i.e. the incremental stress-strain for each single element, and the incremental load-deformation behaviour of the global problem. The former calculation uses exactly the same algorithm as in the case of the triaixal stress-strain calculation explained in chapter 3. The latter one, on the other hand, has to deal with a slightly more complicated situation, which will be discussed in this section.

6.4.1 Incremental stress-strain solution at element level

The incremental stress-strain solution at the element level is still based on rate-dependent calculations mentioned in section 3.9.3. However, there exists no requirement for a constraint statement during the finite element calculation. The incremental response can be rewritten in the form:

$$-\frac{\partial^2 \hat{g}}{\partial \sigma_i \partial \sigma_j} d\sigma_j = d\varepsilon_i + \left\{ \int \left(\frac{\partial^2 \hat{g}}{\partial \sigma_i \partial \hat{\alpha}_j} \cdot \frac{\partial w}{\partial \hat{\chi}_j} \right) d\eta \right\} dt \tag{6.4}$$

or, in the matrix form: $$\mathbf{A} \cdot \mathbf{d\sigma} = \mathbf{d\varepsilon} - \left\{ \int (\mathbf{B} \cdot \mathbf{C}) d\eta \right\} dt \tag{6.5}$$

where $\mathbf{A} = -\frac{\partial^2 \hat{g}}{\partial \sigma_i \partial \sigma_j}$, $\mathbf{B} = -\frac{\partial^2 \hat{g}}{\partial \sigma_i \partial \hat{\alpha}_j}$, and $\mathbf{C} = \frac{\partial w}{\partial \hat{\chi}_j}$.

The incremental stress can be solved from equation 6.5 in the form $\mathbf{d\sigma} = \mathbf{A}^{-1} \cdot \left(\mathbf{d\varepsilon} - \left\{ \int (\mathbf{B} \cdot \mathbf{C}) d\eta \right\} dt \right)$. Compared with the formulation of the elasto-plastic constitutive matrix, the relation between incremental stress and incremental strain takes the form $\mathbf{d\sigma} = \mathbf{D} \cdot \left(\mathbf{d\varepsilon} - \mathbf{d\varepsilon^p} \right)$, where $\mathbf{D}$ or $\mathbf{A}^{-1}$ represents the purely elastic stiffness matrix.

6.4.2 Modified Newton-Raphson (MNR) method

Commonly, the analysis of any boundary value problems can be expressed by the governing finite element equations which can be reduced to the following incremental form:

$$\mathbf{K_G}^i \cdot \mathbf{\Delta d_{nG}}^i = \mathbf{\Delta f_G}^i \tag{6.6}$$

where $\mathbf{K_G}^i$ is the incremental global stiffness matrix, $\mathbf{\Delta d_{nG}}^i$ is the vector of incremental nodal displacements, $\mathbf{\Delta f_G}^i$ is the vector of incremental nodal forces and

superscript i is the increment number. To obtain a solution to the boundary value problem, the change in boundary conditions is normally applied in the form of a series of increments, in which the governing equation of each increment must be solved. The final solution is obtained by summing the results of each increment. Normally, the incremental global stiffness matrix $\mathbf{K}_G^{\,i}$ depends on the current stress and strain level and therefore is not constant, except in the linear elasticity case. If sufficiently small increments are used, the integration of piecewise linear increments represents non-linear constitutive behaviour. There are several strategies to solve the non-linear governing equation. However, only two categories of solution algorithm are considered: the Euler scheme and Newton-Raphson (NR) scheme (Burd, 1986).

The simplest solution strategy is the Euler scheme, also called the tangential stiffness method. According to this approach, the incremental stiffness matrix is assumed constant over each increment and is calculated by using the current state from the beginning of each increment (i.e. $\mathbf{K}_G^{\,i}$ is calculated by using $\Delta\mathbf{d}_{nG}^{\,i}$). This is equivalent to making a piecewise linear approximation to the non-linear constitutive behaviour as illustrated in Figure 6.1(a). Explicitly, the accuracy of the solution depends on the size of load increments. For example, if the increment size was reduced so that more increments were needed to reach the same accumulated load, the tangent stiffness solution would be nearer to the true solution.

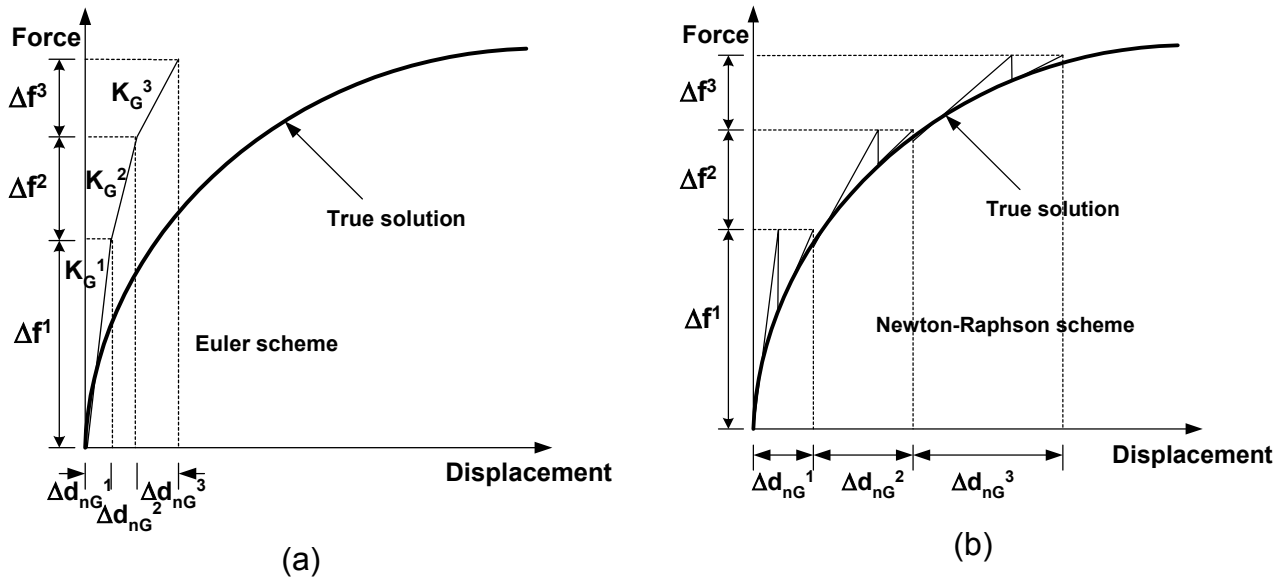

Figure 6.1 Solution schemes for Finite Element Analysis;
(a) Euler scheme, (b) Newton-Raphson (NR) scheme

An alternative is the NR method as illustrated in Figure 6.1(b). This method uses the equilibrium equation. The first calculation is essentially the same as in the Euler method. However, there will be a solution error after the first increment, and the predicted incremental displacements are used to calculate the unbalanced force (or residual load), a measure of the error in the analysis. After that, a residual load is calculated, and the step repeated. The iterative process is repeated until the residual is small. The incremental displacements are equal to the sum of the iterative displacements. The next increment is equal to the amount of the unbalanced load plus the usual increment. This scheme will reduce the amount of the error accumulation due to the unbalanced load of each calculation step. Nonetheless, it is observed that this scheme might be unstable if too large an increment is applied. This is because a huge unbalanced force is reapplied in the next calculation stage. The numerical stability can be improved by using a factor (normally between 0 and 1), which scales down the unbalanced force. This method has to recalculate and invert the incremental global stiffness matrix for each iteration. This is the most time-consuming process.

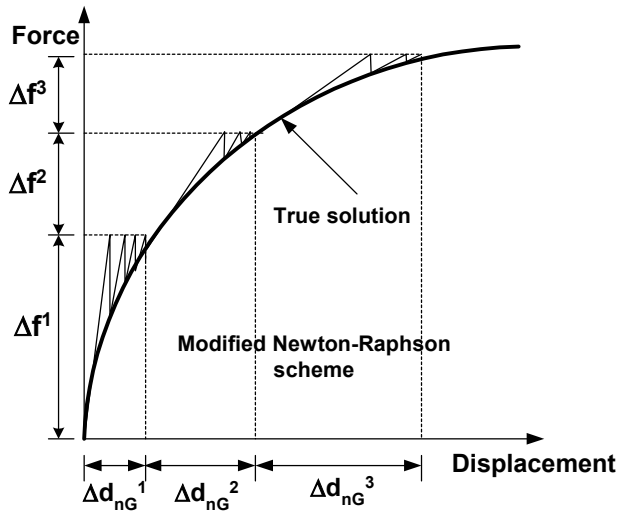

Figure 6.2 Modified Newton-Raphson (MNR) method

A further solution technique called the Modified Newton-Raphson (MNR) method, Potts and Zdravkovic (1999), improve the time-consuming in each increment by using the stiffness of the first iteration or the elastic stiffness rather than recalculation of the tangential stiffness for each iteration (see Figure 6.2). This may requires storage in the computer memory to memorise all elements of the stiffness matrix during the updated process.

The present version of OXFEM employs the NR algorithm. The OXFEM code could be improved by introducing the MNR algorithm. This might need some modification of storage to memorise all elements of the stiffness matrix. However, the NR algorithm has proved to be acceptable for this research.

6.5 Choice of element type

In finite element analysis, the geometry of the boundary value problem must be defined. Simplifications and approximations may, however, be necessary during this process, and the geometry of the problem must be approximated as accurately as possible. The isoparametric formulation employs shape functions in terms of coordinates and nodal displacements. For the two-dimensional problem, high order isoparametric elements with mid-side nodes can be reasonably used to reproduce curved boundaries.

The simple three-noded triangle can generate only a linear boundary, and offers a constant strain inside its element, and is thus inappropriate for this research. The chosen element for the research is the six-noded triangle for two-dimensional analysis (Figure 6.3), which requires three nodes at each corner and three nodes in the mid-side. Hence, it can produce a parabolic curved boundary.

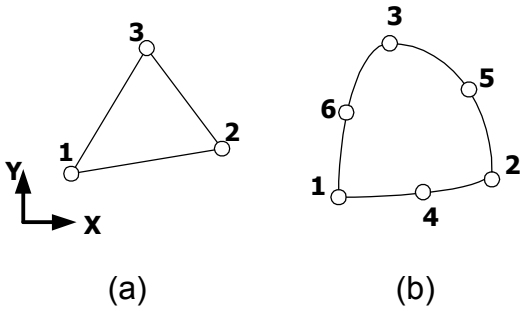

Figure 6.3 Two-dimensional elements used to model the soil;
(a) Three-noded triangle, (b) Six-noded triangle

6.6 Analysis types

In solid mechanics, the constitutive behaviour is formulated as a relationship between changes in total stress and strain, whereas in geotechnical problems the constitutive behaviour is expressed in term of effective stress parameters. The finite element formulation employed here can be used to analyse the following two classes of problems:

1. Fully drained problems (effective stress analysis) in which there is no change in pore pressure, $\Delta u = 0$. This implies that the changes in effective and total stress are the same, i.e. $\mathbf{\Delta\sigma} = \mathbf{\Delta\sigma'}$, and that the stiffness matrix **D** contains the effective components. For example, in the case of linear elastic behaviour **D** will be based on a drained Young's modulus, E', and drained Poisson's ratio, υ'.

2. Fully undrained problems (total stress analysis) in which the stiffness matrix **D** is expressed in terms of total stress parameters. For linear elasticity **D** is based on an undrained Young's modulus, E_u, and undrained Poisson's ratio, υ_u.

The results from both problems are classified in terms of changes in total stress. No information is provided on changes in pore pressure.

6.7 Test problems

The triaxial formulation of the MCC and KHMCC model have been tested and validated with experimental data from AIT and Chulalongkorn University as presented in chapter 5. However, before the implementation of the generalised model, testing of the two-dimensional formulation should be made. The FEM result should be consistent with the calculation from the single element program. The purpose of these tests is to verify the new material subroutine, the interface between old OXFEM code and the new subroutine as well as the rate-dependent algorithm, before applying them to geotechnical field problems.

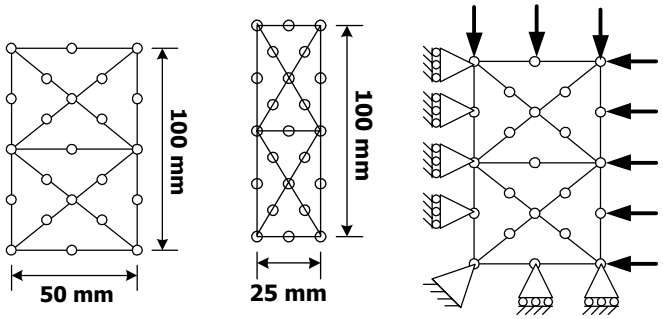

Figure 6.4 Test models for triaxial problem;
(a) plane strain case, (b) axi-symmetry case, (c) boundary conditions

A series of artificial triaxial tests is carried out by both the single element program and the FEM model presented in Table 6.4. The tests are simplified as plane

strain condition (PS) and axi-symmetry (AS). Eight 6-noded elements are used, the dimensions of which are shown in Figures 6.4(a) and 6.4(b) for the PS and AS analyses. The boundary conditions are illustrated in Figure 6.4(c).

Three material subroutines are called from the main OXFEM program: the Elastic Von Mises soil model (EVM), the MCC model and the KHMCC model. The parameters for the EVM model are assumed as: elastic shear modulus $G = 1000\text{kPa}$, Poisson's ratio $\upsilon = 0.35$, and undrained shear strength $s_u = 100\text{kPa}$. For the MCC and KHMCC models, the parameters used are as in Tables 5.1 and 5.2.

Firstly, all tests are simulated by applying a series of equivalent nodal loads simulating confining pressures during the consolidation stage. The equivalent nodal force is calculated based on the virtual work principle, which assumes that the work done by the equivalent nodal load must be equal to the amount of work done by the pressure. All tests are consolidated to 100kPa. Then, applying negative loading allows the samples to swell back to 80kPa. Thus, after the consolidation stage, all specimens are lightly overconsolidated (OCR = 1.25). Next, the applied displacement is applied solely at the top during the shearing stage. The displacement prescribed is applied incrementally until the sample goes beyond yield. The increment details for each test are illustrated in Table 6.4.

Table 6.4 Artificial Triaxial Tests for Validation of KHMCC and MCC models

No.	Model	Problem (PS/AS)	Consolidation stage			Shearing stage		
			Cal. Step	Inc. per step	Real time step (sec)	Cal. Step	Inc. per step	Real time step (sec)
1	EVM	PS	20	5kPa	-	20	$5\text{x}10^{-4}$m	-
2	EVM	AS	20	5kPa	-	20	$5\text{x}10^{-4}$m	-
3	MCC	AS	10^4	10^{-2}kPa	10	10^3	10^{-5}m	0.1
4	KHMCC	AS	10^4	10^{-2}kPa	10	10^3	10^{-5}m	0.1

6.8 Comparison of results

For the EVM model, only 10 steps per loading stage have been calculated since the elastic stiffness matrix is based on the closed form solution. The elastic calculation is sufficiently robust for a large loading stage. The plane strain and axi-symmetric elastic result can be calculated by using Hooke's law, which are:

Plane strain (PS):

$$\varepsilon_1 = \frac{(1-\upsilon^2)}{E}\cdot\left(\sigma_1 - \frac{\upsilon}{1-\upsilon}\sigma_2\right),\ \varepsilon_2 = \frac{(1-\upsilon^2)}{E}\cdot\left(\sigma_2 - \frac{\upsilon}{1-\upsilon}\sigma_1\right),\ \varepsilon_3 = 0$$

Axi-symmetry (AS):

$$\varepsilon_1 = \frac{1}{E}\cdot(\sigma_1 - 2\upsilon\sigma_3),\ \varepsilon_2 = \varepsilon_3 = \frac{1}{E}\cdot(\sigma_3 - \upsilon(\sigma_1 + \sigma_3))$$

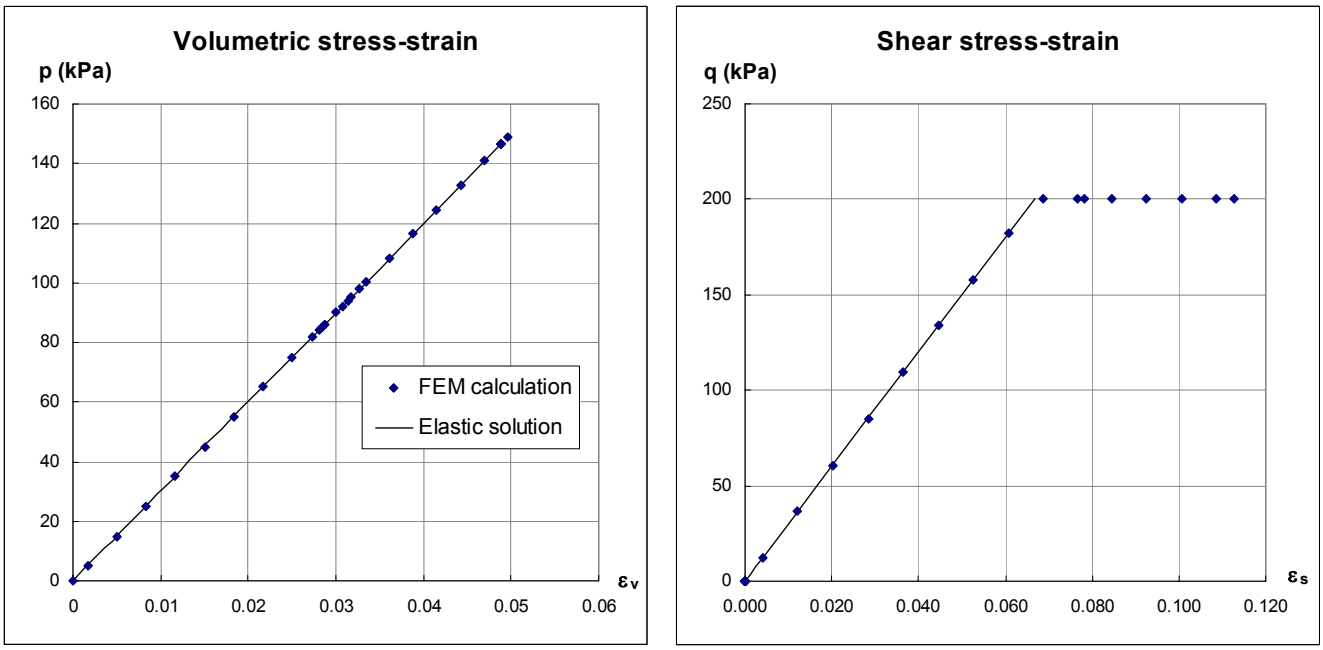

(a) (b)

Figure 6.5 Finite element calculation based on the EVM model;
(a) Volumetric stress-strain curve, (b) Shear stress-strain curve

For example, Figure 6.5 shows the FEM calculation of test no.2. At yield state ($\sigma_1 = 280\text{kPa}$, and $\sigma_3 = 80\text{kPa}$), the strain should be $\varepsilon_1 = 0.082963$, $\varepsilon_3 = -0.017037$ based on the elastic solution. This stress state just reaches the yield condition and is the maximum shear stress that is still in the elastic range. Thus, compare the elastic solution with the results from the FEM analysis, which are $\sigma_1 = 280.061\text{kPa}$, $\sigma_3 = 80.061\text{kPa}$ and $\varepsilon_1 = 0.082396$, $\varepsilon_3 = -0.017079$. The errors are in the range of 0.08% for the stress and 0.68% for the strain which are sufficiently acceptable. Applied loading cannot be applied beyond this state; otherwise a huge amount of plastic strain would cause a numerical problem. However, by prescribing the displacement it is possible to avoid this problem. After yield, the stresses remain the same due to the EVM yield condition. On the other hand, the plastic strain will

cause the shear strain to keep increasing. Figure 6.5 illustrates that the FEM calculation give an accurate result for the EVM material behaviour.

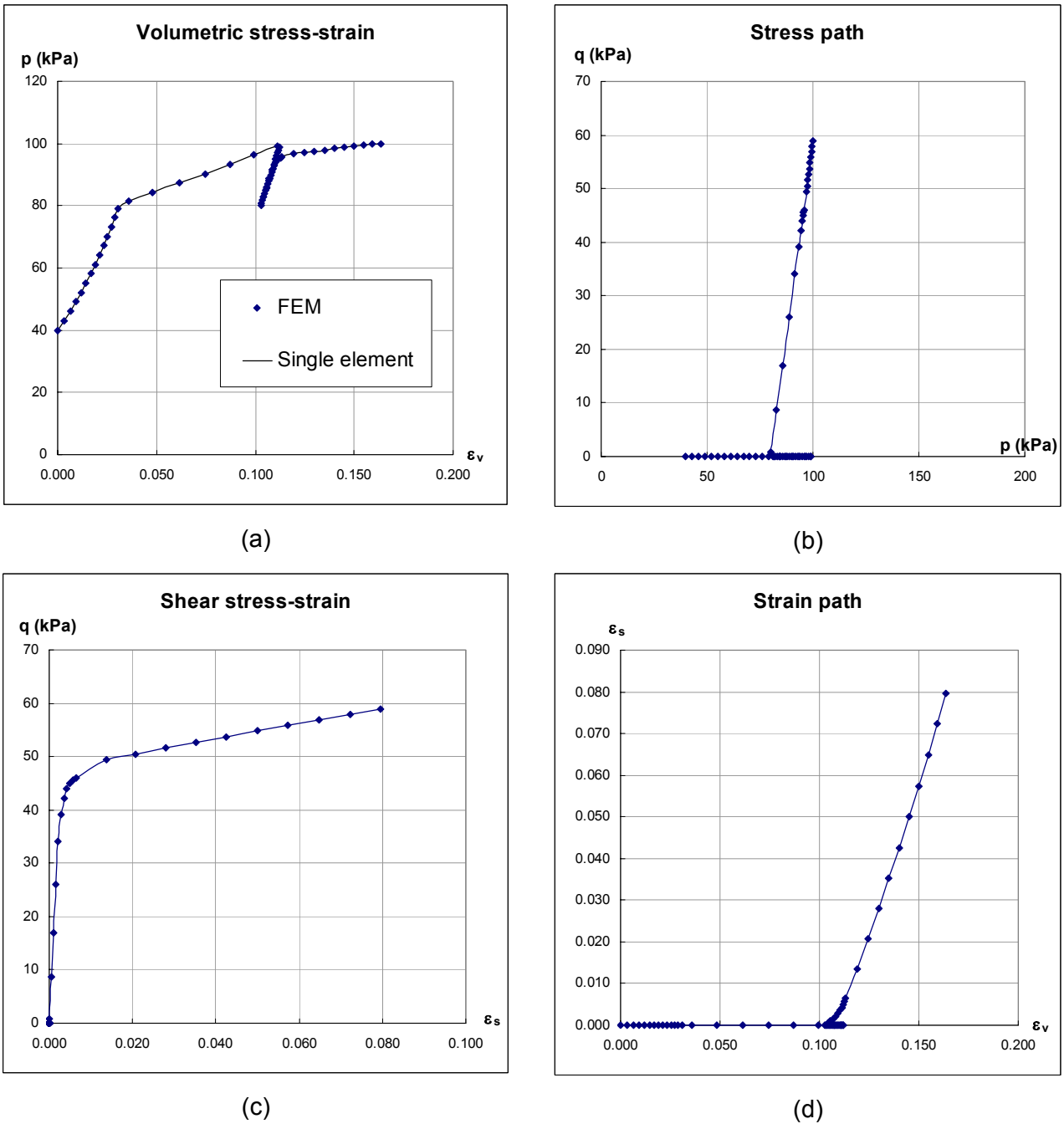

Figure 6.6 Comparison of Finite element and Single element calculations based on the MCC model; (a) Volumetric stress-strain curve, (b) Stress path, (c) Shear stress-strain curve, (d) Strain path.

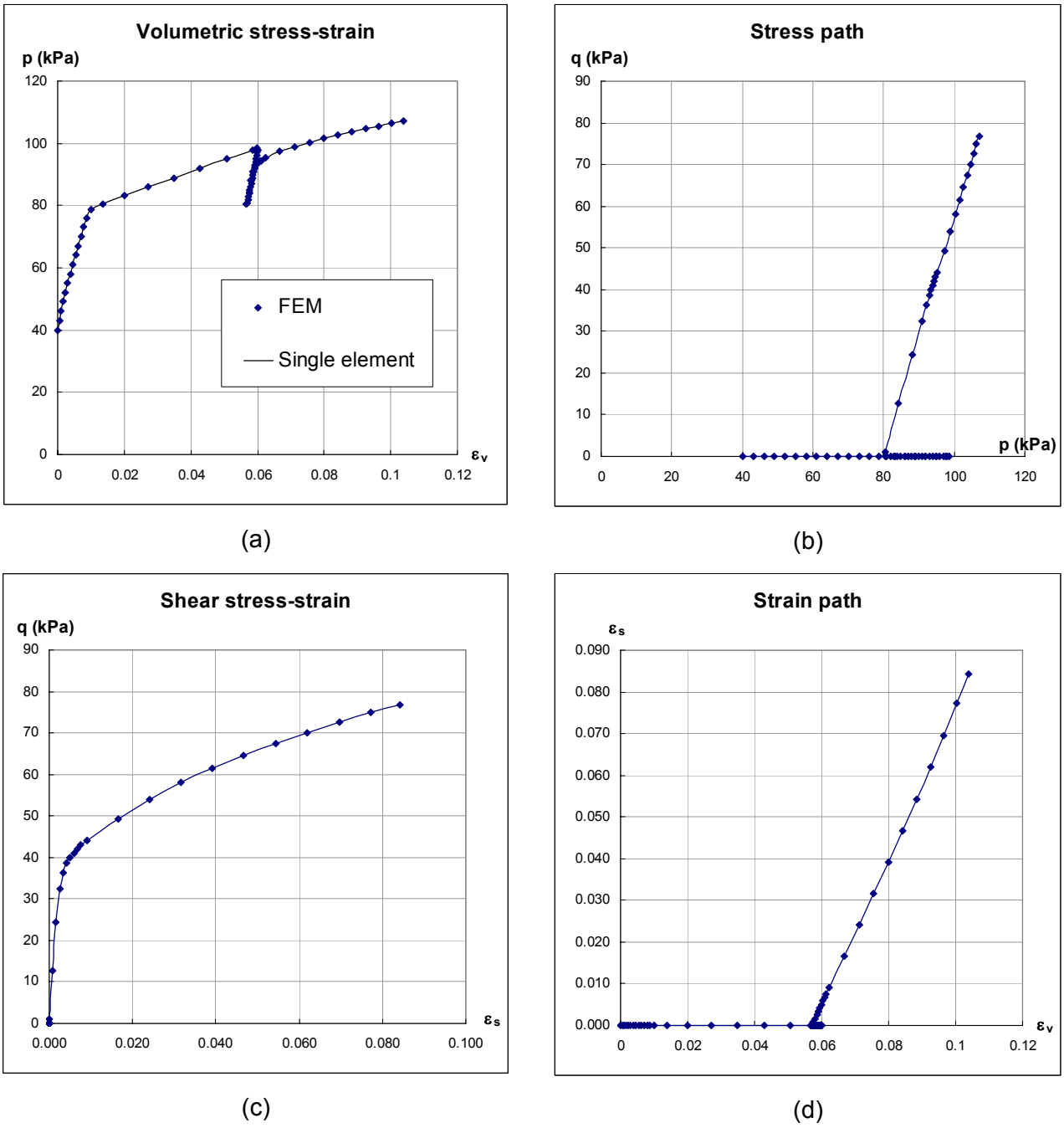

Figure 6.7 Comparison of Finite element and Single element calculations based on the KHMCC model; (a) Volumetric stress-strain curve, (b) Stress path, (c) Shear stress-strain curve, (d) Strain path.

For the rate-dependent calculation of the MCC and KHMCC models, the calculation must be applied with very small increments. This is because instability of the plastic strain will occur when the displacement is applied in large steps. There is no closed form solution for the MCC and KHMCC models unlike the EVM model. The comparison can be made only between the FEM and the single element calculation. The eight elements of the FEM calculations are not significantly different

from the single element. The difference between two calculations is in the order of 10^{-4}kPa (0.0001%) for the stresses and 10^{-7} (0.0002%) for the strains. Figures 6.6 and 6.7 show the results of tests no. 3 and 4 as compared with the single element calculations where the line represents the single element calculation. The data points represents the FEM results which are the average from the Gauss points of the top element. The number of data points plotted is reduced by a factor of 100 and 1000 during the consolidation and shearing stages respectively.

6.9 Conclusion

The models based on triaxial stress-strain parameters are developed from experimental data on Bangkok clay as described in chapter 5. However, implementation in the finite element program OXFEM is required for the generalised models. As a result, this chapter presented the translation of models in the terms of the generalised stress-strain parameters. This procedure needs some mathematical processes and programming. Artificial triaxial tests are analysed to verify the material subroutine and calculation procedure. The computer codes for rate-dependent calculation of the MCC and KHMCC models are presented in Appendix B.

The analyses discovered that the numerical calculations are very robust in the elastic range. The increments in the elastic range can be quite large. After the tests reach yield state the numerical instability may occur, especially in the EVM and MCC model. This comes from a sudden change of the behaviour from the elastic to the plastic region. In the EVM model, the plastic range is unable to be observed by load control because the perfectly plastic behaviour will occur after yield. The calculations are processed using rate-independence. The analysis result is in an acceptable range compared with the elastic solution. For the MCC and KHMCC model, the numerical calculations are carried out using rate-dependence which is able to control the numerical instability. By comparing between single element and FEM analyses, the results found are that the difference is tiny. Thus, this exercise verifies that the subroutine developed can be employed for the geotechnical field problem, which will be discussed in the next chapter.

In addition, the analyses also found that the numerical calculation using displacement control is slightly more robust than load control. Especially in the shearing process where load control is not possible because a large plastic strain will occur when the sample reaches yield. The rate-dependent algorithm with

displacement control will respond giving a smooth stress-strain behaviour, whereas for load control it gives a slight non-smooth stress-strain response. This is because the strain and strain rate are constant at any calculation step of the displacement controlled problem.

Chapter 7
Application to Geotechnical Problems

This chapter presents the application of the finite element method to the analysis of geotechnical construction problems. This exercise applying the finite element method is presented for the purpose of demonstrating the new constitutive model. This is to prove that the newly developed model can be employed in engineering practice as stated in the objectives of the research. Any further advanced analysis such as considering the boundary effect is beyond the scope of the research and will therefore be disregarded.

The construction problems can be categorised into two classes which are equilibrium dominated and deformation compatibility dominated. The former relates to the strength problem for example, shallow foundations and embankment problem. The analysis with the advanced soil model is expected to offer an indifferent strength prediction from the analysis with simple soil model. However, the latter deals with the deformation problem such as earth retaining structures, and tunnelling problems. A better deformation prediction is expected to be generated if the advanced soil model is employed. The construction of a road embankment and tunnelling-induced settlement are selected as two examples for this research.

7.1 Road embankment

Earth embankments are built frequently for highway purposes in Thailand. The subsoil conditions for the road embankment are mainly thick soft clay which is of low strength and high compressibility. The design of road elevations and fill thickness are based on the classical Terzaghi consolidation theory, which employs compression ratio (CR) and recompression ratio (RR) as two key parameters for the prediction of settlement and uses undrained shear strength as a strength parameter.

Embankment geometry is usually simple but, due to the weakness of the subsoil, the embankment can be built only to a height of approximately 3m to 4m. However, higher embankments are regularly needed in lowland area to protect from floods. As a result, special construction methods such as reinforcement with geotextiles and/or staged construction are necessary. In staged construction, the embankment is constructed in stages and after each stage, a consolidated time is

required for dissipation of excess pore water pressures. This process leads to a gain in soil strength of the soft clay.

Highway No. 34 (Bangna-Trad) is one of the most economically important highways, and problems have occurred with excessive settlement caused by the underlying poor compressible subsoil along the route (Figure 7.1). A study of settlement of highway no. 34 is presented by Seah (1998). The highway was initially constructed as a two-lane highway in 1969 with design elevation of 2 to 2.8m (above mean sea level) from chainage 0km to 55km. Ultimately, the highway was upgraded to an eight-lane highway, and some part of roadway was on improved subsoil, using soil cement column ground improvement.

Figure 7.1 Route of Highway No. 34 (Bangna-Trad Road), Seah (1998)

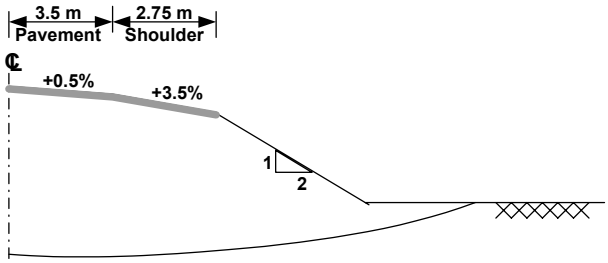

Figure 7.2 Typical Cross section of Highway No. 34, Seah (1998)

7.1.1 Embankment geometry and soil conditions

The construction of Bangna-Trad highway has been documented by the Department of Highway Thailand since 1980. The typical highway cross section is shown in Figure 7.2. However, the historical record provides only a single settlement point at any section of road embankment. The settlement profiles are unavailable for comparison with settlement analyses. The comparison can be only made using the maximum settlement at the centre of the road embankment.

The original ground conditions and consolidation characteristics before construction are represented by Seah (1998). The subsoil condition is composed of a thick layer of very soft Bangkok clay, together with a sand layer underneath. The

thickness of the compressible clay layer varies from 14 to 24m (average 20m) as shown in Figure 7.3. It can be assumed that the sand layer is rigid and a drainage boundary. The soft clays have not commonly experienced greater vertical stresses in the past. Consequently, they are normally or very lightly overconsolidated. The typical unit weight of Bangkok soft clay is estimated to be 20kN/m^3 (this value is quite high for a normally consolidated clay; however, it is for the simplicity). However, there is no recorded data on the embankment material. The embankment fill is modelled in the same manner as the soft ground. The unit weight of embankment fill is estimated to be 20kN/m^3.

7.1.2 Data collection

The measurement of settlement data along the outbound highway has been recorded since 1969 without any ground improvement. After that, this route was rehabilitated to raise the pavement in 1981, because of the substantial settlement over ten years. The settlement profile along the 55km recorded in 1979 is shown in Figure 7.4. These numbers include the settlement due to land subsidence or ground water pumping. The land subsidence problem has been a major environmental issue in Bangkok since the 1970s. The Asian Institute of Technology (AIT) and the Department Mineral Resources (DMR) have been conducting research and monitoring programmes to study the effect of pumping on the subground. The typical piezometric pressure profile in Bangkok generated by deep pumping is illustrated in Figure 7.5. The rate of settlement due to the deep pumping in 1979 and 1997 obtained from AIT's reports is around 3 to 5cm per year. Therefore, the settlement due to only land subsidence over ten years is approximately 30 to 50cm. This is a significant result which affects the settlement prediction. Thus, the model predictions should include the effect of land subsidence before being compared with the field data.

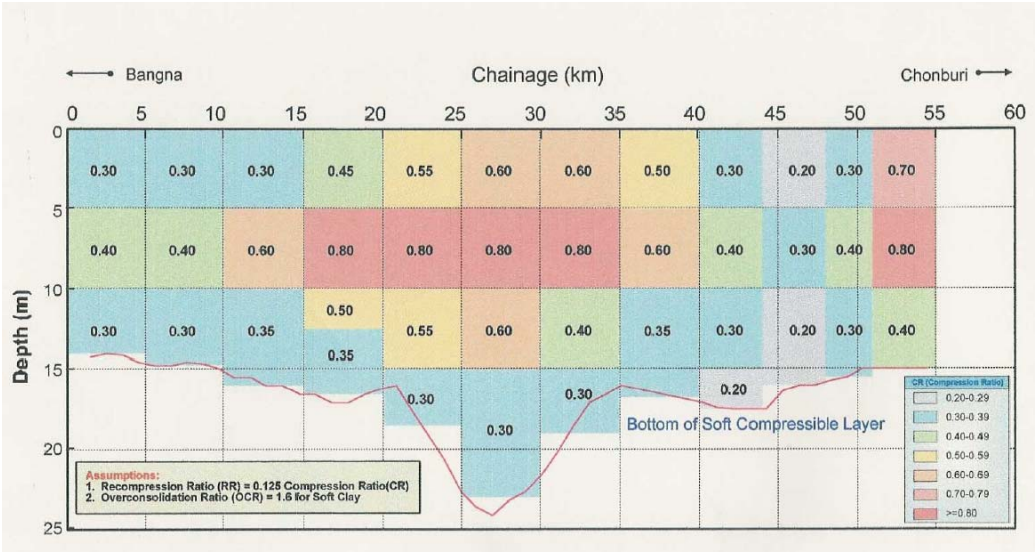

Figure 7.3 Thickness of compressible clay layer along Bangna-Trad highway, Seah (1998)

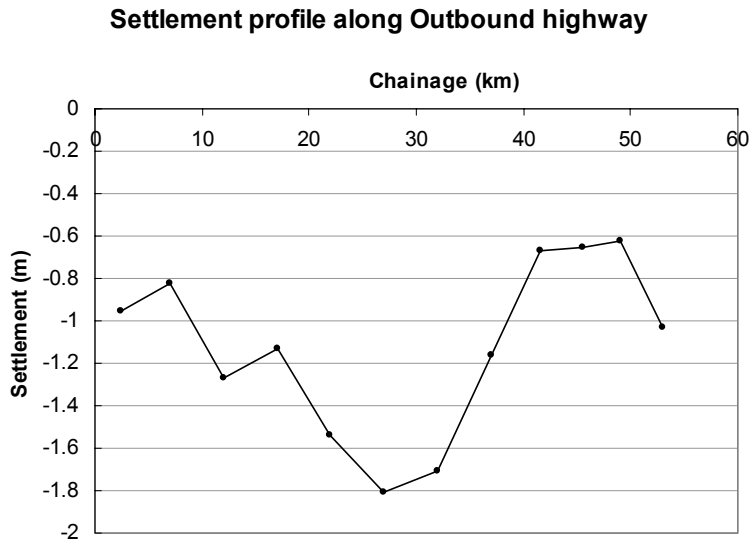

Figure 7.4 Settlement profile along outbound highway in 1979 (10 years after construction), Seah (1998)

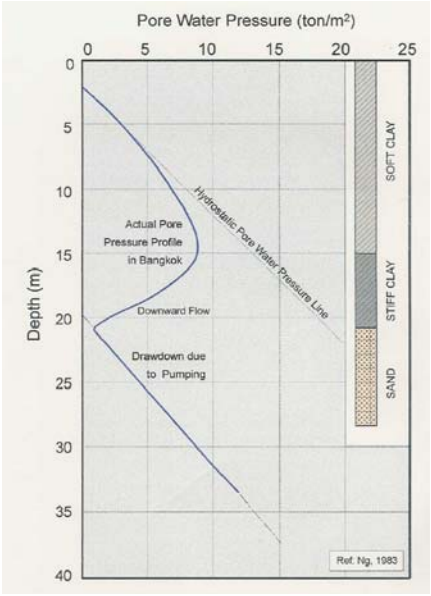

Figure 7.5 Typical piezometric pressure profile in Bangkok due to deep pumping, Seah (1998)

7.1.3 Finite element mesh

As the soft clay is weak, the road embankment is normally built to a height of approximately 2m to 5m. For this research, the height is assumed as 3.5m. The mesh is generated by using the commercial finite element program I-DEAS. The finite element mesh used for the analysis is shown in Figure 7.6. The problem is analysed in two-dimensional plane strain condition, which consists of 449 six noded triangular elements. Due to the symmetry of problem geometry, the finite element mesh can be

reduced by half. The block of ground analysed is 20m thick and 30m wide. It is assumed that there is a 10kPa surcharge applied on the ground surface (representing made ground, vegetation etc.).

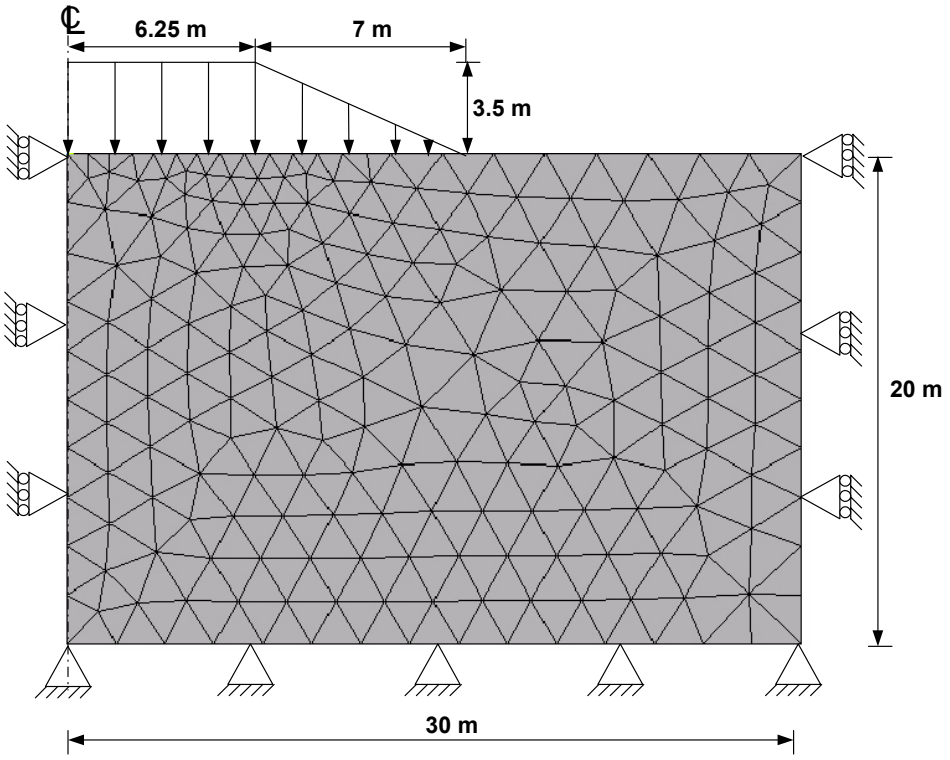

Figure 7.6 Finite Element Mesh for Embankment of Highway No. 34

7.1.4 Constitutive models

The analyses are carried out using three constitutive models; elastic Von Mises (EVM), modified Cam-clay (MCC) and kinematic hardening modified Cam-clay (KHMCC) model. The EVM model parameters are the Elastic shear modulus (G), Poisson's ratio (υ), and Undrained shear strength (s_u). In the case of purely elastic undrained analysis (EVM-1), the υ value is set to be 0.499 rather than 0.5 as the infinite value of bulk modulus will cause a numerical problem, and s_u is set to be very high (10,000kPa). The elastic-plastic undrained analysis (EVM-2) is also considered by setting the value of s_u to be the undrained shear strength soft clay (10kPa). On the other hand, for drained analysis (EVM-3), the υ value is assumed to be 0.2 which is reasonable for soft clay and the value of s_u is set to be high because the purely elastic behaviour is intended in this analysis. The MCC and KHMCC model parameters use almost the same values that are evaluated by parametric study with the experimental data in Table 5.1(a) and 5.1(b), the bulk and shear modulus, however, are modified to

correspond more closely to the field data. A summary of model parameters are shown in Table 7.1 including their physical meanings.

Table 7.1 Input parameters and their physical meaning for road embankment and homogenous soil layering case of tunnelling analyses

FE Run	Model	Parameter	Value	Physical meaning
EM1, TL1	**EVM-1 (Elastic Undrained analysis)**	G	7500 (kPa)	Linear elastic shear modulus
		υ	0.499	Undrained Poisson's ratio
		s_u	10000 (kPa)	Assumed very high value for purely elastic behaviour
EM2, TL2	**EVM-2 (Undrained analysis)**	G	7500 (kPa)	Linear elastic shear modulus
		υ	0.499	Undrained Poisson's ratio
		s_u	10 (kPa)	Undrained shear strength
EM3, TL3, TL6	**EVM-3 (Elastic Drained analysis)**	G	7500 (kPa)	Linear elastic shear modulus
		υ	0.2	Drained Poisson's ratio
		s_u	10000 (kPa)	Assumed very high value for purely elastic behaviour
EM4, EM6, EM8, EM10, TL4, TL7	**MCC**	κ^*	0.05	Slope of swelling consolidation line on log v-log p plot
		λ^*	0.4	Slope of virgin consolidation line on log v-log p plot
		g_x	80	Elastic shear modulus gradient
		M	0.9	Slope of critical state line in q-p plane
EM5, EM7, EM9, EM11, TL5, TL8	**KHMCC**	K	4000 (kPa)	Initial bulk modulus
		a_p	2.0	Non-linear kinematic hardening parameter for p-direction
		b_p	2.5	
		r	0.8	
		g_x	50	Elastic shear modulus gradient
		a_q	3.5	Non-linear kinematic hardening parameter for q-direction
		b_q	2.5	
		M	0.9	Slope of critical state line in q-p plane

7.1.5 Analysis results

The analyses are conducted under plane strain conditions and can be divided into two calculation stages. Firstly, the initial stress, stress history, and self weight of the ground are set up. In addition, the ground is loaded by a 10kN/m^2 surcharge, approximately equivalent to half a metre of soil in the first stage. This surcharge can also eliminate the numerical problem due to the zero stresses at the ground surface elements. The initial effective stress condition is assumed as shown in Figure 7.7(a). After applying the initial conditions; the 3.5m of embankment is applied by means of the vertical distributed nodal point load calculated by the virtual work principle. The effect of the lateral load due to the triangular shape of the embankment is considered later in the analysis. The embankment construction is assumed as a ten staged

construction is which ten steps of calculation is applied for the loading stage. Descriptions of the road embankment analyses are summarised in Table 7.2.

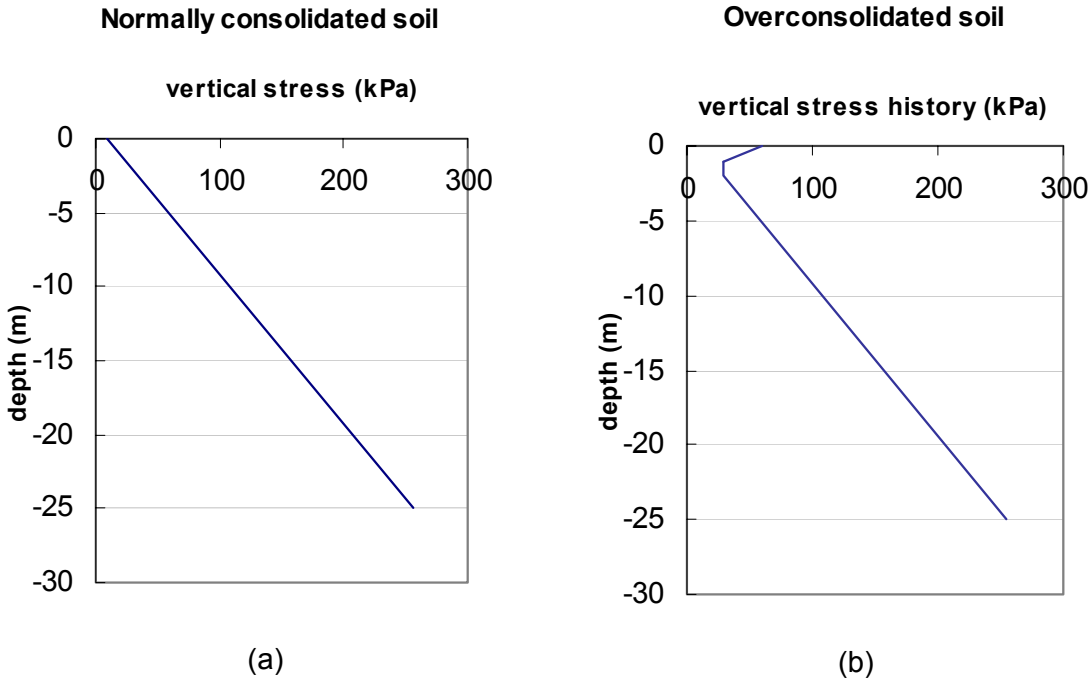

(a) (b)

Figure 7.7 Distribution of vertical stress with depth; (a) in-situ vertical stress for overconsolidated soil and normally consolidated soil. (b) maximum past vertical stress for overconsolidated soil

Table 7.2 Description of finite element analyses of road embankment

FE Run	Model	Analysis type	K_0	Surface crust	Horizontal load	Maximum settlement (cm)
EM1	EVM-1	Undrained	1	-	-	2.06
EM2	EVM-2	Undrained	1	-	-	10.83
EM3	EVM-3	Drained	1	-	-	6.10
EM4	MCC	Drained	1	-	-	32.77
EM5	KHMCC	Drained	1	-	-	20.81
EM6	MCC	Drained	0.7	-	-	42.84
EM7	KHMCC	Drained	0.7	-	-	24.19
EM8	MCC	Drained	1	Yes	-	32.14
EM9	KHMCC	Drained	1	Yes	-	20.43
EM10	MCC	Drained	1	-	Yes	29.74
EM11	KHMCC	Drained	1	-	Yes	19.67

The ground settlement profiles for analyses EM1 to EM5 are shown in Figure 7.8. The analyses EM1 and EM3 offer only purely elastic stiffness when the soil

elements do not reach yield. Since the yield stress is set at a very high value the settlement profile show less value than the other profiles. The undrained analysis EM1 shows a small heave outside the embankment. The analysis EM2 with the input being true undrained shear strength gives the large settlement under the embankment and also creates heave outside the embankment. Only analyses EM1 and EM2 show heave outside the embankment because in the undrained analysis the total volume of the ground block must be unchangeable. The heave tries to compensate the volume of trough under the embankment. Analysis EM4 with the MCC model provides the maximum settlement profile due to the sudden change in behaviour from elastic to plastic. Since the soil elements underneath the embankment are subjected to the huge embankment load, the plastic strain dominates. The lower value of plastic stiffness of the MCC model produces the larger plastic strain. The settlement that comes from the accumulation of the vertical displacement of all the elements underneath the embankment is also deeper in the case of the MCC model. In contrast, the shallower settlement trough is expected for the variational plastic stiffness value in the case of the KHMCC model.

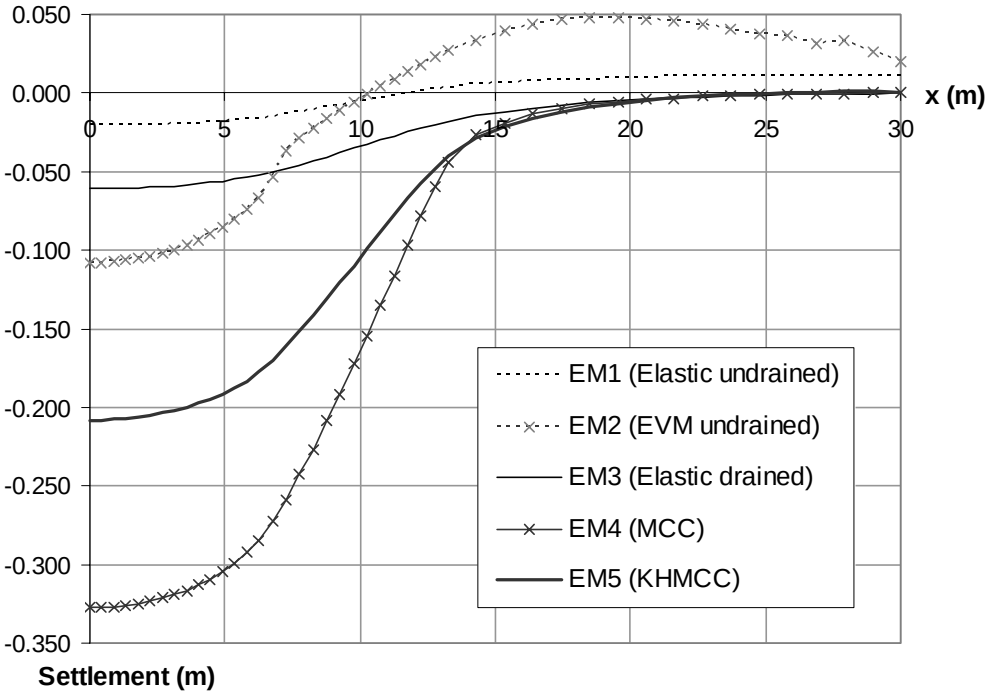

Figure 7.8 Predictions of the settlement profile after the embankment construction

Note that Figure 7.8 implies that right-hand side boundary of the 30m wide ground mesh is not close enough to the embankment to affect the analysis results

except for the analysis EM2 which uses a very low input value of undrained shear strength (10kN/m^2).

The stresses are controlled by the initial ground conditions and applied nodal loads. Therefore, they do not vary significantly in each case from analyses EM1 to EM5. The typical horizontal (σ'_h) and vertical (σ'_v) stress contours selected from analysis EM4 with the MCC model are in the ranges of -200 to 5kPa and -220 to -25kPa respectively as shown in Figures 7.9(a) and (b), where the negative sign convention indicates compression. The strains are controlled by the constitutive model and the analysis condition (i.e. drained or undrained). The horizontal (ε_h) and vertical (ε_v) strain contours of analysis EM4 are in the range of -0.02 to 0.02 and -0.06 to 0.01 respectively as shown in Figures 7.9(c) and (d). The patterns of strain distribution for analyses EM4 and EM5 respectively, using the MCC and KHMCC models, are similar except for the contour range of -0.02 to 0.01 for the KHMCC model as shown in Figure 7.10(d). This is because the analysis EM4 shows a deeper settlement than EM5 and hence higher plastic strains are expected for the lower plastic stiffness. The analyses EM1 and EM3 with purely elastic responses exhibit a unique pattern of strain distribution. The maximum compressive strain of analysis EM3 however is two times larger than analysis EM1 due to the difference between undrained and drained analysis as shown in Figures 7.10(a) and (c). For the undrained analysis EM2 with low s_u, the strain distribution takes no identifiable form: the plot is scattered, however it can be represented as a slip line under the embankment (see Figures 7.10 (b) and 7.11(d)). This is because the stress amplitude of almost all elements reaches yield as shown in Figure 7.11(b). The stress amplitude ($(\sigma'_{\max} - \sigma'_{\min})/2$) and strain amplitude ($(\varepsilon_{\max} - \varepsilon_{\min})/2$) values can imply the state of stress and strain in the yield condition. Figures 7.11(a) and (c) show the typical stress and strain amplitude contours of the embankment, which are selected from analysis EM4.

Figure 7.12(a) shows the nodal force vector for all nodal points in the problem. The nodal force is determined by the boundary conditions and ground conditions. The force on the surface boundary corresponds to the applied surcharge load from the embankment. Both sides of the boundaries correspond to the roller support condition (fixed horizontal movement) and the nodal forces distribute in a triangular pattern which corresponds to the horizontal stress. The nodal forces at the bottom boundary

correspond to the total reaction force due to the gravity load and the applied surcharge embankment. The nodal displacement vectors for all nodal points of analyses EM4, EM2 and EM3 are shown in Figures 7.12(b), (c) and (d) respectively. For undrained analysis EM2 (Figure 7.12(c)), all displacement vectors move outward due to the embankment surcharge as expected. On the other hand, all displacements for drained analyses EM4 and EM3 (Figures 7.12(b) and (d)) surprisingly move inward due to the embankment surcharge. There are still no obvious evidence that shows this phenomenon occurring for the drained case. The critical process of embankments on soft clay is during the construction, which must be analysed as undrained or partially drained, rather than drained condition. Few data exist for drained settlement of embankment on soft clays.

Analyses EM6 and EM7 consider the effect of effective stress ratio (K_0). In analyses EM1 to EM5, an assumption of $K_0 = 1$ is made. However, the actual ground does not have isotropic stress conditions. Several experimental data from AIT such as Kim (1991) and Khan (1999) conclude that the value of K_0 is less than unity and around 0.6 to 0.8. Thus, in analysis EM6 and EM7, $K_0 = 0.7$ is assumed.

In addition, the most critical issue for embankments on soft clay is the strength of the clay. The top soil layer normally has a high strength and OCR value due to its stress history. The crust can have a marked effect on the behaviour of an embankment. To illustrate the effect of the surface crust, analyses EM8 and EM9 with a distribution of OCR as shown in Figure 7.7 have been performed. The comparisons of the results after considering the effect of K_0 and the effect of the surface crust are shown in Figure 7.13.

The effect of surface crust makes the settlement profile slightly shallower as shown in Figure 7.13. This stress history effect can be modelled by specifying the maximum past stress (see input to OXFEM in appendix A). In contrast, the effect of K_0 makes the settlement profile deeper, when reducing the K_0 value from 1.00 to 0.70.

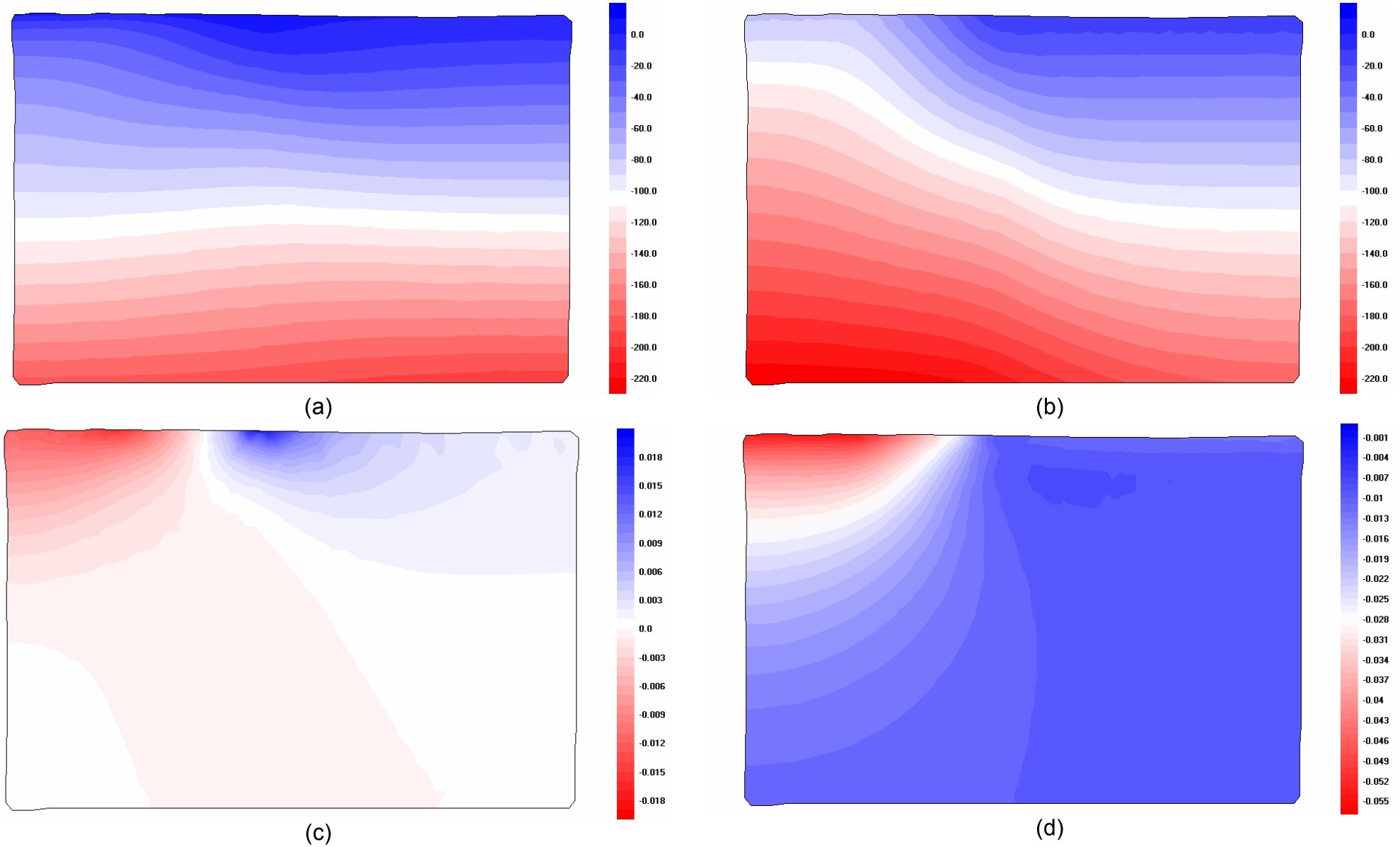

Fig 7.9 The stress and strain contours of the analysis EM4 with MCC model

(a) horizontal stress contour (σ'_h , kPa); (b) vertical stress contour (σ'_v , kPa);(c) horizontal strain contour (ε_h , -); (d) vertical strain contour (ε_v , -)

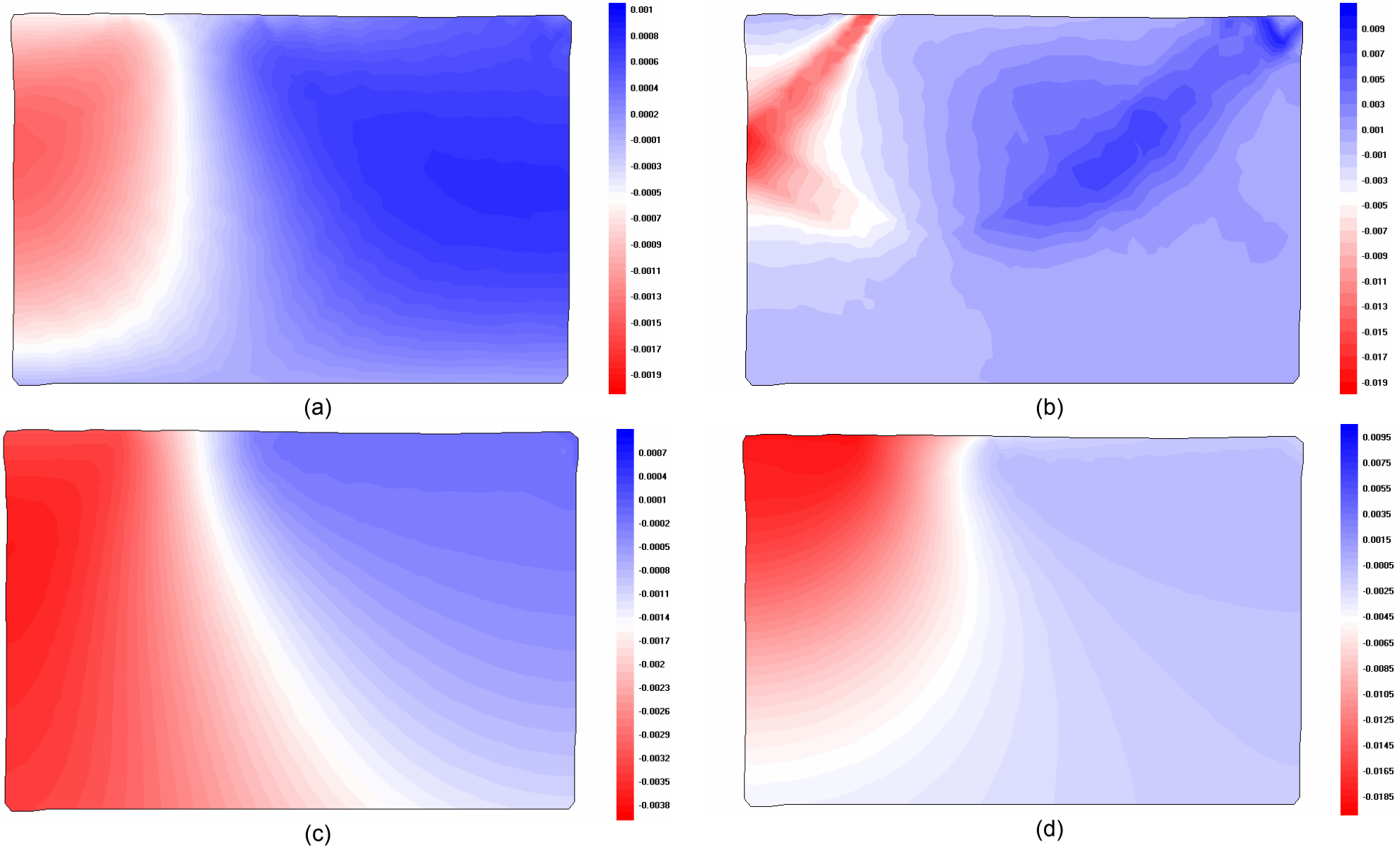

Fig 7.10 The vertical strain contour (ε_v , -) of the analyses EM1, EM2, EM3 and EM5
(a) EM1; (b) EM2; (c) EM3; (d) EM5

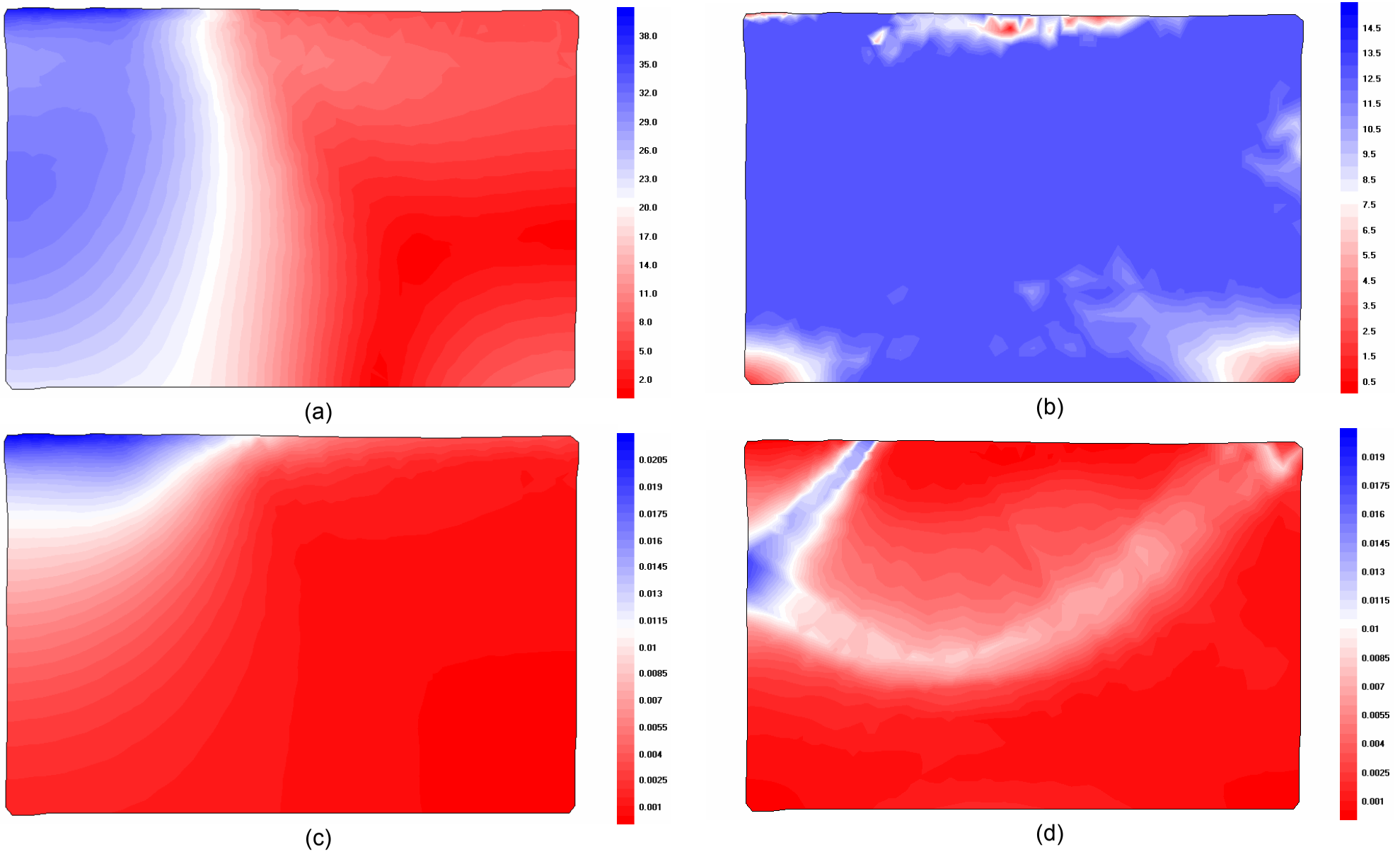

Fig 7.11 The stress and strain amplitude contour of the analyses EM4 and EM2
(a) and (c) are the stress amplitude of EM4 and EM2 respectively, kPa; (b) and (d) are the strain amplitude of EM4 and EM2 respectively

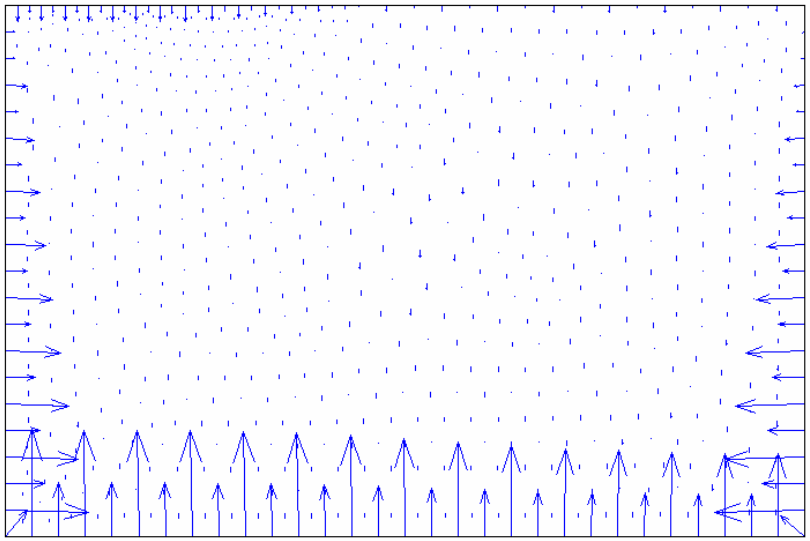

(a)

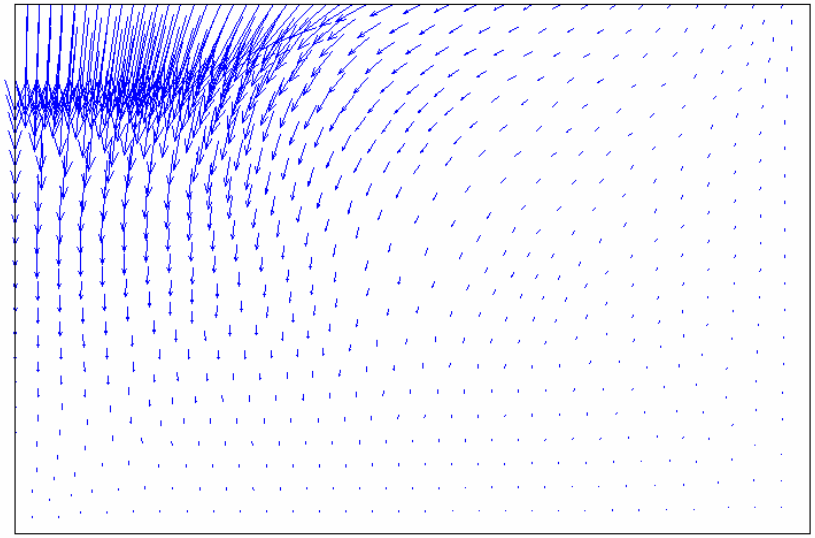

(b)

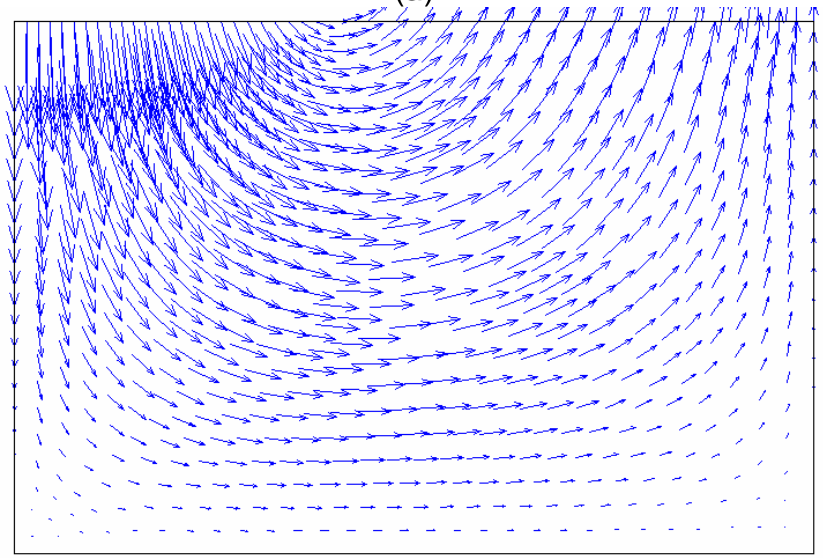

(c)

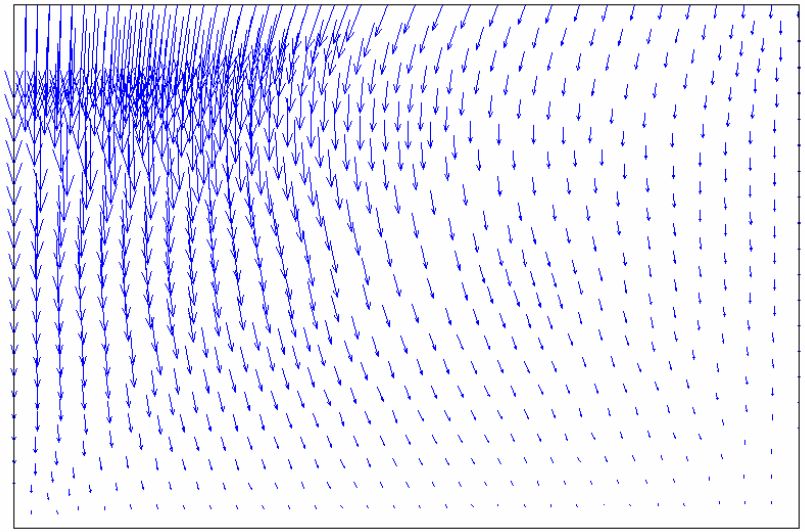

(d)

Fig 7.12 The nodal force and displacement vector of the analyses EM2, EM3, EM4
(a) The nodal force vector of EM4; (b), (c) and (d) are the nodal displacement vector of EM4, EM2 and EM3 respectively

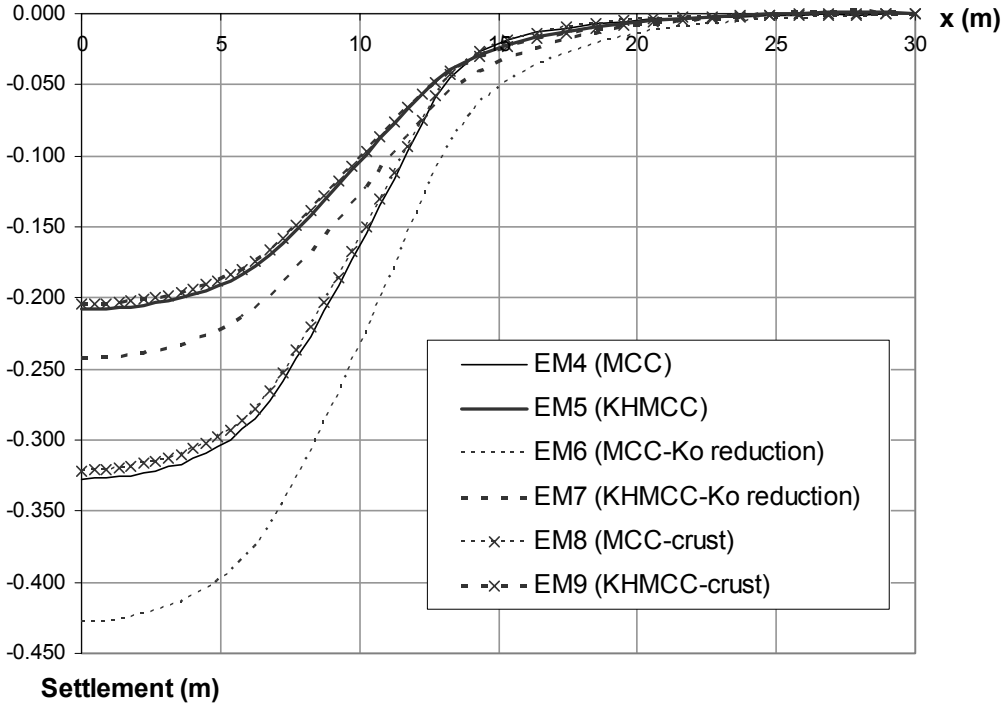

Figure 7.13 Predictions of the settlement profile with effect of the surface crust and stress ratio (K_0)

The replacement of the soil embankment by a vertical nodal load can accurately approximate a uniform wide embankment. The triangular embankment should be replaced by vertical and horizontal distributed nodal load. However, the horizontal load is relatively small compared with the whole size of the embankment. The approximations of embankment nodal loads in the analyses are displayed in Figures 7.14(a) and (b). The evaluation of horizontal loads starts from the definition of active pressure: $\sigma_a = K_a \sigma_v$ and then calculates the active force: $P_a = 1/2\, K_a \sigma_v h$. The summation of all horizontal nodal loads must be equal $P_a = 1/2\, K_a \sigma_v h$ and this amount has to triangularly distribute along the distance L as shown in Figure 7.14(c). The analysis results of EM10 and EM11 considering the effect of horizontal nodal load are presented in Figure 7.15. As the displacement vector moves inward, the lateral load on the opposite side will cancel the displacement vector. Thus, the lateral load makes the trough slightly shallower and wider.

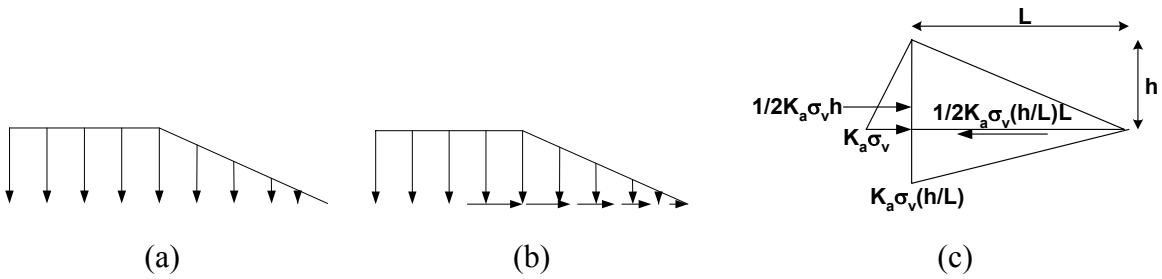

Figure 7.14 Equivalent nodal force of soil embankment load
(a) Vertical nodal load; (b) Effect of lateral nodal load; (c) Estimation of lateral nodal load

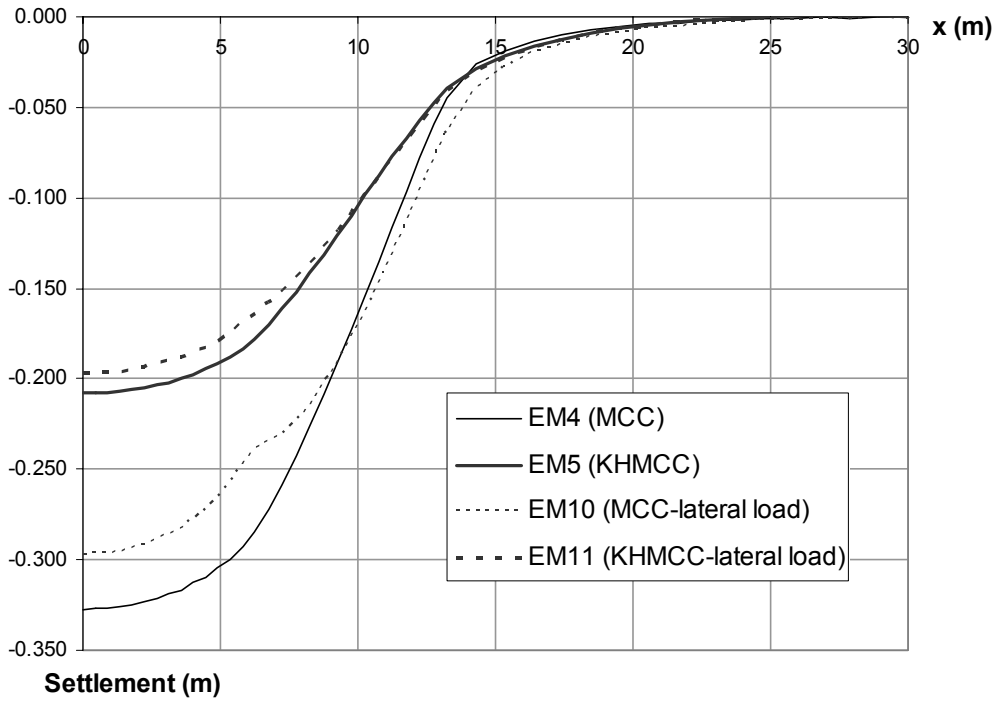

Figure 7.15 Predictions of the settlement profile with effect of lateral nodal load

Figure 7.16(a) presents the effect of the horizontal shear nodal force under the triangular embankment. The horizontal shear force tries to drag the horizontal displacement in the outward direction from the embankment. This leads to the reduction of the vertical settlement and can be illustrated by the displacement vector as shown in Figure 7.16(b).

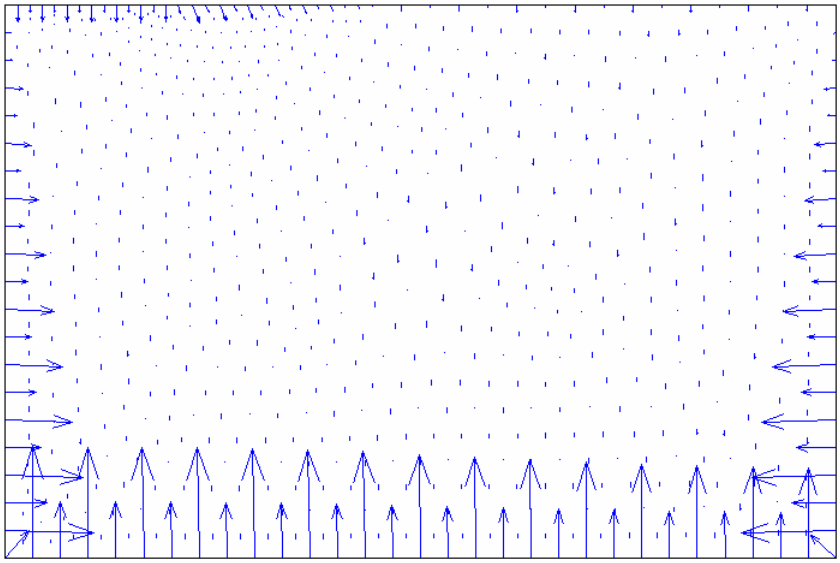

(a)

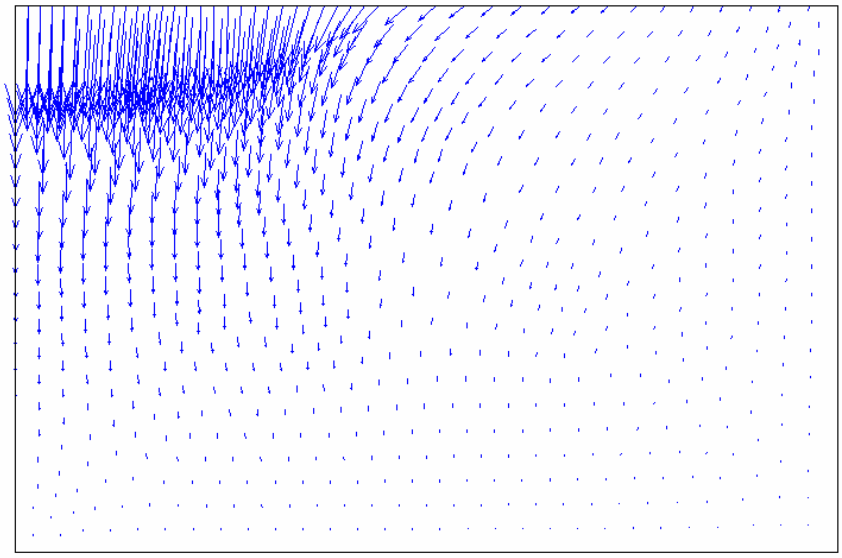

(b)

Figure 7.16 The nodal force and displacement vector of the analyses EM10
(a) The nodal force vector of EM10; (b) The nodal displacement vector of EM10

7.2 Tunnelling

The analysis of tunnels using the finite element method is commonly used in practical design. In the conventional designs, the load characteristics are determined by a technique which is mostly elastic and movements by a technique which is principally empirical. Nevertheless, there two techniques are not linked. In order to progress the understanding of design methods for building interaction with tunnelling-induced settlements, much research on tunnelling has been conducted such as Lee and Rowe (1989) and Addenbrooke *et al.* (1997).

The Civil Engineering Research Group at Oxford University has also been undertaken the tunnelling research since 1993. A number of two-dimensional finite element analyses of a building and ground were carried out by Liu (1997). A nested yield surface model offering a variation of stiffness was implemented in the finite element for this study. The other factors affecting the tunnelling-induced settlement such as percentage of volume loss, in-situ stress ratio ($K = \sigma_h / \sigma_v$), density of soil, choice of external fixity to lining, and modification of parameters for the nested yield surface model were further studied by Bloodworth (2002).

For three-dimensional numerical modelling, the tunnelling processes for assessment of damage to buildings were analysed by Augarde (1997). Then, three-dimensional finite element modelling of lined tunnelling problems was performed by Augarde and Burd (2001). The choice of structural liner was studied using two different elements to model the tunnel lining.

As stated in the introduction, this tunnelling problem is used to demonstrate the new constitutive model. The analysis procedure here is performed by following the standard approach from previous research by Bloodworth (2002).

7.2.1 Empirical prediction of tunnelling-induced settlement

An empirical formulation for predicting the short-term transverse settlement trough could be approximated by a normal distribution or Gaussian curve. The equation for the assumed trough shape is:

$$S = S_{\max} \cdot \exp\left(-\frac{x^2}{2i^2} \right) \tag{7.1}$$

where $S_{\max}$ is the maximum settlement above the tunnel axis and x is the transverse distance from the tunnel axis. The width of the settlement trough is defined by the

parameter i (distance from the axis to the inflexion point of Gaussian curve) which varies according to the depth of the tunnel and the nature of the ground. O'Reilly and New (1991) expressed the trough width parameter in the form of $i = K \cdot z$, where z is the depth of the tunnel axis below ground level. For cohesive soil K is normally in the range of 0.4 to 0.5.

Another parameter to control the amount of settlement is the volume loss (V_L). The volume loss can be estimated by using the volume of the settlement trough (V_s) or the displacement of tunnel lining after excavation. For the undrained analysis, the volume losses calculated from both definitions must be the same. Integrating equation 7.1 to evaluate the volume of the trough, the expression becomes $V_s = \sqrt{2\pi} \cdot iS_{\max}$.

7.2.2 Model ground conditions and input soil properties

The numerical research and design on tunnelling, especially in soft clay are widely studied in Thailand due to the fact that a large tunnel project for a subway system is currently under construction by the Metropolitan Rapid Transit Authority (MRTA). The typical geological condition of MRTA project is displayed in Figure 7.17(a). The tunnel mainly involves excavation in stiff to very stiff clay using an Earth Pressure Balance shield (EPB). The dimension of the shield machine is 6.45m in diameter and 6m in length and the cutting speed can reach to 100mm/min.

Lin *et al.* (2002) has been studied three-dimensional deformation due to use of EPB shield tunnelling in Bangkok subsoil. Additionally, this analysis presents the field instrumented data of the MRT Blue Line Subway tunnel (RE-5T-06). The observations of settlement trough at various depths for various stages of tunnel advancement are recorded. The plane strain condition can be assumed when the tunnel goes far enough through the observed station. The tunnel lies on the dense sand layer, which is assumed to be rigid and a drainage boundary for analysis as shown in Figure 7.17(b).

The two-dimensional plane strain condition is assumed for the analysis of MRTA project, as shown in Figure 7.17(b). In general, the soils have much stiffer behaviour when further soils have been deposited on the top. The first 2.5m is made ground, and can be assumed as a crust. However, this crust has not induced much effect on the settlement trough, so the high OCR value of the top soil layer can be

disregarded. Therefore, the 14m top of Soft Clay to Medium Clay can be modelled as normally or very lightly overconsolidated. Next, the second layer of Stiff Clay to Very Stiff Clay can be assumed for the rest of ground between 14m to 25m. The typical unit weight of Bangkok soft clay is still estimated to be 20kN/m^3 for all layers and the initial stress and stress history can also be assumed as in Figure 7.12(a).

The typical construction design and analysis in Bangkok assumes the first dense sand layer as a rigid layer. This is due to the fact that the engineering properties such as compressibility, strength and drainage are distinctively different from the adjacent clay layers. The analysis here therefore approximates the first dense sand as a rigid foundation as shown in Figure 7.17(b).

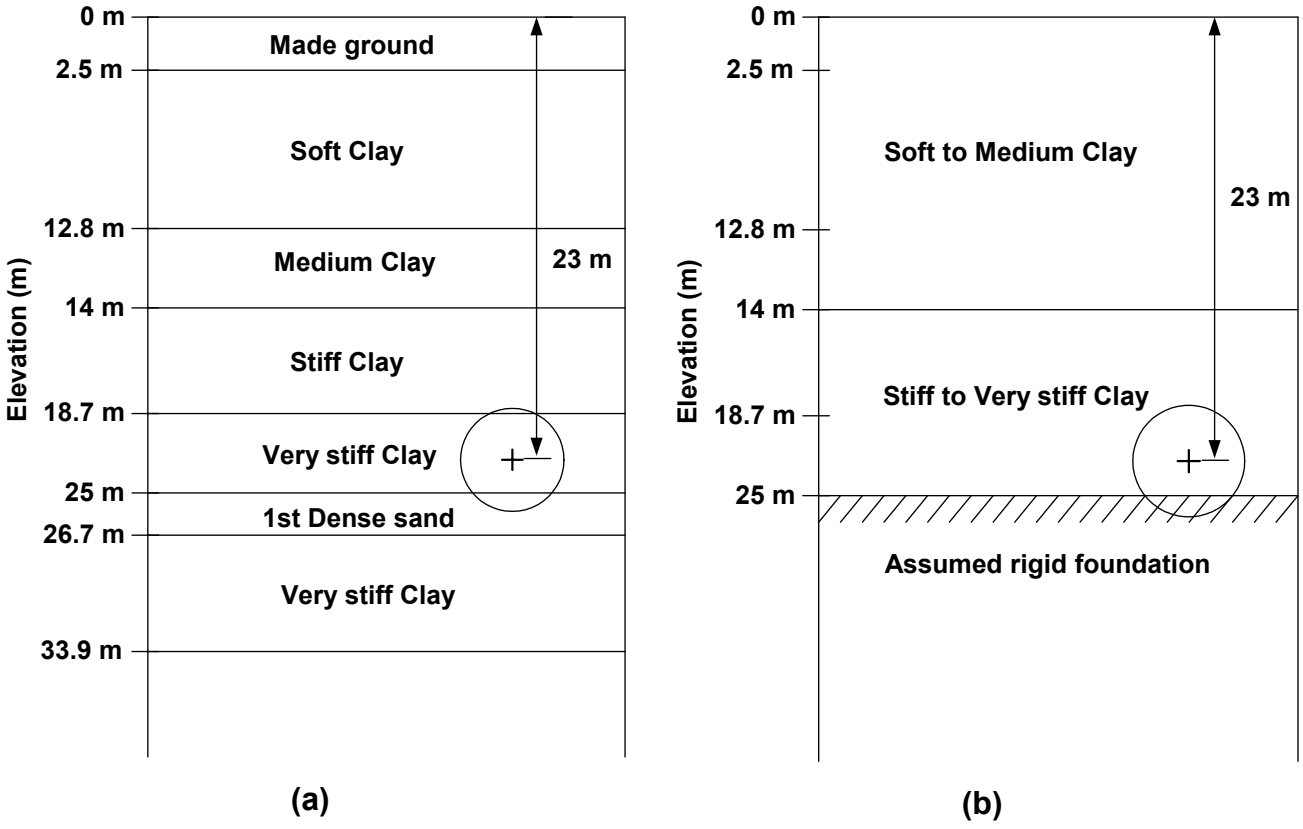

Figure 7.17 (a) Typical geological condition of Metropolitan Rapid Transit Authority (MRTA) project at Bangkok Thailand; (b) Assumed ground condition for analysis of MRTA project, Lin *et. al* (2002)

7.2.3 Model of lining

In order to model the concrete lining for the MRTA project, there are several alternatives to model the lining; both in terms of the liner structures and constitutive laws. In Augarde and Burd (2001), a comparison between the linings modelled by shell elements and continuum elements was made. The paper reported that the liner

behaviour depends on the stiffness ratio between soil and liner (E_{soil}/E_{liner}). For small values of this stiffness ratio, the liner behaves as a stiff tube and displacements are small. For the larger values of the stiffness ratio, the liner response is more flexible and displacements are larger. In addition, the paper noted that the shell element formulations do not exhibit flexural behaviour that is excessively stiff (called over-stiff).

In this research, the liner structural elements use 16 six-noded continuum elements with an aspect ratio (thickness/radius) of 0.1. The elastic Von Mises (EVM) constitutive law is selected for modelling of concrete lining. The concrete properties were assumed as follows: Young's modulus E = 24GPa, Poisson's ratio υ = 0.2, and compressive strength f_c' = 30MPa. These properties can be converted to the EVM's parameters where shear modulus G = 10GPa, and s_u =15MPa. The liner behaves as a flexible liner according to Augarde and Burd (2001). This is because the stiffness ratio between soil and liner (E_{soil}/E_{liner}) is around 0.3 to 0.5.

7.2.4 Finite element mesh

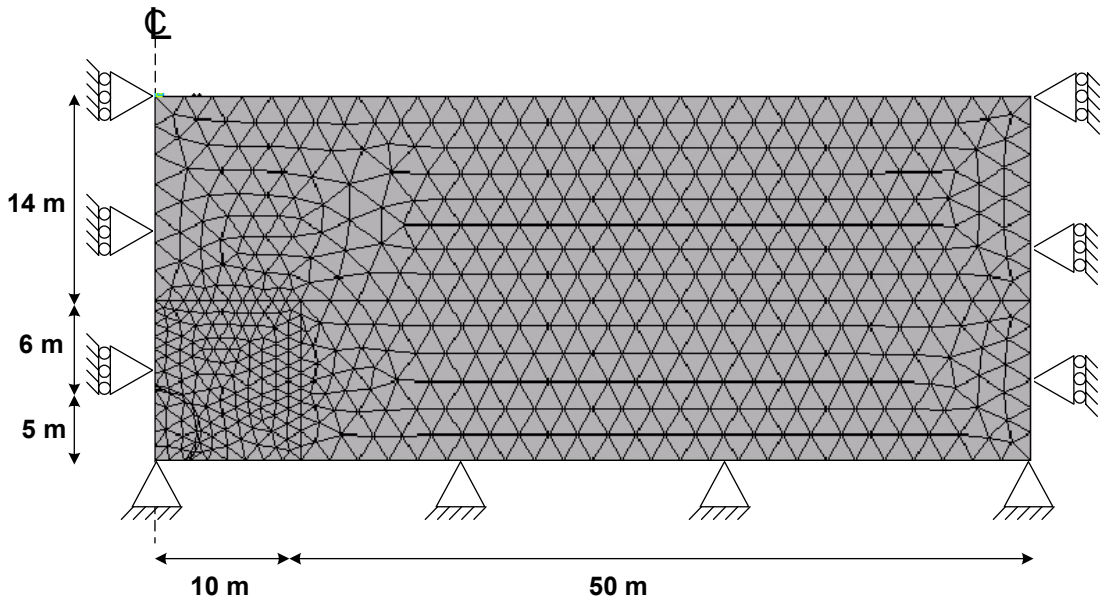

(a)

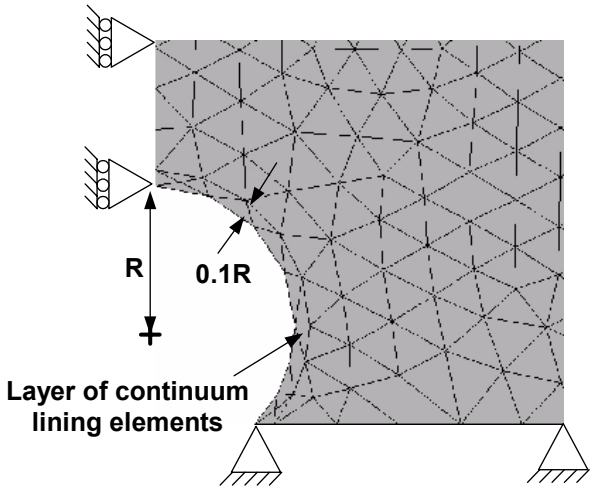

(b)

Figure 7.18 (a) Finite element mesh for MRTA project; (b) Tunnel lining details

The mesh for tunnel problem is generated by using the commercial finite element program I-DEAS. In this study, the tunnel problem is simulated as a two-dimensional plane strain problem with 1105 six-noded triangular elements. By taking advantage of the symmetry of the problem one can reduce the amount of calculation by half. The boundary conditions are assumed as roller supports for the side and fixed supports for the bottom. The finite element mesh for the MRTA project is presented in Figure 7.18(a). Moreover, the detail of tunnel lining mesh is shown in Figure 7.18(b).

7.2.5 Choice of constitutive model

The analyses of the tunnel problem have been carried out using several advanced soil models. The models are generally claimed their own advantages for prediction of the settlement trough due to tunnel excavation. The simplest linear elasticity model is still used to analyses the tunnel problem; however, some modifications have been added such as anisotropic or nonlinear elasticity, Addenbrooke *et al*. (1997). The results of elastic analyses indicate that the settlement profile is too shallow and too wide when being compared with field data. Linear isotropic elasticity predicts a profile of the wrong shape. Linear anisotropic elasticity offers a better shape of the settlement profiles. However, it does not considerably improve the prediction. Nonlinear elasticity provides a transition of stiffness; however, the unloading stiffness is still based on the exact loading curve which is in the wrong direction. To provide this, the plasticity models are recommended.

For plasticity models, several elastic perfectly plastic soil models have been proposed. For instance Von Mises, Mohr-Coulomb, Drucker-Prager (1952) and Matsuoka-Nakai (1974). However, the critical state model known as the MCC model is also used. These models offer the elastic behavior solely within the yield surface. Thus, using them to predict the settlement may not be correct, especially for overconsolidated soils. Several advanced models such as the Bubble model, (Al-Tabbaa and Wood, 1987) and MIT-E3 model, (Whittle, 1993) are still difficult to use according to the complication of their expressions, which may not be implemented in numerical code easily.

The Three-surface kinematic hardening model, (Atkinson and Stallebrass, 1991) has been employed in the CRISP finite element program to demonstrate the effect of recent stress history on a two-dimensional tunnel problem, (Stallebrass, Jovicic and Taylor, 1994). The study illustrates that the surface settlement profiles were significantly affected by the recent stress history. This evidence implies that the multiple yield surfaces model, which explains the immediate stress history, is able to improve the numerical prediction of ground movements around a tunnel. Thus, the KHMCC model with multiple kinematic hardening yield surfaces should exhibit the effects of immediate stress history on tunnelling-induced settlement.

7.2.6 Analysis result

The analyses are done in plane strain conditions for different soil models. The analyses are divided into three calculation stages. At first, initial stress, stress history, and self-weight of the ground are set up. In addition, the ground is loaded by a $10kN/m^2$ surcharge, which is approximately equivalent to 0.5m of soil. Next, the tunnel elements are removed and the lining elements are inserted. Finally, the internal pressure is incrementally applied, divided into 100 steps of loading. The internal pressure, which controls the volume loss, is calculated and replaced by the nodal force. The volume loss can be calculated from either the surface trough or the displacement of the lining. In general, the volume loss should be controlled in the range of 1 or 2% of tunnel volume.

All descriptions of the two-dimensional plane strain finite element analyses are summarised in Table 7.3. Analyses TL1 to TL5 for homogeneous soil have been performed using three models (i.e. EVM, MCC and KHMCC). Three different sets of EVM can be categorised, i.e. EVM-1 for elastic undrained analysis, EVM-2 for elastic

Von Mises undrained analysis and EVM-3 for elastic drained analysis as given in Table 7.1. For MCC and KHMCC the model parameters in the analyses TL4, TL5, TL6 and TL8 are presented in Table 7.1. Furthermore, the effect of K_0 has been considered in analyses TL6 to TL8. In analyses TL9 to TL11 the soil stratum is separated into two layers: the top soft to medium clay layer of 14m and the bottom stiff to very stiff clay layer of 9m as illustrated in Figure 7.17(b). The input parameters are modified for both layers as summarised in Table 7.4.

Table 7.3 Description of finite element analyses of MRTA-project

FE Run	Model	Analysis type	K_0	No. of layer	Volume loss (%)
TL1	EVM-1	Undrained	1	1	1.582
TL2	EVM-2	Undrained	1	1	3.639
TL3	EVM-3	Drained	1	1	1.811
TL4	MCC	Drained	1	1	1.037
TL5	KHMCC	Drained	1	1	1.314
TL6	EVM-3	Drained	0.7	1	1.758
TL7	MCC	Drained	0.7	1	1.503
TL8	KHMCC	Drained	0.7	1	1.565
TL9	EVM-3	Drained	1	2	1.430
TL10	MCC	Drained	1	2	0.828
TL11	KHMCC	Drained	1	2	0.886

Table 7.4 Input parameters for two layer analyses

FE Run	Model	Parameter	Top layer	Bottom layer
TL9	**EVM-3 (Elastic Drained analysis)**	G	6000 (kPa)	9000 (kPa)
		υ	0.2	0.2
		S_u	10000 (kPa)	10000 (kPa)
TL10	**MCC**	κ^*	0.0625	0.0417
		λ^*	0.4	0.4
		g_x	64	96
		M	0.9	0.9
TL11	**KHMCC**	K	3200 (kPa)	4800 (kPa)
		a_p	2.0	2.0
		b_p	2.5	2.5
		R	0.8	0.8
		g_x	40	60
		a_q	3.5	3.5
		b_q	2.5	2.5
		M	0.9	0.9

The ground settlement profiles for three different constitutive models as well as the empirical formula prediction are shown in Figure 7.19. Using the empirical

formula in equation 7.1 to predict a settlement trough; assuming the parameter $i = 0.5 \cdot z$, the volume loss can be calculated as 1.295%. All predictions are consistent with the observed data from MRTA project (Lin *et. al*, 2002) except TL2. All calculations are done without consolidation analysis (i.e. fully undrained analysis or fully drained analysis), the undrained analyses TL1 and TL2 only show the total stress result. In analysis TL1 undrained conditions are assumed with very high undrained shear strength, thus the settlement trough is much shallower than the result from TL2. Analysis TL2 gives the deepest trough as the analysis is done with the actual undrained shear strength, which is at a lower strength than in other analyses.

On the other hand, the drained analyses TL3, TL4 and TL5 show effective stress behaviour. All predicted troughs are consistent with the empirical formula and the field data as shown in Figure 7.19(a). However, this cannot confirm the accuracy of the model behaviour since only one set of field data is used as a comparison. Analysis TL3 with the EVM model illustrates a slightly deeper and wider trough than the other predictions do. Analysis TL4 with the MCC model shows a small heave at the far end of the boundary. This may be due to the flow direction of strain vectors which move inward to the tunnel for the elements near the tunnel and move upward for the ground surface elements at the farther side. Analysis TL5 with the KHMCC model gives a shallower and wider trough shape than TL4. These predictions can be improved by modifying the ground, such as stress history or soil layering.

The analyses TL6, TL7 and TL8 with a reduction of K_0 from 1.00 to 0.70 show a deeper and narrower trough than TL3, TL4 and TL5. This may be due to the direction of major principal stress which is in the vertical direction when K_0 less than 1.00, and this results in the major principal strain also approximately in the vertical direction. Thus, the vertical displacement is expected to be higher than in analysis with K_0 equal to 1.00. This was also found by Addenbrooke *et. al* (1997), in which analyses were carried out reducing of K_0 from 1.50 to 0.50 around the tunnel zone. The settlement troughs of TL6, TL7 and TL8 are illustrated in Figure 7.19(b), and compared with TL3, TL4 and TL5.

The analyses improved by splitting the ground into two regions as shown in Figure 7.19(b) as presented in analyses TL9, TL10 and TL11. In these analyses, the stiffness values of the top and bottom layer can be adjusted until satisfied. For the consistency of all model comparisons, however, the stiffness parameters are modified from the analyses TL3, TL4 and TL5 by a factor of 0.8 and 1.2 for the top and bottom

soil layers respectively as illustrated in Figure 7.20. The analyses results of TL9, TL10 and TL11 are displayed in Figure 7.19(c), and are comparable with TL3, TL4 and TL5.

The horizontal (σ'_h) and vertical (σ'_v) stress contours for analysis TL4 with the MCC model are in the range of -390 to 0kPa and -490 to -10kPa respectively as presented in Figures 7.21(a) and (b). This case is presented since the stresses are similar for each of analyses TL1 to TL11. The horizontal stress increases at the crown and reduces at the springline of the tunnel as shown in the contour plot in Figure 7.21(a). On the other hand, the vertical stress decreases at the crown and becomes greater at the springline of the tunnel. The strains, however, depend principally on the choice of the constitutive model and the analysis conditions (i.e. drained or undrained analysis). The horizontal (ε_h) and vertical (ε_v) strain contours from analysis TL4 are in the range of -0.005 to 0.007 and -0.006 to 0.005 respectively shown in Figures 7.21(c) and (d). Figure 7.22 presents four examples of vertical strain contours from analyses TL2, TL5, TL7 and TL10. The undrained analysis TL2 with the low input shear strength as shown in Figure 7.22(a) indicates that the vertical strains are tensile for all elements above the tunnel. This causes a deep settlement trough. The result of analysis TL5 (Figure 7.22(b)) with the KHMCC model shows a smoother transition of vertical strain than for the MCC model. The reduction of K_0 leads to an increase in the vertical strain as shown in Figure 7.22(c). Figure 7.22(d) shows the discontinuity of the stress contour at the boundary between soft and stiff clay due to the sudden change of stiffness from a soft to a stiff layer.

The stress and strain amplitude contours from analyses TL4 and TL2 are presented in Figure 7.23. Figures 7.23(b) and 7.23(d) illustrate the state of soil elements around the tunnel reaching the yield state (i.e. $(\varepsilon_{\max} - \varepsilon_{\min}) = s_u / G$). This comes from the fact that the soil elements near the tunnel reach the yield state first and then the stress will gradually transfer to the adjacent elements. Figures 7.23(a) and 7.23(c) exhibit the typical stress and strain amplitude contour of analysis TL4 since they are moderately similar in each analysis except in some details such as magnitude of contours.

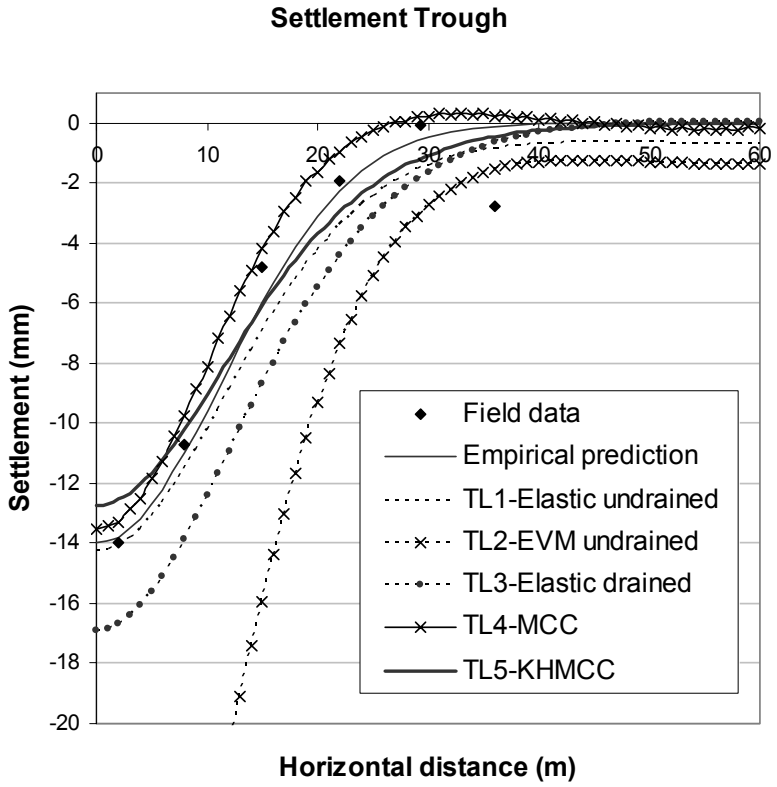
Settlement Trough
Settlement (mm)
Horizontal distance (m)
0
-2
-4
-6
-8
-10
-12
-14
-16
-18
-20
0
10
20
30
40
50
60
Field data
Empirical prediction
TL1-Elastic undrained
TL2-EVM undrained
TL3-Elastic drained
TL4-MCC
TL5-KHMCC

(a)

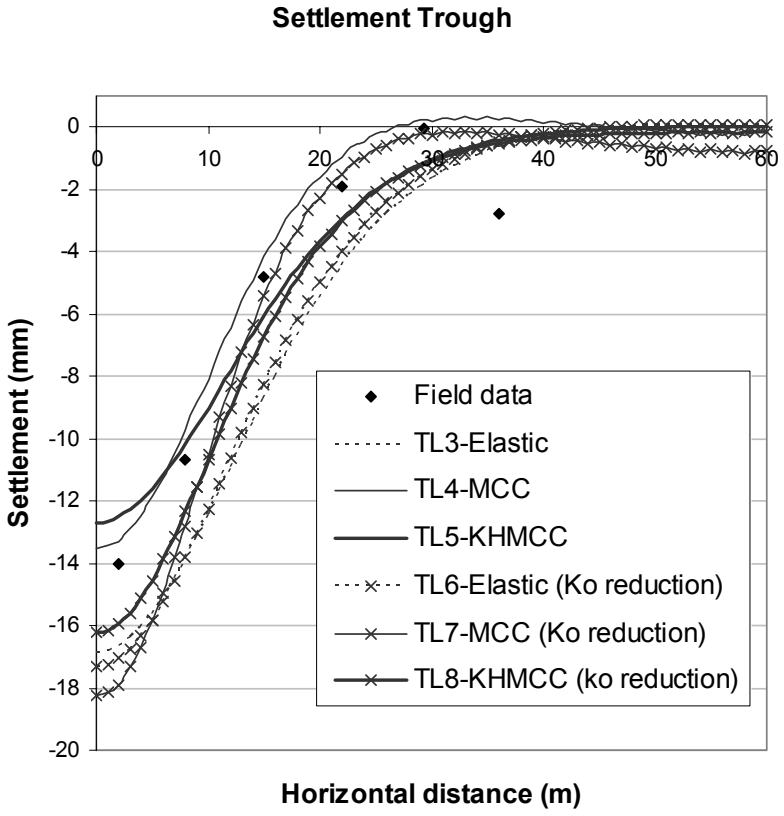
Settlement Trough
Settlement (mm)
Horizontal distance (m)
0
-2
-4
-6
-8
-10
-12
-14
-16
-18
-20
0
10
20
30
40
50
60
Field data
TL3-Elastic
TL4-MCC
TL5-KHMCC
TL6-Elastic (Ko reduction)
TL7-MCC (Ko reduction)
TL8-KHMCC (ko reduction)

(b)

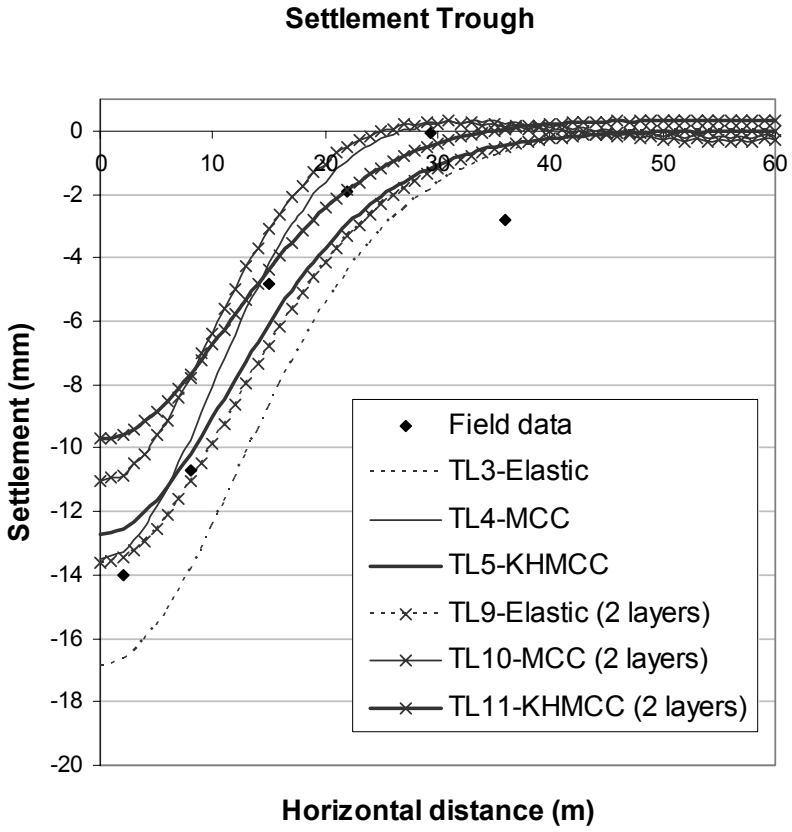

(c)

Figure 7.19 Predictions of settlement trough for MRTA-project; (a) Homogenous soil layering analyses (TL1 to TL5), (b) Effect of K_0 analyses (TL6 to TL8), (c) Two soil layer analyses (TL9 to TL11)

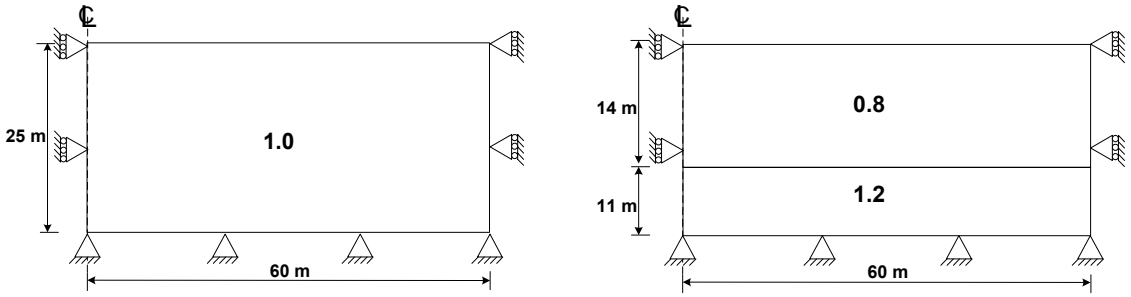

Figure 7.20 Relative input stiffness parameters between homogenous and two layering analyses

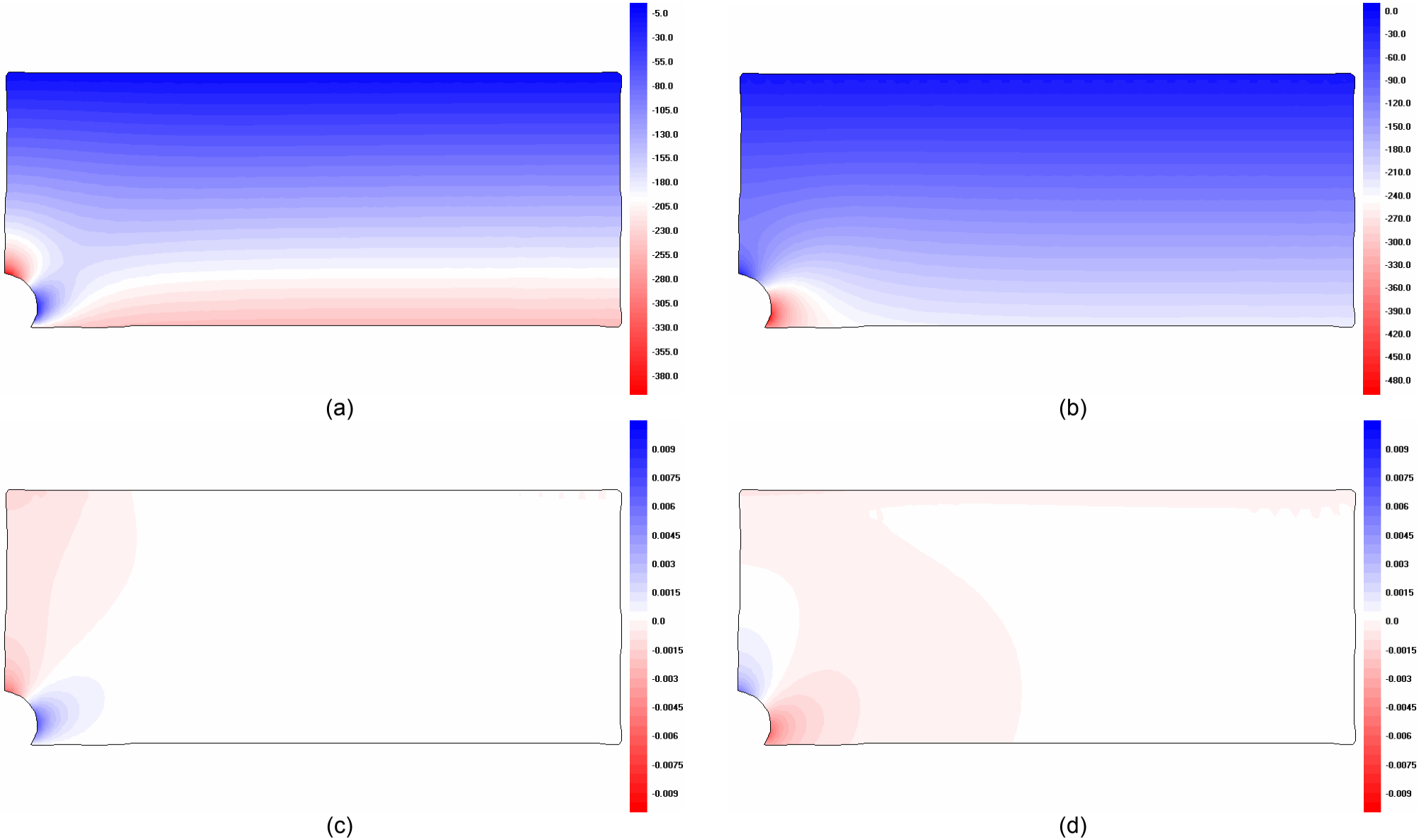

Fig 7.21 The stress and strain contours of the analysis TL4 with MCC model

(a) horizontal stress contour (σ'_h , kPa); (b) vertical stress contour (σ'_v , kPa);(c) horizontal strain contour (ε_h , -); (d) vertical strain contour (ε_v , -)

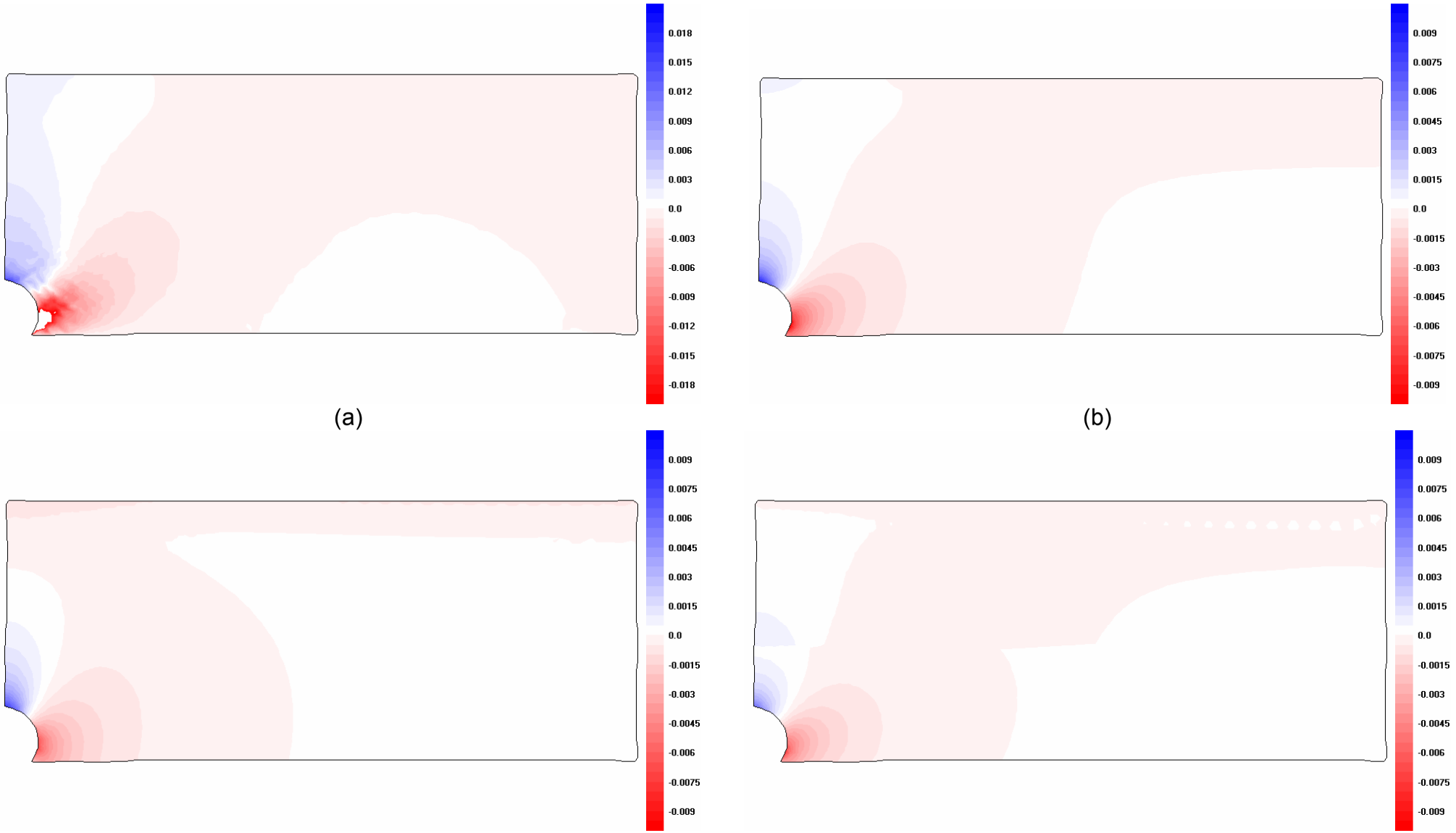

Fig 7.22 The vertical strain contour (ε_v, -) of the analyses TL2, TL5, TL7 and TL10
(a) TL2; (b) TL5; (c) TL7; (d) TL10

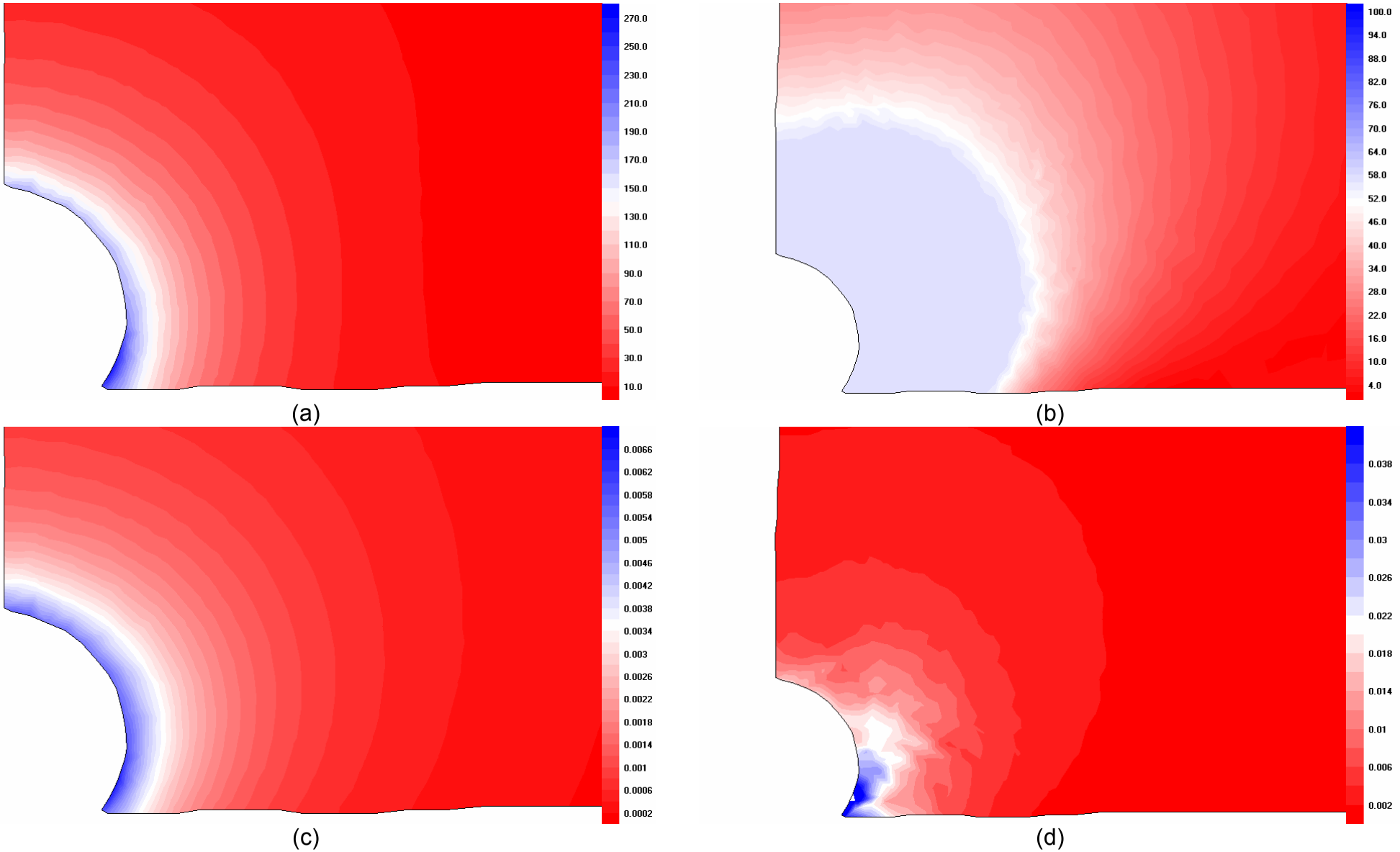

Fig 7.23 The stress and strain amplitude contour of the analyses TL4 and TL2 around tunnel
(a) and (b) are the stress amplitude of TL4 and TL2 around tunnel, kPa; (c) and (d) are the strain amplitude of TL4 and TL2 around tunnel

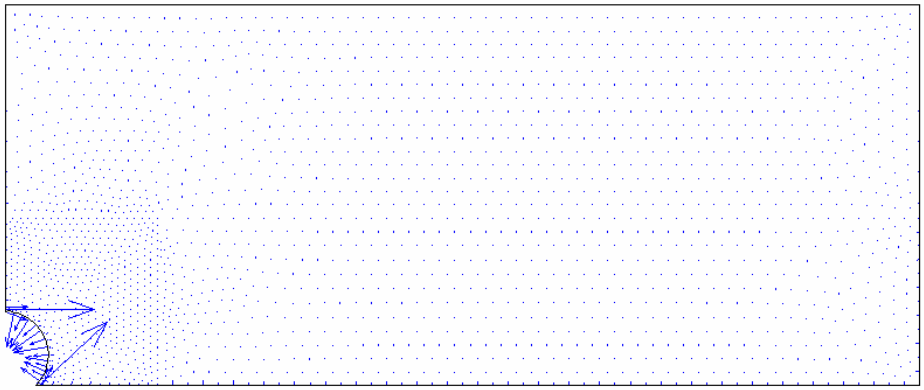

(a)

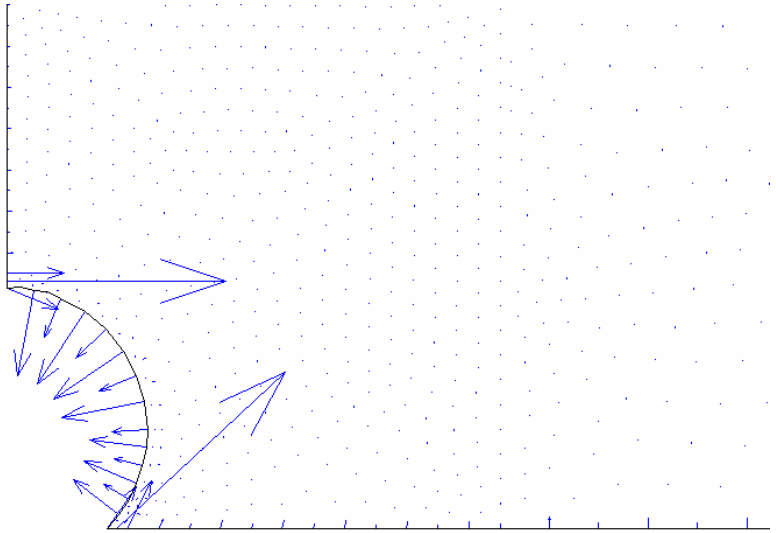

(b)

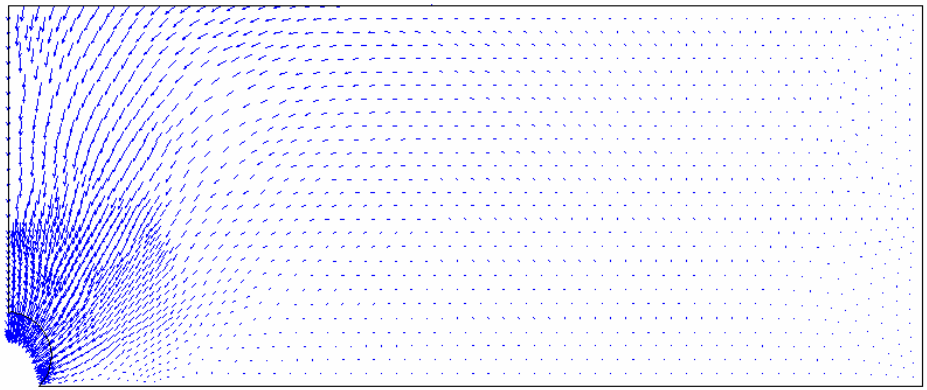

(c)

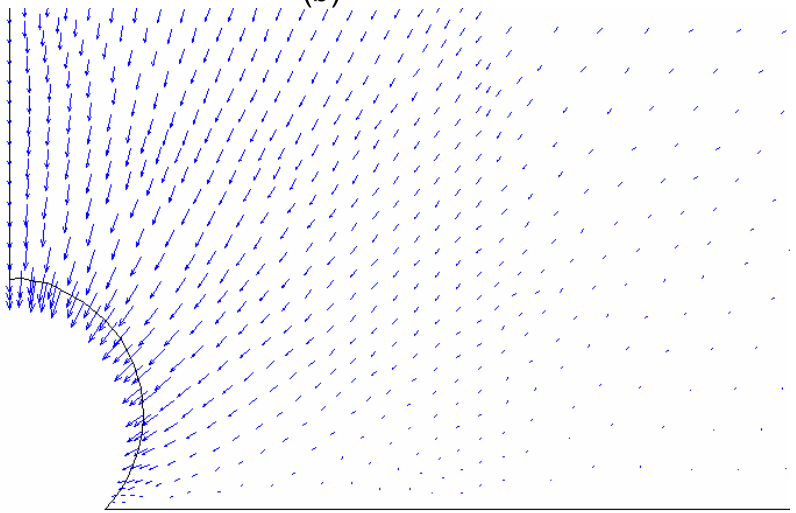

(d)

Fig 7.24 The nodal force and displacement vector of the analyses TL4 with MCC model
(a) and (c) are nodal force and displacement vector respectively; (b) and (d) are nodal force and displacement vector around the tunnel

Figures 7.24(a) and (b) show the nodal force vectors for all nodal points around the tunnel in analysis TL4. The nodal forces for all analyses should be the same because they are constrained by the same boundary and ground conditions. The surface boundary corresponds to the applied surcharge load. Both side boundaries utilise the roller support condition. The nodal forces at the bottom boundary conform with the total reaction force due to the gravity load and the applied surcharge load. The nodal force around the lining presents the reaction of the concrete lining subjected to the simulated internal pressure. The nodal displacement vector for all nodal points in analysis TL4 is shown in Figures 7.24(c) and (d). The nodal displacements are concentrated around the tunnel and reduce to small values in the far field. All displacements are toward to the tunnel as expected. The movements are significant at the crown and decrease towards the springline.

7.3 Conclusion

These two exercises on finite element analysis are presented in this chapter to illustrate the soil models as applied to Bangkok clay. The road embankment problem is related to the strength of the soft ground. The problem is analysed under two-dimensional plane strain conditions in order to reduce the amount of calculation. Using 449 six-noded triangular elements is sufficient to model a ground block. The undrained analysis can be only carried out using the EVM model (EM1 and EM2) because of the limitation of OXFEM code. For the rest of the analyses (EM3 to EM11), drained condition are analysed using the EVM, MCC and KHMCC models. The analyses found that the strength does not vary too much among the constitutive laws, whereas the deformation shape depends much on the constitutive law. The analysis results exhibit a smooth distribution of stresses and strains as shown in the contour plots. These two-dimensional analyses concern some factors such as surface crust and K_0. The effect of a surface crust makes the settlement profile slightly shallower due to the higher stiffness of the overconsolidated state of the crust layer. The reduction of K_0 from 1.0 to 0.7 makes the settlement profile much deeper. The approximation of the soil embankment by nodal forces can be reasonably assumed. However, the triangular embankment should be replaced by not only the vertical nodal force but also the horizontal nodal force. The analysis considering the effect of lateral load discovered that the effect can be disregarded, because the horizontal load is relatively small compared with the load from whole embankment.

The critical problem for the tunnel is not the strength of soil but rather the excessive settlement trough. An empirical formulation to predict tunnelling-induced settlement is widely used in practice. However, there is no better solution than finite element analysis to calculate the stress-strain behaviour around a tunnel. In this study, the tunnel is simulated as a two-dimensional plane strain problem with 1105 six-noded triangular elements, analysed by using three different models i.e. the EVM, MCC and KHMCC models. The undrained analysis can only be analysed using the EVM model (TL1 and TL2) and the other analyses (TL3 to TL11) are carried out in drained conditions. The comparisons of the settlement trough prediction found that all predicting troughs except TL2 are consistent with the empirical formula and the field data. However, this cannot guarantee the accuracy of all models since only one set of field data is used for comparison. The analyses with a reduction of K_0 show deeper and narrower troughs as expected. A discontinuity of the stress-strain contours is found from the two layer analyses, and this is due to the sudden change of stiffness from soft to stiff.

For the embankment problem with 449 nodes, the analysis time is roughly about 30 minutes whereas it is spent almost 2 hours for the tunnelling problem with 1105 nodes. The running time of the analysis with KHMCC model using 50 yield surfaces is slightly longer than the MCC case (single yield surface) about 10-20%. This is implied that the analysis time mainly uses for the global load-deformation matrix operation rather than the updating of the stress-strain at element level. The former is controlled by size of problems, but the latter depends on the choice of constitutive model used.

However, these two examples of analysis prove the ability of soil model to be employed in practice. In further analysis, more complicated factors need to be dealt with, such as consolidation analysis, because the limitation on total stress calculation in the present version of OXFEM is constrained to analyse problems for only fully undrained or drained conditions.

Chapter 8
Concluding Remarks

8.1 Summary of research

Research at Oxford University on constitutive modelling for soils concentrates principally on the use of plasticity theory for building soil models. In much of the recent work there has been an emphasis on the use of thermodynamic principles to develop a new approach to plasticity modelling termed hyperplasticity. This project is a programme of development of practical soil models, especially clay models, based on hyperplasticity theory.

There are many soil models with their authors each claiming their advantages over other soil models. There is still no explicit model which explains fully the behaviour of soil subjected to general construction processes. Since some of the models are based on laboratory research and are described in terms of sophisticated expressions, they are rarely used in practice. This project tries to develop a practical constitutive soil model to employ in geotechnical work. The research tasks can be separated into three main areas:

(i) building a theoretical soil model based on the hyperplasticity concept,

(ii) evaluation the soil model parameters based on experimental data, and

(iii) implementation of the soil model in a finite element program.

8.1.1 Theoretical soil models

The most important feature of the new approach is that the entire constitutive behaviour can be derived from two scalar potentials. Applying the hyperplasticity idea to soil models, the kinematic hardening model is selected as a key stage in developing a model with a continuous internal functional. The continuous kinematic hardening functional model can accommodate a smooth transition of stiffness during unloading and reloading below the maximum past stresses. While the continuous hyperplasticity approach can offer a continuous smooth stress-strain response, in numerical applications, the continuous function has to be replaced by a series of piecewise linear functions, which are implemented in terms of multiple internal variables.

This research develops a new constitutive model for soil mechanics that makes use of two underlying stress-strain relationships: linear and logarithmic. At this stage, the development of research is directed to an elasto-plastic model with a continuous hardening function in terms of triaxial stress-strain parameters. The ultimate model is called kinematic hardening modified Cam-clay model (KHMCC), which requires eight parameters (for linear stiffness), or seven parameters (for logarithmic stiffness) plus one parameter (μ) for rate-dependence.

8.1.2 Evaluation of model parameters

In order to evaluate the model parameters, the experimental data for Bangkok clay obtained from Asian Institute of Technology (AIT) and Chulalongkorn University are employed. The experimental data at both the small strain level and large strain are required to explain the variation of stiffness from small to large strain levels. The AIT data contains information on triaxial tests at large strain level. On the other hand, the small strain data is provided by the research on cyclic undrained shear at Chulalongkorn University.

Based on the results of the study, the linear stress-strain model is proposed for this study. All predictions are simulated by assuming uniform stress-strain distribution in axi-symmetry conditions. Every sample is consolidated following its stress history and sheared in its specific condition such as undrained, drained or cyclic undrained condition where the rate effects are concerned. Utilising these results, model parameters for Bangkok clay are proposed.

8.1.3 Implementation of software

From a numerical aspect, an incremental response calculation is required to evaluate the stress-strain response. There are two calculation algorithms (i.e. rate-independent and rate-dependent) considered here. These two algorithms are initially implemented using FORTRAN 90 for the triaxial calculation. Further development of soil models in the form of generalised stress-strain parameters is performed to link the model to the OXFEM finite element program. This research considers special conditions, such as two-dimensional plane strain and axi-symmetry. The model requires the transformation from generalised stress-strain to two-dimensional stress-strain relation.

The calculation of global incremental load-deformation behaviour has to deal with a slightly more complicated algorithm than the incremental stress-strain in a single element calculation. The present version of OXFEM employs the Newton-Raphson (NR) algorithm. Before starting the analysis, some triaxial problems are tested to make sure that the subroutines developed and the link between the old code and new subroutine are correct.

8.1.4 Applications

Two application examples of geotechnical construction are selected: analysis of a road embankment and estimation of tunnelling-induced settlement. The problems are simplified into two-dimensional plane strain conditions, and symmetry is used to reduce the amount of calculation. The mesh is generated using the I-DEAS commercial programme. These finite element analyses are calculated using OXFEM including the subroutines developed by the author. All analyses are carried out using three constitutive models: elastic Von Mises (EVM), modified Cam-clay (MCC) and kinematic modified Cam-clay (KHMCC) model. The model parameters are employed from the parameters derived from laboratory testing except in the EVM model, which have been estimated from the MCC parameters.

8.2 Conclusions

The conclusions from this research can be summarised as follows:

1. The KHMCC model is categorised as a multiple yield surface model. However, there is another idea called bounding surface plasticity which addresses some of the weak points of critical state soil models. Although the bounding surface concept, such as in the MIT-E3 model (Whittle, 1993), offers efficient computation and a sufficiently accurate prediction of stress-strain-strength behaviour, there are still two major drawbacks. The bounding surface concept requires some arbitrary functions (such as a mapping rule and a hardening rule) without obvious physical meaning, and the concept cannot explain the effect of immediate past history such as a hysteresis loop on unloading-reloading. These two deficiencies can be described by the multiple yield surface idea. There are also some disadvantages of the multiple yield surface model; for example the nested yield surface model (Mroz *et al*., 1982). The multiple yield surface model requires a considerable amount of calculation in each yield surface and needs a large number of hardening parameters. These problems can be

eliminated by introducing a functional (loosely defined as function of a function). This mathematical framework provides the concept that all yield surfaces are reduced to a single structure with different sizes and a large number of kinematic parameters are replaced by a function. These have been included in the current research.

2. A bubble model (Al Tabbaa and Wood, 1989) applies the kinematic hardening idea to the MCC model. An improvement on the bubble model, to consider the effect of immediate stress history, has been explored in the three-surface kinematic hardening (3-SKH) soil model (Atkinson and Stallebrass, 1991). This model was intended to improve the original bubble model by adding an extra intermediate yield surface in order to deal with moderate strain levels. However, there is still a question whether it is logical to limit the number of multiple yield surfaces to three surfaces. The models cannot produce the response to cyclic loading behaviour which has a small change of stress amplitude. These models could be extended to an infinite number of yield surfaces. This can be dealt with by using a continuous functional which provides a mathematical framework for generating a smooth curve. This concept has been applied in the KHMCC model.

3. All recent soil models aim to generate plasticity behaviour inside the SBS which could not be achieved by the MCC model. Some models contain many advantages of theories such as anisotropic yield surface, hysteretic formulation and process of destructuration. Therefore, they give a better quality in term of laboratory prediction. However, these theories make the model too sophisticated. They are rarely used in practice. This research tries to link between the theoretical and practical sides. Although the new model does not give the best predictive qualities, it can resolve some of the weak points that cannot be explained by other models.

4. In order to define the continuous kinematic hardening model, we need an expression for the kinematic hardening function, which relates to the observed stress-strain curve. This process involves much trial and error in order to define the mathematical formulae. The research leads to a recommendation for a hyperbolic function. The hyperbolic shape is controlled by four parameters (i.e. E, a, b and r referred to equation 3.38), which have physical meaning. The initial slope of the curve (E) refers to the elastic modulus while the asymptotic slope (related to

parameter *r*) defines the plastic modulus. The remaining parameters (*a* and *b*), which control rate of change of slope, can be evaluated by the definition of secant modulus and/or tangential modulus at particular stresses.

5. Both numerical approaches to determine the incremental stress-strain (rate-independent and rate-independent) are implemented. The rate-independent calculation requires some consistency conditions which involve a higher complexity of computation than rate-dependence. It also requires some error control that the rate-dependent algorithm does not need. The most obvious benefit of the rate-dependent calculation is the inclusion of rate dependency for materials which can exhibit any significant rate effects. In addition, for the rate-independent approach, the updated strain increment, consistency condition, hardening rule as well as the error controls are included in the governing matrix. In contrast, only the updated strain increment appears in the governing matrix for the rate-dependent calculation. Therefore, the algorithm for rate-independence has to deal with larger sizes of governing matrix than the rate-dependent. As a result, the rate-dependence reduces the computing time considerably.

6. The KHMCC model prediction of consolidation behaviour is more accurate than its prediction of other behaviours. This is because the consolidation prediction only acts on the *p* term of the model but does not deal with the *p*-*q* coupling term. The prediction of pure shear behaviour (i.e. CID-90 and CID-270) can be used to estimate critical state parameters (M_C, M_E). However, M_E is normally slightly higher than M_C. For simplicity, the assumption of $M_C = M_E$ is made in this research. The isotropic consolidated drained tests are accurately predicted in terms of stress path and shear strength using KHMCC model. On the other hand, the anisotropic consolidated drained predictions are slightly inaccurate, especially in terms of stress path. The prediction of the variation of shear stiffness is relatively accurate for both isotropic and anisotropic consolidated tests. The simulation of the cyclic undrained tests gives accurate results. The variation of the shear modulus and the damping ratio are accurately simulated by the KHMCC model. The main advantage of the model is that it can predict both the monotonic loading and cyclic loading response by the same constitutive law.

7. The road embankment problem based on the field data from the Bangkok project was selected as the first problem for study of a geotechnical application. The most critical issue of embankments on soft clay is the strength of soft ground during the construction period, as a low undrained shear strength cannot resist the high embankment load. The analyses discovered that the stress fields do not vary much among the constitutive soil models. Although, this study does not predict the undrained behaviour with the soil models used, the drained long-termed settlement prediction is calculated. This restriction in the analysis comes from a constraint of the present version of the OXFEM finite element program, in which it does not include code dealing with consolidation analysis. The comparison of the settlement profile with field data can not be made, because only a single settlement point at each road section was recorded. In addition, this series of two-dimensional analyses also includes studies of some aspects of the embankment problem such as the effect of a surface crust, K_0 and lateral shear force. The effect of a surface crust makes the ground response stiffer. On the other hand, the ground response is softer when the K_0 is reduced. Theoretically, the lateral shear force must be included in the nodal force for the embankment analysis. However, the research found that this effect can be disregarded according to the small effect of lateral load compared with the whole size of the embankment.

8. The second geotechnical problem considered in this study is the biggest public transportation underground tunnel in Bangkok named MRTA. The important problem of the tunnel is not the strength of soil but the excessive settlement trough. The series of two-dimensional analyses also include some modifications to the ground such as anisotropic ground (reduction of K_0) and layered ground. The analyses found that the displacement fields depend much on the models used. The result of analysis with the KHMCC model offers a better transition of stress-strain than the MCC model. The reduction of K_0 leads to an increase in the vertical strains which lead to a deeper and narrower settlement trough. The two-layer analyses show a discontinuity of the stress contour at the boundary between soft and stiff clay due to the sudden change of stiffness from the soft to stiff layer.

9. From the analyses of two geotechnical problems, it can be concluded that for the analysis of the strength problem it is not necessary to utilise an advanced soil model.

The models such as the EVM and the MCC model can also provide a sufficient strength prediction. In contrast, for the analysis of displacement problem, the advanced soil models which give a transition of stiffness from small strain to large strain level are recommended. The KHMCC model is therefore one of the possible soil models used to predict this problem. The effect of past stress history and K_0 can also be described by the KHMCC model.

8.3 Recommendations

Research on constitutive models for soils requires further work. Some recommendations for future research are as follows:

1. To improve the stress-strain response, the continuous hardening function ($\hat{H}(\eta)$) should be modified to generate a better stress-strain curve. The present version of the KHMCC model assumes the stress-strain curve to be hyperbolic. Other forms of continuous hardening function might be introduced.

2. The fact that soils are likely to be anisotropic, with their behaviour depending on the direction of deposition, is important. The multiple yield surface concept can accommodate the anisotropic behaviour by means of memorisation of the yield surface locations from the past stress history. However, this is still not sufficient to explain the experimental results. To improve this, the model should introduce other yield criteria or/and anisotopic yield surface shape. Firstly, this is because the yield criteria such as the Matsuoka-Nakai criterion offer a smooth change of yield strength in the deviatoric plane. In the Matsuoka-Nakai criterion, the magnitude of critical state cone will depend on where the stress state is in the deviatoric plane. Secondly, the anisotropic yield surface shape, e.g. the deformed elliptical shape or the rotating elliptical shape, is believed to be able to describe the anisotropic behaviour.

3. The laboratory investigation shows that every sheared sample is not necessarily enforced to reach the same critical state as stated in the CSSM assumption. This is especially the case for samples on the dry side of CSL. An improvement of the model prediction should introduce some ideas to account for the aforementioned phenomenon. The concepts of localisation and strain softening are believed to be able to explain the behaviour of heavily overconsolidated clay. The localisation idea

assumes that all material elements do not necessary reach the yield state at the same time. The material consists of both an elastic zone and a shear band (plastic zone), where the ratio of these two volumes controls the material behaviour. In contrast, strain softening allows the yield surface to move inward or reduce its size when the stress state touches yield surface.

4. Although the cyclic undrained triaxial tests are predicted quite well by the KHMCC model, the prediction of behaviour of soil at small strain level needs still to be improved in future research. Experimental results for the Bangkok clay at small strain levels from apparatus such as a directional shear cell and hollow cylinder are currently unavailable.

5. Development of rate process theory (Houlsby and Purzin, 2002) could provide improvements to the prediction of short-term consolidation behaviour (before the end of primary consolidation) as well as long term creep behaviour.

6. A constraint of the present version of the OXFEM finite element program is that it does not include the code dealing with consolidation analysis. Thus, the consolidation code should be added in the OXFEM program.

7. In future analyses, the use of techniques other than the Newton-Raphson (NR) method for solution of the incremental load-deformation is recommended to improve the running speed and/or accuracy, particularly for larger size problems including three-dimensional analyses.

This research aims to build a new constitutive soil model, in particular clay model. Based on the continuous hyperplasticity concept, the research produces a satisfied model which can generate the smooth transition behaviour from elastic to plastic. Although the model does not substantially improve the prediction qualities, it can describe the effects of immediate stress history which is a strong point of the model. The model also includes the rate effect which is useful for the analysis of a staged construction process. Two geotechnical applications of the model confirm that it is undoubtedly used for the geotechnical engineering.

REFERENCES

Addenbrooke, T.I., Potts, D.M., and Puzrin, A.M. (1997), "The influence of pre-failure soil stiffness on the numerical analysis of tunnel construction", *Geotechnique,* Vol. 47, No. 3, pp. 693-712

Al-Tabbaa A. and Wood D.M. (1989), "An experimentally based 'bubble' model for clay", *Pro. of Int. Conf. Numerical models in geomechanics NUMOG 3,* Edt. Pietruszczak and Pande, Balkema, pp 91-99

Atkinson, J.H., Richardson, D., and Stallebrass, S.E. (1990), "Effect of recent stress history on stiffness of overconsolidated soil", *Geotechnique*, Vol. 40, pp. 531-540

Atkinson, J.H. and Sallfors, G. (1991), "Experimental determination of stress-strain-time characteristics in laboratory and in-situ tests", *Proc. of X ECSMFE*, Florence, (Eds. Associazione Geotecnica Italiana), pp 915-956 Rotterdam: A. A. Balkema

Atkinson, J.H. and Stallebrass, S.E. (1991), "A model for recent stress history and non-linearity in the stress-strain behaviour of overconsolidated soil", *Proc. 7^{ih} Int. Cof. On Computer Methods and Advances in Geomechanics*, Cairns, Vol. 1, pp555-560

Augarde, C.E. (1997), "Numerical modelling of tunnelling processes for assessment of damage to buildings", *D.Phil. Thesis*, University of Oxford

Augarde, C.E. and Burd, H.J. (2001), "Three-dimensional finite element analysis of lined tunnels", *Int. J. Numer. Anal. Meth. Geomech*., Vol. 25, pp 243-262

Bloodworth, A.G. (2002), "Three-dimensional analysis of tunnelling effects on structures to develop design method", *D.Phil. Thesis*, University of Oxford

Burd, H.J. (1986), "A large displacement finite element analysis of a reinforced unpaved road", *D.Phil. Thesis*, University of Oxford

Butterfield, R. (1979), "A natural compression law for soils (an advance on *e*-log p')", *Geotechnique,* Vol. 29, No.4, pp 469-480

Coleman, B.D. and Gurtin, M.E. (1967), "Thermodynamics with internal state variables", *J. Chem. Phys*. Vol. 47, pp. 597-613

Collins, I.F. and Houlsby G.T. (1997), "Application of thermomechanical principles to the modelling of geotechnical materials", *Proc. Royal Society of London*, Series A, Vol. 453, pp 1975-2001

Dafalias, Y. and Herrmann, L.R. (1982), "Bounding surface formulation of soil plasticity", *Soil Mechanics Cyclic and Transient Loads* (G. N. Pande and O. C. Zienkiewicz, eds), Chapter 10, pp 253-282, New York, John Wiley & Sons

Drucker, D. C. and Prager, W. (1952), "Soil Mechanics and plastic analysis or limit design", *Quarterly of Applied Mechanics*, Vol. 10(2), pp. 157-165

Einav, I., Puzrin, A.M and Houlsby, G.T. (2000), "Continuous hyperplastic models for overconsolidated clays", *Proc. Symp. on Mathematical Models in Geomechanics, Scilla di Reggio Calabria*, 19-22 Sept., Vol. 37, No. 5/6, pp 515-523

Graham, J. and Houlsby, G.T. (1983), "Anisotropic elasticity of a natural clay", *Geotechnique*, Vol. 33, No. 2, pp165-180

Gurung, S.B. (1992), "Yielding of soft Bangkok clay below the boundary surface under compression conditions", *M. Eng. Thesis*, GT-91-11, AIT, Bangkok

Hashiguchi, K. (1985), "Two- and Three-surface models of plasticity", *Proc. 5th Int. Cof. Numerical Methods in Geomechancis*, Nagoya, pp 285-292

Houlsby, G.T. (1999), "A model for the variable stiffness of undrained clay", *Proc. Int. Symp. on Pre-Failure Deformation of Soils*, Torino, 26-29 September, Balkema, ISBN 9058090760, Vol. 1, pp 443-450

Houlsby, G.T. and Puzrin, A.M. (1999), "An approach to plasticity based on generalised thermodynamics", *Proc. of the International Symposium on Hypoplasticity, Horton*, Greece, pp 233-245 in press

Houlsby, G.T. and Puzrin, A.M. (2000), "A thermomechanical framework for constitutive models for rate-independent dissipative materials", *International Journal of Plasticity*, Vol. 16 No. 9, pp 1017-1047

Houlsby, G.T. and Puzrin, A.M. (2002), "Rate-dependent plasticity models derived from potential functions", *Journal of Rheology*, Vol. 46, No. 1, pp 113-126.

Howatson, A.M., Lund, P.G., and Todd, J.D. (1991), "Engineering tables and data", Chapman & Hall, London

Hueckel, T. and Nova, R. (1979), "Some hysteresis effects of the behaviour of geologic media", *International Journal of Solids and Structures*, Vol. 15, pp. 625-642

Iwan, W.D. (1967), "On the class of models for the yielding behavior of continuous and composite systems", Transactions of the American Society of Mechanical Engineers, *Journal of Applied Mechanics*, Vol. 34, pp 612-617

Khan, M.R.A. (1999), "Stress-strain behaviour of soft Bangkok clay below the state boundary surface under anisotropic conditions", *M. Eng. Thesis*, AIT Bangkok

Kim, S.R. (1991), "Stress-strain behaviour and strength characteristics of lightly overconsolidated clays", *Doctoral Dissertation*, GT-90-2, AIT, Bangkok

Kolymbas, D. (1977), "A rate-dependent constitutive equation for soils", *Mech. Res. Comm.*, Vol. 4, pp. 367-372

Lee, K.M. and Rowe, R.K. (1989), "Deformations caused by surface loading and tunnelling: the role of elastic anisotropy", *Geotechnique,* Vol. 39, No. 1, pp. 125-140

Likitlersuang, S. (2000), “Elasto-plastic analysis of soft clay behaviour”, *M. Eng. Thesis*, AIT, Bangkok

Lin, D.G., Tseng, C.T., Phienwej, N., and Suwansawat, S. (2002), “3-D deformation analysis of earth pressure balance shield tunnelling in Bangkok subsoil”, *Journal of Southeast Asian Geotechnical Society*, Vol. 33, April 2002, pp13-27

Liu, G. (1997), "Numerical modelling of damage to masonry buildings due to tunnelling" *D.Phil. Thesis*, University of Oxford

Lubliner, J. (1972), “On the thermodynamic foundation of non-linear solid mechanics”, *Int. J. of Non-linear Mechanics*

Matsuoka, H. and T. Nakai (1974), “Stress-deformation and strength characteristics of soil under three different principal stresses” *Proceedings, JSCE*, no. 232, Dec, 1974, pp. 59-70

Mitchell, J.K. (1976), “Fundamentals of soil behavior”, John Wiley and Sons, New York

Mroz, Z. (1967), “On the description of antisotropic workhardening”, *J. Mech. Phys. Solids*, Vol. 15, pp. 163-175

Mroz, Z. and Norris, V.A. (1982), “Elastoplastic and viscoplastic constitutive models for soils with application to cyclic loading”, *Soil Mechanics Cyclic and Transient Loads* (G. N. Pande and O. C. Zienkiewicz, eds), Chapter 8, pp 173-218, New York, John Wiley & Sons

Navaneethan, T. (1999), “Extension behaviour of soft Bangkok clay with selected applied stress paths”, *M. Eng. Thesis,* AIT, Bangkok

O'Reilly, M. P. and New, B. M. (1991), “Tunnelling induced ground movements; predicting their magnitude and effects”, *4th International Conference on Ground Movements and Structures*, Cardiff invited review paper, Pentech Press, pp.671-697

Pestana, J.M. and Whittle, A.J. (1999), “Formulation of a unified constitutive model for clays and sands”, *International Journal for Numerical and Analytical Methods in Geomechanics*, Vol. 23, pp. 1215-1243

Potts, D.M. and Zdravkovic, L. (1999), “Finite element analysis in geotechnical engineering Volume I, II”: *Theory and Application*, Tomas Telford, ISBN 0727727532

Prevost, J.H. (1978), “Plasticity theory for soil stress-strain behaviour”, Proceedings of the American Society of Civil Engineers, *Journal of the Engineering Mechanics Division,* Vol. 104, No. EM5, October, pp 1177-1194

Puzrin, A.M. and Burland, J.B. (1996), "A logarithmic stress-strain function for rocks and soils", *Geotechnique*, Vol. 46, No. 1, pp 157-164

Puzrin, A.M. and Burland, J.B. (1998), "Non-linear model of small-strain behaviour of soils", *Geotechnique*, Vol. 48, No. 2, pp 217-233

Puzrin, A.M. and Houlsby, G.T. (2001a), "Strain-based plasticity models for soils and the BRICK model as an example of hyperplasticity approach", *Geotechnique*, Vol. 51, No. 2, pp 169-172

Puzrin, A.M. and Houlsby, G.T. (2001b), "Fundamentals of kinematic hardening hyperplasticity", *International Journal of Solids and Structures*, Vol. 38, pp 3771-3794

Puzrin, A.M. and Houlsby, G.T. (2001c) "On the non-intersection dilemma in multi-surface plasticity", *Geotechnique*, Vol. 51, No. 4, pp 369-372

Puzrin, A.M. and Houlsby, G.T. (2001d), "A thermomechanical framework for rate-independent dissipative materials with internal functions", *International Journal of Plasticity*, Vol. 17, pp 1147-1165

Puzrin, A.M. and Houlsby, G.T. (2003), "Rate-dependent hyperplasticity with internal functions", Proceedings of the American Society of Civil Engineers, *Journal of the Engineering Mechanics Division*, Vol. 129, No. 3, March, pp 252-263

Roscoe, K. H., Schofield, A. N. and Thurairajah, A. (1963), "Yielding of clays in state wetter than critical" *Geotechnique*, Vol. 13, No. 3, pp. 211-240

Roscoe, K.H. and Burland, J.B. (1968), "On the generalised behaviour of 'wet' clay", *Engineering Plasticity,* (Heyman, J. and Leckie, F.A. eds.), Cambridge University Press, pp. 535-610

Rouainia, M. and Wood, D.M. (2000), "A kinematic hardening constitutive model for natural clays with loss of structure", *Geotechnique*, Vol. 50, No. 2, pp. 153-164

Schofield, A.N. and Wroth, C.P. (1968), "Critical state soil mechanics", McGraw Hill, London

Seah, T.H. (1990), "Anisotropy of normally consolidated Boston blue clay", *Sc.D. Thesis*, MIT.

Seah, T.H. (1998), "Differential settlements in highway no. 34 pavement caused by construction of Bangna-Bangpli-Bangpakong expressway", Report submitted to Expressway Transit Authority of Thailand

Seah, T.H. and Juirnarongrit, T. (1999), "Constant rate of strain consolidation with radial drainage", in press

Seah, T.H. and Hassan, S.I. (1999), "Constant rate of strain consolidation testing on Bangkok clay", in press

Soga, K., Nakagawa, K., and Mitchell, J.K. (1995), "Measurement of stiffness degradation characteristics of clays using a torsional shear device", *First International Conference on Earthquake Geotechnical Engineering*, Tokyo, Nov. 14-16, pp. 107-112

Stallebrass, S.E., Jovicic, V. and Taylor, R.N. (1994), "The influence of recent stress history on ground movements around tunnels", *Pre-failure Deformation of Geomaterials* (Shibuya, Mitachi and Miura eds), pp 615-620, Balkema, Hotterdam, ISBN 905410399

Stallebrass, S.E. and Taylor, R.N. (1997), "The development and evaluation of a constitutive model for the prediction of ground movements in overconsolidated clay", *Geotechnique*, Vol. 47, No. 2, pp. 225-253

Teachavorasinskun, S., Thongchim, P., and Lukkunaprasit, P. (2001), "Shear modulus and damping ratio of clay during undrained cyclic loading", *Geotechnique*, Vol 51, No. 5, pp 467-470

Teachavorasinskun, S., Thongchim, P., and Lukkunaprasit, P. (2002), "Stress rate effect on the stiffness of a soft clay from cyclic", compression and extension triaxial tests, *Geotechnique,* Vol. 52, No. 1, pp 51-54

Tuladhar, L. (2000), "Behaviour of soft clay below the state boundary surface with stress Paths from extension to compression", *M. Eng. Thesis*, AIT, Bangkok

Uchaipichat, A. (1998), "Triaxial tests on soft Bangkok clay with different applied stress paths", *M. Eng. Thesis*, GT-97-13, AIT, Bangkok

Vaid, P. and Campanella, R.G. (1974), "Triaxial and plane strain behaviour of natural clay", *Journal of Geotechnical Engineering, ASCE*, Vol. 100, No.3, pp 207

Whittle, A.J. (1993), "Evaluation of a constitutive model for overconsolidated clays", *Geotechnique*, Vol. 43, No. 2, pp 289-313

Whittle, A.J., DeGroot, D.J., Ladd, C.C., and Seah, T.H. (1994), "Model prediction of anisotropic behaviour of Boston Blue Clay"*, Journal of Geotechnical Engineering, ASCE*, Vol. 120, pp 199-224

Wood, D.M. (1995), "Kinematic hardening model for structured soil", *Numerical models in geomechanics NUMOG 5* (Eds. G.N. Pande & S. Pietruszczak), pp 83-88 Rotterdam: A. A. Balkema

Zdravkovic, L., Potts, D.M., and Jardine, R.J. (2001), "A parametric study of the pull-out capacity of bucket foundations in soft clay", *Geotechnique,* Vol. 51, No. 1, pp. 55-67

Zdravkovic, L., Potts, D.M., and Hight D.W. (2002), "The effect of strength anisotropy on behaviour of embankments on soft ground", *Geotechnique,* Vol. 52, No. 6, pp 447-457

Ziegler, H. (1983), “An introduction to thermomechanics”, North Holland, Amsterdam

APPENDIX A

This following section lists the new input modules for OXFEM. These will be included in the OXFEM manual. The new input modules are for specifying two material types, initial states and rate-dependent calculation.

Material properties

***MATERIALS**

For **mtyp = 9**; Kinematic Hardening Modified Cam Clay model (KHMCC)

Property number (in specification list)	Constant properties	Descriptions
p_1	K	Initial bulk modulus
p_2	a_p	Non-linear kinematic hardening parameter in isotropic (p) direction
p_3	b_p	
p_4	r	
p_5	g_x	Elastic shear modulus gradient
p_6	a_q	Non-linear kinematic hardening parameter in deviatoric (q) direction
p_7	b_q	
p_8	M	Slope of critical state line
p_9	μ	Viscosity coefficient (for rate-dependent calculation)

For **mtyp = 12**; Modified Cam Clay model (MCC)

Property number (in specification list)	Constant properties	Physical meaning
p_1	κ^*	Slope of swelling consolidation line on log v-log p plot
p_2	λ^*	Slope of virgin consolidation line on log v-log p plot
p_3	g_x	Elastic shear modulus gradient
p_4	M	Slope of critical state line
p_5	μ	Viscosity coefficient (for rate-dependent calculation)
p_6	p_{x0}	Reference stress of initial yield surface

Specification of initial states

***INITIAL_STATE**

$z_1 \quad \sigma_{h1} \quad \sigma_{v1} \quad \sigma_{h1\max} \quad \sigma_{v1\max}$

$z_2 \quad \sigma_{h2} \quad \sigma_{v2} \quad \sigma_{h2\max} \quad \sigma_{v2\max}$

… etc.

This module follows the *INTIAL module which contains information about initial stresses in the order of σ_h, σ_v (initial horizontal and vertical stress) and also includes the information of stress history in the order of $\sigma_{h\max}, \sigma_{v\max}$ (maximum past horizontal and vertical stress).

Calculation information

***CALCULATION_TIME**

filename

$nstep_1$ tol_1 $time_1$

$nstep_2$ tol_2 $time_2$

… etc.

The **CALCULATION** module contains calculation information especially for rate-independent model. In order to provide the rate-dependent calculation, $\mathbf{time_i}$ (calculation time in i^{th} loading stages) is introduced into the **CALCULATION_TIME** module.

APPENDIX B

```
!******************************** MCC - Subroutine ************************************!
!
! This file contains a range of subroutines for a  Modified Cam Clay model. These
! routines have been written by Suched Likitlersuang. Feb 2003

!******************************** Mathematic Definition*******************************!

double precision function ilog(x)  ! ~~~~~~~~ Integration of log(x)
   use utils
   implicit none
   real (kind=dp), intent(in) :: x
   ilog=x*log(x)-x
end function ilog

!******************************** Constitutive Equation ******************************!

subroutine makeAA_MCC(STRESS,PROP,alpha,AA) ! ~~~~~~~~~ Elastic Compliance (d2g/dsigma2)
   use utils
   use maxdim
   use values
   implicit none
   real (kind=dp), intent(in)  :: STRESS(MSTR),PROP(MPROP),alpha(MSTR)
   real (kind=dp), intent(out) :: AA(MSTR,MSTR)
   real (kind=dp), external :: delta
   real (kind=dp) :: kappa,gx,p,divSTS(MSTR),divSTS2
   integer :: iSTR,jSTR
   kappa = PROP(1)
   gx    = PROP(3)
   p     = (STRESS(1)+STRESS(2)+STRESS(3))/3.0d0
   divSTS2=0.0d0
   do iSTR=1,MSTR
      divSTS(iSTR)=STRESS(iSTR)-p*delta(iSTR)
      if (iSTR==4) then
         divSTS2=divSTS2+2*divSTS(iSTR)**2
      else
         divSTS2=divSTS2+divSTS(iSTR)**2
      end if
   end do
   do iSTR=1,MSTR
      do jSTR=1,MSTR
                  if ((iSTR<=3).and.(jSTR<=3)) then
            if (iSTR==jSTR) then
               AA(iSTR,jSTR)=(kappa/(9.0d0*abs(p)))+(1.0d0/(3.0d0*gx*abs(p))) &
                        +(divSTS2/(18.0d0*gx*abs(p)**3))-(divSTS(iSTR)/(3.0d0*gx*p**2))
            else
               AA(iSTR,jSTR)=(kappa/(9.0d0*abs(p)))-(1.0d0/(6.0d0*gx*abs(p))) &
                        +(divSTS2/(18.0d0*gx*abs(p)**3))-((divSTS(iSTR)+divSTS(jSTR))/(6.0d0*gx*p**2))
                       end if
                  else if ((iSTR<=4).and.(jSTR<=4)) then
            if ((iSTR==4).and.(jSTR==4)) then
               AA(iSTR,jSTR)=1.0d0/(gx*abs(p))
            else
               AA(iSTR,jSTR)=-STRESS(4)/(3.0d0*gx*p**2)
            end if
                  else
                     AA(iSTR,jSTR)=0.0d0
         end if
      end do
   end do
end subroutine makeAA_MCC

subroutine makeBB_MCC(STRESS,alpha,BB)     ! ~~~~~~~~~ Stress-plastic coupling term (d2g/dalphadsigma)
   use utils
   use maxdim
   use values
   implicit none
   real (kind=dp), intent(in)  :: STRESS(MSTR),alpha(MSTR)
   real (kind=dp), intent(out) :: BB(MSTR,MSTR)
   real (kind=dp), external :: delta
   integer :: iSTR,jSTR
   do iSTR=1,MSTR
       do jSTR=1,MSTR
          if (iSTR==jSTR) then
             BB(iSTR,jSTR)=1.0d0
```

```
            else
                BB(iSTR,jSTR)=0.0d0
            end if
        end do
    end do
end subroutine makeBB_MCC

subroutine makeCC_MCC(STRESS,PROP,alpha,CC)  ! ~~~~~~~~~ Plastic Rate-dependent (dw/dchi)
    use utils
    use maxdim
    use values
    implicit none
    real (kind=dp), intent(in)  :: STRESS(MSTR),PROP(MPROP),alpha(MSTR)
    real (kind=dp), intent(out) :: CC(MSTR)
    real (kind=dp), external :: macaulay,delta
    real (kind=dp) :: kappa,lambda,gx,M,px0,mu
       real (kind=dp) :: px
    real (kind=dp) :: p,divSTS2,chip,divchi2,alphap,divalpha2
    real (kind=dp), dimension(MSTR) :: divSTS,divchi,divalpha
    real (kind=dp) :: chi(MSTR),Yhat,temp
    integer :: iSTR
    kappa  = PROP(1)
    lambda = PROP(2)
    gx     = PROP(3)
    M      = PROP(4)
    mu     = PROP(5)
    px0    = PROP(6)
    p      = (STRESS(1)+STRESS(2)+STRESS(3))/3.0d0
    do iSTR=1,MSTR
       divSTS(iSTR)=STRESS(iSTR)-p*delta(iSTR)
    end do
    alphap=alpha(1)+alpha(2)+alpha(3)
    px    =px0*exp(abs(alphap)/(lambda-kappa))
    do iSTR=1,MSTR
        divalpha(iSTR)=alpha(iSTR)-(alphap/3.0d0)*delta(iSTR)
        if ((iSTR==1).or.(iSTR==2).or.(iSTR==3)) then
           chi(iSTR)=STRESS(iSTR)-px
              else
                    chi(iSTR)=STRESS(iSTR)
        end if
    end do
    chip=(chi(1)+chi(2)+chi(3))/3.0d0
    divchi2=0.0d0
    do iSTR=1,MSTR
        divchi(iSTR)=chi(iSTR)-chip*delta(iSTR)
        if ((iSTR==1).or.(iSTR==2).or.(iSTR==3)) then
           divchi2=divchi2+divchi(iSTR)**2
        else
           divchi2=divchi2+2.0d0*divchi(iSTR)**2
        end if
    end do
    do iSTR=1,MSTR
        temp=sqrt(chip**2+1.50d0*(divchi2)/M**2)
        Yhat=temp-abs(px)
        if (Yhat==0.0d0) then
            CC(iSTR)=0.0d0
        else if (temp==0.0d0) then
            CC(iSTR)=0.0d0
              else if (STRESS(iSTR)==0.0d0) then
                 CC(iSTR)=0.0d0
        else
            if ((iSTR==1).or.(iSTR==2).or.(iSTR==3)) then
               CC(iSTR)=macaulay(Yhat)/(2.0d0*temp*mu)*(2.0d0/3.0d0*chip+3.0d0*divchi(iSTR)/M**2)
                    else
               CC(iSTR)=macaulay(Yhat)/(2.0d0*temp*mu)*(3.0d0*divchi(iSTR)/M**2)
            end if
        end if
    end do
end subroutine makeCC_MCC

subroutine makeiAA_MCC(STRESS,PROP,iAA)  ! ~~~~~~~~~ Elastic Stiffness (AA^-1)
    use utils
    use maxdim
    use values
    implicit none
```

```
   real (kind=dp), intent(in) :: STRESS(MSTR), PROP(MPROP)
   real (kind=dp), intent(out) :: iAA(MSTR,MSTR)
   real (kind=dp) :: kappa,gx,p
   integer :: iSTR,jSTR
   kappa = PROP(1)
   gx    = PROP(3)
   p     = (STRESS(1)+STRESS(2)+STRESS(3))/3.0d0
   do iSTR=1,MSTR
      do jSTR=1,MSTR
                  if ((iSTR<=3).and.(jSTR<=3)) then
            if (iSTR==jSTR) then
               iAA(iSTR,jSTR)=(4.0d0/3.0d0*gx*abs(p))+STRESS(iSTR)*STRESS(jSTR)/(kappa*abs(p))
            else
               iAA(iSTR,jSTR)=(-2.0d0/3.0d0*gx*abs(p))+STRESS(iSTR)*STRESS(jSTR)/(kappa*abs(p))
                     end if
                else if ((iSTR<=4).and.(jSTR<=4)) then
            if ((iSTR==4).and.(jSTR==4)) then
               iAA(iSTR,jSTR)=(gx*abs(p))+(STRESS(iSTR)*STRESS(jSTR)/(kappa*abs(p)))
            else
               iAA(iSTR,jSTR)=STRESS(iSTR)*STRESS(jSTR)/(kappa*abs(p))
            end if
                  else
                     iAA(iSTR,jSTR)=0.0d0
         end if
      end do
   end do
end subroutine makeiAA_MCC

! ******************************** Calculation Strain ***************************************!

subroutine makeSTRAN_MCC(STRESS,PROP,alpha,STRAN)  ! ~~~~~~~~~~~ Calculation strain
   use utils
   use maxdim
   use values
   implicit none
   real (kind=dp), intent(in) :: STRESS(MSTR),PROP(MPROP),alpha(MSTR)
   real (kind=dp), intent(out) :: STRAN(MSTR)
   real (kind=dp), external :: delta
   real (kind=dp) :: kappa,gx,px0,p0,p,divSTS(MSTR),divSTS2
   integer :: iSTR
   kappa = PROP(1)
   gx    = PROP(3)
   px0   = PROP(6)
   p0    = 2.0d0*px0      ! Reference pressure
   p     = (STRESS(1)+STRESS(2)+STRESS(3))/3.0d0
   divSTS2= 0.0d0
   do iSTR=1,MSTR
      divSTS(iSTR)=STRESS(iSTR)-p*delta(iSTR)
      if ((iSTR==1).or.(iSTR==2).or.(iSTR==3)) then
         divSTS2=divSTS2+divSTS(iSTR)**2
      else
         divSTS2=divSTS2+2.0d0*divSTS(iSTR)**2
      end if
   end do
   do iSTR=1,MSTR
      if ((iSTR==1).or.(iSTR==2).or.(iSTR==3)) then
         STRAN(iSTR)=(kappa/3.0d0)*log(abs(p/p0))*(p/abs(p))+divSTS(iSTR)/(2.0d0*gx*abs(p)) &
                -(divSTS2/(12.0d0*gx*p**2))+alpha(iSTR)
      else
                 STRAN(iSTR)=divSTS(iSTR)/(gx*abs(p))+alpha(iSTR)
      end if
   end do
end subroutine makeSTRAN_MCC

!************************* Creation of Elastic Stiffness Matrix ********************************!

subroutine mtyMCCD(INDEX,PROP,STRESS,STATE,D)
   use utils
   use maxdim
   use values
   implicit none
   integer, intent(in) :: INDEX(MINFO)
   real (kind=dp), intent(in) :: PROP(MPROP),STATE(MAXSTA),STRESS(MSTR)
   real (kind=dp), intent(out) :: D(MSTR,MSTR)
   call makeiAA_MCC(STRESS,PROP,D)
```

```
end subroutine mtyMCCD

!****************************** Main MCC model subroutine ************************************!

subroutine MCC(INDEX,PROP,dt,DSTRAN,STATE,STRESS)
   use utils
   use maxdim
   use values
   implicit none
   integer, intent(in) :: INDEX(MINFO)
   integer :: NPROP,NGAU,NSTR,MP
   integer :: iSTR,jSTR
   real (kind=dp), external :: delta
   real (kind=dp), intent(in)  :: dt,PROP(MPROP),DSTRAN(MSTR)
   real (kind=dp), intent(inout) :: STRESS(MSTR),STATE(MAXSTA)
   real (kind=dp) :: alpha(MSTR)
   real (kind=dp) :: iAA(MSTR,MSTR)
   real (kind=dp) :: STRAN(MSTR),dsig(MSTR)
   real (kind=dp) :: AA(MSTR,MSTR),BB(MSTR,MSTR),CC(MSTR)
   real (kind=dp) :: D(MSTR,MSTR),H(MSTR)

   MP=matMCC

   if (MP==matMCC) then ! for MCC model
   do iSTR=1,MSTR
      alpha(iSTR)=STATE(iSTR)
   end do
      !call makeAA_MCC(STRESS,PROP,alpha,AA)          ! ~~~~~~ elastic flexibility matrix
      call makeBB_MCC(STRESS,alpha,BB)               ! ~~~~~~ stress-plastic coupling
      call makeCC_MCC(STRESS,PROP,alpha,CC)          ! ~~~~~~ plastic (rate-dependent)
      call makeiAA_MCC(STRESS,PROP,iAA)              ! ~~~~~~ elastic stiffness matrix

     ! ~~~~~~ Calculation process
      do iSTR=1,MSTR
         do jSTR=1,MSTR
            D(iSTR,jSTR)=BB(iSTR,jSTR)*CC(jSTR)
         end do
            H(iSTR)=DSTRAN(iSTR)-SUM(D(iSTR,1:MSTR))*dt
      end do
         do iSTR=1,MSTR
            dsig(iSTR)=SUM(iAA(iSTR,1:MSTR)*H(1:MSTR))
         end do

      ! ~~~~~~ update STATE (STRESS,STRAN,alpha)
      do iSTR=1,MSTR
         STRESS(iSTR)=STRESS(iSTR)+dsig(iSTR)
         alpha(iSTR)=alpha(iSTR)+CC(iSTR)*dt
         STATE(iSTR)=alpha(iSTR)
      end do
   end if
end subroutine MCC


!**************** Initialisation of State variables (Yield surface location) ***************!

subroutine makeINI_MCC(MP,STRESS0,PSTRESS,PROP,STATE)
   use utils
   use maxdim
   use values
   integer, intent(in) :: MP
   real (kind=dp), intent(in) :: STRESS0(MSTR),PSTRESS(MSTR)
   real (kind=dp), intent(out) :: STATE(MAXSTA)
   real (kind=dp), intent(inout) :: PROP(MPROP)
   real (kind=dp) :: alpha(MSTR)
   real (kind=dp) :: kappa,lambda,gx,M,mu
   real (kind=dp) :: px0,pmax,p0
   real (kind=dp) :: dsig(MSTR), CC(MSTR), STRESS(MSTR)
            real (kind=dp) :: STRLEN, dt
   integer :: iSTR,iYIELD,istep,nstep,istage
   STATE(1:MAXSTA) = 0.0d0
   p0 = (STRESS0(1)+STRESS0(2)+STRESS0(3))/3.0d0      ! ~~~~~~~ initial mean stress
   pmax = (PSTRESS(1)+PSTRESS(2)+PSTRESS(3))/3.0d0    ! ~~~~~~~ historical mean stress
   px0  = pmax/2.0d0
   if (abs(p0) > abs(pmax)) then
      print*, "ERROR INPUT STRESS HISTORY"
```

```
    stop
  end if

  if (MP == matMCC) then   ! ~~~~~~~~  MCC model
    kappa   = PROP(1)
    lambda  = PROP(2)
    gx      = PROP(3)
    M       = PROP(4)
    mu      = PROP(5)
    PROP(6) = px0        ! Reference yield surface
    do iSTR=1,MSTR
                    if ((iSTR==1).or.(iSTR==2).or.(iSTR==3)) then
                      STRESS(iSTR)=px0
                    else
                            STRESS(iSTR)=0.0d0
                    end if
                    alpha(iSTR)=0.0d0
    end do
    do istage=1,2
                    if (istage == 1) then
                            do iSTR=1,MSTR
                                    if ((iSTR==1).or.(iSTR==2).or.(iSTR==3)) then
                                            dsig(iSTR)=(PSTRESS(iSTR)-STRESS(iSTR))
                                    else
                                            dsig(iSTR)=0.0d0
                                    end if
                            end do
                    else if (istage == 2) then
                            do iSTR=1,MSTR
                                    if ((iSTR==1).or.(iSTR==2).or.(iSTR==3)) then
                                            dsig(iSTR)=(STRESS0(iSTR)-PSTRESS(iSTR))
                                    else
                                            dsig(iSTR)=0.0d0
                                    end if
                            end do
      end if
                    STRLEN=sqrt(dsig(1)**2+dsig(2)**2+dsig(3)**2)
                    if (STRLEN < 1.0d-2) then
                            nstep=1
                            dt=1.0d1
                    else if (STRLEN < 1.0d1) then
                            nstep=10
                            dt=1.0d2
                    else if (STRLEN < 1.0d2) then
                            nstep=100
                            dt=1.0d3
                    else if (STRLEN > 1.0d2) then
                            nstep=1000
                            dt=1.0d4
                    end if
                    do istep=1,nstep
                            call makeCC_MCC(STRESS,PROP,alpha,CC)      ! ~~~~~~ plastic (rate-dependent)
                            ! ~~~~~~ update STATE (STRESS,alpha)
                            do iSTR=1,MSTR
                                    STRESS(iSTR)=STRESS(iSTR)+(dsig(iSTR)/nstep)
                                    alpha(iSTR)=alpha(iSTR)+CC(iSTR)*dt
                                    STATE(iSTR)=alpha(iSTR)
                            end do
                    end do
            end do
      end if
end subroutine makeINI_MCC
```

```
!******************************** KHMCC - Subroutine *********************************!
!
! This file contains a range of subroutines for a Kinematic Hardening Modified Cam Clay model. These
! routines have been written by Suched Likitlersuang. Feb 2003

!******************************** Mathematic Definition*******************************************!

double precision function macaulay(x) ! ~~~~~~~~~ Macaulay function
   use utils
   implicit none
   real (kind=dp), intent(in) :: x
   macaulay=(x+ABS(x))/2.0d0
end function macaulay

double precision function delta(i)    ! ~~~~~~~~~ Kronecker's delta
   implicit none
   integer, intent(in) :: i
   if ((i==1).or.(i==2).or.(i==3)) then
       delta=1.0d0
   else
       delta=0.0d0
   end if
end function delta

!******************************** Constitutive Equation ***********************************!

subroutine makeAA_KHMCC(STRESS,PROP,alpha,AA) ! ~~~~~~~~~ Elastic Compliance (d2g/dsigma2)
   use utils
   use maxdim
   use values
   implicit none
   real (kind=dp), intent(in)  :: STRESS(MSTR),PROP(MPROP),alpha(MSTR,MAXYIELD)
   real (kind=dp), intent(out) :: AA(MSTR,MSTR)
   real (kind=dp), external :: delta
   real (kind=dp) :: K,gx,p,divSTS(MSTR),divSTS2
   integer :: iSTR,jSTR
   K  = PROP(1)
   gx = PROP(5)
   AA(1:MSTR,1:MSTR) = 0.0d0
   p  = (STRESS(1)+STRESS(2)+STRESS(3))/3.0d0
   divSTS2 = 0.0d0
   do iSTR=1,MSTR
      divSTS(iSTR)=STRESS(iSTR)-p*delta(iSTR)
      if (iSTR==1.or.iSTR==2.or.iSTR==3) then
         divSTS2=divSTS2+divSTS(iSTR)**2
      else
         divSTS2=divSTS2+2.0d0*divSTS(iSTR)**2
      end if
   end do
   do iSTR=1,MSTR
      do jSTR=1,MSTR
            if ((iSTR<=3).and.(jSTR<=3)) then
            if (iSTR==jSTR) then
               AA(iSTR,jSTR)=(1.0d0/(9.0d0*K))+(1.0d0/(3.0d0*gx*abs(p))) &
               +(divSTS2/(18.0d0*gx*abs(p)**3))-(divSTS(iSTR)/(3.0d0*gx*p**2))
            else
               AA(iSTR,jSTR)=(1.0d0/(9.0d0*K))-(1.0d0/(6.0d0*gx*abs(p))) &
               +(divSTS2/(18.0d0*gx*abs(p)**3))-(divSTS(iSTR)+divSTS(jSTR))/(6.0d0*gx*p*p)
            end if
                 else if ((iSTR<=4).and.(jSTR<=4)) then
            if ((iSTR==4).and.(jSTR==4)) then
               AA(iSTR,jSTR)=1.0d0/(gx*abs(p))
            else
               AA(iSTR,jSTR)=-STRESS(4)/(3.0d0*gx*p**2)
            end if
                  else
                     AA(iSTR,jSTR)=0.0d0
         end if
      end do
   end do
end subroutine makeAA_KHMCC

subroutine makeBB_KHMCC(STRESS,alpha,BB)   ! ~~~~~~~~~ Stress-plastic coupling term (d2g/dalphadsigma)
   use utils
   use maxdim
```

```
    use values
    implicit none
    real (kind=dp), intent(in)  :: STRESS(MSTR),alpha(MSTR,MAXYIELD)
    real (kind=dp), intent(out) :: BB(MSTR,MSTR,MAXYIELD)
    real (kind=dp), external :: delta
    integer :: iSTR,jSTR
    BB(1:MSTR,1:MSTR,1:MAXYIELD) = 0.0d0
    do iSTR=1,MSTR
       do jSTR=1,MSTR
         if (iSTR==jSTR) then
           BB(iSTR,jSTR,1:MAXYIELD)=1.0d0
         else
           BB(iSTR,jSTR,1:MAXYIELD)=0.0d0
         end if
       end do
    end do
end subroutine makeBB_KHMCC

subroutine makeCC_KHMCC(STRESS,PROP,alpha,CC)   ! ~~~~~~~~~ Plastic Rate-dependent (dw/dchi)
    use utils
    use maxdim
    use values
    implicit none
    real (kind=dp), intent(in)  :: STRESS(MSTR),PROP(MPROP),alpha(MSTR,MAXYIELD)
    real (kind=dp), intent(out) :: CC(MSTR,MAXYIELD)
    real (kind=dp), external :: macaulay,delta
    real (kind=dp) :: K,ap,bp,r,gx,aq,bq,M,mu,eta
    real (kind=dp) :: p,chip,divchi2,alphap,divalpha2
    real (kind=dp), dimension(MSTR) :: divchi,divalpha
    real (kind=dp) :: chi(MSTR,MAXYIELD),hp(MAXYIELD),hq(MAXYIELD),Yhat,temp
    integer :: iSTR,iYIELD
    K  = PROP(1)
    ap = PROP(2)
    bp = PROP(3)
    r  = PROP(4)
    gx = PROP(5)
    aq = PROP(6)
    bq = PROP(7)
    M  = PROP(8)
    mu = PROP(9)
    divchi(1:MSTR) = 0.0d0
    divalpha(1:MSTR) = 0.0d0
    CC(1:MSTR,1:MAXYIELD) = 0.0d0
    p  = (STRESS(1)+STRESS(2)+STRESS(3))/3.0d0
    do iYIELD=1,MAXYIELD
       eta=real(iYIELD)/real(MAXYIELD)
       hp(iYIELD)=K*(1.0d0-r*eta)**bp/(2.0d0*(ap-1.0d0))
       hq(iYIELD)=3.0d0*gx*abs(p)*(1.0d0-eta)**bq/(2.0d0*(aq-1.0d0))
       if (iYIELD==MAXYIELD) then
          hq(MAXYIELD)=3.0d0*gx*abs(p)*(1.0d-5)**bq/(2.0d0*(aq-1.0d0))
       end if
       alphap=alpha(1,iYIELD)+alpha(2,iYIELD)+alpha(3,iYIELD)
       do iSTR=1,MSTR
          divalpha(iSTR)=alpha(iSTR,iYIELD)-(alphap/3.0d0)*delta(iSTR)
          if ((iSTR==1).or.(iSTR==2).or.(iSTR==3)) then
             chi(iSTR,iYIELD)=STRESS(iSTR)-hp(iYIELD)*alphap &
                        -2.0d00*hq(iYIELD)*divalpha(iSTR)/3.0d0
          else
                     chi(iSTR,iYIELD)=STRESS(iSTR)-hq(iYIELD)/3.0d0*divalpha(iSTR)
                  end if
       end do
       chip=(chi(1,iYIELD)+chi(2,iYIELD)+chi(3,iYIELD))/3.0d0
       divchi2=0.0d0
       do iSTR=1,MSTR
          divchi(iSTR)=chi(iSTR,iYIELD)-chip*delta(iSTR)
          if (iSTR==1.or.iSTR==2.or.iSTR==3) then
             divchi2=divchi2+divchi(iSTR)**2
          else
             divchi2=divchi2+2.0d0*divchi(iSTR)**2
          end if
       end do
       do iSTR=1,MSTR
          temp=sqrt(chip**2+1.50d0*(divchi2)/M**2)
          Yhat=temp-hp(iYIELD)*abs(alphap)*eta
          if (Yhat==0.0d0) then
```

```
            CC(iSTR,iYIELD)=0.0d0
          else if (temp==0.0d0) then
            CC(iSTR,iYIELD)=0.0d0
                else if (STRESS(iSTR)==0.0d0) then
                    CC(iSTR,iYIELD)=0.0d0
          else
            if ((iSTR==1).or.(iSTR==2).or.(iSTR==3)) then
              CC(iSTR,iYIELD)=macaulay(Yhat)/(2.0d0*temp*mu)*(2.0d0/3.0d0*chip+3.0d0*divchi(iSTR)/M**2)
            else
              CC(iSTR,iYIELD)=macaulay(Yhat)/(2.0d0*temp*mu)*(3.0d0*divchi(iSTR)/M**2)
            end if
          end if
      end do
  end do
end subroutine makeCC_KHMCC

subroutine makeiAA_KHMCC(STRESS,PROP,iAA)  ! ~~~~~~~~~~ Elastic Stiffness (AA^-1)
   use utils
   use maxdim
   use values
   implicit none
   real (kind=dp), intent(in) :: STRESS(MSTR), PROP(MPROP)
   real (kind=dp), intent(out) :: iAA(MSTR,MSTR)
   real (kind=dp) :: K,gx,p
   integer :: iSTR,jSTR
   K  = PROP(1)
   gx = PROP(5)
   iAA(1:MSTR,1:MSTR) = 0.0d0
   p  = (STRESS(1)+STRESS(2)+STRESS(3))/3.0d0
   do iSTR=1,MSTR
      do jSTR=1,MSTR
           if ((iSTR<=3).and.(jSTR<=3)) then
           if (iSTR==jSTR) then
              iAA(iSTR,jSTR)=(4.0d0/3.0d0*gx*abs(p))+K*STRESS(iSTR)*STRESS(jSTR)/p**2
           else
              iAA(iSTR,jSTR)=(-2.0d0/3.0d0*gx*abs(p))+K*STRESS(iSTR)*STRESS(jSTR)/p**2
                   end if
               else if ((iSTR<=4).and.(jSTR<=4)) then
           if ((iSTR==4).and.(jSTR==4)) then
              iAA(iSTR,jSTR)=(gx*abs(p))+(K*STRESS(iSTR)*STRESS(jSTR)/p**2)
           else
              iAA(iSTR,jSTR)=K*STRESS(iSTR)*STRESS(jSTR)/p**2
           end if
                else
                  iAA(iSTR,jSTR)=0.0d0
         end if
      end do
   end do
end subroutine makeiAA_KHMCC

! ******************************** Calculation Strain ****************************************!

subroutine makeSTRAN_KHMCC(STRESS,PROP,alpha,STRAN)  ! ~~~~~~~~~~~ Calculation strain
   use utils
   use maxdim
   use values
   implicit none
   real (kind=dp), intent(in) :: STRESS(MSTR),PROP(MPROP),alpha(MSTR,MAXYIELD)
   real (kind=dp), intent(out) :: STRAN(MSTR)
   real (kind=dp), external :: delta
   real (kind=dp) :: K,gx,p,divSTS(MSTR),divSTS2
   integer :: iSTR,deta
   K  = PROP(1)
   gx = PROP(5)
   STRAN(1:MSTR) = 0.0d0
   p  = (STRESS(1)+STRESS(2)+STRESS(3))/3.0d0
   divSTS2=0.0d0
   do iSTR=1,MSTR
      divSTS(iSTR)=STRESS(iSTR)-p*delta(iSTR)
      if (iSTR==1.or.iSTR==2.or.iSTR==3) then
         divSTS2=divSTS2+divSTS(iSTR)**2
      else
         divSTS2=divSTS2+2.0d0*divSTS(iSTR)**2
      end if
   end do
```

```
   deta=1.0d0/real(MAXYIELD)
   do iSTR=1,MSTR
      if (iSTR==1.or.iSTR==2.or.iSTR==3) then
         STRAN(iSTR)=p/(3.0d0*K)+divSTS(iSTR)/(2.0d0*gx*abs(p))-(divSTS2/(12.0d0*gx*p**2)) &
               +SUM(alpha(iSTR,1:MAXYIELD))*deta
      else
         STRAN(iSTR)=divSTS(iSTR)/(gx*abs(p))+SUM(alpha(iSTR,1:MAXYIELD))*deta
      end if
   end do
end subroutine makeSTRAN_KHMCC

!************************* Creation of Elastic Stiffness Matrix ********************************!

subroutine mtyKHMCCD(INDEX,PROP,STRESS,STATE,D)
   use utils
   use maxdim
   use values
   implicit none
   integer, intent(in) :: INDEX(MINFO)
   real (kind=dp), intent(in) :: PROP(MPROP),STATE(MAXSTA),STRESS(MSTR)
   real (kind=dp), intent(out) :: D(MSTR,MSTR)
   D(1:MSTR,1:MSTR) = 0.0d0
   call makeiAA_KHMCC(STRESS,PROP,D)
end subroutine mtyKHMCCD


!****************************** Main KHMCC model subroutine ***********************************!

subroutine KHMCC(INDEX,PROP,dt,DSTRAN,STATE,STRESS)
   use utils
   use maxdim
   use values
   implicit none
   integer, intent(in) :: INDEX(MINFO)
   integer :: NPROP,NGAU,NSTR,MP
   integer :: iYIELD,iSTR,jSTR
   real (kind=dp), external :: delta
   real (kind=dp), intent(in)  :: dt,PROP(MPROP),DSTRAN(MSTR)
   real (kind=dp), intent(inout) :: STRESS(MSTR),STATE(MAXSTA)
   real (kind=dp) :: alpha(MSTR,MAXYIELD)
   real (kind=dp) :: iAA(MSTR,MSTR)
   real (kind=dp) :: STRAN(MSTR),dsig(MSTR)
   real (kind=dp) :: eta,deta
   real (kind=dp) :: AA(MSTR,MSTR),BB(MSTR,MSTR,MAXYIELD),CC(MSTR,MAXYIELD)
   real (kind=dp) :: D(MSTR,MSTR,MAXYIELD),H(MSTR)

   MP=matKHMCC
   if (MP==matKHMCC) then ! for mutiyield surface kinematic hardeing MCC model
      deta=1.0d0/real(MAXYIELD)
      do iSTR=1,MSTR
         do iYIELD=1,MAXYIELD
            alpha(iSTR,iYIELD)=STATE((iSTR-1)*MAXYIELD+iYIELD)
         end do
      end do
      !call makeAA_KHMCC(STRESS,PROP,alpha,AA)          ! ~~~~~~ elastic flexibility matrix
      call makeBB_KHMCC(STRESS,alpha,BB)                  ! ~~~~~~ stress-plastic coupling
      call makeCC_KHMCC(STRESS,PROP,alpha,CC)             ! ~~~~~~ plastic (rate-dependent)
      call makeiAA_KHMCC(STRESS,PROP,iAA)           ! ~~~~~~ elastic stiffness matrix

   ! ~~~~~~ Calculation process
      do iSTR=1,MSTR
         do jSTR=1,MSTR
            do iYIELD=1,MAXYIELD
               D(iSTR,jSTR,iYIELD)=BB(iSTR,jSTR,iYIELD)*CC(jSTR,iYIELD)
            end do
         end do
         H(iSTR)=DSTRAN(iSTR)-(SUM(D(iSTR,1:MSTR,1:MAXYIELD))*deta)*dt
      end do
      do iSTR=1,MSTR
         dsig(iSTR)=SUM(iAA(iSTR,1:MSTR)*H(1:MSTR))
      end do

   ! ~~~~~~ update STATE (STRESS,STRAN,alpha)
      do iSTR=1,MSTR
         STRESS(iSTR)=STRESS(iSTR)+dsig(iSTR)
```

```
        do iYIELD=1,MAXYIELD
          alpha(iSTR,iYIELD)=alpha(iSTR,iYIELD)+CC(iSTR,iYIELD)*dt
          STATE((iSTR-1)*MAXYIELD+iYIELD)=alpha(iSTR,iYIELD)
        end do
      end do
    end if
end subroutine KHMCC

!**************** Initialisation of State variables (Yield surface location) ***************!

subroutine makeINI_KHMCC(MP,STRESS0,PSTRESS,PROP,STATE)
    use utils
    use maxdim
    use values
    integer, intent(in) :: MP
    real (kind=dp), intent(in) :: STRESS0(MSTR),PSTRESS(MSTR)
    real (kind=dp), intent(out) :: STATE(MAXSTA)
    real (kind=dp), intent(inout) :: PROP(MPROP)
    real (kind=dp) :: alpha(MSTR,MAXYIELD), hp(MAXYIELD)
    real (kind=dp) :: K,ap,bp,r,gx,aq,bq,M,mu,p,alphap,chip
    real (kind=dp) :: px0,pmax,p0
    real (kind=dp) :: CC(MSTR,MAXYIELD)
    real (kind=dp) :: dsig(MSTR), STRESS(MSTR)
            real (kind=dp) :: STRLEN, dt
    integer :: iSTR,iYIELD,istep,nstep,istage
    STATE(1:MAXSTA) = 0.0d0
    p0 = (STRESS0(1)+STRESS0(2)+STRESS0(3))/3.0d0      ! ~~~~~~~ initial mean stress
    pmax = (PSTRESS(1)+PSTRESS(2)+PSTRESS(3))/3.0d0    ! ~~~~~~~ historical mean stress
    px0  = pmax/2.0d0
    if (abs(p0) > abs(pmax)) then
      print*, "WARNING: ERROR INPUT STRESS HISTORY"
    end if
    if (MP==matKHMCC) then  ! ~~~~~~~~ KHMCC model
      K    = PROP(1)
      ap   = PROP(2)
      bp   = PROP(3)
      r    = PROP(4)
      gx   = PROP(5)
      aq   = PROP(6)
      bq   = PROP(7)
      M    = PROP(8)
      mu   = PROP(9)
      do iSTR=1,MSTR
        if ((iSTR==1).or.(iSTR==2).or.(iSTR==3)) then
          STRESS(iSTR)=px0
                                    do iYIELD=1,MAXYIELD
          eta=real(iYIELD)/real(MAXYIELD)
          hp(iYIELD)=K*(1.0d0-r*eta)**bp/(2.0d0*(ap-1.0d0))
          alpha(iSTR,iYIELD)=px0/(3.0d0*hp(iYIELD))
        end do
        else
          alpha(iSTR,1:MAXYIELD)=0.0d0
        end if
      end do
      do istage=1,2
                                  if (istage == 1) then
                                        do iSTR=1,MSTR
                                              if ((iSTR==1).or.(iSTR==2).or.(iSTR==3)) then
                                                    dsig(iSTR)=(PSTRESS(iSTR)-STRESS(iSTR))
                                              else
                                                    dsig(iSTR)=0.0d0
                                              end if
                                        end do
                                  else if (istage == 2) then
                                        do iSTR=1,MSTR
                                              if ((iSTR==1).or.(iSTR==2).or.(iSTR==3)) then
                                                    dsig(iSTR)=(STRESS0(iSTR)-PSTRESS(iSTR))
                                              else
                                                    dsig(iSTR)=0.0d0
                                              end if
                                        end do
        end if
                                  STRLEN=sqrt(dsig(1)**2+dsig(2)**2+dsig(3)**2)
                                  if (STRLEN < 1.0d-2) then
                                        nstep=1
```

```
                                        dt=1.0d0
                                else if (STRLEN < 1.0d1) then
                                        nstep=10
                                        dt=1.0d0
                                else if (STRLEN < 1.0d2) then
                                        nstep=100
                                        dt=1.0d1
                                else if (STRLEN > 1.0d2) then
                                        nstep=1000
                                        dt=1.0d2
                                end if
                                do istep=1,nstep
                                        call makeCC_KHMCC(STRESS,PROP,alpha,CC)     ! ~~~~~~ plastic (rate-
dependent)
                                        ! ~~~~~~ update STATE (STRESS,alpha)
                                        do iSTR=1,MSTR
                                                STRESS(iSTR)=STRESS(iSTR)+(dsig(iSTR)/nstep)
                                                do iYIELD=1,MAXYIELD

        alpha(iSTR,iYIELD)=alpha(iSTR,iYIELD)+CC(iSTR,iYIELD)*dt
                                                        STATE((iSTR-
1)*MAXYIELD+iYIELD)=alpha(iSTR,iYIELD)
                                                end do
                                        end do
                                end do
                        end do
   end if
end subroutine makeINI_KHMCC
```